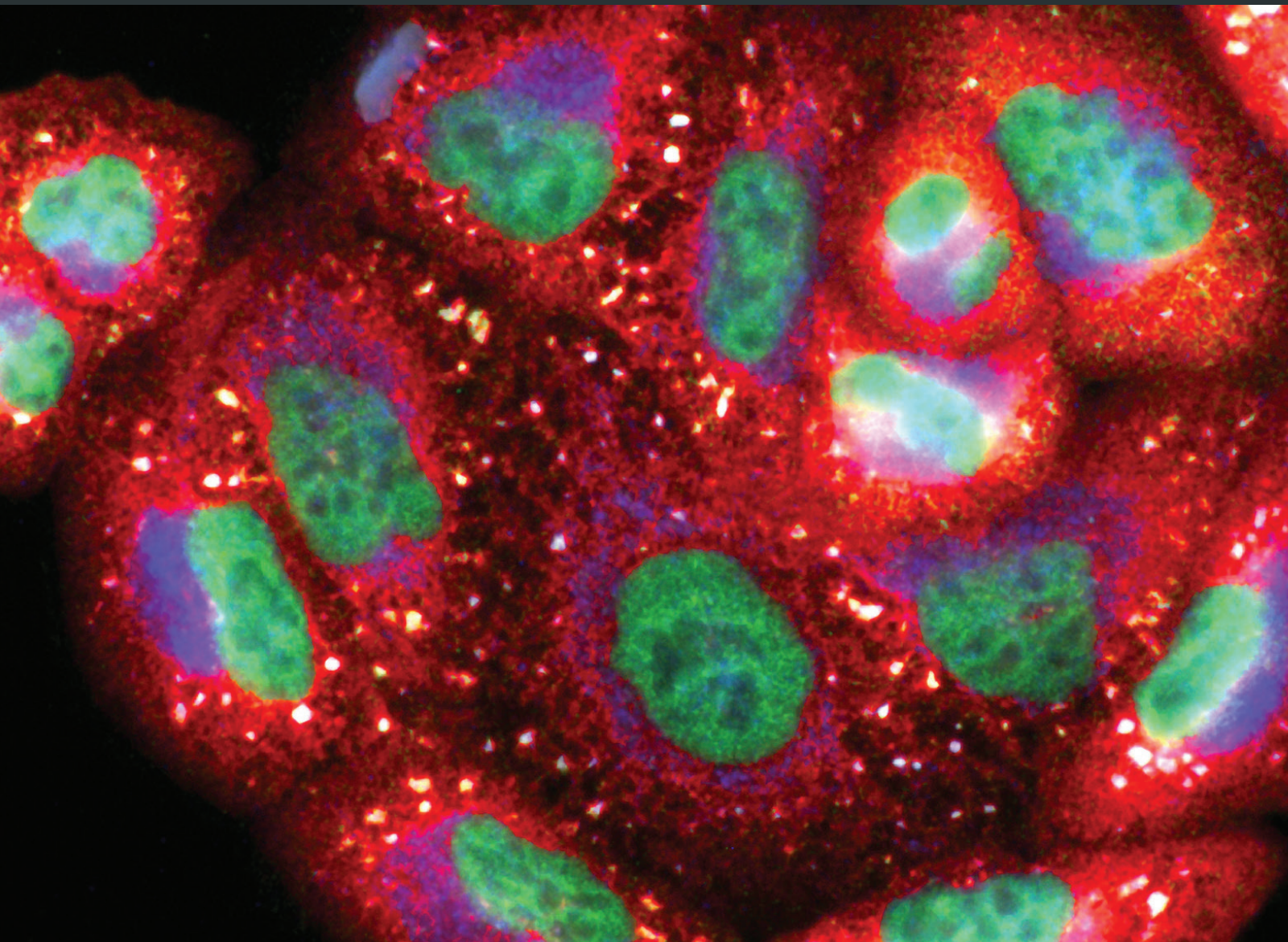# Oxidative Stress and Inflammation Interaction in Ischemia Reperfusion Injury: Role of Programmed Cell Death

Lead Guest Editor: Weifeng Yao
Guest Editors: Lydia W. Tai, Ziqing Hei, Yiwei Liu, and Haobo Li

Oxidative Stress and Inflammation Interaction in Ischemia Reperfusion Injury: Role of Programmed Cell Death

Oxidative Stress and Inflammation Interaction in Ischemia Reperfusion Injury: Role of Programmed Cell Death

Lead Guest Editor: Weifeng Yao
Guest Editors: Lydia W. Tai, Ziqing Hei, Yiwei Liu, and Haobo Li

Editorial Board

Contents

Editorial

Oxidative Stress and Inflammation Interaction in Ischemia Reperfusion Injury: Role of Programmed Cell Death

Weifeng Yao [1], **Lydia Wai Tai,** [2] **Yiwei Liu,** [3] **Ziqing Hei** [1] **and Haobo Li** [4]

[1]Department of Anesthesiology, The Third Affiliated Hospital of Sun Yat-sen University, Guangdong 510630, China
[2]University of Hong Kong, Pokfulam, Hong Kong
[3]St. Jude Children's Research Hospital, Memphis 38105, USA
[4]Corrigan-Minehan Heart Center and Cardiology Division, Massachusetts General Hospital, Harvard Medical School, Boston, MA 02114, USA

Correspondence should be addressed to Weifeng Yao; yaowf3@mail.sysu.edu.cn

Ischemia-reperfusion-induced tissue injuries and organ failure are key contributors to postoperative mortality and morbidity [1]. Different types of programmed cell death mediated by oxidative stress and inflammation play critical roles in this pathology [2].

Initiation of programmed cell death by reactive oxygen species- (ROS-) induced oxidative stress plays important roles in ischemia-reperfusion injury (IRI) in multiple organs [3]. In this special issue, W. Yao et al. reported that oxidative stress induced hepatic cell apoptosis and liver dysfunction after orthotopic autologous liver transplantation (OALT), while inhibiting oxidative stress with either anesthetic propofol or selective NADPH oxidase inhibitor VAS2870, reduced hepatic cell apoptosis, and attenuated liver injury after OALT. Further, the induction of pyroptosis and disruption of autophagy also play critical roles in organ dysfunction as reported in this special issue. G.-H. Zheng et al. demonstrated that the induction of pyroptotic cell death mediated via nod-like receptor protein-3 (NLRP3) inflammasome is critical in high-fat diet-induced kidney damage and that the downregulation of vascular endothelial growth factor receptor-2 (VEGFR2) not only reduced NLRP3 activation but also attenuated kidney injury in high-fat diet-treated mice. Moreover, Y. Wang et al. reported that in mouse transient global cerebral ischemia (TGCI), decreased autophagy was accompanied by increased apoptosis in neurons that were associated with neurological dysfunction. Lentiviral or specific agonist overexpression of transient receptor potential

mucolipin-1 (TRPML1) enhanced autophagy but inhibited apoptosis and attenuated neurological dysfunction in TGCI.

The importance of oxidative stress in the cause of IRI has been well recognized [4]. Thus, therapies that reduce oxidative stress either by increasing antioxidant capacity or by decreasing ROS production may protect organs against IRI. In this special issue, W. Yao et al. reported that pretreatment with intravenous anesthetic propofol, a potent ROS scavenger that protects the heart against IRI, mitigated OALT-induced cell apoptosis and liver injury. Moreover, G.-H. Zheng et al. reported that purple sweet potato color, a natural anthocyanin, conferred its renal protection through reducing ROS and the subsequent NLRP3 activation in high-fat diet-treated mice. On the other hand, Y. Wang et al. showed that microRNAs (miR-214 and miR-133a), delivered by bone marrow mesenchymal stem cell-derived exosomes, by downregulating CaMKII (by miR-214) and phospholamban (by miR-133a), reduced cardiac stem cell apoptosis under oxidative stress.

Aggravation and persistence of inflammation, secondary to oxidative stress, have been shown to induce programmed cell death and contribute to IRI and organ injury [5]. In this special issue, G.-H. Zheng et al. reported that 20 weeks of high-fat diet treatment-induced ROS overproduction and inflammation, which subsequently activates NLRP3 (mediator of inflammation-induced pyroptosis), leads to kidney injury. Treatment with α-lipoic acid, a ROS scavenger, not only mitigated high-fat diet-induced inflammation but also

deactivated NLRP3 and attenuated kidney damage. Similarly, W. Yao et al. reported in this special issue that OALT-induced oxidative stress and inflammation were associated with hepatic apoptosis and liver damage and that the application of propofol or NADPH oxidase inhibitor reduced oxidative stress and inflammation, attenuating liver damage. These findings suggest the potential interaction of oxidative stress and inflammation in the induction of programmed cell death during IRI. It is worth noticing that attempts to attenuate organ injury by solely decreasing inflammation or increasing antioxidant capacity have achieved limited success [6, 7], indicating that multifaceted therapies combining anti-inflammatory and antioxidant approaches may be necessary for effective treatment. Thus, further in-depth studies regarding the interaction of inflammation and oxidative stress in the setting of IRI may facilitate our understanding of the pathophysiology of IRI and the development of new therapies for the disease.

We hope that the research articles presented in this special issue contribute to the understanding of current advancements and the mechanisms of oxidative stress and inflammation-mediated programmed cell death in IRI. It is also our hope to stimulate further efforts in the pathological investigation of IRI and the development of therapy for this disease.

We would like to express our gratitude toward the authors for submitting their exciting research for consideration for publication and to the reviewers for sharing their expertise and precious time in reviewing the manuscripts. Thanks to all of those who contributed to the success of this special issue.

Conflicts of Interest

The authors declare that there is no conflicts of interest regarding the publication of this Special Issue.

Authors' Contributions

Haobo Li and Weifeng Yao wrote the editorial; Lydia Wai Tai, Ziqing Hei, and Yiwei Liu revised the editorial; Weifeng Yao, Lydia Wai Tai, Ziqing Hei, Yiwei Liu, and Haobo Li approved the content of the editorial.

Weifeng Yao
Lydia Wai Tai
Yiwei Liu
Ziqing Hei
Haobo Li

References

[1] H. Li, W. Yao, Z. Liu et al., "Hyperglycemia abrogates ischemic postconditioning cardioprotection by impairing adipor1/caveolin-3/stat3 signaling in diabetic rats," *Diabetes*, vol. 65, no. 4, pp. 942–955, 2016.

[2] G. A. Kurian, R. Rajagopal, S. Vedantham, and M. Rajesh, "The role of oxidative stress in myocardial ischemia and reperfusion injury and remodeling: revisited," *Oxidative Medicine and Cellular Longevity*, vol. 2016, Article ID 1656450, 14 pages, 2016.

[3] A. Shekhar, P. Heeger, C. Reutelingsperger et al., "Targeted imaging for cell death in cardiovascular disorders," *JACC: Cardiovascular Imaging*, vol. 11, no. 3, pp. 476–493, 2018.

[4] T. Wang, X. Mao, H. Li et al., "*N*-Acetylcysteine and allopurinol up-regulated the Jak/STAT3 and PI3K/Akt pathways via adiponectin and attenuated myocardial postischemic injury in diabetes," *Free Radical Biology & Medicine*, vol. 63, pp. 291–303, 2013.

[5] W. Yao, H. Li, G. Luo et al., "SERPINB1 ameliorates acute lung injury in liver transplantation through ERK1/2-mediated STAT3-dependent HO-1 induction," *Free Radical Biology & Medicine*, vol. 108, pp. 542–553, 2017.

[6] M. F. Tsan, "Superoxide dismutase and pulmonary oxygen toxicity: lessons from transgenic and knockout mice (review)," *International Journal of Molecular Medicine*, vol. 7, no. 1, pp. 13–19, 2001.

[7] R. J. van Klaveren, D. Dinsdale, J. L. Pype, M. Demedts, and B. Nemery, "N-Acetylcysteine does not protect against type II cell injury after prolonged exposure to hyperoxia in rats," *American Journal of Physiology-Lung Cellular and Molecular Physiology*, vol. 273, no. 3, pp. L548–L555, 1997.

Research Article

High Glucose Enhances Bupivacaine-Induced Neurotoxicity via MCU-Mediated Oxidative Stress in SH-SY5Y Cells

**Zhong-Jie Liu, Wei Zhao, Hong-Yi Lei, Hua-Li Xu, Lu-Ying Lai, Rui Xu [ID],
and Shi-Yuan Xu [ID]**

*Department of Anesthesiology, Zhujiang Hospital, Southern Medical University, No. 253 Middle Gongye Street, Guangzhou,
510282 Guangdong, China*

Correspondence should be addressed to Rui Xu; xuruky@hotmail.com and Shi-Yuan Xu; xsy998@smu.edu.cn

Bupivacaine, a typical local anesthetic, induces neurotoxicity via reactive oxygen species regulation of apoptosis. High glucose could enhance bupivacaine-induced neurotoxicity through regulating oxidative stress, but the mechanism of it is not clear. Mitochondrial calcium uniporter (MCU), a key channel for regulating the mitochondrial Ca^{2+} (mCa^{2+}) influx, is closely related to oxidative stress via disruption of mCa^{2+} homeostasis. Whether MCU is involved in high glucose-sensitized bupivacaine-induced neurotoxicity remains unknown. In this study, human neuroblastoma (SH-SY5Y) cells were cultured with high glucose and/or bupivacaine, and the data showed that high glucose enhanced bupivacaine-induced MCU expression elevation, mCa^{2+} accumulation, and oxidative damage. Next, Ru360, an inhibitor of MCU, was employed to pretreated SH-SY5Y cells, and the results showed that it could decrease high glucose and bupivacaine-induced mCa^{2+} accumulation, oxidative stress, and apoptosis. Further, with the knockdown of MCU with a specific small interfering RNA (siRNA) in SH-SY5Y cells, we found that it also could inhibit high glucose and bupivacaine-induced mCa^{2+} accumulation, oxidative stress, and apoptosis. We propose that downregulation expression or activity inhibition of the MCU channel might be useful for restoring the mitochondrial function and combating high glucose and bupivacaine-induced neurotoxicity. In conclusion, our study demonstrated the crucial role of MCU in high glucose-mediated enhancement of bupivacaine-induced neurotoxicity, suggesting the possible use of this channel as a target for curing bupivacaine-induced neurotoxicity in diabetic patients.

1. Introduction

About 113.9 million Chinese and over 300 million worldwide suffer from diabetes mellitus, and the number is expected to enlarge further in the future [1, 2]. Polyneuropathy, a common complication of diabetes, afflicts about 50%-60% of diabetic patients and is closely related to poor glycemic control [3, 4]. Patients with diabetic polyneuropathy receiving intrathecal anesthesia or analgesia are at increased risk of neurological dysfunction, but the mechanism remains unclear [5].

Sufficient evidence has confirmed that local anesthetics, including bupivacaine, lidocaine, and ropivacaine, induce neurotoxic damage in cell and animal models [6–9]. In addition, previous studies have provided detailed evidence on local anesthetic-induced neurotoxicity triggered by oxidative stress [10]. Bupivacaine, one of the commonly used local anesthetics in clinics, induces cell apoptosis via reactive oxygen species (ROS). Compared with other local anesthetics, it has a more significant neurotoxic effect [11, 12]. Studies have confirmed some key factors for synergism to regulate bupivacaine-induced ROS overproduction. It can decrease respiratory chain complex activity, uncouple oxidative phosphorylation, and inhibit ATP production which leads to mitochondrial membrane potential collapse [13]. ATP production dysfunction leads to adenosine monophosphate-activated protein kinase activation and aggravates ROS overproduction, leading to bupivacaine-induced apoptosis and neurotoxicity [14]. Hyperglycemia also causes neurotoxicity through inducing oxidative stress [15, 16]. Our previous study has shown that bupivacaine-induced neurotoxicity was enhanced in neuronal cell incubation with high glucose [17]. However,

the mechanism responsible for the above phenomenon remains unknown.

Mitochondrial calcium uniporter (MCU), a key channel of mitochondrial Ca^{2+} (mCa^{2+}) uptake, is widely expressed in a number of tissue cells, including neurons, cardiomyocytes, and pancreatic β-cells [18–20]. Recent studies show that MCU plays a crucial role in cell signal transduction, energy metabolism, and apoptosis via regulating Ca^{2+} uptake into the mitochondrial matrix [21–23]. MCU excessive activation could induce a higher mCa^{2+} uptake rate and mitochondrial ROS (mROS) elevation and mediate cell apoptosis [24]. During oxidative stress, mitochondrial reenergization allows the recovery of membrane potential via MCU-driven Ca^{2+} uptake into the mitochondria and subsequently induces mCa^{2+} overload. Above events result in mitochondrial dysfunction and more severe mROS overproduction via opening the mitochondrial transition pore (mPTP) which initiates mitochondrial pathway apoptosis [25–27]. Whether MCU activity is changed and whether it mediates oxidative damage leading to high glucose enhancing bupivacaine-induced neurotoxicity have not been reported.

Human neuroblastoma (SH-SY5Y) cell, similar to the biological characteristic of normal neural cell, is used to research local anesthetic-induced neurotoxicity [12]. In the present study, we used it to build a cell model of bupivacaine-induced neurotoxicity and estimate the role of MCU in high glucose-mediated enhancement of bupivacaine-induced neurotoxicity. This study could provide reference for the treatment of bupivacaine-induced neurotoxicity in diabetic patients.

2. Materials and Methods

2.1. Reagents. The SH-SY5Y cell line was purchased from Shanghai Institutes for Biological Sciences (Shanghai, China). Dulbecco's modified Eagle medium (DMEM)/F12 (including 17.5 mM glucose) and fetal bovine serum were purchased from Gibco company (Grand Island, NY, USA). Bupivacaine hydrochloride, glucose, Ru360, and dimethyl sulfoxide (DMSO) were purchased from Sigma-Aldrich (St. Louis, MO, USA). Rhod-2-acetoxymethyl ester (Rhod-2/AM) was purchased from Invitrogen (Carlsbad, CA, USA). Other reagents are the following: $2',7'$-dichlorofluorescein diacetate (DCFH-DA) (Beyotime, Haimen, China), propidium iodide and annexin V-fluorescein isothiocyanate (FITC) (KeyGEN, Nanjing, China), anti-MCU (Abcam, Cambridge, MA, USA), and anti-β-actin (KangChen Biotech, Shanghai, China).

2.2. Cell Culture. SH-SY5Y cells were cultured in a DMEM/F12 medium and 5% CO_2 at 37°C. The medium was mixed with 10% FBS and 1% penicillin/streptomycin and replaced every two days during cell growth. Bupivacaine hydrochloride and glucose were dissolved in the culture media.

2.3. Cell Viability Assay. Cell viability was measured according to the manufacturer's instructions with the MTT assay (Dallas, TX, USA). Briefly, after treatment, MTT (10 μl, 5 mg/ml) was added into each well and final concentration was 0.5 mg/ml. The cells were incubated at 37°C for 4 h.

Formazan generated by cells was solubilized in DMSO. Absorbance was read at 540 nm with a microplate reader (Bio-Rad, CA, USA). Cell viability of every group was analyzed as percentage of the control group.

2.4. Detection of 8-Hydroxydeoxyguanosine (8-OHdG) by ELISA. The 8-OHdG production in SH-SY5Y cells was determined using an ELISA kit (R&D Systems, MN, USA) according to the manufacturer's instructions. Cell DNA was extracted using a DNeasy tissue kit and sample was assayed in duplicate. Average concentration of 8-OHdG (ng/ml) for every group was analyzed.

2.5. Quantitative Real-Time Polymerase Chain Reaction (qRT-PCR). After extraction of the total RNA and reverse transcription synthesis of cDNA using TRIzol (Invitrogen, Carlsbad, CA) and PrimeScript® RT Master Mix (Takara, Otsu, Japan), PCR was carried out with SYBR Green Master Mix Kit (Takara) and LightCycler 480 (Applied Biosystems, Foster City, CA). MCU mRNA subtypes were quantified with the $2^{-\Delta\Delta C_T}$ method as described previously [28]. The primers were human MCU and β-actin: MCU: forward: 5′-GGACTGTGTAGGCATCTTCTG-3′, reverse: 5′-CAATGA CAGCTCCCACAAAG-3′ and β-actin: forward: 5′-TGGA TCAGCAAGCAGGAGTA-3′, reverse: 5′-TCGGCCACA TTGTGAACTTT-3′.

2.6. Western Blot Assay. Total protein extraction, protein content determination, electrophoresis, transfer membrane, and immunoblotting were performed as described previously [29]. Immunoblotting was performed with an anti-MCU antibody (1:500) and anti-β-actin antibody (1:1,000) overnight at 4°C. Analysis of protein density of the target band was performed using Quantity One analysis software (Bio-Rad, Hercules, CA). MCU protein expression was characterized by measuring the intensities of bands and compared to corresponding β-actin and control bands.

2.7. Measurement of mCa^{2+} Levels. The Ca^{2+} fluorescent indicator Rhod-2/AM was used to measure mCa^{2+} levels in cells as described previously [30]. The data were recorded at 552 nm (excitation wavelength) and 581 nm (emission wavelength). Rhod-2/AM fluorescence intensities of cells were analyzed using flow cytometry (BD Biosciences, Franklin Lakes, NJ, USA) and a confocal scanning laser microscope (FV300, Olympus, Tokyo, Japan).

2.8. Detection of mROS Production. Mitochondrial ROS production was detected by analyzing fluorescence intensity of the MitoSOX probe (Invitrogen, Carlsbad, CA). MitoSOX selectively binds to mitochondrial superoxide and is used to evaluate mROS production. The MitoSOX probe was added into the culture medium and its final concentration is 50 μM. Cells were cultured for 30 min at 37°C. After cleaning, the emission of 580 nm was determined by 488 nm wavelength excitation.

2.9. Knockdown of MCU with Small Interfering RNAs (siRNAs). MCU siRNAs (5′-GCCAGAGACAGACAAUAC UdTdT-3′ and 3′-dTdTGGUCUCUGUCUGUUAUGA-5′)
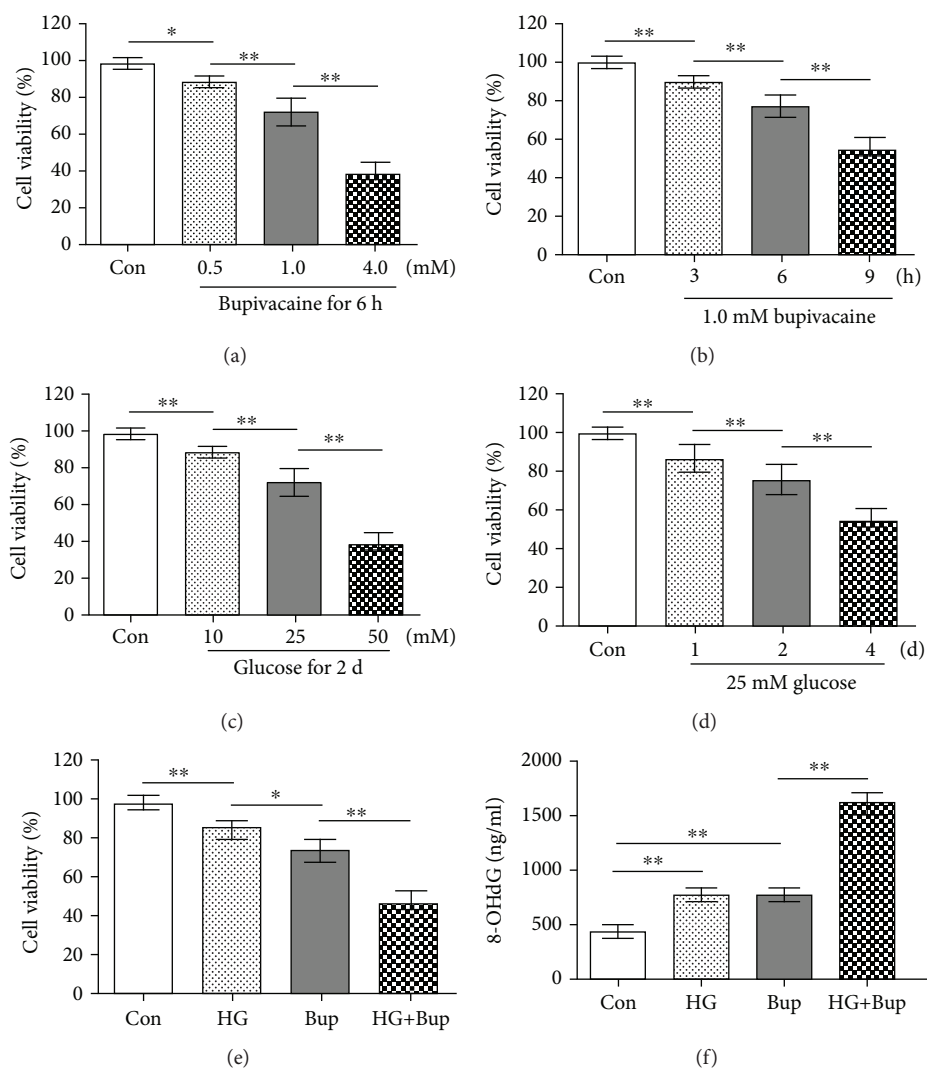
FIGURE 1: High glucose enhanced bupivacaine-induced cell viability inhibition and oxidative damage in SH-SY5Y cells. Con: untreated cells; HG: cells treated with 25 mM glucose for 2 days; Bup: cells treated with 1.0 mM bupivacaine for 6 h; HG+Bup: cells cultured with 25 mM glucose for 2 days and treated with 1.0 mM bupivacaine for 6 h. (a) Cell viability was measured with MTT assay in cells treated with different concentrations (0.5, 1.0, or 4.0 mM) of bupivacaine for 6 h. (b) Cell viability was measured with MTT assay in cells treated with 1.0 mM bupivacaine for different times (3, 6, or 12 h). (c) Cell viability was measured with MTT assay in cells treated with different concentrations (10, 25, or 50 mM) of glucose for 2 days. (d) Cell viability was measured with MTT assay in cells treated with 25 mM glucose for different times (1, 2, or 4 days). (e) Cell viability was measured with MTT assay in cells cultured with 25 mM glucose for 2 days and treated with 1.0 mM bupivacaine for 6 h. (f) The 8-OHdG level was measured with ELISA in cells cultured with 25 mM glucose for 2 days and treated with 1.0 mM bupivacaine for 6 h. Values are the mean ± SD ($n = 6$); $^*P < 0.05$, $^{**}P < 0.01$.

and silencer negative control siRNA (5′-GCCUAAGAACG ACAAAUCAdTdT-3′ and 3′-dTdTCGGAUUCUUGCUG UUUAGU-5′) were designed and purchased from Sigma-Aldrich (St. Louis, MO, USA). These siRNAs were transfected into SH-SY5Y cells according to the manufacturer's instructions. Cells were incubated with siRNAs for 48 h before experimental treatment.

2.10. Mitochondrial Membrane Potential (ΔΨm) Assay. Mitochondrial depolarization was measured with JC-1. After treatments, cells were washed with PBS twice. Then, JC-1 (1 ml, 10 μg/ml) staining solution was added into each well. Plates were incubated with 5% CO_2 at 37°C for 20 min.

Finally, cells were tested with flow cytometry or fluorescence microscopy. Red fluorescence represents the JC-1 polymer, indicating high mitochondrial membrane potential. Green fluorescence represents the JC-1 monomer, indicating the dissipation of mitochondrial membrane potential. The fluorescence intensity ratio of the polymer/monomer was used to analyze mitochondrial depolarization.

2.11. Apoptosis Assay by Flow Cytometry. After treatments, cells were washed with PBS (2 ml) and incubated with 0.25% trypsin (0.5 ml). Cell suspension was transferred from the plates to the centrifuge tube. Annexin V-FITC (1.25 μl) was added into the tube and reacted for 15 min under room

(a)

(b)

(c)
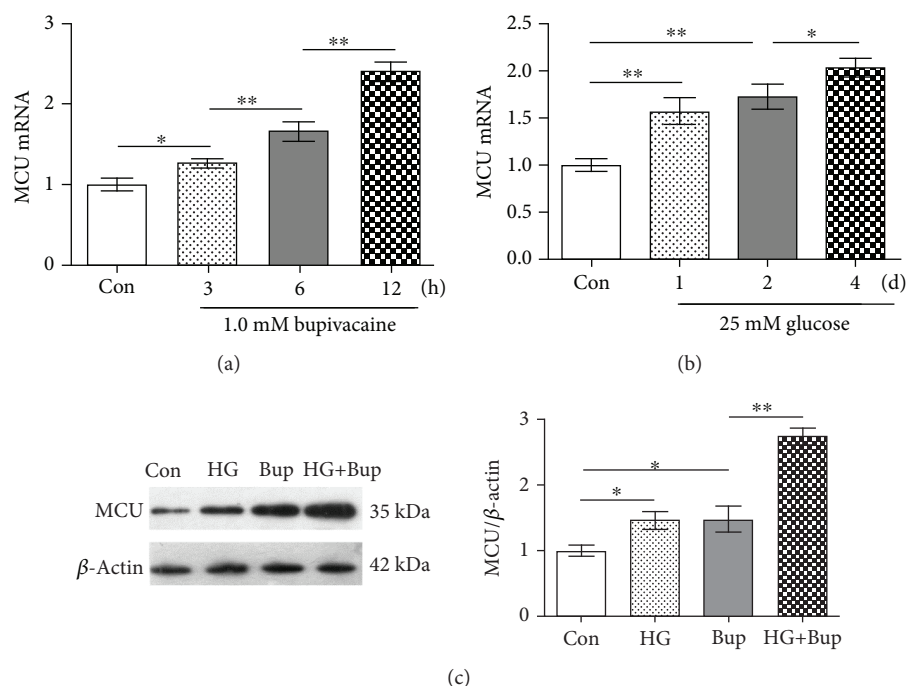
FIGURE 2: High glucose enhanced bupivacaine-induced MCU expression elevation. Con: untreated cells; HG: cells treated with 25 mM glucose for 2 days; Bup: cells treated with 1.0 mM bupivacaine for 6 h; HG+Bup: cells cultured with 25 mM glucose for 2 days and treated with 1.0 mM bupivacaine for 6 h. (a) MCU mRNA was measured with qRT-PCR in cells treated with 1.0 mM bupivacaine for different times (3, 6, or 12 h). (b) MCU mRNA was measured with qRT-PCR in cells treated with 25 mM glucose for different times (1, 2, or 4 days). (c) MCU protein expression was measured with western blotting in cells cultured with 25 mM glucose for 2 days and treated with 1.0 mM bupivacaine for 6 h. Values are the mean $\pm$ SD ($n = 3$); $^{*}P < 0.05$, $^{**}P < 0.01$.

temperature. After centrifugation for 5 min and supernatant removing, propidium iodide (10 μl) was added into the tube for measuring cell apoptosis with flow cytometry (BD Biosciences, Franklin Lakes, NJ, USA).

2.12. Statistical Analysis. Data are expressed as mean $\pm$ standard deviation (SD). Paired sample t-test was used for analyzing differences between two groups, and one-way analysis of variance (ANOVA) was used for analyzing multiple comparisons among groups followed by post hoc Dunnett's multiple comparison test with SPSS software 13.0 (SPSS Inc. Chicago, IL). Statistical significance was defined as $P < 0.05$.

3. Results

3.1. High Glucose Enhanced Bupivacaine-Induced Cell Viability Inhibition and 8-OHdG Level Elevation in SH-SY5Y Cells. As shown in Figure 1, the MTT assay and 8-OHdG level were measured to evaluate cell viability and oxidative damage. First, cells were exposed to different concentrations (0.5, 1.0, or 4.0 mM) of bupivacaine for 6 h. Compared to the control group, cell viability was significantly inhibited in cells exposed to bupivacaine (0.5, 1.0, or 4.0 mM) ($P < 0.05$). Next, SH-SY5Y cells were exposed to 1.0 mM bupivacaine for different times (3, 6, or 12 h). Compared to the control group, cell viability was significantly inhibited in cells exposed to 1.0 mM bupivacaine for 3, 6, or 12 h ($P < 0.05$). SH-SY5Y cells were exposed to different

concentrations (10, 25 or 50 mM) of glucose for 2 days. Compared to the control group, cell viability was significantly inhibited in cells exposed to high glucose (10, 25, or 50 mM) ($P < 0.05$). Next, SH-SY5Y cells were exposed to 25 mM glucose for different times (1, 2, or 4 days). Compared to the control group, cell viability was significantly inhibited in cells exposed to 25 mM glucose for 1, 2, or 4 days ($P < 0.05$).

Cells were cultured with 25 mM glucose for 2 days and treated with 1.0 mM bupivacaine for 6 h. Compared to cells exposed to bupivacaine only, cell viability inhibition and 8-OHdG level elevation were significantly enhanced in cells treated with high glucose and bupivacaine ($P < 0.05$).

3.2. High Glucose Enhanced Bupivacaine-Induced MCU Expression Elevation in SH-SY5Y Cells. As shown in Figure 2, SH-SY5Y cells were exposed to 1.0 mM bupivacaine for different times (3, 6, or 12 h) or exposed to 25 mM glucose for different times (1, 2, or 4 days). Compared to the control group, MCU mRNA expression was significantly upregulated in cells exposed to bupivacaine in a time-dependent manner ($P < 0.05$). Next, cells were cultured with 25 mM glucose for different times (1, 2, or 4 days). Compared to the control group, MCU mRNA expression was upregulated significantly in cells exposed to high glucose in a time-dependent manner ($P < 0.05$). Last, SH-SY5Y cells were cultured with 25 mM glucose for 2 days and treated with 1.0 mM bupivacaine for 6 h. Compared to cells exposed

(a)

(b)

(c)

(d)
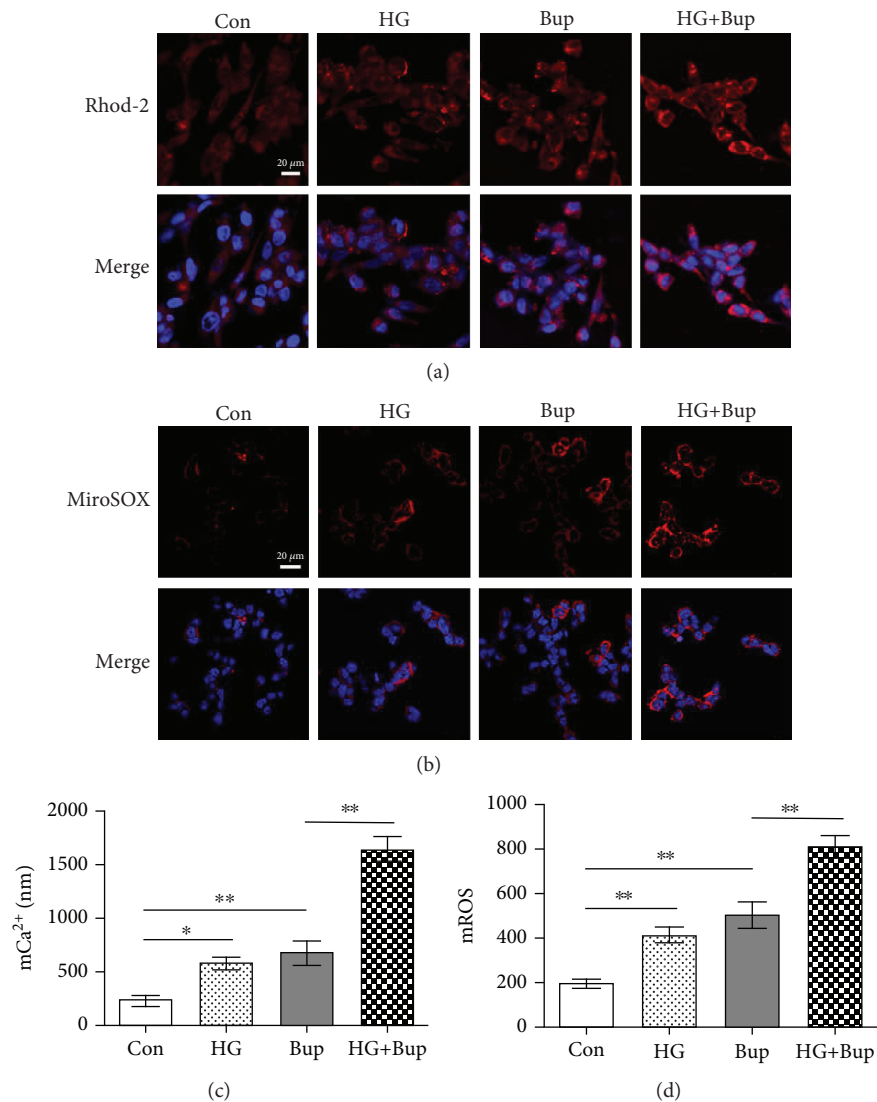
FIGURE 3: High glucose enhanced bupivacaine-induced mCa^{2+} accumulation and mROS overproduction. Con: untreated cells; HG: cells treated with 25 mM glucose for 2 days; Bup: cells treated with 1.0 mM bupivacaine for 6 h; HG+Bup: cells cultured with 25 mM glucose for 2 days and treated with 1.0 mM bupivacaine for 6 h. (a) Mitochondrial Ca^{2+} was shown with the confocal scanning laser microscope. (b) Mitochondrial ROS was shown with the confocal scanning laser microscope. (c) Summarized data show mCa^{2+} measured with flow cytometry. (d) Summarized data show mROS measured with flow cytometry. Values are the mean ± SD ($n = 3$); $^*P < 0.05$, $^{**}P < 0.01$.

to bupivacaine only, MCU protein expression elevation was enhanced significantly in cells exposed to high glucose and bupivacaine ($P < 0.05$).

3.3. High Glucose Enhanced Bupivacaine-Induced mCa^{2+} Accumulation and mROS Overproduction in SH-SY5Y Cells.
As shown in Figure 3, SH-SY5Y cells were cultured with/-without 25 mM glucose for 2 days before treatment with 1.0 mM bupivacaine for 6 h. Compared to the control group, mCa^{2+} accumulation and mROS overproduction were elevated in cells treated with high glucose or bupivacaine ($P < 0.05$). Compared to cells exposed to bupivacaine only, mCa^{2+} accumulation and mROS overproduction were significantly enhanced in cells treated with high glucose and bupivacaine ($P < 0.05$).

3.4. Ru360 or Knockdown of MCU Could Attenuate Bupivacaine-Induced Cell Viability Inhibition and 8-OHdG Level Elevation in SH-SY5Y Cell Incubation with High Glucose.
As shown in Figures 4(a) and 4(b), after pretreatment with different concentrations (5, 10, or 20 μM) of Ru360 for 30 min, cells were cultured with/without 25 mM glucose for 2 days and incubated with 1.0 mM bupivacaine for 6 h. Compared to cells cultured with high glucose and bupivacaine, cell viability inhibition and 8-OHdG level elevation were decreased in cells pretreated with Ru360 and cultured with high glucose and bupivacaine ($P < 0.05$).

As shown in Figure 4(c), SH-SY5Y cells were transfected with MCU siRNA or negative control siRNA. Compared to the control group, MCU expression was downregulated significantly in cells transfected with MCU siRNA ($P < 0.05$).
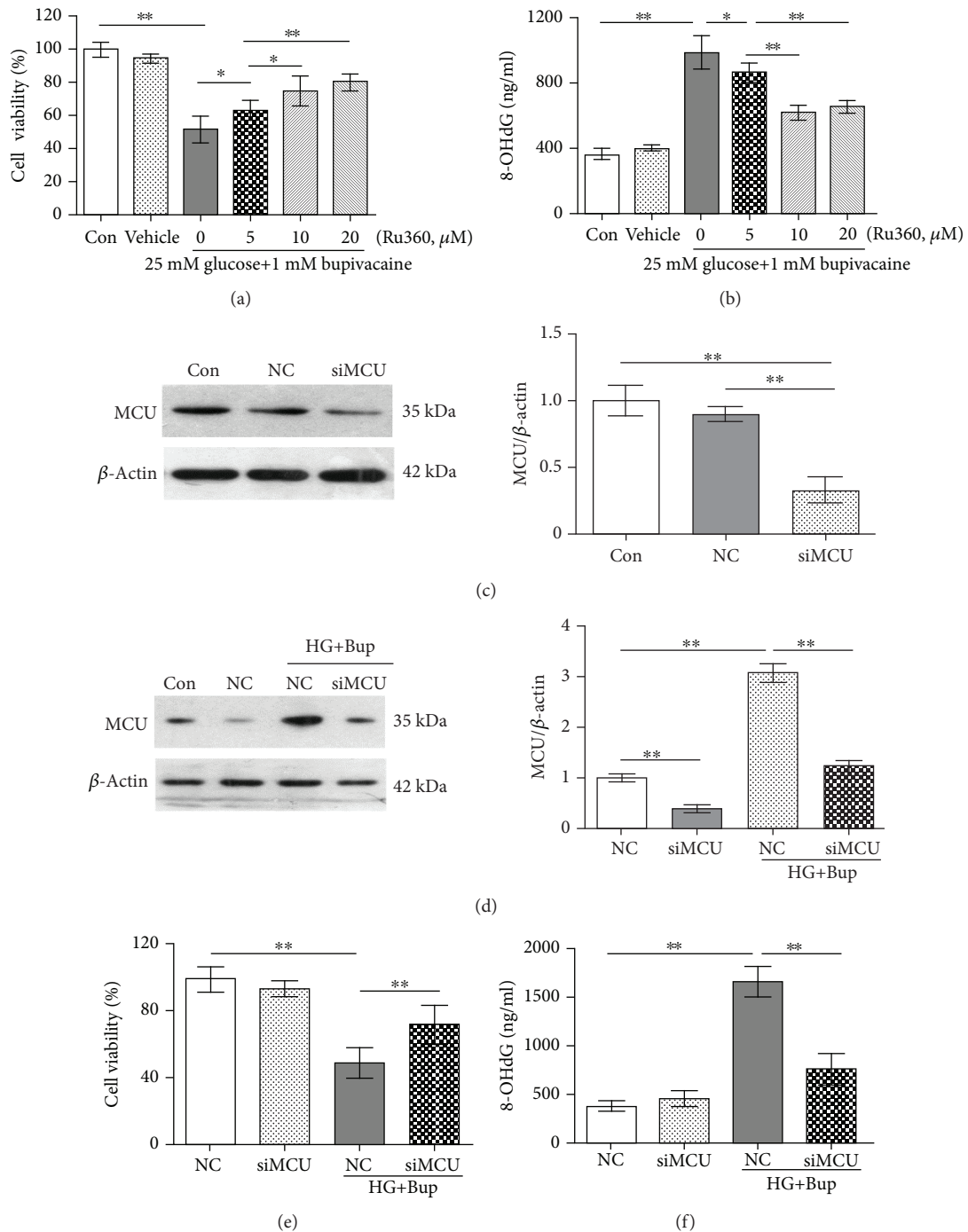
FIGURE 4: Ru360 or the knockdown of MCU could attenuate bupivacaine-induced cell viability inhibition and oxidative damage in SH-SY5Y cell incubation with high glucose. Con: untreated cells; Vehicle: cells cultured with media containing DMSO; NC: cells transfected with silencer negative control siRNA; siMCU: cells transfected with MCU siRNA; HG+Bup: cells cultured with 25 mM glucose for 2 days and treated with 1.0 mM bupivacaine for 6 h. (a) Cell viability was measured with MTT assay in cells cultured with 5, 10, or 20 μM Ru360 for 30 min and then treated with 1.0 mM bupivacaine for 6 h after being cultured with 25 mM glucose for 2 days. (b) The 8-OHdG level was measured with ELISA in cells cultured with 5, 10, or 20 μM Ru360 for 30 min and then treated with 1.0 mM bupivacaine for 6 h after being cultured with 25 mM glucose for 2 days. (c) MCU protein expression was measured with western blotting in cells treated with silencer negative control or MCU siRNA. (d) MCU protein expression was measured with western blotting in cells transfected with silencer negative control or MCU siRNA and treated with 1.0 mM bupivacaine for 6 h after being cultured with 25 mM glucose for 2 days. (e) Cell viability inhibition was measured with MTT assay in cells transfected with silencer negative control or MCU siRNA and treated with 1.0 mM bupivacaine for 6 h after being cultured with 25 mM glucose for 2 days. (f) The 8-OHdG level was measured with ELISA in cells transfected with silencer negative control or MCU siRNA and treated with 1.0 mM bupivacaine for 6 h after being cultured with 25 mM glucose for 2 days. Values are the mean ± SD ($n = 3$); *$P < 0.05$, **$P < 0.01$.

(a)

(b)

(c)

(d)
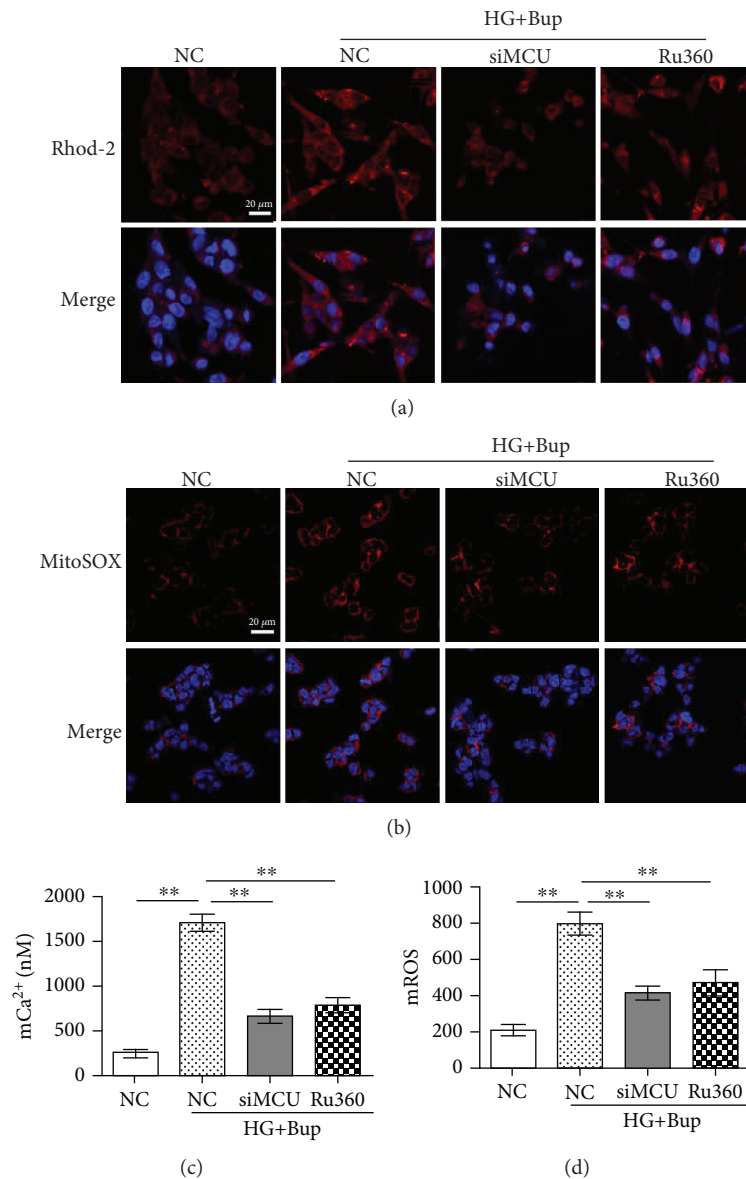
FIGURE 5: Ru360 or the knockdown of MCU could attenuate bupivacaine-induced mCa^{2+} accumulation and mROS overproduction in SH-SY5Y cell incubation with high glucose. NC: cells transfected with silencer negative control siRNA; siMCU: cells transfected with MCU siRNA; Ru360: cells pretreated with $10\,\mu M$ Ru360 for 30 min; HG+Bup: cells cultured with 25 mM glucose for 2 days and treated with 1.0 mM bupivacaine for 6 h. (a) Mitochondrial Ca^{2+} was shown with the confocal scanning laser microscope. (b) Mitochondrial ROS was shown with the confocal scanning laser microscope. (c) Summarized data show mCa^{2+} measured with flow cytometry. (b) Summarized data show mROS measured with flow cytometry. Values are the mean $\pm$ SD ($n = 3$); $^{*}P < 0.05$, $^{**}P < 0.01$.

Compared to the control group, MCU expression in cells transfected with negative control siRNA was not significantly different ($P > 0.05$). As shown in Figure 4(d), compared to cells cultured with high glucose and bupivacaine, MCU expression was downregulated significantly in cells transfected with siMCU and treated with high glucose and bupivacaine ($P > 0.05$).

As shown in Figure 4(e) and Figure 4(f), after being transfected with MCU siRNA, cells were cultured with/without 25 mM glucose for 2 days and incubated with 1.0 mM bupivacaine for 6 h. Compared to cells exposed to high glucose and bupivacaine, MCU expression and 8-OHdG level elevation were decreased; cell viability inhibition was

improved in the cell knockdown of MCU and treated with high glucose and bupivacaine ($P < 0.05$).

3.5. Ru360 or Knockdown of MCU Could Attenuate Bupivacaine-Induced mCa^{2+} Accumulation, mROS Overproduction, $\Delta\Psi m$ Decline, and Apoptosis in SH-SY5Y Cell Incubation with High Glucose. As shown in Figures 5 and 6, after being pretreated with $10\,\mu M$ Ru360 for 30 min or transfected with MCU siRNA, cells were cultured with/without 25 mM glucose for 2 days and incubated with 1.0 mM bupivacaine for 6 h. Compared to cells exposed to high glucose and bupivacaine, Ru360 or the knockdown of MCU could attenuate high glucose

(a)

(b)
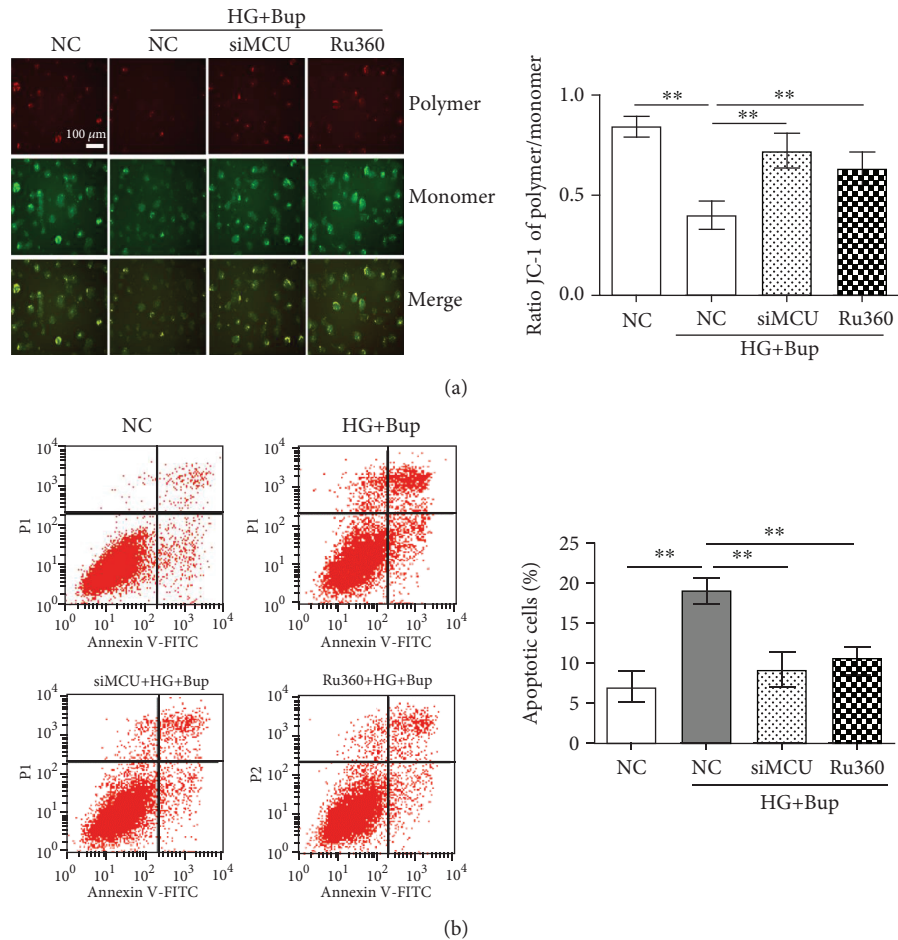
FIGURE 6: Ru360 or the knockdown of MCU could attenuate bupivacaine-induced mitochondrial oxidative damage and apoptosis in SH-SY5Y cell incubation with high glucose. NC: cells transfected with silencer negative control siRNA; siMCU: cells transfected with MCU siRNA; Ru360: cells pretreated with $10 \mu M$ Ru360 for 30 min; HG+Bup: cells cultured with 25 mM glucose for 2 days and treated with 1.0 mM bupivacaine for 6 h. (a) Mitochondrial damage was measured with JC-1. (b) Apoptotic cells (early apoptotic cells at the lower right quadrant for Annexin V-FITC-positive and PI-negative) were measured with flow cytometry. Values are the mean ± SD ($n = 3$); $^*P < 0.05$, $^{**}P < 0.01$.

and bupivacaine-induced mCa^{2+} accumulation, mROS overproduction, $\Delta\Psi m$ decline, and apoptosis ($P < 0.05$).

4. Discussion

There are three main findings for confirming the role of MCU in high glucose potentiating bupivacaine-induced neurotoxicity in this study. First, high glucose enhanced bupivacaine-induced mCa^{2+} accumulation and oxidative stress. Second, high glucose enhanced bupivacaine-induced MCU expression elevation. Third, downregulation or inhibition activity of MCU attenuated the high glucose-mediated enhancement of bupivacaine-induced mCa^{2+} accumulation, oxidative stress, and apoptosis. Collectively, our findings demonstrate that high glucose enhances bupivacaine-induced neurotoxicity via MCU-mediated oxidative stress.

Neurotoxic injury induced by clinically used local anesthetic has been confirmed in cell and animal models [6–9, 31]. Studies have shown that ROS-mediated apoptosis plays a crucial role in local anesthetic-induced neurotoxicity [9,

11, 29]. Bupivacaine, a typical local anesthetic, induces cell apoptosis through specific inhibition of respiration complexes I and III, promoting ROS overproduction [13]. Hyperglycemia magnifies oxidative damage by stimulating ROS production in diabetes [32]. It causes a decrease of the mitochondrial oxidative phosphorylation and leads to advanced glycation end product- (AGE-) mediated oxidative stress [33]. AGEs promote ROS overproduction through enhancing glucose autoxidation, reducing low molecular weight antioxidants, and inhibiting superoxide dismutase activity, resulting in peripheral neuropathy [4]. In the present study, the data showed that either bupivacaine or high glucose exerted concentration- and time-dependent toxicity via elevating ROS generation in SH-SY5Y cells. At the same time, high glucose enhanced bupivacaine-induced ROS overproduction and oxidative damage.

The mitochondria are the main production organelles and targets of ROS which mediate oxidative stress and apoptosis [34]. Ca^{2+} is closely related to the regulation of the mitochondrial function [35]. Its uptake into the

mitochondria is involved in buffering and influencing cytosolic Ca^{2+}, energy metabolism, and even initiating cell apoptosis [36, 37]. Ca^{2+} overload is involved in the early signal transduction and the mitochondrial membrane permeability changes in the early stage of apoptosis. An excessive uptake of Ca^{2+} triggers mitochondrial dysfunction through an mPTP opening, leading to mROS production and rupture of the mitochondrial outer membrane [38]. The latter results in the release of Ca^{2+} in the intermembrane cavity and cytosolic Ca^{2+} accumulation, which initiates multiple signal transduction pathways and causes ROS overproduction [39]. Our previous study has demonstrated that bupivacaine could induce mCa^{2+} accumulation, mitochondrial membrane potential decline, ROS overproduction, and apoptosis in SH-SY5Y cells and dorsal root ganglion neurons [40]. In this study, the results showed that either bupivacaine or high glucose could cause mCa^{2+} accumulation and mROS overproduction, and high glucose enhanced bupivacaine-induced mCa^{2+} accumulation and mROS overproduction. These results suggest that high glucose enhances bupivacaine-induced oxidative damage by elevating mCa^{2+} accumulation.

The MCU channel, the principal mCa^{2+} transport system, participated in the process of the above mechanism. MCU was related to mROS production through regulating the mCa^{2+} influx during stress stimulation [41]. Elevating MCU activity could stimulate mCa^{2+} uptake and overload, mROS overproduction, and even cell death [24]. Recent studies demonstrated that Ru360, an inhibitor of MCU, could attenuate Fe^{2+} overload-induced ROS production in the brain mitochondria [42]. However, application of Ru360 and the knockdown of MCU potentiated Pb^{2+}--induced oxidative stress and neurotoxicity [30]. All these events show that MCU plays a crucial role in regulating oxidative stress, but its different roles in oxidative stress need to be further explored. Our study indicated that MCU expression was elevated in a time-dependent manner in cells treated with bupivacaine or high glucose. At the same time, high glucose augmented bupivacaine-induced MCU expression elevation. We investigated the involvement of MCU in mCa^{2+} uptake in SH-SY5Y cells treated with high glucose and bupivacaine. We found that Ru360 inhibited the increase of mCa^{2+} levels, mROS overproduction, and apoptosis. MCU-specific siRNA effectively reduced high glucose-mediated enhancement of bupivacaine-induced mitochondrial oxidative stress and apoptosis. Thus, MCU-mediated mCa^{2+} uptake plays a key role in high glucose-mediated enhancement of bupivacaine-induced neurotoxicity in SH-SY5Y cells. However, the effects of MCU activity on bupivacaine induced the changes of the mPTP opening off state, and respiration complex activity has not been researched in this model. It is worthy of being determined in further studies.

Some limitations in this study need to be noted. First, the clinically used concentration of bupivacaine is 0.5% or 0.75%, but the concentration of bupivacaine for treating SH-SY5Y cells was 1.0 mM which was equal to 0.03% and not precisely clinically relevant. Second, we did not conduct animal experiments to support our conclusions.

In conclusion, our study reveals that MCU plays a crucial role in high glucose-mediated enhancement of bupivacaine-induced oxidative stress and suggests the possible use of this channel as a target for curing bupivacaine-induced neurotoxicity in diabetic patients.

Abbreviations

MCU: Mitochondrial calcium uniporter
ROS: Reactive oxygen species
mCa^{2+}: Mitochondrial Ca^{2+}
mROS: Mitochondrial ROS
mPTP: Mitochondrial transition pore
8-OHdG: 8-Hydroxydeoxyguanosine
$\Delta\Psi m$: Mitochondrial membrane potential.

Data Availability

The data used to support the findings of the current study are included in the article.

Conflicts of Interest

The authors do not declare any conflict of interests relevant to this paper.

Authors' Contributions

The conception and design of the research were done by Zhong-Jie Liu and Shi-Yuan Xu. Zhong-Jie Liu, Wei Zhao, and Hong-Yi Lei performed the experiments; Hua-Li Xu and Lu-Ying Lai analyzed the data; Zhong-Jie Liu and Wei Zhao drafted the manuscript; Lu-Ying Lai prepared the figures; Shi-Yuan Xu and Rui Xu edited and revised the manuscript. Zhong-Jie Liu and Wei Zhao contributed equally.

Acknowledgments

References

[1] Y. Xu, L. Wang, J. He et al., "Prevalence and control of diabetes in Chinese adults," *Journal of the American Medical Association*, vol. 310, no. 9, pp. 948–959, 2013.

[2] S. Wild, G. Roglic, A. Green, R. Sicree, and H. King, "Global prevalence of diabetes: estimates for the year 2000 and projections for 2030," *Diabetes Care*, vol. 27, no. 5, pp. 1047–1053, 2004.

[3] S. Lupachyk, P. Watcho, R. Stavniichuk, H. Shevalye, and I. G. Obrosova, "Endoplasmic reticulum stress plays a key role in the pathogenesis of diabetic peripheral neuropathy," *Diabetes*, vol. 62, no. 3, pp. 944–952, 2013.

[4] A. M. Vincent, B. C. Callaghan, A. L. Smith, and E. L. Feldman, "Diabetic neuropathy: cellular mechanisms as therapeutic targets," *Nature Reviews Neurology*, vol. 7, no. 10, pp. 573–583, 2011.

[5] J. R. Hebl, S. L. Kopp, D. R. Schroeder, and T. T. Horlocker, "Neurologic complications after neuraxial anesthesia or analgesia in patients with preexisting peripheral sensorimotor neuropathy or diabetic polyneuropathy," *Anesthesia & Analgesia*, vol. 103, no. 5, pp. 1294–1299, 2006.

[6] M. Verlinde, M. Hollmann, M. Stevens, H. Hermanns, R. Werdehausen, and P. Lirk, "Local anesthetic-induced neurotoxicity," *International Journal of Molecular Sciences*, vol. 17, no. 3, p. 339, 2016.

[7] T. Arai and S. Hoka, "Neurotoxicity of intrathecal local anesthetics," *Journal of Anesthesia*, vol. 21, no. 4, pp. 540-541, 2007.

[8] I. A. Radwan, S. Saito, and F. Goto, "The neurotoxicity of local anesthetics on growing neurons: a comparative study of lidocaine, bupivacaine, mepivacaine, and ropivacaine," *Anesthesia & Analgesia*, vol. 94, no. 2, pp. 319–24, table of contents, 2002.

[9] S. Sakura, "Research on local anesthetic neurotoxicity using intrathecal and epidural rat models," *Journal of Anesthesia*, vol. 21, no. 4, pp. 533-534, 2007.

[10] A. Okamoto, M. Tanaka, C. Sumi et al., "The antioxidant *N*-acetyl cysteine suppresses lidocaine-induced intracellular reactive oxygen species production and cell death in neuronal SH-SY5Y cells," *BMC Anesthesiology*, vol. 16, no. 1, p. 104, 2016.

[11] C. J. Park, S. A. Park, T. G. Yoon, S. J. Lee, K. W. Yum, and H. J. Kim, "Bupivacaine induces apoptosis *via* ROS in the Schwann cell line," *Journal of Dental Research*, vol. 84, no. 9, pp. 852–857, 2005.

[12] A. Malet, M. O. Faure, N. Deletage, B. Pereira, J. Haas, and G. Lambert, "The comparative cytotoxic effects of different local anesthetics on a human neuroblastoma cell line," *Anesthesia & Analgesia*, vol. 120, no. 3, pp. 589–596, 2015.

[13] O. Cela, C. Piccoli, R. Scrima et al., "Bupivacaine uncouples the mitochondrial oxidative phosphorylation, inhibits respiratory chain complexes I and III and enhances ROS production: results of a study on cell cultures," *Mitochondrion*, vol. 10, no. 5, pp. 487–496, 2010.

[14] J. Lu, S. Y. Xu, Q. G. Zhang, and H. Y. Lei, "Bupivacaine induces reactive oxygen species production via activation of the AMP-activated protein kinase-dependent pathway," *Pharmacology*, vol. 87, no. 3-4, pp. 121–129, 2011.

[15] A. L. Waldron, P. A. Schroder, K. L. Bourgon et al., "Oxidative stress-dependent MMP-13 activity underlies glucose neurotoxicity," *Journal of Diabetes and its Complications*, vol. 32, no. 3, pp. 249–257, 2018.

[16] S. Saberi Firouzi, N. Namazi Sarvestani, A. Bakhtiarian et al., "Sildenafil protective effects on high glucose-induced neurotoxicity in PC12 cells: the role of oxidative stress, apoptosis, and inflammation pathways in an *in vitro* cellular model for diabetic neuropathy," *Neurological Research*, vol. 40, pp. 1–13, 2018.

[17] Z.-J. Liu, W. Zhao, Q.-G. Zhang et al., "OGG1 involvement in high glucose-mediated enhancement of bupivacaine-induced oxidative DNA damage in SH-SY5Y cells," *Oxidative Medicine and Cellular Longevity*, vol. 2015, Article ID 683197, 11 pages, 2015.

[18] J. Qiu, Y. W. Tan, A. M. Hagenston et al., "Mitochondrial calcium uniporter Mcu controls excitotoxicity and is transcriptionally repressed by neuroprotective nuclear calcium signals," *Nature Communications*, vol. 4, no. 1, p. 2034, 2013.

[19] M.-l. A. Joiner, O. M. Koval, J. Li et al., "CaMKII determines mitochondrial stress responses in heart," *Nature*, vol. 491, no. 7423, pp. 269–273, 2012.

[20] M. R. Alam, L. N. Groschner, W. Parichatikanond et al., "Mitochondrial Ca^{2+} uptake 1 (MICU1) and mitochondrial Ca^{2+} uniporter (MCU) contribute to metabolism-secretion coupling in clonal pancreatic β-cells," *Journal of Biological Chemistry*, vol. 287, no. 41, pp. 34445–34454, 2012.

[21] C. Petrungaro, K. M. Zimmermann, V. Küttner et al., "The Ca^{2+}-dependent release of the Mia40-induced MICU1-MICU2 dimer from MCU regulates mitochondrial Ca^{2+} uptake," *Cell Metabolism*, vol. 22, no. 4, pp. 721–733, 2015.

[22] K. Mallilankaraman, P. Doonan, C. Cárdenas et al., "MICU1 is an essential gatekeeper for MCU-mediated mitochondrial Ca (2+) uptake that regulates cell survival," *Cell*, vol. 151, no. 3, pp. 630–644, 2012.

[23] M. Patron, A. Raffaello, V. Granatiero et al., "The mitochondrial calcium uniporter (MCU): molecular identity and physiological roles," *Journal of Biological Chemistry*, vol. 288, no. 15, pp. 10750–10758, 2013.

[24] Z. Dong, S. Shanmughapriya, D. Tomar et al., "Mitochondrial Ca^{2+} uniporter is a mitochondrial luminal redox sensor that augments MCU channel activity," *Molecular Cell*, vol. 65, no. 6, pp. 1014–1028.e7, 2017.

[25] A. P. Halestrap, "What is the mitochondrial permeability transition pore?," *Journal of Molecular and Cellular Cardiology*, vol. 46, no. 6, pp. 821–831, 2009.

[26] G. De Jesús García-Rivas, A. Guerrero-Hernández, G. Guerrero-Serna, J. S. Rodríguez-Zavala, and C. Zazueta, "Inhibition of the mitochondrial calcium uniporter by the oxo-bridged dinuclear ruthenium amine complex (Ru360) prevents from irreversible injury in postischemic rat heart," *FEBS Journal*, vol. 272, no. 13, pp. 3477–3488, 2005.

[27] M. A. Matlib, Z. Zhou, S. Knight et al., "Oxygen-bridged dinuclear ruthenium amine complex specifically inhibits Ca^{2+} uptake into mitochondria in vitro and in situ in single cardiac myocytes," *Journal of Biological Chemistry*, vol. 273, no. 17, pp. 10223–10231, 1998.

[28] T. D. Schmittgen and K. J. Livak, "Analyzing real-time PCR data by the comparative C (T) method," *Nature Protocols*, vol. 3, no. 6, pp. 1101–1108, 2008.

[29] Z. Liu, W. Zhao, Q. Zhang et al., "Increased oxidative damage and reduced DNA repair enzyme XPD involvement in high glucose-mediated enhancement of levobupivacaine-induced neurotoxicity," *Neurochemical Research*, vol. 40, no. 9, pp. 1919–1928, 2015.

[30] X. Yang, B. Wang, H. Zeng et al., "Role of the mitochondrial Ca^{2+} uniporter in Pb^{2+}-induced oxidative stress in human neuroblastoma cells," *Brain Research*, vol. 1575, pp. 12–21, 2014.

[31] T. Muguruma, S. Sakura, Y. Kirihara, and Y. Saito, "Comparative somatic and visceral antinociception and neurotoxicity of intrathecal bupivacaine, levobupivacaine, and dextrobupivacaine in rats," *Anesthesiology*, vol. 104, no. 6, pp. 1249–1256, 2006.

[32] F. Giacco, X. du, A. Carratú et al., "GLP-1 cleavage product reverses persistent ROS generation after transient hyperglycemia by disrupting an ROS-generating feedback loop," *Diabetes*, vol. 64, no. 9, pp. 3273–3284, 2015.

[33] O. Brouwers, P. M. Niessen, I. Ferreira et al., "Overexpression of glyoxalase-I reduces hyperglycemia-induced levels of advanced glycation end products and oxidative stress in diabetic rats," *Journal of Biological Chemistry*, vol. 286, no. 2, pp. 1374–1380, 2011.

[34] S. Raha and B. H. Robinson, "Mitochondria, oxygen free radicals, and apoptosis," *American Journal of Medical Genetics*, vol. 106, no. 1, pp. 62–70, 2001.

[35] D. C. Musial, G. H. Bomfim, J. A. Arranz-Tagarro et al., "Altered mitochondrial function, calcium signaling, and catecholamine release in chromaffin cells of diabetic and SHR rats," *European Journal of Pharmacology*, vol. 815, pp. 416–426, 2017.

[36] C. J. Hwang, H. P. Lee, D. Y. Choi et al., "Inhibitory effect of thiacremonone on MPTP-induced dopaminergic neurodegeneration through inhibition of p38 activation," *Oncotarget*, vol. 7, no. 30, pp. 46943–46958, 2016.

[37] E. Penna, J. Espino, D. De Stefani, and R. Rizzuto, "The MCU complex in cell death," *Cell Calcium*, vol. 69, pp. 73–80, 2018.

[38] P. D. Khare, L. Shao-Xi, M. Kuroki et al., "Specifically targeted killing of carcinoembryonic antigen (CEA)-expressing cells by a retroviral vector displaying single-chain variable fragmented antibody to CEA and carrying the gene for inducible nitric oxide synthase," *Cancer Research*, vol. 61, no. 1, pp. 370–375, 2001.

[39] A. Görlach, K. Bertram, S. Hudecova, and O. Krizanova, "Calcium and ROS: a mutual interplay," *Redox Biology*, vol. 6, pp. 260–271, 2015.

[40] X. J. Yu, W. Zhao, Y. J. Li et al., "Neurotoxicity comparison of two types of local anaesthetics: amide-bupivacaine versus ester-procaine," *Scientific Reports*, vol. 7, no. 1, p. 45316, 2017.

[41] N. E. Hoffman, H. C. Chandramoorthy, S. Shanmughapriya et al., "SLC25A23 augments mitochondrial Ca^{2+} uptake, interacts with MCU, and induces oxidative stress-mediated cell death," *Molecular Biology of the Cell*, vol. 25, no. 6, pp. 936–947, 2014.

[42] J. Sripetchwandee, J. Sanit, N. Chattipakorn, and S. C. Chattipakorn, "Mitochondrial calcium uniporter blocker effectively prevents brain mitochondrial dysfunction caused by iron overload," *Life Sciences*, vol. 92, no. 4-5, pp. 298–304, 2013.

Research Article

Fenofibrate Improved Interstitial Fibrosis of Renal Allograft through Inhibited Epithelial-Mesenchymal Transition Induced by Oxidative Stress

Yishu Wang,[1] Lei Pang [ID],[2] Yanghe Zhang,[1] Jiahui Lin,[1] and Honglan Zhou [ID][3]

[1]*Key Laboratory of Pathobiology, Ministry of Education, Jilin University, Changchun, 130021 Jilin, China*
[2]*Department of Anesthesiology, The First Hospital of Jilin University, Changchun, 130021 Jilin, China*
[3]*Department of Urology, The First Hospital of Jilin University, Changchun, 130021 Jilin, China*

Correspondence should be addressed to Honglan Zhou; walkerzhouhl@163.com

The best treatment for end-stage renal disease is renal transplantation. However, it is often difficult to maintain a renal allograft healthy for a long time following transplantation. Interstitial fibrosis and tubular atrophy (IF/TA) are significant histopathologic characteristics of a compromised renal allograft. There is no effective therapy to improve renal allograft function once IF/TA sets in. Although there are many underlying factors that can induce IF/TA, the pathogenesis of IF/TA has not been fully elucidated. It has been found that epithelial-mesenchymal transition (EMT) significantly contributes to the development of IF/TA. Oxidative stress is one of the main causes that induce EMT in renal allografts. In this study, we have used H_2O_2 to induce oxidative stress in renal tubular epithelial cells (NRK-52e) of rats. We also pretreated NRK-52e cells with an antioxidant (N-acetyl L-cysteine (NAC)) 1 h prior to the treatment with H_2O_2. Furthermore, we used fenofibrate (a peroxisome proliferator-activated receptor α agonist) to treat NRK-52e cells and a renal transplant rat model. Our results reveal that oxidative stress induces EMT in NRK-52e cells, and pretreatment with NAC can suppress EMT in these cells. Moreover, fenofibrate suppresses fibrosis by ameliorating oxidative stress-induced EMT in a rat model. Thus, fenofibrate may effectively prevent the development of fibrosis in renal allograft and improve the outcome.

1. Introduction

Renal transplantation is the best approach for the management of end-stage renal disease. However, it brings along with it the risk of graft failure or transplant rejection. With the use of novel and effective immunosuppressive agents, the incidence of transplant rejection has reduced substantially in recent years [1]. However, the long-term outcome of renal allograft has not improved much. Although the annual survival rate of renal transplant has reached more than 90%, there is a 4–5% loss of function in the renal graft per year. The 5-year survival rate of renal transplant is approximately 70%, whereas the 10-year survival rate is only around 50% [1]. The main cause of this sharp decline is the development of chronic allograft nephropathy (CAN) [2, 3]. In the new Banff 2007 scheme, the term chronic allograft nephropathy has been replaced by interstitial fibrosis/tubular atrophy (IF/TA) [4].

Clinical research has shown that IF/TA is a significant histopathologic characteristic of a compromised renal allograft [5] and IF/TA is associated with chronic renal allograft dysfunction [6]. Multiple studies have been conducted in the past decades to understand the pathogenesis of IF/TA. These studies have shown that a wide range of factors and mechanisms are involved in the progress of IF/TA. These factors can be classified into two main categories: immune and nonimmune. The immune factors are mostly immunosuppressive drug toxicity and antibody-mediated injury, while the nonimmune factors are vasoconstriction, oxidative stress, fibroblast activation, transforming growth factor beta- (TGF-) β1-mediated epithelial-mesenchymal transition (EMT), etc. [5].

EMT has been identified in many biological functions, including tissue regeneration, scars following injury, epithelial-derived tumor invasion, and metastases [7, 8]. Three types of EMT have been identified: (i) type I EMT which is involved in embryo development and organ formation, (ii) type II EMT which is involved in adult tissue repair and fibrosis, and (iii) type III EMT which refers to the phenotypic transformation of epithelial malignancies [9]. The results of sequential renal biopsies in a study performed 3 and 12 months posttransplant have demonstrated a close correlation between the development of IF/TA and expression of EMT markers [10]. Some researchers have compared the biopsies obtained from dysfunctional renal allografts with IF/TA and renal allografts with stable renal function. They have shown that the expression of epithelial markers (E-cadherin and cytokeratin) in tubular epithelial cells (TECs) of kidneys with IF/TA is significantly decreased and the distribution of the markers is altered as compared to the functional kidneys [11]. In the damaged and atrophic tubules, some TECs also expressed mesenchymal markers including vimentin, S100A4, and alpha-smooth muscle actin (α-SMA). These findings indicate that TEC damage is associated with EMT [11].

Oxidative stress is the main contributor to IF/TA [12]. Renal transplant recipients always manifest persistent oxidative stress during the early period posttransplant [13]. It was shown that oxidative stress increases in all the biopsy specimens with allograft dysfunction [14]. The oxidative stress occurring in the transplanted kidneys is mainly induced by immunosuppressive drugs involving cells of epithelial, endothelial, and mesenchymal origin. This also results in toxic effects and fibrosis of the renal allografts [15]. There is evidence that oxidative stress is involved in the pathogenesis of EMT in chronic IF/TA of renal allograft. One *in vitro* study using proximal tubular epithelial cells has demonstrated that reactive oxygen species (ROS) play an important role in TGF-β1-induced EMT through activation of mitogen-activated protein kinase (MAPK) and Smad pathways [16]. Another study using a rat model of kidney transplant revealed that EMT is involved in the development of IF/TA and it coexists with enhanced oxidative stress [17]. In this particular study, kidneys from Fisher 344 rats were transplanted in Lewis rats to develop a model of IF/TA. The presence of EMT was characterized by increased α-SMA and collagen I and III levels along with a decreased E-cadherin expression and increased superoxide anion and iNOS and eNOS levels depicting an increased oxidative stress. These observations suggest that EMT occurs concurrently with oxidative stress in IF/TA. Therefore, oxidative stress induced by immunosuppressive drugs may result in EMT and contribute to the development of IF/TA in a renal allograft [17].

Peroxisome proliferator-activated receptor α (PPARα) is a member of the nuclear receptor superfamily, involved in the regulation of β-oxidation of fatty acids. PPARα displays its biological functions by inducing the transcription of downstream target genes. PPARα also has several antioxidant effects. A study has shown that fenofibrate (a PPARα agonist) can significantly reduce the oxidative stress in kidneys of spontaneously hypertensive rats by reducing the activity of renal nicotinamide adenine dinucleotide phosphate (NADPH) oxidase, increasing the activity of Cu-Zn-superoxide dismutase, and decreasing the phosphorylation of p38 MAPK and c-Jun N-terminal kinase (JNK) signals [18]. Some authors have also shown that fenofibrate can restore the phenotypic change induced by the deficiency of LKB1 in TEC [19]. Another study has also revealed that fenofibrate markedly suppresses fibrosis in a mouse model of chronic kidney disease (CKD) by improving fatty acid oxidation [20]. However, it is unclear whether fenofibrate suppresses fibrosis by decreasing the oxidative stress levels in the transplant kidneys. Therefore, we hypothesize that fenofibrate treatment may suppress EMT by reducing oxidative stress levels in the renal tubular epithelial cells and may improve long-term outcome in renal transplant recipients.

2. Materials and Methods

2.1. Detection of Cell Viability.
Collected NRK-52e cells were cultured in a DMEM. These cells were implanted into a 96-well plate and treated with 100 μmol/L H_2O_2 for 0.5 h, 1 h, 1.5 h, 2 h, and 2.5 h. Subsequently, CCK8 was added and was incubated for 1 h. The optical density (OD) was recorded at 450 nm.

2.2. ROS and Malondialdehyde (MDA) Estimation.
(i) ROS-dichloro-dihydro-fluorescein diacetate (DCFH-DA) method: 10 μmol/L DCFH-DA was diluted by a serum-free DMEM and incubated at 37°C for 20 min in the dark and then again washed by the serum-free medium. Fluorescence intensity was detected by BioTek Epoch with an excitation wavelength at 488 nm and an emission wavelength at 525 nm. (ii) ROS-dihydroethidium (DHE) method: 5 μmol/L of DHE was incubated at 37°C for 30 min in the dark. Subsequently, cells were incubated in 1X Hoechst 33342 for 30 min, and cells were washed in phosphate-buffered saline (PBS) thrice. Fluorescence microscopy was used to detect the fluorescence intensity. (iii) Malondialdehyde-thiobarbituric acid (MDA-TBA) method: collected medium with different treatments. By following the standard procedure, agential nos. 1, 2, 3, and 10 nmol/mL standard substance were added to the medium and incubated at 95°C for 40 min and then centrifuged at 4000 rpm for 10 min. The OD was detected using a microplate reader at 532 nm.

2.3. Western Blot Analysis.
The collected cells were treated with H_2O_2, N-acetyl L-cysteine (NAC), and/or fenofibrate. These cells were lysed using RIPA lysis buffer containing a protease inhibitor cocktail and a phosphatase inhibitor. The sample concentrations were measured by the bicinchoninic acid (BCA) assay. The proteins were loaded and separated by 5%, 8%, or 10% sodium dodecyl sulfate (SDS) polyacrylamide gels, electrotransferred to PVDF membranes, and incubated for about 12 h at 4°C with the following antibodies: E-cadherin, N-cadherin, vimentin, Snail, cleaved caspase-3, S100A4, and GAPDH. Secondary antibodies (anti-rabbit or

anti-mouse IgG horseradish peroxidase (HRP)) were diluted by tris-buffered saline and polysorbate 20 (TBST) and incubated for 1 h. The blots were detected by enhanced chemiluminescence.

2.4. Quantitative Real-Time PCR Analysis. Total RNA was prepared from rat renal tubular epithelial cells (NRK-52e) using an RNeasy Mini Kit. 500 ng of total RNA was reverse-transcribed using a cDNA archival kit. Quantitative real-time polymerase chain reaction was performed using an ABI 7300 real-time PCR System involving SYBR Green Master Mix, 3-step standard cycling conditions, and sequence-specific primers. The melting curve was examined to verify the amplification of a single product. For quantitative analysis, all the samples were normalized to ubiquitin C gene expression using the $\Delta\Delta CT$ value method.

2.5. Renal Transplant Model. Sprague Dawley rats were used as donors, and Wistar rats were used as recipients for transplantation of the left kidneys. Donor operation: 125 U/mL heparin saline was injected through the lumbar vein of the donor rat. Styptic clips were used to stop the blood supply. Perfusion was conducted through the aorta abdominalis, and the left renal vein was cut off at the same time. When perfusion finished, the left renal artery, vein, and ureter were ligated. The left kidney was separated and dipped into heparin saline at the temperature of 0~4°C. Recipient operation: the blood supply was stopped with styptic clips and the left kidney was separated. The renal artery, renal vein, and ureter of the donor were anastomosed to those of the recipient. The blood supply was restored after anastomotic surgery. Postoperative management: 5 mL saline was injected into the abdominal cavity after closing the abdomen. After renal transplantation, the Wistar rats were treated with penicillin for 3 days and cyclosporin A for 1 week. The rats were followed up for 8 weeks for the development of IF/TA.

2.6. Histological and Immunohistochemical Examination. Following 8 weeks posttransplant, the rats were euthanized and a section of both the kidneys was excised. The excised tissues were embedded in paraffin and optimal cutting temperature compound (OTC) to be made into paraffin sections and frozen sections (used into the ROS-DHE examination). Subsequently, the tissues were stained with different staining techniques such as hematoxylin and eosin (HE), periodic acid-Schiff (PAS), periodic acid-silver methenamine (PASM), Masson trichrome, and immunohistochemical examination.

2.6.1. HE. The paraffin sections were dewaxed with a series of xylene and ethyl alcohol. Then, the sections were stained with hematoxylin (3 min) and eosin (10 min). Sections were dehydrated and then sealed with neutral resins.

2.6.2. PAS. Dewaxed sections were stained with 1% periodic acid solution (10 min), then washed with water (10 min). These sections were dipped into Schiff solution (10 min) and washed with water (5 min). Then, these sections were stained with hematoxylin (3 min). Finally, sections were

dehydrated with a series of ethyl alcohol and xylene and then sealed with neutral resins.

2.6.3. PASM. Dewaxed sections were stained with 1% periodic acid solution (10 min), then washed with water (10 min). These sections were dipped into silver methenamine solution (1 h) and 3% sodium thiosulfate (20 s). Then, these sections were stained with hematoxylin for 3 min, dehydrated, and sealed.

2.6.4. Masson. Dewaxed sections were stained with hematoxylin (3 min) and washed with water. Then, these sections were dipped into a ponceau-acid fuchsin solution (5 min), 2% glacial acetic acid (30 s), 1% phosphomolybdic acid (5 min), and aniline blue (5 min). Finally, sections were dehydrated and then sealed with neutral resins.

2.6.5. Immunohistochemical Examination. Specific antibodies to Snail, S100A4, and vimentin were used, followed by an addition of horseradish peroxidase- (HRP-) conjugated secondary antibodies and 3,3-diaminobenzidine (DAB) for signal detection.

2.7. Statistical Analysis. The continuous variables were expressed as mean and standard deviation. One-way analysis of variance was performed followed by the least significant difference test. A p value of < 0.05 was considered statistically significant.

3. Results

3.1. Oxidative Stress Induces EMT in Rat Renal Tubular Epithelial Cells. To determine whether oxidative stress is associated with EMT, we treated the rat renal tubular epithelial cell line (NRK-52e cells) with 100 μmol/L H$_2$O$_2$ and studied the phenotypic changes. With longer exposure to H$_2$O$_2$, the cell viability decreased (Figure 1(a)), and there was a significant difference among each group. H$_2$O$_2$ treatment for 2 h increased the ROS (DCFH-DA method) and MDA levels in the cells (Figure 1(b)). The ROS level detected using a fluorescence microscope (Figures 1(c) and 1(d)) also demonstrated that H$_2$O$_2$ treatment induced oxidative stress.

To define whether oxidative stress induces EMT in NRK-52e cells, we conducted Western blots to detect EMT-related markers. We found that the expression of N-cadherin, S100A4, vimentin, collagen I, and Snail appears to increase in the cells treated with H$_2$O$_2$ (Figures 2(a) and 2(b)).

To further clarify that EMT in NRK-52e cells was induced by oxidative stress, we pretreated the NRK-52e cells with an antioxidant (NAC) for 1 h, followed by a treatment with 100 μmol/L H$_2$O$_2$ for 2 h. Our results revealed that NAC pretreatment significantly decreased the ROS level (Figures 1(c) and 1(d)) and reversed the phenotypic changes as evidenced by the decreased expression of N-cadherin, S100A4, vimentin, collagen I, and Snail (Figures 2(c) and 2(d)). As oxidative stress induces cell apoptosis, we also tested the expression of cleaved caspase-3, and our results demonstrated that NAC decreased the cleaved caspase-3 expression (Figures 2(c) and 2(d)). These results indicated

(a)

(b)

(c)

(d)
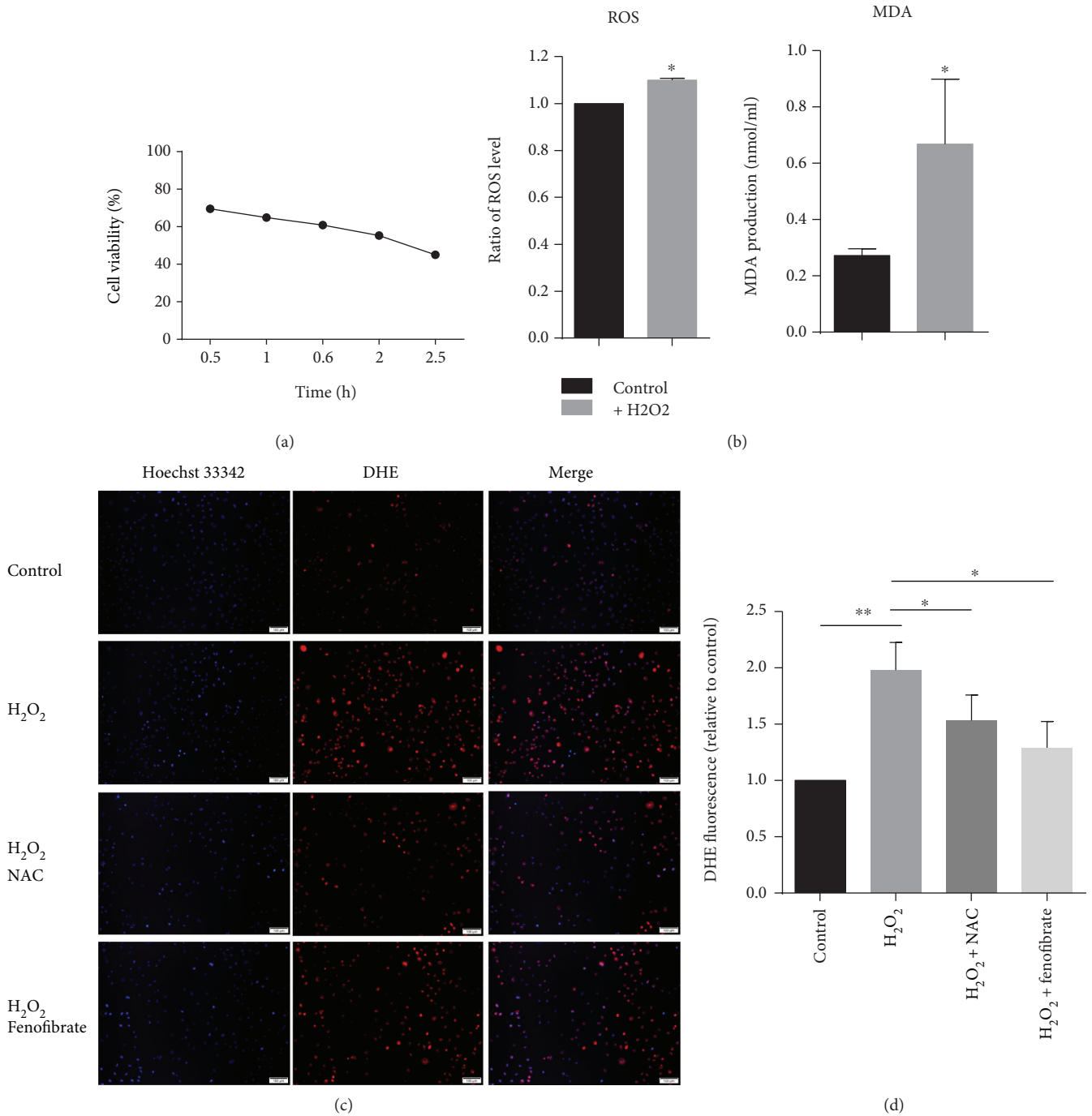
Figure 1: H_2O_2 treatment induced oxidative stress in rat renal tubular epithelial cells. (a) NRK-52e cells were treated with 100 μmol/L H_2O_2 for 0.5 h, 1 h, 1.5 h, 2 h, and 2.5 h, and cell viability was detected with CCK8. (b) NRK-52e cells were treated with 100 μmol/L H_2O_2 for 1 h and 2 h; relative ROS levels were detected with the DCFH-DA method. Cells were treated with H_2O_2, and the medium of the control group was changed at the same time, and then, the medium of cells was collected with or without H_2O_2 treatment 2 h later, and MDA levels were detected. (c) NRK-52e cells were pretreated with 1 mmol/L NAC or 1 μmol/L fenofibrate for 1 h, followed by treatment with 100 μmol/L H_2O_2 for 2 h. DHE and Hoechst 33342 were incubated for 30 min, and a fluorescence microscope was used to observe the fluorescence intensity (red, DHE, exposure time (1.3 s); blue, Hoechst 33342, exposure time (70 ms)). (d) Quantitative analysis was conducted with Image-Pro Plus. $^*p < 0.05$, $^{**}p < 0.01$.

that enhanced oxidative stress induced EMT in renal tubular epithelial cells.

3.2. Fenofibrate Reduced EMT via Suppression of Oxidative Stress in Rat Tubular Epithelial Cells. We studied the effect

of fenofibrate on oxidative stress. We treated the NRK-52e cells with H_2O_2 and/or fenofibrate and detected the oxidative stress level. When treated with fenofibrate, the mRNA and protein levels of PPARα were increased (Figures 3(a) and 3(b)), and the ROS and MDA levels were significantly

(a)

(b)

(c)

(d)
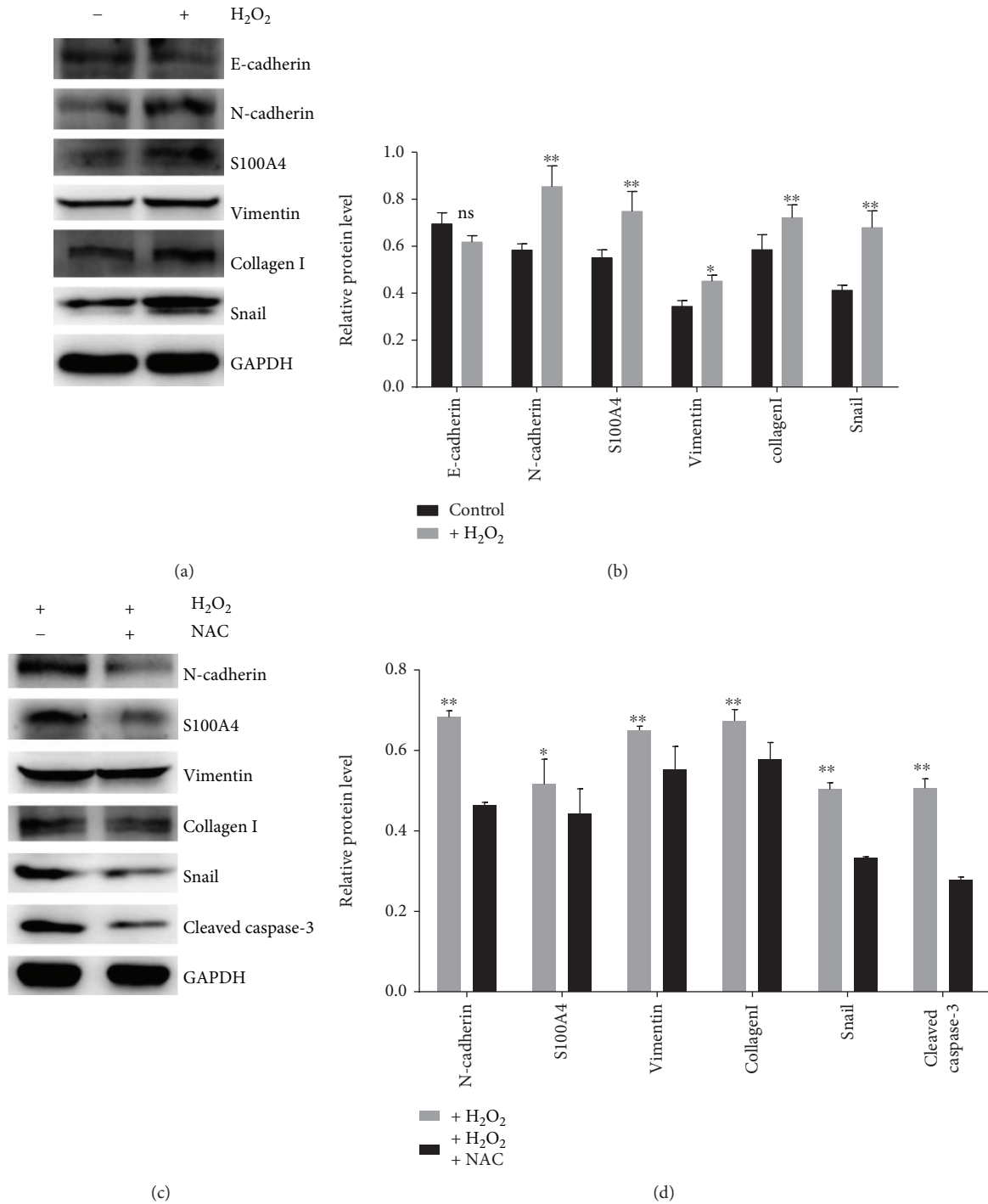
FIGURE 2: Oxidative stress-induced EMT in rat renal tubular epithelial cells. (a) NRK-52e cells were treated with 100 μmol/L H_2O_2 for 2 h and cultured for 24 h, and then Western blot was conducted to detect protein expression. (b) Quantitative analyses were conducted with ImageJ. (c) The cells were pretreated with 1 mM NAC, then treated with 100 μmol/L H_2O_2 for 2 h. The expression of N-cadherin, vimentin, S100A4, collagen I, Snail, and cleaved caspase-3 was detected by Western blot. (d) Quantitative analyses were conducted with ImageJ. $^*p < 0.05$, $^{**}p < 0.01$.

reduced (Figures 1(c), 1(d), and 3(c)). Further, we tested whether fenofibrate can reverse the phenotypic change of the cells induced by oxidative stress. We conducted Western blots to detect the expression of N-cadherin, S100A4, vimentin, collagen I, and Snail, and all these were found to be

reduced (Figures 3(d) and 3(e)). These results indicate that fenofibrate can suppress oxidative stress-induced EMT.

3.3. Fenofibrate Suppresses Fibrosis of Transplant Kidneys in Rats. Our results indicate that fenofibrate suppressed EMT

(a)

(b)

(c)

(d)

(e)
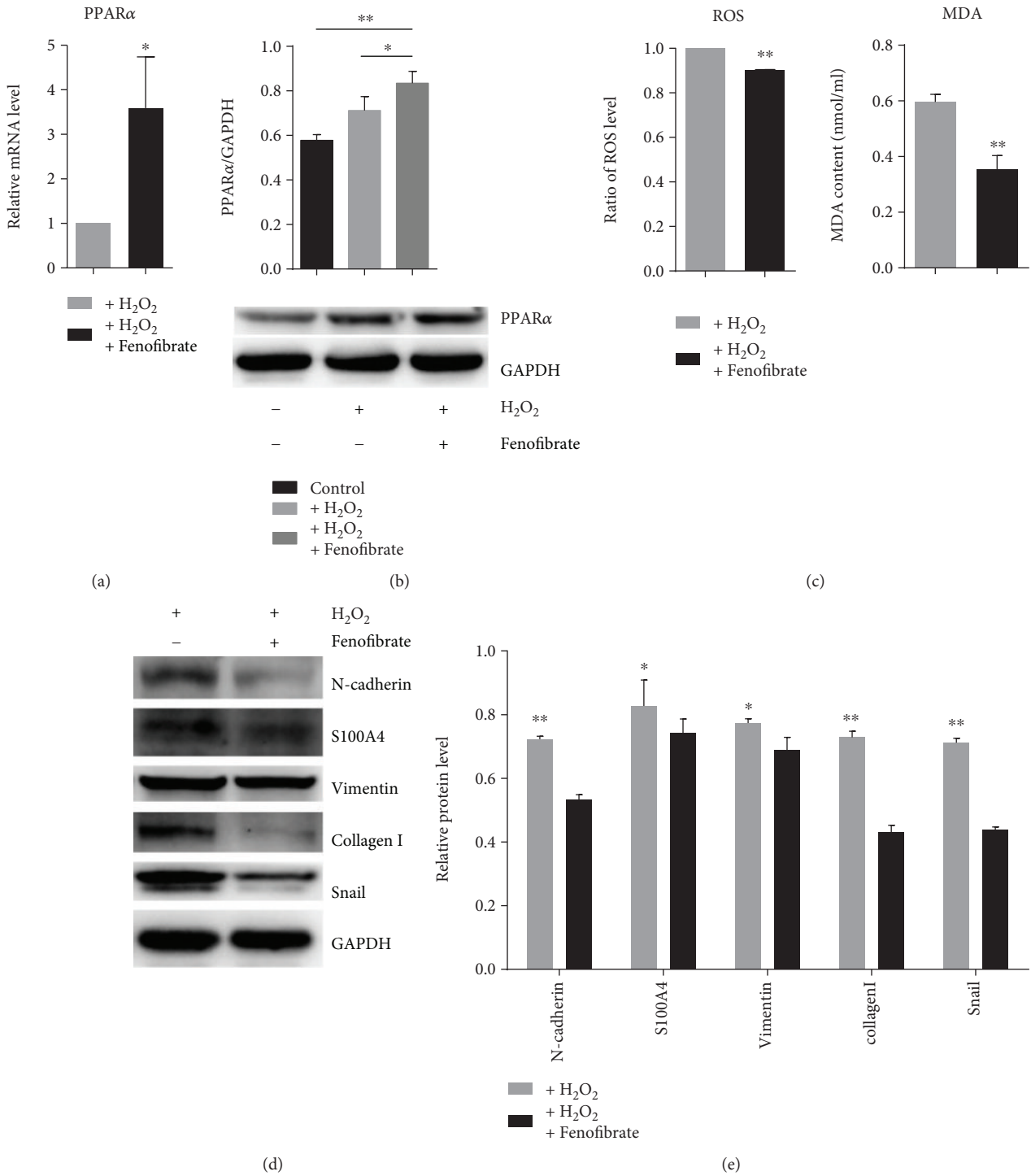
FIGURE 3: Fenofibrate recovered phenotypic changes induced by oxidative stress. (a, b) PPARα expression level assessed *via* quantitative RT-PCR and Western blot analysis in NRK-52e cells treated with H_2O_2 for 2 h and then with fenofibrate for 24 h. (c) Relative ROS and MDA levels after treatment with fenofibrate and H_2O_2. (d, e) Western blot and quantitative analysis for the expression of N-cadherin, S100A4, vimentin, collagen I, and Snail with ImageJ. $^*p < 0.05$, $^{**}p < 0.01$.

by decreasing oxidative stress level in an *in vitro* model. Based on these results, we hypothesize that fenofibrate may inhibit interstitial fibrosis in a renal allograft. To further validate our conjecture, we used Sprague Dawley rats as donors and Wistar rats as recipients in the renal transplantation model (Figure 4(a)). One group was treated with fenofibrate

for 10 d and another group was treated with solvent as a control posttransplantation. The rats were euthanized 8 weeks after transplantation, and the kidneys were excised. We used these kidney tissues for histochemical staining, including HE, Masson, PAS, and PASM, to define the therapeutic effect of fenofibrate for fibrosis of the transplanted kidneys. Our

(a)

(b)

(c)

(d)
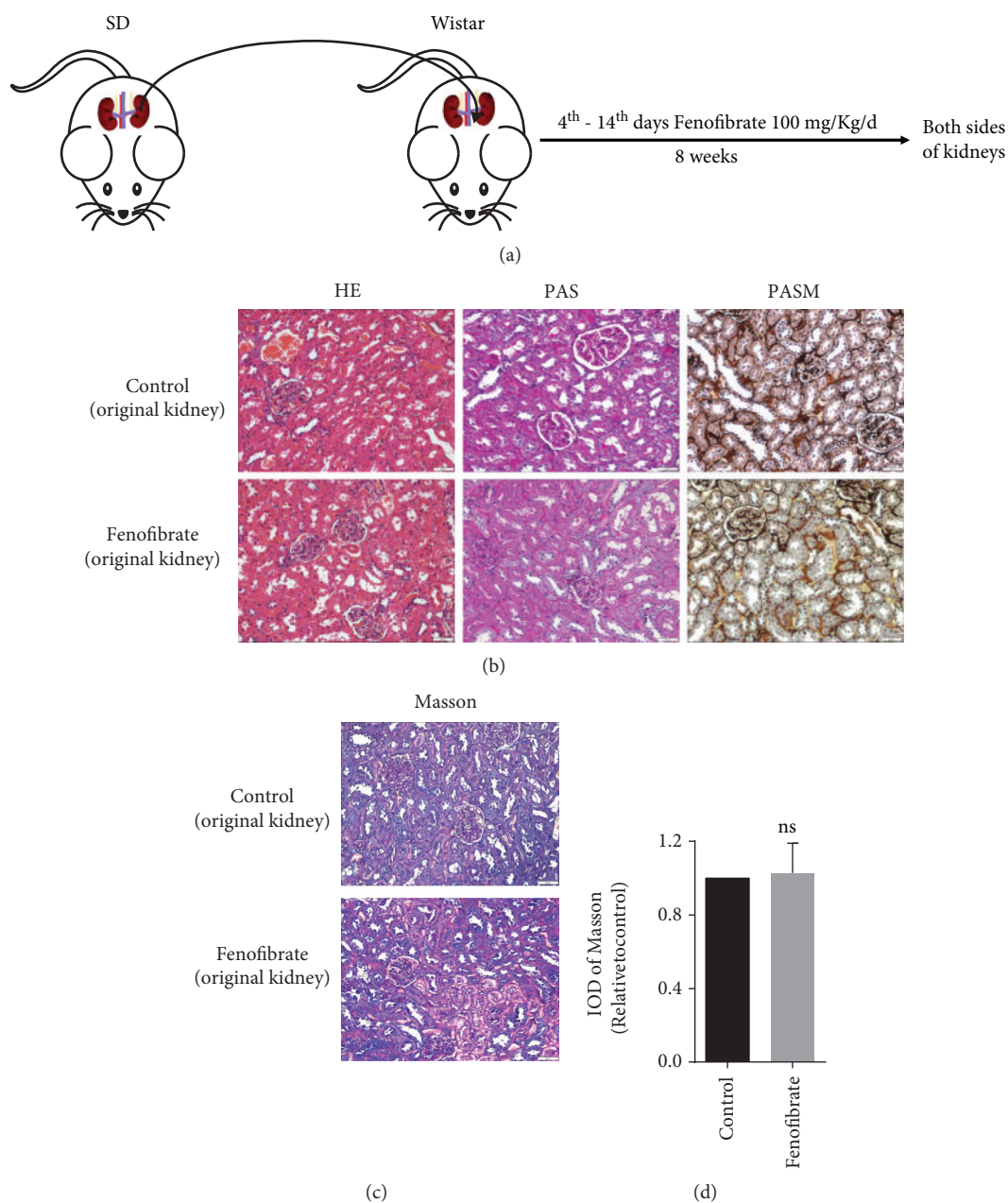
FIGURE 4: Renal transplantation models were established. (a) Wistar rats were used to make unilateral kidney transplant models with kidneys obtained from Sprague Dawley rats. The experimental group was pretreated with 100 mg/kg/d of fenofibrate for 10 d, and the control group was treated with the same solvent after transplant. (b) HE, PAS, and PASM histochemical stains for the original kidneys of the 2 groups of rats. (c) Masson histochemical stains for the original kidneys of the 2 groups of rats. (d) Quantitative analyses were conducted with Image-Pro Plus. IOD: integrated optical density.

results revealed that the nontransplanted kidneys had no significant changes. The structure of renal glomerulus and renal tubules was normal, the capillary loops of the renal glomerulus were open, and there was no or little inflammatory cell infiltration in the renal mesenchyme (Figure 4(b)). There is also no significant difference of collagen fiber deposition in the original kidneys of the two groups (Figures 4(c) and 4(d)).

The transplanted kidneys derived from the control group demonstrated tubulitis, renal glomerular shrinkage, renal tubular atrophy, capillary loop occlusion, a large number of inflammatory cell infiltrations, collagen fiber deposition,

and calcification (Figures 5(a), 5(b), and 5(c)). Fenofibrate significantly improved the fibrotic changes in renal allografts. In the fenofibrate-treated groups, the structure of the glomerulus and tubules was relatively normal, the capillary loops of the renal glomerulus were open, and there were only minor inflammatory cell infiltrations, tubulitis, and collagen fiber depositions (Figures 5(a), 5(b), and 5(c)). In addition, fenofibrate treatment of the transplanted kidney significantly decreased the ROS level (Figures 6(a) and 6(b)). Immunohistochemical findings also showed that Snail, S100A4, and vimentin were positively expressed in

(a)

(b)

(c)
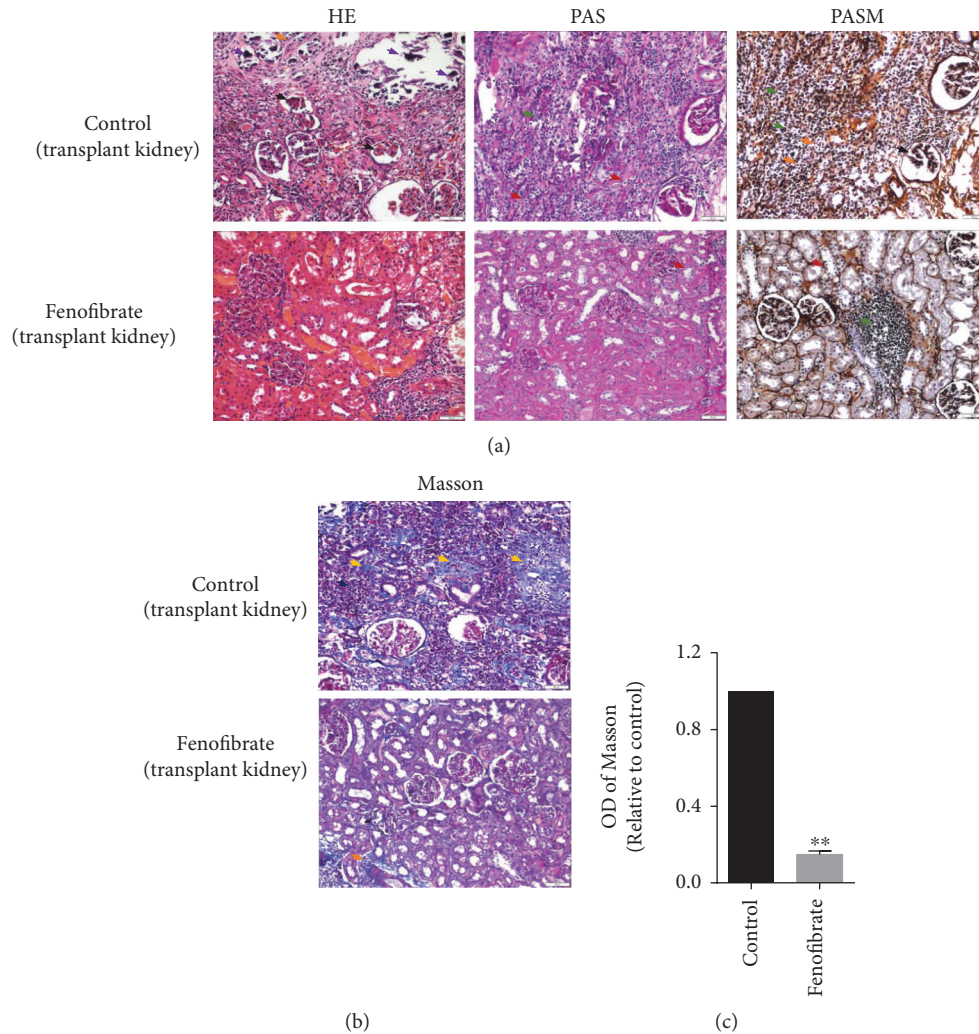
FIGURE 5: Fenofibrate improved fibrosis of renal allografts. (a, b) HE, PAS, PASM, and Masson histochemical stains for transplanted kidneys of 2 groups of rats (black arrow, renal glomerular shrinkage and capillary loop occlusion; red arrow, tubulitis; orange arrow, renal tubular atrophy; green arrow, inflammatory cell infiltrations; purple arrow, calcification; and yellow arrow, collagen fiber deposition). (c) Quantitative analyses were conducted with Image-Pro Plus. IOD: integrated optical density. $^{**}p < 0.01$.

the control group, and the fenofibrate treatment decreased the expression of these proteins (Figures 6(c) and 6(d)). These results further suggested that fenofibrate suppressed EMT in renal allografts. Taken together, our results exhibited that fenofibrate markedly improved chronic fibrosis of the renal allograft by suppressing EMT.

4. Discussion

In our study, we defined that H_2O_2 increased the oxidative stress level in NRK-52e cells. EMT was induced by strengthened oxidative stress, and the fenofibrate treatment suppressed EMT induced by oxidative stress *in vitro*. To further determine the therapeutic effect of fenofibrate for IF/TA in the renal allograft, we established rat renal transplantation models and treated the models with fenofibrate. Results *in vivo* showed that fenofibrate significantly improved fibrosis and pathological injury in the renal allograft; that is, the structure of the glomerulus and tubules

was relatively normal, the capillary loops of the renal glomerulus were open, and there were only minor inflammatory cell infiltrations, tubulitis, and collagen fiber depositions. The fenofibrate treatment also decreased the ROS level and suppressed EMT in the renal allograft (Figure 7).

Oxidative stress often leads to injury and fibrosis in a renal allograft following transplantation. The balance between the production of ROS and the defense against ROS defines the degree of oxidative stress *in vivo*. ROS act as signal and regulatory molecules to participate in cell proliferation, differentiation, and apoptosis [21–23]. A prooxidant microenvironment can alter and denature carbohydrates, nucleic acids, proteins, and lipids resulting in cell toxicity. There are multiple reports revealing the deleterious effects of oxidative stress resulting in different pathophysiologic states, such as neoplasm [24], aging [25, 26], cardiovascular diseases [27–31], and CKD [32–35].

Transplant surgery certainly leads to perioperative acute kidney injury (AKI) from ischemia-reperfusion (IR). It is to

(a)

(b)

(c)

(d)
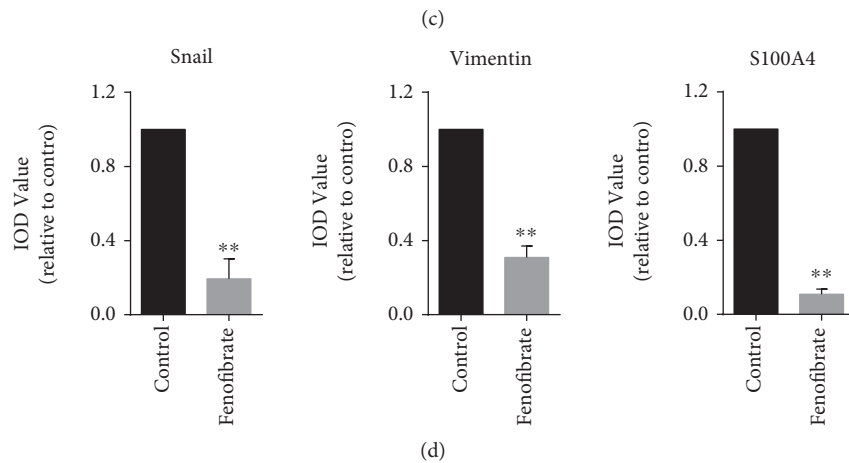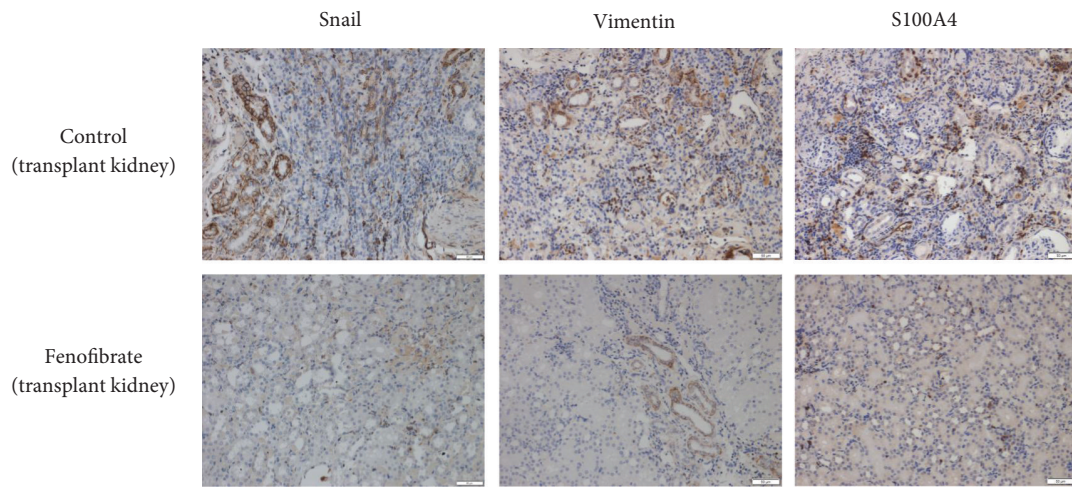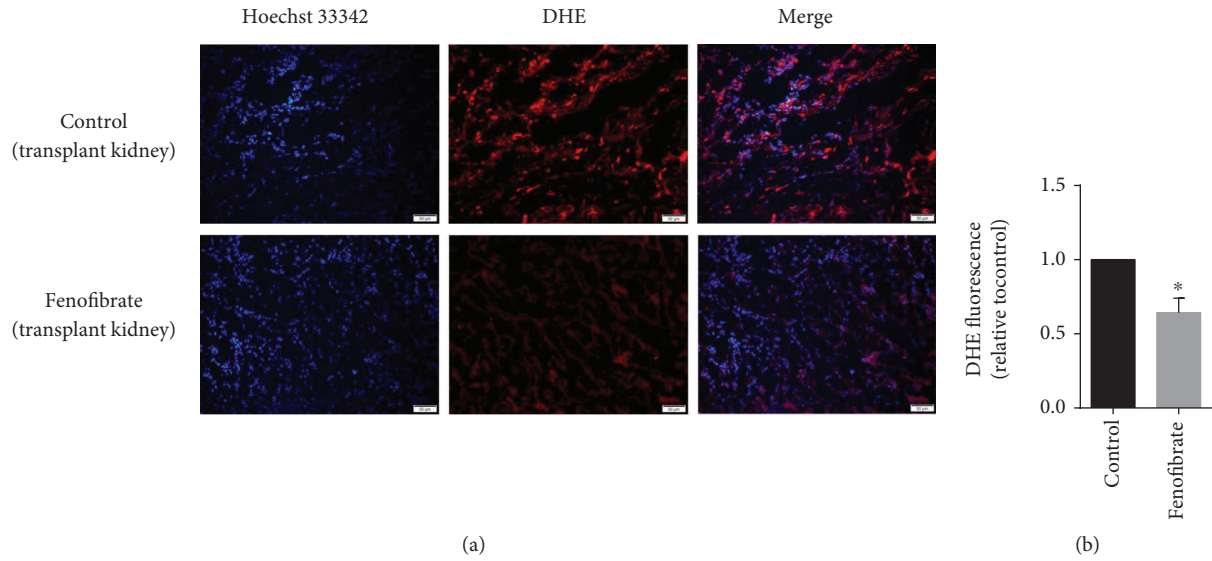
FIGURE 6: Fenofibrate suppresses EMT of renal allografts. (a) ROS detection with frozen sections. (red, DHE, exposure time (1.5 s); blue, Hoechst 33342, exposure time (50 ms). (b) Quantitative analyses were conducted with Image-Pro Plus. (c, d) Immunohistochemical findings and quantitative analysis for Snail, S100A4, and vimentin expressions. $^*p < 0.05$, $^{**}p < 0.01$.

be noted here that AKI itself induces ROS generation and cell apoptosis, which contributes to the process of interstitial fibrosis [36]. However, AKI occurred in an early stage after the operation of renal transplant; IF/TA is a long-term and tardy course of the renal allograft. There are also multiple other factors leading to a higher oxidative stress, and one of which is the use of immunosuppressant drugs. All the renal transplant recipients experience a higher oxidative stress as
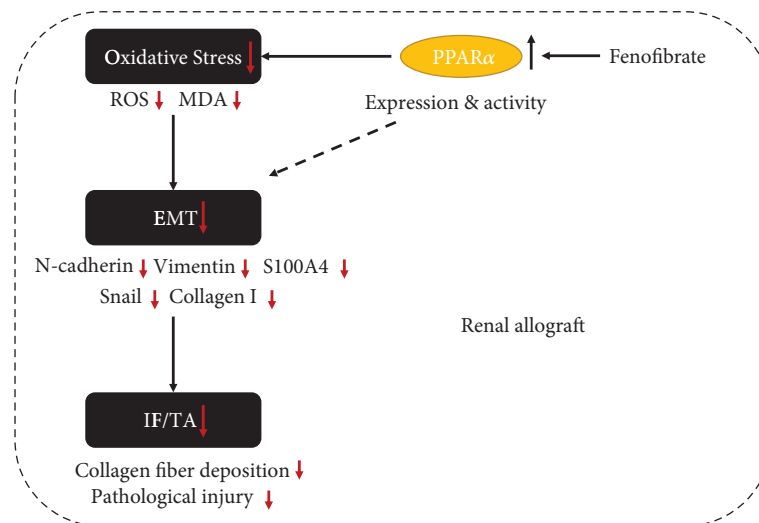
FIGURE 7: Model. Fenofibrate improved interstitial fibrosis of the renal allograft through inhibiting EMT induced by oxidative stress. Fenofibrate increased the expression and activity of PPARα and suppressed EMT induced by oxidative stress (imaginary line showed other mechanisms, such as the fatty acid oxidation pathway), thereby reducing collagen fiber deposition and improving pathological injury of the renal allograft. Fenofibrate effectively delays the progress of IF/TA.

evidenced by elevated specific biomarkers [12, 37–42]. As discussed, oxidative stress is a common mechanism of injury in chronic allograft IF/TA which leads to EMT [12]. From this study, we have demonstrated that increased oxidative stress in rat renal tubular epithelial cells induces EMT.

PPARα is a transcription factor which is widely expressed in multiple organs like the liver, heart, and kidney. Activation of PPARα results in the protection against ischemia-reperfusion injury induced by myocardial ischemia [43]. The activation of PPARα protects myocardial cells by increased expression and activation of superoxide dismutase (SOD1, SOD2) and catalase and suppresses the generation of ROS in myocardial ischemia [43]. Fenofibrate (a PPARα agonist) treatment for 18 weeks had shown to suppress the expression of P47$^{\text{phox}}$ (a subunit of NADPH oxidase) and increase the activation and expression of Cu/Zn-SOD in a spontaneously hypertensive rat model [44]. Fenofibrate also exerted protective effects in hypertensive nephropathy and improved renal tubule interstitial fibrosis, glomerular sclerosis, and inflammatory cell infiltration [18]. The activation of PPARα exhibits protection by suppressing oxidative stress in multiple animal models including alcoholic liver disease [45–47], diabetic retinopathy [48], and Parkinson's disease [49].

In this study, fenofibrate decreased the oxidative stress level and suppressed EMT in NRK-52e cells. PPARα displays its biological functions by transcription regulation and activates multiple endogenous antioxidants, including SOD1, SOD2, and catalase [50]. PPARα is an important transcription factor involved in crucial metabolic pathways like β-oxidation of fatty acids. Multiple studies have demonstrated that increased fatty acid oxidation improves interstitial fibrosis in CKD [19, 20]. Fenofibrate may also suppress EMT by the fatty acid oxidation pathway in the transplanted kidneys. In our study, fenofibrate treatment after kidney transplant

decreased the injury of the renal allograft and improved the fibrosis state. However, the mechanism of suppression of EMT by fenofibrate may not be solely explained by the decreased oxidative stress, and it may also involve fatty acid oxidation pathways. Further mechanistic studies are warranted to investigate this role of fenofibrate in suppressing EMT in renal allografts.

In conclusion, fenofibrate suppressed EMT induced by oxidative stress *in vitro* and *in vivo*. The oxidative stress level was increased in the renal allograft of rats, which is a factor to contribute to IF/TA. Fenofibrate treatment decreased the ROS level of the renal allograft. The EMT progress was also suppressed by fenofibrate. Taken together, fenofibrate may delay the progress of IF/TA in the renal allograft through suppressing EMT induced by oxidative stress.

Data Availability

The data used to support the findings of this study are available from the corresponding author upon request.

Conflicts of Interest

The authors declare that they have no competing interest.

Authors' Contributions

Yishu Wang and Lei Pang contributed equally to this work.

Acknowledgments

References

[1] N. Vadivel, S. G. Tullius, and A. Chandraker, "Chronic allograft nephropathy," *Seminars in Nephrology*, vol. 27, no. 4, pp. 414–429, 2007.

[2] L. C. Paul, "Chronic renal transplant loss," *Kidney International*, vol. 47, no. 6, pp. 1491–1499, 1995.

[3] B. J. Nankivell, R. J. Borrows, C. L.-S. Fung, P. J. O'Connell, R. D. M. Allen, and J. R. Chapman, "The natural history of chronic allograft nephropathy," *The New England Journal of Medicine*, vol. 349, no. 24, pp. 2326–2333, 2003.

[4] K. Solez, R. B. Colvin, L. C. Racusen et al., "Banff '05 meeting report: differential diagnosis of chronic allograft injury and elimination of chronic allograft nephropathy ("CAN")," *American Journal of Transplantation*, vol. 7, no. 3, pp. 518–526, 2007.

[5] X. Li and S. Zhuang, "Recent advances in renal interstitial fibrosis and tubular atrophy after kidney transplantation," *Fibrogenesis & Tissue Repair*, vol. 7, no. 1, p. 15, 2014.

[6] J. R. Chapman, P. J. O'Connell, and B. J. Nankivell, "Chronic renal allograft dysfunction," *Journal of the American Society of Nephrology*, vol. 16, no. 10, pp. 3015–3026, 2005.

[7] F. Strutz, H. Okada, C. W. Lo et al., "Identification and characterization of a fibroblast marker: FSP1," *The Journal of Cell Biology*, vol. 130, no. 2, pp. 393–405, 1995.

[8] M. Iwano, D. Plieth, T. M. Danoff, C. Xue, H. Okada, and E. G. Neilson, "Evidence that fibroblasts derive from epithelium during tissue fibrosis," *The Journal of Clinical Investigation*, vol. 110, no. 3, pp. 341–350, 2002.

[9] R. Kalluri and R. A. Weinberg, "The basics of epithelial-mesenchymal transition," *The Journal of Clinical Investigation*, vol. 119, no. 6, pp. 1420–1428, 2009.

[10] A. Hertig, D. Anglicheau, J. Verine et al., "Early epithelial phenotypic changes predict graft fibrosis," *Journal of the American Society of Nephrology*, vol. 19, no. 8, pp. 1584–1591, 2008.

[11] A. Vongwiwatana, A. Tasanarong, D. C. Rayner, A. Melk, and P. F. Halloran, "Epithelial to mesenchymal transition during late deterioration of human kidney transplants: the role of tubular cells in fibrogenesis," *American Journal of Transplantation*, vol. 5, no. 6, pp. 1367–1374, 2005.

[12] A. Djamali, "Oxidative stress as a common pathway to chronic tubulointerstitial injury in kidney allografts," *American Journal of Physiology. Renal Physiology*, vol. 293, no. 2, pp. F445–F455, 2007.

[13] M. Zahmatkesh, M. Kadkhodaee, M. Mahdavi-Mazdeh et al., "Oxidative stress status in renal transplant recipients," *Experimental and Clinical Transplantation*, vol. 1, pp. 38–44, 2010.

[14] A. Kumar, A. Hammad, A. K. Sharma, F. Mc-Cardle, R. Rustom, and S. E. Christmas, "Oxidative stress in kidney transplant biopsies," *Experimental and Clinical Transplantation*, vol. 1, pp. 207–213, 2015.

[15] K. Kędzierska, M. Domański, K. Sporniak-Tutak, B. Dołęgowska, and K. Ciechanowski, "Oxidative stress and renal interstitial fibrosis in patients after renal transplantation: current state of knowledge," *Transplantation Proceedings*, vol. 43, no. 10, pp. 3577–3583, 2011.

[16] D. Y. Rhyu, Y. Yang, H. Ha et al., "Role of reactive oxygen species in TGF beta1–induced mitogen–activated protein kinase activation and epithelial–mesenchymal transition in renal tubular epithelial cells," *Journal of the American Society of Nephrology*, vol. 16, no. 3, pp. 667–675, 2005.

[17] A. Djamali, S. Reese, J. Yracheta, T. Oberley, D. Hullett, and B. Becker, "Epithelial–to–mesenchymal transition and oxidative stress in chronic allograft nephropathy," *American Journal of Transplantation*, vol. 5, no. 3, pp. 500–509, 2005.

[18] X. Hou, Y. H. Shen, C. Li et al., "PPARα agonist fenofibrate protects the kidney from hypertensive injury in spontaneously hypertensive rats via inhibition of oxidative stress and MAPK activity," *Biochemical and Biophysical Research Communications*, vol. 394, no. 3, pp. 653–659, 2010.

[19] S. H. Han, L. Malaga-Dieguez, F. Chinga et al., "Deletion of Lkb1 in renal tubular epithelial cells leads to CKD by altering metabolism," *Journal of the American Society of Nephrology*, vol. 27, no. 2, pp. 439–453, 2016.

[20] H. M. Kang, S. H. Ahn, P. Choi et al., "Defective fatty acid oxidation in renal tubular epithelial cells has a key role in kidney fibrosis development," *Nature Medicine*, vol. 21, no. 1, pp. 37–46, 2015.

[21] J. Gutierrez, S. W. Ballinger, V. M. Darley-Usmar, and A. Landar, "Free radicals, mitochondria, and oxidized lipids: the emerging role in signal transduction in vascular cells," *Circulation Research*, vol. 99, no. 9, pp. 924–932, 2006.

[22] D. A. Hildeman, T. Mitchell, J. Kappler, and P. Marrack, "T cell apoptosis and reactive oxygen species," *The Journal of Clinical Investigation*, vol. 111, no. 5, pp. 575–581, 2003.

[23] S. Ueda, H. Masutani, H. Nakamura, T. Tanaka, M. Ueno, and J. Yodoi, "Redox control of cell death," *Antioxidants & Redox Signaling*, vol. 4, no. 3, pp. 405–414, 2002.

[24] J. E. Klaunig and L. M. Kamendulis, "The role of oxidative stress in carcinogenesis," *Annual Review of Pharmacology and Toxicology*, vol. 44, no. 1, pp. 239–267, 2004.

[25] K. B. Beckman and B. N. Ames, "The free radical theory of aging matures," *Physiological Reviews*, vol. 78, no. 2, pp. 547–581, 1998.

[26] T. Finkel and N. J. Holbrook, "Oxidants, oxidative stress and the biology of ageing," *Nature*, vol. 408, no. 6809, pp. 239–247, 2000.

[27] M. A. Haidara, H. Z. Yassin, M. Rateb, H. Ammar, and M. A. Zorkani, "Role of oxidative stress in development of cardiovascular complications in diabetes mellitus," *Current Vascular Pharmacology*, vol. 4, no. 3, pp. 215–227, 2006.

[28] D. Jay, H. Hitomi, and K. K. Griendling, "Oxidative stress and diabetic cardiovascular complications," *Free Radical Biology & Medicine*, vol. 40, no. 2, pp. 183–192, 2006.

[29] G. Nickenig and D. G. Harrison, "The AT1-type angiotensin receptor in oxidative stress and atherogenesis," *Circulation*, vol. 105, no. 3, pp. 393–396, 2002.

[30] P. Minuz, P. Patrignani, S. Gaino et al., "Increased oxidative stress and platelet activation in patients with hypertension and renovascular disease," *Circulation*, vol. 106, no. 22, pp. 2800–2805, 2002.

[31] N. D. Vaziri and B. Rodríguez-Iturbe, "Mechanisms of disease: oxidative stress and inflammation in the pathogenesis of hypertension," *Nature Clinical Practice. Nephrology*, vol. 2, no. 10, pp. 582–593, 2006.

[32] J. Himmelfarb and E. McMonagle, "Albumin is the major plasma protein target of oxidant stress in uremia," *Kidney International*, vol. 60, no. 1, pp. 358–363, 2001.

[33] J. Himmelfarb, E. McMonagle, and E. McMenamin, "Plasma protein thiol oxidation and carbonyl formation in chronic renal failure," *Kidney International*, vol. 58, no. 6, pp. 2571–2578, 2000.

[34] J. Himmelfarb, P. Stenvinkel, T. A. Ikizler, and R. M. Hakim, "The elephant in uremia: oxidant stress as a unifying concept of cardiovascular disease in uremia," *Kidney International*, vol. 62, no. 5, pp. 1524–1538, 2002.

[35] B. Payson Oberg, E. McMenamin, F. L. E. E. Lucas et al., "Increased prevalence of oxidant stress and inflammation in patients with moderate to severe chronic kidney disease," *Kidney International*, vol. 65, no. 3, pp. 1009–1016, 2004.

[36] C. Chen, W. Yao, S. Wu et al., "Crosstalk between connexin 32 and mitochondrial apoptotic signaling pathway plays a pivotal role in renal ischemia reperfusion–induced acute kidney injury," *Antioxidants & Redox Signaling*, 2018.

[37] M. Campise, F. Bamonti, C. Novembrino et al., "Oxidative stress in kidney transplant patients," *Transplantation*, vol. 76, no. 10, pp. 1474–1478, 2003.

[38] J. P. Cristol, C. Vela, M. F. Maggi, B. Descomps, and G. Mourad, "Oxidative stress and lipid abnormalities in renal transplant recipients with or without chronic rejection," *Transplantation*, vol. 65, no. 10, pp. 1322–1328, 1998.

[39] D. S. C. Raj, G. Lim, M. Levi, C. Qualls, and S. K. Jain, "Advanced glycation end products and oxidative stress are increased in chronic allograft nephropathy," *American Journal of Kidney Diseases*, vol. 43, no. 1, pp. 154–160, 2004.

[40] S. Simic-Ogrizovic, T. Simic, Z. Reljic et al., "Markers of oxidative stress after renal transplantation," *Transplant International*, vol. 11, no. s1, pp. S125–S129, 1998.

[41] E. M. Simmons, A. Langone, M. T. Sezer et al., "Effect of renal transplantation on biomarkers of inflammation and oxidative stress in end–stage renal disease patients," *Transplantation*, vol. 79, no. 8, pp. 914–919, 2005.

[42] I. H. C. Vos, J. A. Joles, and T. J. Rabelink, "The role of nitric oxide in renal transplantation," *Seminars in Nephrology*, vol. 24, no. 4, pp. 379–388, 2004.

[43] L. Ibarra-Lara, E. Hong, E. Soria-Castro et al., "Clofibrate PPARα activation reduces oxidative stress and improves ultrastructure and ventricular hemodynamics in no–flow myocardial ischemia," *Journal of Cardiovascular Pharmacology*, vol. 60, no. 4, pp. 323–334, 2012.

[44] H. W. Chung, J. H. Lim, M. Y. Kim et al., "High–fat diet–induced renal cell apoptosis and oxidative stress in spontaneously hypertensive rat are ameliorated by fenofibrate through the PPARα–FoxO3a–PGC–1α pathway," *Nephrology, Dialysis, Transplantation*, vol. 27, no. 6, pp. 2213–2225, 2012.

[45] M. Yoon, "PPARαin obesity: sex difference and estrogen involvement," *PPAR Research*, vol. 2010, Article ID 584296, 16 pages, 2010.

[46] L. Kong, W. Ren, W. Li et al., "Activation of peroxisome proliferator activated receptor alpha ameliorates ethanol induced steatohepatitis in mice," *Lipids in Health and Disease*, vol. 10, no. 1, p. 246, 2011.

[47] Y. M. Nan, R. Q. Wang, and N. Fu, "Peroxisome proliferator–activated receptor α, a potential therapeutic target for alcoholic liver disease," *World Journal of Gastroenterology*, vol. 20, no. 25, pp. 8055–8060, 2014.

[48] A. C. Keech, P. Mitchell, P. A. Summanen et al., "Effect of fenofibrate on the need for laser treatment for diabetic retinopathy (FIELD study): a randomised controlled trial," *Lancet*, vol. 370, no. 9600, pp. 1687–1697, 2007.

[49] J. K. Barbiero, R. Santiago, F. S. Tonin et al., "PPAR–α agonist fenofibrate protects against the damaging effects of MPTP in a rat model of Parkinson's disease," *Progress in Neuro-Psychopharmacology and Biological Psychiatry*, vol. 53, pp. 35–44, 2014.

[50] G. D. Girnun, F. E. Domann, S. A. Moore, and M. E. C. Robbins, "Identification of a functional peroxisome proliferator–activated receptor response element in the rat catalase promoter," *Molecular Endocrinology*, vol. 16, no. 12, pp. 2793–2801, 2002.

Research Article

Yiqi-Huoxue Granule (YQHX) Downregulates Prothrombotic Factors by Modulating KLF2 and NF-𝜅B in HUVECs following LPS Stimulation

Hong Wu [iD],[1,2] Xinzhou Wang [iD],[1] Shuibo Gao [iD],[1] Liping Dai [iD],[3] Haibin Tong [iD],[4] Haixia Gao [iD],[1] Zhen Lei,[1] Yongjun Han [iD],[1] Zhentao Wang [iD],[2] Lihua Han [iD],[2] and Dake Qi [iD][5]

[1]Laboratory of Cell Imaging, Henan University of Chinese Medicine, Zhengzhou 450002, China
[2]Institute of Cardiovascular Disease, Henan University of Chinese Medicine, Zhengzhou 450002, China
[3]School of Pharmacy, Henan University of Chinese Medicine, Zhengzhou 450046, China
[4]College of Life and Environmental Science, Wenzhou University, Wenzhou 325035, China
[5]Memorial University of Newfoundland, Division of Biomedical Sciences, Faculty of Medicine, Newfoundland, Canada A1B 3V6

Correspondence should be addressed to Hong Wu; wuhong@hactcm.edu.cn and Shuibo Gao; gaoshuibo@hactcm.edu.cn

The Yiqi-Huoxue granule (YQHX) is a traditional Chinese medication widely used in the therapy of the traditional Chinese medicine diagnosis "Qi deficiency" or "blood stasis" in China. Both these symptoms are related to inflammation, but the mechanisms of YQHX against inflammation are largely unknown. Thus, our present study investigated the effects of YQHX on regulating inflammatory responses induced by lipopolysaccharides (LPS) in HUVECs. Our data found that YQHX remarkably inhibits the production of prothrombotic factors, plasminogen activator inhibitor-1 (PAI-1) and tissue factor (TF), while it upregulates the protein expression of Kruppel-like factor 2 (KLF2). The increase in PAI-1 and TF was significantly attenuated through a transgenic knockdown in KLF2 with a Lenti-shKLF2 vector. YQHX also decreases the phosphorylation of nuclear factor-𝜅B (NF-𝜅B) p65 and I𝜅B following LPS stimulation, and it effectively suppresses PAI-1 and TF via a NF-𝜅B-dependent mechanism. Taken together, our results suggest that YQHX provides a notable antithrombotic activity via regulating the KLF2 expression and NF-𝜅B signaling pathway in HUVECs. The KLF2 and NF-𝜅B may be potential therapeutic targets for interventions of inflammation associated with atherosclerosis.

1. Introduction

Acute ischemic heart disease is a leading cause of death and disability worldwide [1]. It is usually associated with luminal thrombosis resulting from vulnerable atherosclerotic erosion or plaque rupture initiated by endothelial dysfunction [2]. Chronic inflammation is involved in the development of luminal thrombosis [3], due to its role in exacerbating endothelial injury and provoking atherosclerotic plaque rupture [2, 4]. However, current antiatherosclerotic agents and antiplatelet therapy only prevent the physical formation of thrombosis [5, 6], but do not alleviate inflammation or endothelial dysfunction. Thus, developing new strategies

aimed at protecting against inflammation and endothelial dysfunction may have important clinical implications in antithrombotic therapies.

The Yiqi-Huoxue granule (YQHX) is a traditional Chinese medication widely used in the therapy of the traditional Chinese medicine diagnosis "Qi deficiency" or "blood stasis" in China. It is composed of Ginseng Radix et Rhizoma (*Panax ginseng* C. A. Mey), Astragali Radix (*Astragalus membranaceus* (Fisch.) Bge.), Paeoniae Rubra Radix (*Paeonia veitchii* Lynch), and Carthami Flos (*Carthamus tinctorius* L.). The Paeoniae Rubra Radix, Carthami Flos, and Ginseng Radix et Rhizoma extracts have been recognized to produce antithrombotic effects [7–9]. The components of Ginseng

Radix et Rhizoma and Astragali Radix in YQHX are effective to inhibit inflammatory responses [10, 11]. Our previous studies have demonstrated that YQHX could inhibit the expression of prothrombotic factors, plasminogen activator inhibitor-1 (PAI-1) and tissue factor (TF), induced by thrombin in human umbilical vein endothelial cells (HUVECs) [12]. It also reduces platelet aggregation associated with myocardial infarction in rats [13]. However, so far, it is largely unknown if the antithrombotic effect of YQHX is associated with its anti-inflammatory activity.

Kruppel-like factor 2 (KLF2) is a transcriptional regulator highly expressed in endothelial cells. Overexpression of KLF2 prolongs thrombotic time and mediates *in vivo* rapamycin-induced arterial thrombosis in mice [14, 15]. Conversely, KLF2 deficiency inhibits antithrombotic genes [16]. KLF2 also mediates acute and chronic inflammations [17, 18]. The anti-inflammatory effects of KLF2 mechanistically are linked to the suppression of nuclear factor-kappa B (NF-κB) signaling [17, 19] that regulates a variety of genes related to inflammatory responses [20, 21]. Thus, KLF2 may be a key thrombotic regulator due to its effects on regulating both endothelial function and inflammation.

Lipopolysaccharide (LPS) is a component of Gram-negativebacteria. It alters the fibrinolytic system leading to a procoagulant state or thrombosis [22, 23]. LPS stimulates both proinflammatory mediators [24, 25] and prothrombotic factors [26, 27]. In the present study, we used a LPS-incubatedendothelial cell model to mimic inflammatory conditions in human atherosclerotic lesions. We investigated the effects of YQHX on regulating the NF-κB signaling pathway and KLF2 expression in response to inflammatory stimulation. We also examined if the production of prothrombotic factors PAI-1 and TF could function as a downstream readout to test the potential therapeutic effects of YQHX against cardiovascular diseases.

2. Materials and Methods

2.1. Reagents. Endothelial cell culture media (ECM), endothelial cell growth supplies (ECGS), and fetal bovine serum (FBS) were purchased from ScienCell Research Laboratories (ScienCell, CA, USA) or Gibco (Gibco, CA, USA). All of the chemicals, including LPS, simvastatin (ST), pyrrolidine dithiocarbamate (PDTC), and 3-(4,5-dimethyl-2-thiazolyl)-2, and 5-diphenyl-2-H-tetrazolium bromide (MTT) dye, were purchased from Sigma-Aldrich (St. Louis, MO, USA). The antibodies against PAI-1 (sc-5297), TF (sc-393657), KLF2 (sc-28675), p65 (sc-109), p-p65 (sc-33020), IκB (sc-371), p-IκB (sc-8404), GAPDH (sc-47724), and β-actin (sc-47778) were obtained from Santa Cruz Biotechnology (Santa Cruz, CA, USA). Horseradish peroxidase- (HRP-) conjugated anti-mouse IgG (SA00001-1) and anti-rabbit IgG (SA00001-2) antibodies were purchased from Proteintech Biotechnology (Proteintech Ltd., Wuhan, China). Lipofectamine 2000 was obtained from Thermo Fisher Scientific (Thermo, MA, USA). YQHX, composed of Ginseng Radix et Rhizoma, Astragali Radix, Paeoniae Rubra Radix, and Carthami Flos, was produced by Sichuan Neo-Green Pharmaceutical

Technology Development Co., Ltd. (Sichuan, China). It was freshly prepared in a phosphate-buffered solution before use.

2.2. HUVECs. The HUVECs were purchased from ScienCell Research Laboratories (ScienCell, CA, USA), and they were cultured in an incubator at 37°C with 5% CO$_2$ in ECM medium supplemented with 5% FBS and 0.03 mg/ml ECGS. The HUVECs (around 70-80% confluence) were incubated with YQHX (from 0.25 to 1.25 mg/ml) and ST (3 μM) for 3 hours. This was followed by LPS stimulation (25 μg/ml) for 12 hours.

2.3. Cell Viability. The HUVECs were seeded in 96-well plates with a density of 0.7×10^4 cells/well and cultured overnight. The cells were then incubated with YQHX at a concentration of 0-10.0 mg/ml prior to treatment with 10 μl of MTT. The absorbance at 570 nm was detected using a microplate reader (Thermo Fisher Scientific, Waltham, USA).

2.4. Transfection of HUVECs. 293T cells in the logarithmic growth phase were cotransfected with recombinant pBOB plasmid, PAX-2, and VSV-G for 48 h. The supernatant was centrifuged at $4000g$ for 10 min at 4°C to remove cell debris and further concentrated to obtain lentivirus. To overexpress KLF2, the HUVECs were infected with lentivirus containing a KLF2-overexpressing sequence (Lenti-KLF2). As shown in Table 1, the KLF2 short hairpin RNA (Lenti-shKLF2, Cyagen Biosciences Inc., Guangzhou, China) was used to knockdown KLF2 as described previously. The cells were also transfected with a scrambled Lenti-GFP as the negative control. The efficiency of transfection was detected with fluorescence microscopy.

2.5. Western Blot Analysis. The cellular lysates extracted from HUVECs were used to quantify protein expression by Western blot. Briefly, the protein concentration was determined by a BCA protein assay kit, and equal amounts of proteins were loaded into 10% SDS-PAGE gels. Following transfer and blocking with 5% skim milk for 1 h at room temperature, the membranes were then incubated with primary antibodies against KLF2 (1 : 200 dilution), PAI-1 (1 : 500 dilution), TF (1 : 500 dilution), p65 (1 : 500 dilution), p-p65 (1 : 500 dilution), IκB (1 : 500 dilution), p-IκB (1 : 500 dilution), GAPDH (1 : 2000 dilution), or β-actin (1 : 2000 dilution) overnight at 4°C. Following incubation with a secondary antibody and ECL, the proteins were visualized using a Bio-Rad Gel Doc XR$^+$ Imaging System (Bio-Rad, CA, USA). The intensity of the bands was assessed using ImageJ software (available at http://rsbweb.nih.gov/ij/).

2.6. Statistical Analysis. The data were analyzed using either parametric test or nonparametric Mann-Whitney U test depending on the pattern of data distribution, and the results are presented as the mean ± SD. A p value less than 0.05 was considered statistically significant.

3. Results

3.1. LPS Upregulates PAI-1 and TF Expression in a Time-Dependent Manner. LPS regulates PAI-1 and TF in both cell and animal models [26, 27]. The present study investigated

TABLE 1: The sequence of specific KLF2 shRNAs used in the present study. All of the shRNAs correspond to *Homo sapiens*.

Name	Sense (5′-3′)	Antisense (5′-3′)
KLF2 (shRNA1)	GCTGCACATGAAACGGCACAT	ATGTGCCGTTTCATGTGCAGC
KLF2 (shRNA2)	TTGTGATGCCTTGTGAGAAAT	ATTTCTCACAAGGCATCACAA
KLF2 (shRNA3)	CCAAACTGTGACTGGTATTTA	TAAATACCAGTCACAGTTTGG
NC (scramble shRNA)	CCTAAGGTTAAGTCGCCCTCG	CGAGGGCGACTTAACCTTAGG
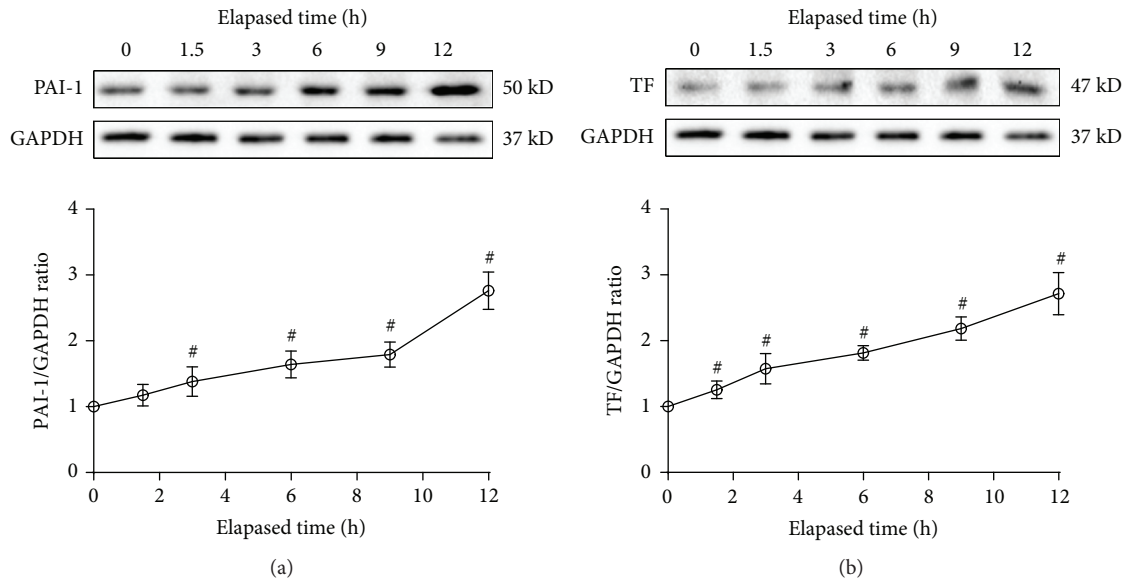
FIGURE 1: LPS upregulates the protein level of PAI-1 and TF in HUVECs. The cells were treated with 25 μg/ml LPS from 0 to 12 h. The levels of (a) PAI-1 and (b) TF were determined using Western blot. Data are expressed as means ± SD ($n = 4$). $^{\#}p < 0.05$ vs. 0 h.

the effects of LPS on regulating the expressions of prothrombotic factors, PAI-1 and TF, in HUVECs. We observed that following LPS stimulation (25 μg/ml), the protein levels of PAI-1 and TF significantly increased in a time-dependent manner in HUVECs (Figure 1). The parallel enhancement of PAI and TF suggests that LPS treatment significantly induces prothrombotic reactions in HUVECs by upregulating both PAI-1 and TF.

3.2. YQHX Inhibits LPS-Induced Expressions of PAI-1 and TF in HUVECs.

A low concentration of YQHX (no more than 1.25 mg/ml) incubated with HUVECs did not affect cell survival (Figure 2(a)). Thus, we cotreated the cells with YQHX and LPS in order to identify the protective effects of YQHX on regulating LPS-induced prothrombotic reactions. Our previous study has demonstrated that YQHX could inhibit thrombin-induced PAI-1 and TF expressions in HUVECs [12]. Our present findings further indicate that YQHX at a low concentration can inhibit LPS-induced PAI-1 and TF (Figure 2(b)). The inhibitory effect of YQHX on both prothrombotic factors PAI-1 and TF is similar to the effect of simvastatin (ST), which is an HMG CoA reductase inhibitor [28] (Figure 2(b)).

3.3. YQHX Inhibits LPS-Induced PAI-1 and TF Expression through KLF2.

KLF2 regulates both acute and chronic inflammation and owns antithrombotic properties [17, 18].

LPS treatment significantly reduced the expression of KLF2 in HUVECs (Figure 3(a)). In the present study, we then overexpressed KLF2 in HUVECs to identify its effect on the regulation of the prothrombotic factors PAI-1 and TF. Indeed, Lenti-KLF2 transduction in HUVECs upregulates the KLF2 expression in the protein level (Figure 3(b)). It significantly suppresses the expression of PAI-1 and TF with or without LPS stimulation (Figure 3(c)). In contrast, shRNA targeting KLF2 downregulates the expression of KLF2 in HUVECs (Figure 4(a)), which results in increased PAI-1 and TF expression in the presence or absence of LPS (Figure 4(b)).

At the concentration range of 0.25 mg/ml to 1.25 mg/ml, YQHX was able to overcome the attenuation of KLF2 expression caused by LPS (Figure 3(a)), which is associated with the attenuation of PAI-1 and TF expression. The knockdown of KLF2 with Lenti-shKLF2 failed to inhibit PAI-1 and TF, suggesting that YQHX might modulate the expression of prothrombotic factors through the upregulation of KLF2.

3.4. YQHX Inhibits the Phosphorylation of NF-κB p65 and IκB.

The activation of the NF-κB signaling pathway is initiated by IκB phosphorylation and degradation. To explore if YQHX regulates the prothrombotic factors by the NF-κB signaling pathway, the phosphorylation levels of NF-κB p65 and IκB were quantified by Western blot. Our data suggest that LPS treatment for 3 hours in HUVECs increased the phosphorylation of NF-κB p65 and IκB, and this was
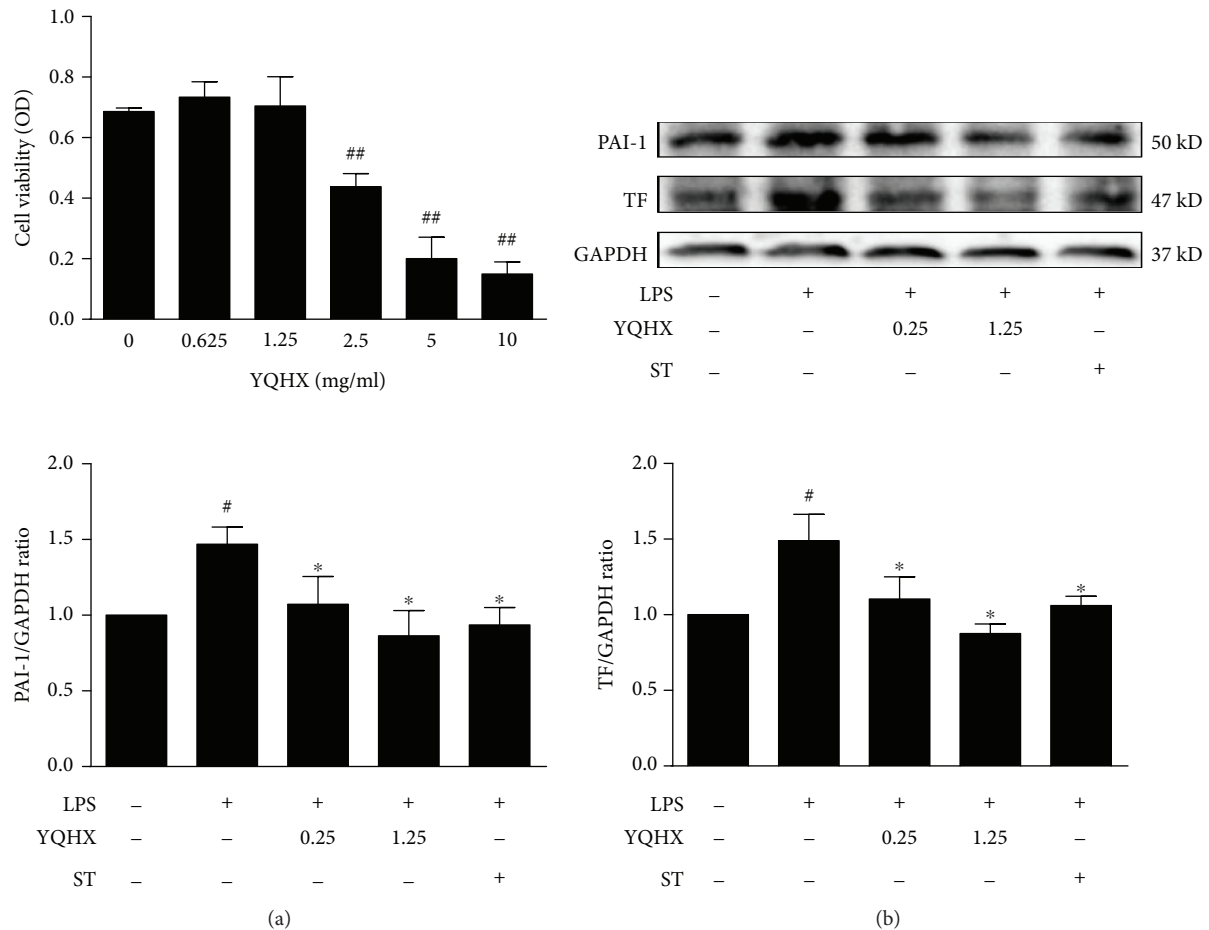
Figure 2: YQHX inhibits LPS-induced PAI-1 and TF expression. (a) HUVECs were incubated with a variable concentration of YQHX (0.625, 1.25, 2.5, 5, and 10 mg/ml) for 15 h. The cell viability was determined by MTT. Data are expressed as means ± SD ($n = 6$). $^{##}p < 0.01$ vs. group without YQHX treatment. (b) HUVECs were pretreated with YQHX (0.25 and 1.25 mg/ml) or ST ($3\,\mu$M) for 3 h prior to LPS treatment (25 μg/ml) for 12 h. Data are expressed as means ± SD ($n = 4$). $^{#}p < 0.05$ vs. control and $^{*}p < 0.05$ vs. group with 25 μg/ml LPS.

significantly inhibited by YQHX at a concentration range of 0.25 to 1.25 mg/ml (Figure 5). The inhibition of phosphorylation of NF-κB p65 and IκB was more robust following a higher concentration (1.25 mg/ml) of YQHX treatment compared to a lower concentration (0.25 mg/ml) (Figure 5). The high concentration of YQHX displayed the same inhibitory effect on the NF-κB signaling pathway as simvastatin, which is a well-known NF-κB-specific inhibitor. Together, our data suggest that YQHX inhibits LPS-induced inflammation by repressing the activation of the NF-κB signaling pathway in a dose-dependent manner.

3.5. YQHX Inhibits PAI-1 and TF through an NF-κB-Dependent Mechanism.

NF-κB regulates KLF2 expression, and KLF2 inhibits PAI-1 and TF. Therefore, we investigated if YQHX inhibits the LPS-induced expression of PAI-1 and TF through the NF-κB signaling pathway. Inhibition of the NF-κB pathway by PDTC, which is a specific inhibitor of NF-κB, successfully reversed the reduction in KLF2 expression caused by LPS (Figure 6). This suggests that the NF-κB pathway is important in mediating KLF2 expression. Interestingly, the upregulated levels of KLF2 following treatments

with PDTC and YQHX were not comparable. The effects of YQHX on KLF2 seem more robust (Figure 6). Furthermore, cotreatment with PDTC and YQHX impeded the ability of YQHX to increase KLF2 expression. This suggests that the upregulation of KLF2 by YQHX is partially mediated by the NF-κB pathway. We also observed that treatment with PDTC significantly reduced the expression of PAI-1 and TF, and PDTC partially attenuates the effects of YQHX on PAI-1 and TF (Figure 6). Together, our results indicate that YQHX may play a key role in modulating the expression of PAI-1 and TF through an NF-κB-dependent mechanism.

3.6. The Schematic Mechanism of YQHX's Antithrombotic Effects following LPS Stimulation.

LPS binds with the cell membrane receptor, TLR4, and activates the NF-κB pathway through a MyD88-dependent pathway. NF-κB then binds with p65 to form a complex, which is further translocated into the nucleus to inhibit KLF2 gene transcription. The KLF2 negatively regulates PAI-1 and TF genes. P65 indirectly promotes the expression of PAI-1 and TF. YQHX downregulates LPS-induced prothrombotic factors through an NF-κB/KLF2 pathway (Figure 7).

(a)

(b)

(c)
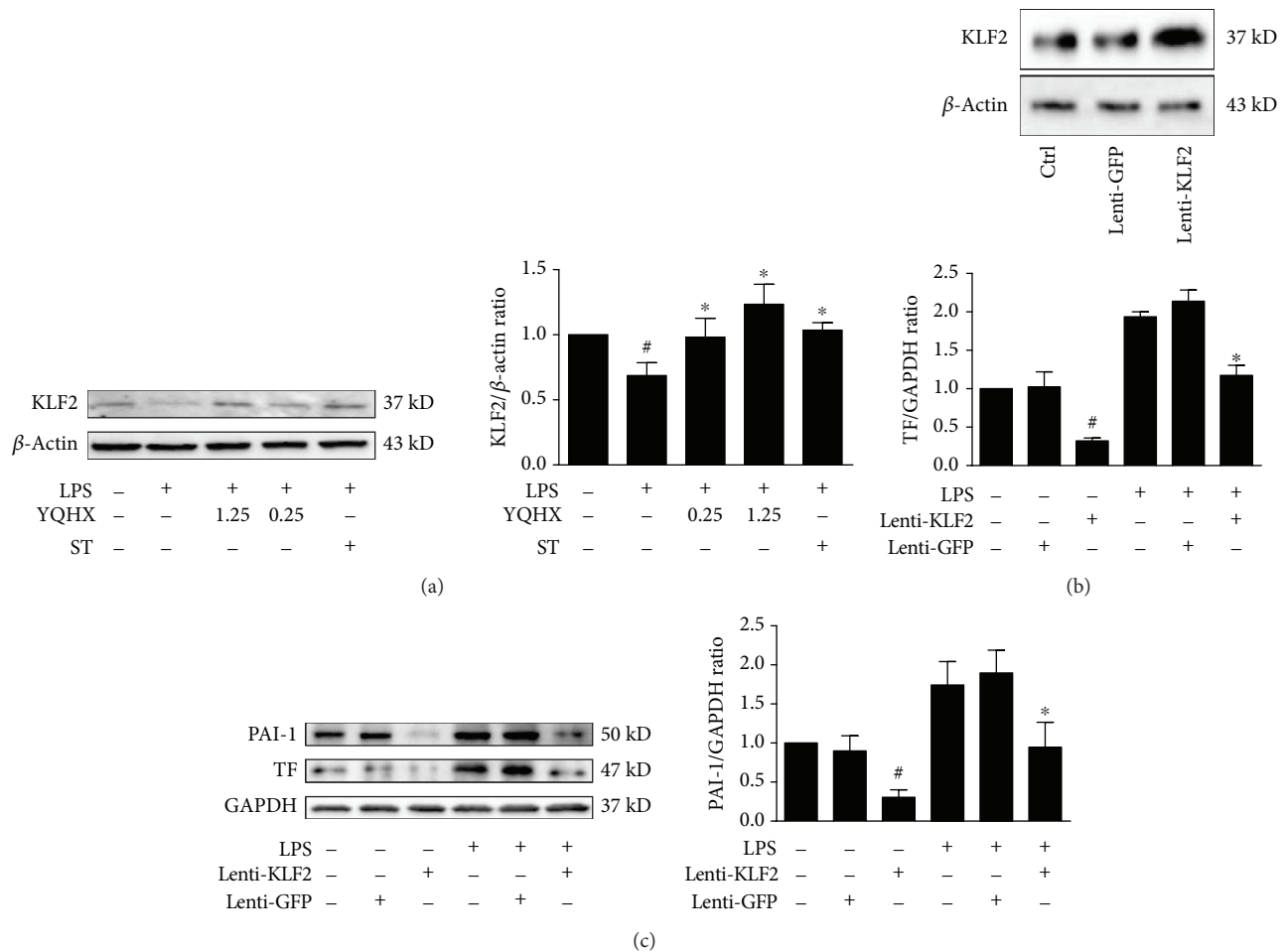
FIGURE 3: YQHX inhibits LPS-induced PAI and TF expression through KLF2. (a) HUVECs were incubated with YQHX (0.25 and 1.25 mg/ml) or ST (3 μM) for 3 h followed with LPS (25 μg/ml) stimulation for 12 h. (b) HUVECs were infected with Lenti-GFP or Lenti-KLF2 for 24 h. (c) HUVECs were preinfected with Lenti-GFP or Lenti-KLF2, followed by LPS (25 μg/ml) stimulation for 12 h. Cell lysates were then prepared, and Western blot analysis was performed to determine the expressions of KLF2, PAI-1, and TF. Data are expressed as means ± SD ($n = 4$). $^{\#}p < 0.05$ vs. control and $^{*}p < 0.05$ vs. group with 25 μg/ml LPS.

4. Discussion

Chinese herbs have been used to prevent cardiovascular diseases for thousands of years in China. YQHX is exclusively prescribed as a traditional Chinese medication for blood stasis of cardiovascular disease in the clinical practice in China. The present study is the first to demonstrate that YQHX attenuates the expression of prothrombotic factors, PAI-1 and TF, following LPS stimulation. YQHX mediates the NF-κB/KLF2 pathway leading to the reduction of the PAI-1 and TF expression in HUVECs. Our study may provide an important insight into the utilization of traditional Chinese medicine in the prevention of thrombosis formation driven by inflammation.

Increasing evidence suggests that inflammation plays a critical role in plaque stability, which eventually leads to rupture and thrombosis [29, 30]. Increased expression of TF and PAI-1 in the endothelium and circulating inflammatory cells might accelerate thrombosis enlargement in patients with acute coronary syndrome (ACS) [31]. Statins have been

recognized to have anti-inflammatory effects independent of their hypolipidemic actions [32]. However, patients with ACS still remain vulnerable even following statin treatment. Ginsenoside Rb1, which is extracted from Ginseng Radix et Rhizoma, was found to potentially inhibit inflammatory responses by skewing macrophages toward the M2 phenotype [33]. The Astragali Radix polysaccharide significantly reduces LPS-induced gene expression of tumor necrosis factor alpha (TNF-α) and interleukin-8 [34]. The extracts of Carthami Flos also possess remarkable anti-inflammatory activity [35]. These findings demonstrate that active extracts from Chinese herbs may regulate inflammation. In fact, a traditional Chinese medicine, Xiangqi Tang (XQT), contains the above active components, and it has an anti-inflammatory function in LPS-treated rat cardiac microvascular endothelial cells. It inhibits the secretion of prothrombotic genes, such as TF and PAI-1, and inflammatory factors, such as TNF-α and intercellular cell adhesion molecule-1 (ICAM-1) [36]. The previous study also found that Tongqiaohuoxue decoction (THD), which includes

(a)

(b)
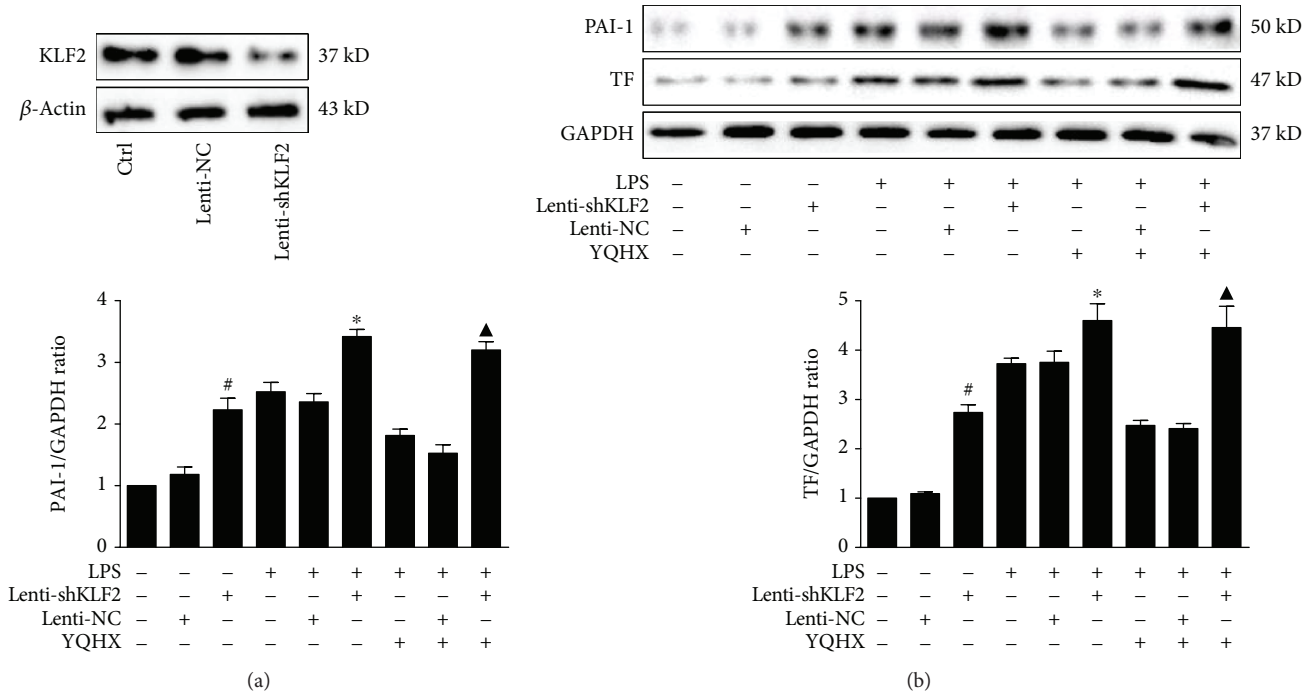
FIGURE 4: YQHX inhibits the PAI-1 and TF expression in a KLF2-dependent manner. (a) HUVECs were infected with Lenti-GFP or Lenti-shKLF2 for 24 h. (b) HUVECs were infected with Lenti-GFP or Lenti-shKLF2. Then, they were incubated with YQHX (1.25 mg/ml) for 3 h prior to 25 μg/ml LPS stimulation for 12 h. Cell lysates were prepared and subjected to Western blot measurements to determine the expression of KLF2, PAI-1, and TF. Data are expressed as means $\pm$ SD ($n = 4$). [#]$p < 0.05$ vs. control, [*]$p < 0.05$ vs. group with 25 μg/ml LPS or LPS plus Lenti-GFP, and [▲]$p < 0.05$ vs. LPS plus YQHX or LPS plus YQHX and Lenti-GFP.

(a)

(b)
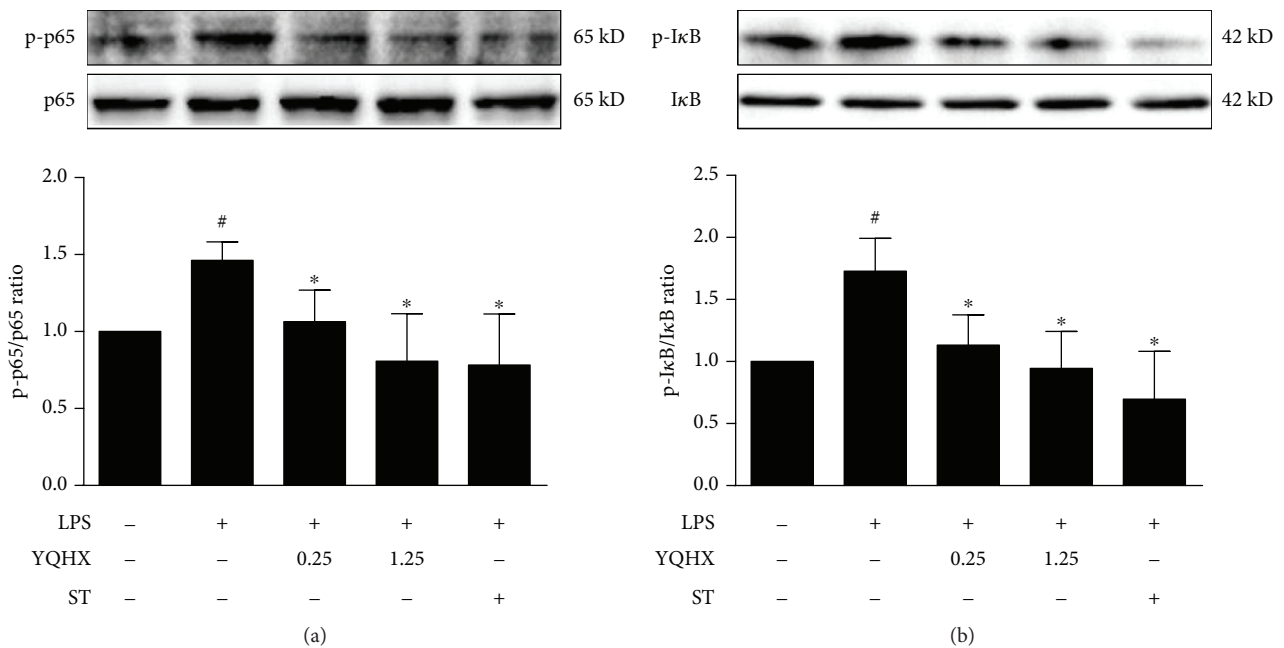
FIGURE 5: YQHX regulates the phosphorylation of NF-κB p65 and IκB. HUVECs were pretreated with YQHX (0.25 and 1.25 mg/ml) or ST (3 μM) for 3 h before being exposed to LPS (25 μg/ml) for 3 h. Cell lysates were prepared and subjected to Western blot analysis to determine the phosphorylation levels of (a) NF-κB p65 and (b) IκB proteins. Data are expressed as means $\pm$ SD ($n = 4$). [#]$p < 0.05$ vs. control and [*]$p < 0.05$ vs. group with 25 μg/ml LPS.
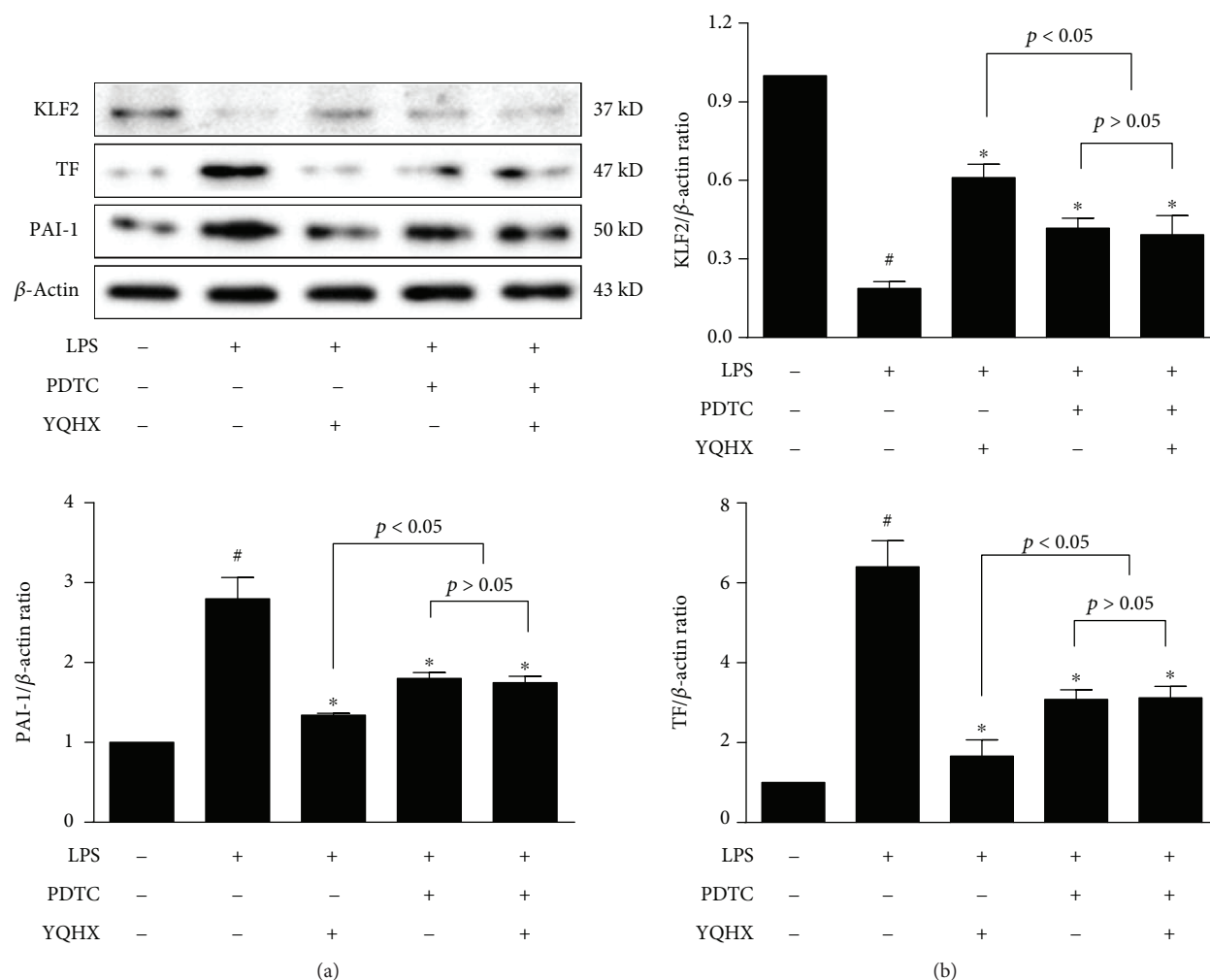
FIGURE 6: YQHX inhibits LPS-induced PAI and TF expression through an NF-κB-dependent mechanism. HUVECs were incubated with 1.25 mg/ml of YQHX or 3 μM of PDTC for 3 h prior to the treatment of LPS (25 μg/ml) for 12 h. Cell lysates were prepared and immunoblotted to determine the expression of KLF2, PAI-1, and TF. Data are expressed as means ± SD ($n = 4$). [#]$p < 0.05$ vs. control and [*]$p < 0.05$ vs. group with 25 μg/ml LPS.

Ginseng Radix et Rhizoma, Astragali Radix, Paeoniae Rubra Radix, and Carthami Flos, also exerts anti-inflammatory and antithrombotic effects by regulating PAI-1 and fibrinolysis [37].

KLF2 functions as a "molecular switch" to regulate vascular homeostasis by maintaining the integrity of the endothelial barrier under physiological and pathological conditions [16]. KLF2 overexpression represses PAI-1 and TF gene expression with or without cytokine TNF-α stimulation [16]. Statins and shear stress also provide antithrombotic actions by stimulating the KLF2 expression in a dose-dependent manner [38–40]. Thus, the upregulation of KLF2 may be a potential therapeutic strategy to limit thrombosis. The present study is the first to demonstrate that YQHX has anti-inflammatory and antithrombotic effects through a KLF2-dependent mechanism. Upregulation of the KLF2 expression by YQHX markedly decreased the production of PAI-1 and TF induced by LPS stimulation, and transgenic knockdown of KLF2 reversed the antithrombotic effects of YQHX.

Typically, NF-κB heterodimers are sequestered with the repressive protein IκBs and are inactive in the cytoplasm. Various inflammatory stimuli activate the NF-κB pathway by inducing the phosphorylation and degradation of IκBs [41, 42]. The activation of NF-κB facilitates the expressions of proinflammatory genes during chronic inflammation and atherosclerotic development [43]. Thus, the suppression of NF-κB is an important strategy for overcoming inflammation [44–46]. Previous studies have indicated that the Chinese traditional medicine, XQT, and its active components promote anti-inflammatory effects by inhibiting mitogen-activated protein kinase (MAPK) and NF-κB signaling pathways [36]. Our results are the first to suggest that YQHX suppresses LPS-induced phosphorylation of both NF-κB p65 and IκB. More importantly, YQHX partially inhibits the production of PAI-1 and TF through an NF-κB-dependent mechanism.

KLF2 inhibits the NF-κB pathway by affecting the recruitment of p300/CBP [19]. In contrast, the NF-κB p65 protein incorporates with histone deacetylase 4 to suppress
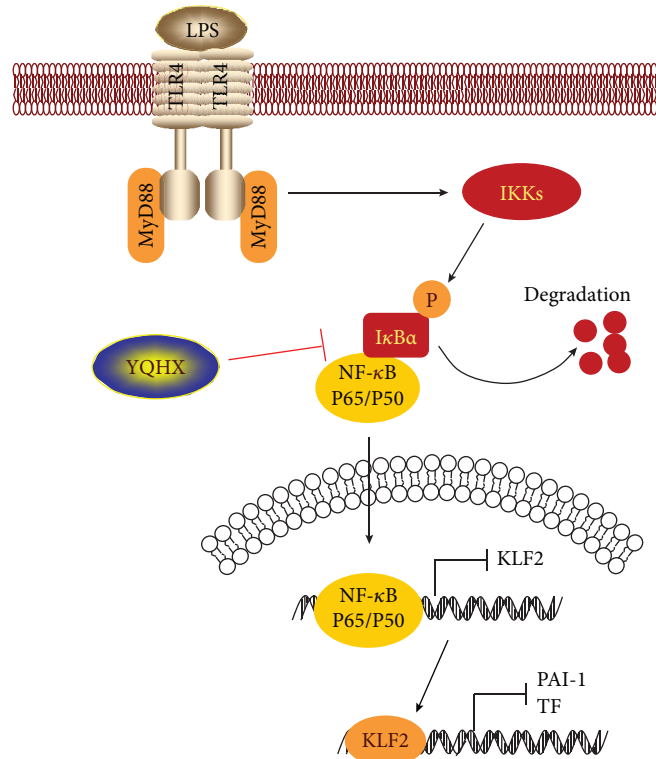
FIGURE 7: Schematic mechanisms of YQHX's antithrombotic effects.

the levels of KLF2. It primarily acts to inhibit the binding of myocyte enhancer factor 2 (MEF2) with the KLF2 promoter [47]. The present study demonstrated that an inhibitor of NF-κB, PDTC, partially inhibits the upregulation of KLF2 induced by YQHX, suggesting that NF-κB is partially involved in YQHX-regulated KLF2 expression.

5. Conclusion

In summary, we demonstrated that YQHX provides anti-inflammatory and antithrombotic effects. It markedly decreases expressions of PAI-1 and TF following stimulation, which are associated with an upregulation of KLF2 in HUVECs. YQHX also inhibits the phosphorylation of NF-κB p65 and IκB proteins, which partially regulate the KLF2 expression. The present findings revealed a mechanism for the inhibitory effects of YQHX on thrombosis formation, suggesting that YQHX may be a promising strategy to prevent inflammation-related diseases.

5.1. Limitations of Our Present Study. Our present findings about YQHX are only based on *in vitro* cell culture models. Our future studies will focus on exploring the effects of YQHX against inflammation or endothelial dysfunction in *in vivo* animal models.

Data Availability

The datasets used or analyzed during the current study are available from the corresponding author on reasonable request.

Conflicts of Interest

No conflict of interest was declared.

Acknowledgments

References

[1] E. J. Benjamin, M. J. Blaha, S. E. Chiuve et al., "Heart disease and stroke statistics-2017 update: a report from the American Heart Association," *Circulation*, vol. 135, no. 10, pp. e146–e603, 2017.

[2] L. Badimon and G. Vilahur, "Thrombosis formation on atherosclerotic lesions and plaque rupture," *Journal of Internal Medicine*, vol. 276, no. 6, pp. 618–632, 2014.

[3] C. Cochain and A. Zernecke, "Macrophages in vascular inflammation and atherosclerosis," *Pflügers Archiv - European Journal of Physiology*, vol. 469, no. 3-4, pp. 485–499, 2017.

[4] P. Shah, S. Bajaj, H. Virk, M. Bikkina, and F. Shamoon, "Rapid progression of coronary atherosclerosis: a review," *Thrombosis*, vol. 2015, no. 634983, 6 pages, 2015.

[5] M. Zhang, J. He, C. Jiang et al., "Plaque-hyaluronidase-responsive high-density-lipoprotein-mimetic nanoparticles for multistage intimal-macrophage-targeted drug delivery and

enhanced anti-atherosclerotic therapy," *International Journal of Nanomedicine*, vol. 12, pp. 533–558, 2017.

[6] N. Papageorgiou, E. Zacharia, A. Ioannou et al., "Novel anti-platelets in stable coronary artery disease," *Current Pharmaceutical Design*, vol. 22, no. 29, pp. 4537–4567, 2016.

[7] Y. H. Li and N. S. Wang, "Antithrombotic effects of Danggui, Honghua and potential drug interaction with clopidogrel," *Journal of Ethnopharmacology*, vol. 128, no. 3, pp. 623–628, 2010.

[8] P. Xie, L. Cui, Y. Shan, and W. Y. Kang, "Antithrombotic effect and mechanism of Radix Paeoniae Rubra," *BioMed Research International*, vol. 2017, Article ID 9475074, 9 pages, 2017.

[9] M. Endale, W. M. Lee, S. M. Kamruzzaman et al., "Ginsenoside-Rp1 inhibits platelet activation and thrombus formation via impaired glycoprotein VI signalling pathway, tyrosine phosphorylation and MAPK activation," *British Journal of Pharmacology*, vol. 167, no. 1, pp. 109–127, 2012.

[10] W. J. Zhang and B. Frei, "Astragaloside IV inhibits NF-κb activation and inflammatory gene expression in LPS-treated mice," *Mediators of Inflammation*, vol. 2015, Article ID 274314, 11 pages, 2015.

[11] J. H. Kim, "Cardiovascular diseases and *Panax ginseng*: a review on molecular mechanisms and medical applications," *Journal of Ginseng Research*, vol. 36, no. 1, pp. 16–26, 2012.

[12] H. Wu, X. Wang, S. Gao, Z. Lei, Z. Wang, and L. Han, "Effect of Yiqi Huoxue decoction on expression of pro-thrombotic factor PAI-1 and TF in endothelial cells induced by thrombin," *Acta Chinese Medicine*, vol. 32, no. 9, pp. 1683–1685, 2017.

[13] L. Han, H. Wu, Z. Wang, and J. Li, "Effects of Yiqi Huoxue decoction on platelet aggregation and aptt/pt/tt in rats after myocardial infarction with left ventricular remodeling," *Jiangsu Zhong Yi Yao*, vol. 26, no. 1, pp. 55-56, 2005.

[14] X. M. Nie, L. X. Su, R. X. Xu, Y. L. Guo, Y. J. Zhou, and J. J. Li, "Kruppel-like factor 2 might mediate the rapamycin-induced arterial thrombosis in vivo: implications for stent thrombosis in patients," *Chinese Medical Journal*, vol. 126, no. 14, pp. 2636–2640, 2013.

[15] L. Nayak, H. Shi, G. B. Atkins, Z. Lin, A. H. Schmaier, and M. K. Jain, "The thromboprotective effect of bortezomib is dependent on the transcription factor Kruppel-like factor 2 (KLF2)," *Blood*, vol. 123, no. 24, pp. 3828–3831, 2014.

[16] Z. Lin, A. Kumar, S. SenBanerjee et al., "Kruppel-like factor 2 (KLF2) regulates endothelial thrombotic function," *Circulation Research*, vol. 96, no. 5, pp. e48–e57, 2005.

[17] L. Nayak, L. Goduni, Y. Takami et al., "Kruppel-like factor 2 is a transcriptional regulator of chronic and acute inflammation," *The American Journal of Pathology*, vol. 182, no. 5, pp. 1696–1704, 2013.

[18] R. Pathak, L. Shao, S. M. Chafekar et al., "IKKβ regulates endothelial thrombomodulin in a Klf2-dependent manner," *Journal of thrombosis and haemostasis*, vol. 12, no. 9, pp. 1533–1544, 2014.

[19] S. SenBanerjee, Z. Lin, G. B. Atkins et al., "Klf2 is a novel transcriptional regulator of endothelial proinflammatory activation," *The Journal of Experimental Medicine*, vol. 199, no. 10, pp. 1305–1315, 2004.

[20] R. M. P. Gutierrez and C. Hoyo-Vadillo, "Anti-inflammatory potential of *Petiveria alliacea* on activated raw264.7 murine macrophages," *Pharmacognosy magazine*, vol. 13, no. 50, pp. 174–178, 2017.

[21] J. Gdula-Argasinska, P. Pasko, K. Sułkowska-Ziaja, K. Kała, and B. Muszyńska, "Anti-inflammatory activities of garlic sprouts, a source of α-linolenic acid and 5-hydroxy-l-tryptophan, in raw 264.7 cells," *Acta Biochimica Polonica*, vol. 64, no. 3, pp. 551–559, 2017.

[22] A. F. Suffredini, P. C. Harpel, and J. E. Parrillo, "Promotion and subsequent inhibition of plasminogen activation after administration of intravenous endotoxin to normal subjects," *The New England Journal of Medicine*, vol. 320, no. 18, pp. 1165–1172, 1989.

[23] P. H. Quax, C. M. van den Hoogen, J. H. Verheijen et al., "Endotoxin induction of plasminogen activator and plasminogen activator inhibitor type 1 mRNA in rat tissues in vivo," *The Journal of Biological Chemistry*, vol. 265, no. 26, pp. 15560–15563, 1990.

[24] Y. H. Choi and H. J. Kang, "Fructus sophorae attenuates secretion of proinflammatory mediators and cytokines through the modulation of NF-κB and MAPK signaling pathways in LPS-stimulated RAW 264.7 macrophages," *General Physiology and Biophysics*, vol. 35, no. 3, pp. 323–331, 2016.

[25] L. A. Cox, L. T. van Eijk, B. P. C. Ramakers et al., "Inflammation-induced increases in plasma endocan levels are associated with endothelial dysfunction in humans in vivo," *Shock*, vol. 43, no. 4, pp. 322–326, 2015.

[26] M. Y. Gao, L. Chen, L. Yang, X. Yu, J. P. Kou, and B. Y. Yu, "Berberine inhibits LPS-induced TF procoagulant activity and expression through NF-κB/p65, Akt and MAPK pathway in THP-1 cells," *Pharmacological Reports*, vol. 66, no. 3, pp. 480–484, 2014.

[27] N. Ohkura, K. Oishi, F. Kihara-Negishi, G. Atsumi, and T. Tatefuji, "Effects of a diet containing Brazilian propolis on lipopolysaccharide-induced increases in plasma plasminogen activator inhibitor-1 levels in mice," *Journal of Intercultural Ethnopharmacology*, vol. 5, no. 4, pp. 439–443, 2016.

[28] Y. Kunieda, K. Nakagawa, H. Nishimura et al., "HMG CoA reductase inhibitor suppresses the expression of tissue factor and plasminogen activator inhibitor-1 induced by angiotensin II in cultured rat aortic endothelial cells," *Thrombosis Research*, vol. 110, no. 4, pp. 227–234, 2003.

[29] I. Tabas, "Macrophage death and defective inflammation resolution in atherosclerosis," *Nature Reviews Immunology*, vol. 10, no. 1, pp. 36–46, 2010.

[30] K. Ley, Y. I. Miller, and C. C. Hedrick, "Monocyte and macrophage dynamics during atherogenesis," *Arteriosclerosis, Thrombosis, and Vascular Biology*, vol. 31, no. 7, pp. 1506–1516, 2011.

[31] T. Sakai, S. Inoue, M. Takei et al., "Activated inflammatory cells participate in thrombus size through tissue factor and plasminogen activator inhibitor-1 in acute coronary syndrome: immunohistochemical analysis," *Thrombosis Research*, vol. 127, no. 5, pp. 443–449, 2011.

[32] G. Vogiatzi, E. Oikonomou, G. Siasos et al., "Statins and inflammation in cardiovascular disease," *Current Pharmaceutical Design*, vol. 23, 2017.

[33] X. Zhang, M. H. Liu, L. Qiao et al., "Ginsenoside Rb1 enhances atherosclerotic plaque stability by skewing macrophages to the M2 phenotype," *Journal of Cellular and Molecular Medicine*, vol. 22, no. 1, pp. 409–416, 2017.

[34] Y. Yuan, M. Sun, and K. S. Li, "Astragalus mongholicus polysaccharide inhibits lipopolysaccharide-induced production of TNF-alpha and interleukin-8," *World Journal of Gastroenterology*, vol. 15, no. 29, pp. 3676–3680, 2009.

[35] Y. Wang, P. Chen, C. Tang, Y. Wang, Y. Li, and H. Zhang, "Antinociceptive and anti-inflammatory activities of extract and two isolated flavonoids of *Carthamus tinctorius* l," *Journal of Ethnopharmacology*, vol. 151, no. 2, pp. 944–950, 2014.

[36] C. L. He, P. F. Yi, Q. J. Fan et al., "Xiang-Qi-Tang and its active components exhibit anti-inflammatory and anticoagulant properties by inhibiting MAPK and NF-κB signaling pathways in LPS-treated rat cardiac microvascular endothelial cells," *Immunopharmacology and Immunotoxicology*, vol. 35, no. 2, pp. 215–224, 2013.

[37] S. H. Kim, H. S. Park, M. J. Hong et al., "Tongqiaohuoxue decoction ameliorates obesity-induced inflammation and the prothrombotic state by regulating adiponectin and plasminogen activator inhibitor-1," *Journal of Ethnopharmacology*, vol. 192, no. 11, pp. 201–209, 2016.

[38] A. Undas, K. E. Brummel-Ziedins, and K. G. Mann, "Anticoagulant effects of statins and their clinical implications," *Thrombosis and Haemostasis*, vol. 111, no. 3, pp. 392–400, 2014.

[39] P. Libby, I. Tabas, G. Fredman, and E. A. Fisher, "Inflammation and its resolution as determinants of acute coronary syndromes," *Circulation Research*, vol. 114, no. 12, pp. 1867–1879, 2014.

[40] R. Sathanoori, F. Rosi, B. J. Gu et al., "Shear stress modulates endothelial KLF2 through activation of P2X4," *Purinergic Signalling*, vol. 11, no. 1, pp. 139–153, 2015.

[41] N. D. Perkins, "Integrating cell-signalling pathways with NF-kappab and IKK function," *Nature Reviews Molecular Cell Biology*, vol. 8, no. 1, pp. 49–62, 2007.

[42] M. Karin and Y. Ben-Neriah, "Phosphorylation meets ubiquitination: the control of NF-κB activity," *Annual Review of Immunology*, vol. 18, no. 1, pp. 621–663, 2000.

[43] A. Oeckinghaus and S. Ghosh, "The NF-kappaB family of transcription factors and its regulation," *Cold Spring Harbor Perspectives in Biology*, vol. 1, no. 4, article a000034, 2009.

[44] X. Palomer, D. Álvarez-Guardia, M. M. Davidson, T. O. Chan, A. M. Feldman, and M. Vázquez-Carrera, "The interplay between NF-kappaB and E2F1 coordinately regulates inflammation and metabolism in human cardiac cells," *PLoS One*, vol. 6, no. 5, article e19724, 2011.

[45] A. Kauppinen, T. Suuronen, J. Ojala, K. Kaarniranta, and A. Salminen, "Antagonistic crosstalk between NF-κB and SIRT1 in the regulation of inflammation and metabolic disorders," *Cellular Signalling*, vol. 25, no. 10, pp. 1939–1948, 2013.

[46] N. Fakhrudin, B. Waltenberger, M. Cabaravdic et al., "Identification of plumericin as a potent new inhibitor of the NF-κB pathway with anti-inflammatory activity *in vitro* and *in vivo*," *British Journal of Pharmacology*, vol. 171, no. 7, pp. 1676–1686, 2014.

[47] A. Kumar, Z. Lin, S. SenBanerjee, and M. K. Jain, "Tumor necrosis factor alpha-mediated reduction of KLF2 is due to inhibition of MEF2 by NF-κB and histone deacetylases," *Molecular and Cellular Biology*, vol. 25, no. 14, pp. 5893–5903, 2005.

Research Article

Apatinib Promotes Apoptosis of Pancreatic Cancer Cells through Downregulation of Hypoxia-Inducible Factor-1α and Increased Levels of Reactive Oxygen Species

Ke He [ID],[1,2,3] **Lu Wu** [ID],[4,5,6] **Qianshan Ding** [ID],[5] **Farhan Haider** [ID],[1,2] **Honggang Yu** [ID],[5] **Haihe Wang** [ID],[1,2] **and Guoan Xiang** [ID][3]

[1]*Department of Biochemistry, Zhongshan School of Medicine, Sun Yat-sen University, Guangzhou 510080, China*
[2]*Center for Stem Cell Biology and Tissue Engineering, Key Laboratory of Ministry of Education, Sun Yat-sen University, Guangzhou 510080, China*
[3]*Department of General Surgery, Guangdong Second Provincial General Hospital, Guangzhou 510317, China*
[4]*Department of Radiation and Medical Oncology, Zhongnan Hospital of Wuhan University, Wuhan University, Wuhan 430071, China*
[5]*Department of Gastroenterology, Renmin Hospital of Wuhan University, Wuhan 430060, China*
[6]*Department of Radiation and Medical Oncology, Hubei Key Laboratory of Tumor Biological Behaviors, Hubei Clinical Cancer Study Center, Zhongnan Hospital, Wuhan University, Wuhan, Hubei 430071, China*

Correspondence should be addressed to Haihe Wang; wanghaih@mail.sysu.edu.cn and Guoan Xiang; guoan_66@163.com

At present, apatinib is considered a new generation agent for the treatment of patients with gastric cancer. However, the effects of apatinib on pancreatic cancer have not been clarified. This study investigated the impact of apatinib on the biological function of pancreatic cancer cells and the potential mechanism involved in this process. Using the Cell Counting Kit-8 method, we confirmed that apatinib treatment inhibited cell proliferation *in vitro*. Moreover, the migration rate of pancreatic cells was inhibited. The effects of apatinib on apoptosis and cell cycle distribution of pancreatic carcinoma cells were detected by flow cytometry. The number of apoptotic cells was significantly increased, and the cell cycle was altered. Furthermore, we demonstrated that apatinib inhibited the expression of hypoxia-inducible factor-1α (HIF-1α), vascular endothelial growth factor, and markers of the phosphoinositide 3-kinase (PI3K)/Akt/mTOR signaling pathway, which increased the levels of reactive oxygen species *in vitro*. Apatinib significantly inhibited the biological function of pancreatic cancer cells. It promoted apoptosis, downregulated the expression of HIF-1α, and increased the levels of reactive oxygen species.

1. Introduction

Emphasized by the close relationship between disease incidence and mortality, pancreatic cancer is a highly fatal disease [1, 2]. Each year, >200,000 individuals die due to pancreatic cancer worldwide. In the USA, the 5-year survival rate of patients with pancreatic cancer is as low as 6% [3]. In most cases, patients with pancreatic cancer are asymptomatic until the disease reaches an advanced state, highlighting that this disease remains one of the most difficult to treat cancer [4]. Pancreatic cancer is not sensitive to radiotherapy or chemotherapy. Thus, an effective and safe treatment is urgently warranted. Over the past decade, it has been shown that the vascular endothelial growth factor (VEGF) and its homologous receptors, that is, the vascular endothelial growth factor receptors (VEGFR), play an important role in carcinogenesis [5–7]. Based on this evidence, therapeutic strategies against these

targets (e.g., bevacizumab and panitumumab) have been widely studied. In addition, ziv-aflibercept and regorafenib were approved as second- and third-line treatment options, respectively [8].

Apatinib—also termed YN968D1—is a novel oral anti-angiogenic small molecule [9]. This agent selectively inhibits VEGFR-2, c-Kit, and c-SRC tyrosine kinases [10, 11]. Now in China, apatinib has been used for the treatment of gastric carcinoma patients [12, 13]. Considering the great patient population and lethality of pancreatic cancer in various countries, it is important to understand the pathobiology and signaling pathways involved in disease progression and develop novel therapeutic approaches. Agents such as aflibercept (a VEGF inhibitor) and axitinib (a VEGFR tyrosine kinase inhibitor) have been tested for the treatment of pancreatic cancers, with limited success [7]. However, the antitumor activity and potential molecular mechanism of apatinib against pancreatic cancer remain to be elucidated.

Activation of hypoxia-inducible factor-1 alpha (HIF-1 alpha) can affect the occurrence and development of pancreatic cancer. The expression of HIF-1α assists pancreatic cancer cells to adapt to hypoxia [14, 15]. In addition, it regulates the expression of downstream genes, such as VEGF. These effects increase the supply of blood to the pancreatic cancer lesions, leading to proliferation, angiogenesis, and metastasis [16]. Although the inhibitory effect of apatinib on VEGFR-2 has been determined, its impact on HIF-1α remains unknown.

In this study, the antitumor activities of apatinib on cell proliferation, cell cycle, migration, and apoptosis were analyzed *in vitro*. In addition, the expression of HIF-1α and alteration of the levels of reactive oxygen species (ROS) were assessed. Moreover, the expressions of markers of the PI3K/AKT/mTOR pathway—an important signaling pathway closely involved in the regulation of cell apoptosis—were detected [17]. We presented evidence that apatinib induced apoptosis in pancreatic cancer cells and exerts an effect on HIF-1α and ROS. These findings provide a novel molecular insight into the targets of apatinib.

2. Materials and Methods

2.1. Antibodies and Reagents. The antibodies used in this study are as follows: GAPDH, HIF-1α rabbit mAb, bcl-2 rabbit mAb, caspase-3 rabbit mAb, Bax rabbit mAb, cleaved caspase-3 rabbit mAb, Akt rabbit mAb, phospho-Akt (Ser473) rabbit mAb, mTOR rabbit mAb, phospho-mTOR (Ser 2448) rabbit mAb, light chain 3B (LC3B) rabbit mAb, and goat secondary antibody to rabbit (horseradish peroxidase-conjugated). All antibodies were provided by Cell Signaling Technology (Cell Signaling, Boston, USA). Apatinib was purchased from Selleck (Houston, USA) and was dissolved in dimethyl sulfoxide. The final concentration of dimethyl sulfoxide in the treatment of the cells was controlled to <0.1% [18].

2.2. Cell Culture. The pancreatic cancer cell lines CFPAC-1 and SW1990 were obtained from the Cell Collection Center of Wuhan University (Wuhan, China). The cells were cultured in Iscove's Modified Dulbecco's Medium (IMDM; Gibco, New York, USA) containing 10% fetal bovine serum (FBS), at 37°C, with 5% CO_2.

2.3. Cell Proliferation Assay. Twenty-four hours prior to treatment, CFPAC-1 and SW1990 cells were inoculated into 96-well plates. Subsequently, different drug concentrations (i.e., 0, 10, 20, 30, 40, and 50 μM) in 10% FBS were used to treat these cells. In each well, 10 μl Cell Counting Kit-8 (Beyotime, Shanghai, China) was mixed and the cells were cultured at 37°C for 1 h. The absorbance was measured using a microplate reader at 450 nm. All experiments were carried out in triplicate.

2.4. Migration and Wound Healing Assay. A cell migration assay was performed using the transwell chambers (8 μM; Corning, New York, USA) [19]. We add the IMDM containing 10% FBS to the bottom of the chamber. Subsequently, CFPAC-1 and SW1990 cells (5×10^4) in a serum-free IMDM, treated with different concentrations of apatinib, were mixed to the upper chamber of each well. Cells which adhered to the membrane were fixed using 4% paraformaldehyde and stained with 0.1% crystal violet dye. Migrated cells in the membrane were photographed from six different angles using an inverted microscope. The confluent monolayer cell plate was scraped using the tip of a 250 μl pipette. Cells were cultured in the serum-free medium to measure the wound healing over a 48 h period.

2.5. Cell Cycle Analysis. After treatment with apatinib for 24 h, these cells were harvested and fixed using 75% ethanol overnight at −20°C. The following day, propidium iodide (PI) (50 μg/ml) and RNase A (1 mg/ml) were added to the cell suspension for 0.5 h examined by flow cytometry (BD FACSCalibur, Becton Dickinson, San Jose, CA) and the proportions of cells in the G1, S, and G2 phases were analyzed [18].

2.6. Analysis of Apoptosis. After reaching a confluence of 50-60%, the cells were treated with various concentrations of apatinib and harvested as previously described [18]. Subsequently, these cells were stained with annexin V-fluorescein isothiocyanate (FITC)/propidium iodide (PI), and the number of apoptotic cells was counted. These cells were analyzed by using the BD FACSCalibur in each experiment. All experiments were carried out in triplicate.

2.7. Reactive Oxygen Species Assay. After treatment with apatinib for 24 h, the cells were collected and incubated in 10 μM 2′-7′dichlorofluorescin diacetate (DCFH-DA) (Beyotime, Shanghai, China) for 20 min at 37°C. Subsequently, the cells were washed and resuspended in a phosphate-buffered saline. The fluorescence intensity was determined using flow cytometry.

2.8. Western Blot Analysis. Briefly, CFPAC-1 and SW1990 cells were first collected using standard procedures. Total protein (40 μg per sample) was then measured by the BCA
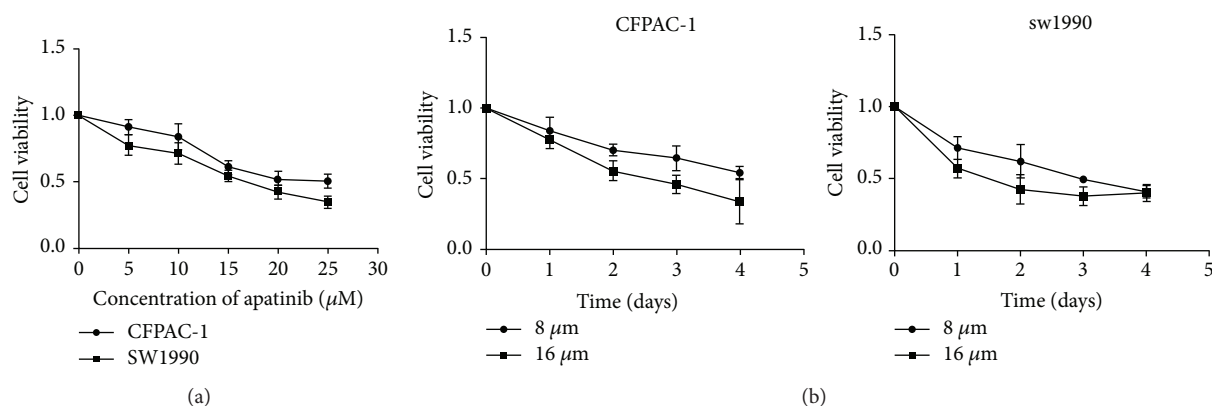
FIGURE 1: Apatinib inhibited cell proliferation in a concentration- and time-dependent manner. (a) Cell viability assays of CFPAC-1 and SW1990 cells treated with low-to-high concentrations of apatinib for 48 h. (b) The CFPAC-1 and SW1990 cells were treated with apatinib ($8\,\mu$M or $16\,\mu$M) for different time intervals. The inhibitory activity was expressed as an inhibition rate. All experiments were performed in triplicate. The results represent mean ± standard deviation; $n = 4$, $P < 0.05$.

Protein Assay Kit (Pierce Biotechnology, Rockford, IL), loaded for sodium dodecyl sulfate gel electrophoresis, and transferred onto polyvinylidene fluoride membranes (Millipore, Billerica, MA). The membranes were then blocked with skimmed milk at room temperature for 1 hour and incubated at 4°C overnight with primary antibodies against GAPDH, HIF-1α, Bax, bcl-2, caspase-3, cleaved caspase-3, Akt, phospho-Akt, mTOR, phospho-mTOR, and LC3B. Total levels of GAPDH were used as a control. Densitometric analysis was performed using the chemiluminescence imaging system (Alpha Innotech Corp., San Leandro, CA), and the relative protein expression was calculated after normalization of the target total protein.

2.9. Statistical Analysis. All experiments were performed in triplicate, and all results are expressed as means ± standard deviation (SD). The data were normally distributed, and the Student's t-test was used to analyze the statistical significance between experimental groups. When $P < 0.05$, the difference was considered to be statistically significant. Graphs were produced using GraphPad Prism 6 (La Jolla, CA). The SPSS V17 Student Edition Software was used for statistical analysis.

3. Results

3.1. Apatinib Inhibited Cell Proliferation in a Concentration- and Time-Dependent Manner. CFPAC-1 and SW1990 cells were treated with low-to-high concentrations (0-50 μM) of apatinib to determine the cytological effect of apatinib on the proliferation of pancreatic cancer cells (Figure 1(a)). The IC$_{50}$ for CFPAC-1 and SW1990 cells were 20.84 ± 1.62 μM and 16.44 ± 1.48 μM, respectively. Therefore, the 8 μM and 16 μM dosages of apatinib were used for further experimentation. Subsequently, we treated CFPAC-1 and SW1990 cells in an increasing time gradient, to further explore the capacity of apatinib to inhibit cell growth in a time-dependent manner. As shown in Figure 1(b), the

inhibition of cell proliferation induced by treatment with apatinib increased in time-dependent manner. Collectively, apatinib inhibited the proliferation of pancreatic cancer cells in a concentration- and time-dependent manner.

3.2. Apatinib Promoted Cell Cycle Arrest of Pancreatic Cancer Cells. Apatinib was used to treat pancreatic cells in a concentration-dependent manner. After 48 h, a relatively normal pattern of cell cycle was observed in untreated cells. CFPAC-1 and SW1990 cells were in the G1 phase (67.81 ± 2.93% and 67.34 ± 1.85%, respectively), while a lower proportion of cells was in the G2 phase peak (8.36 ± 3.41% and 6.36 ± 1.23%, respectively) and the S phase (23.83 ± 3.51% and 26.29 ± 1.34%, respectively). As shown in Figure 2, the cell cycle distribution of CFPAC-1 and SW1990 cells after treatment with 8 μM apatinib was as follows: S phase (13.81 ± 1.56% and 13.69 ± 2.55%, respectively), G1 phase (80.55 ± 3.90% and 79.01 ± 3.15%, respectively), and G2 phase (5.62 ± 2.58% and 7.29 ± 1.46%, respectively). Following treatment with 16 μM apatinib, these distributions were S phase (9.46 ± 0.91% and 10.67 ± 2.01%, respectively) and G1 phase (84.16 ± 3.54% and 85.13 ± 2.34%, respectively). The proportion of treated cells in the G1 phase was significantly increased, whereas that in the S phase was evidently reduced ($P < 0.01$). These results suggested that the effect of apatinib on cell cycle distribution was concentration-dependent, indicating that apatinib regulates pancreatic cancer cells at the G0–G1 phase in the process of karyomitosis.

3.3. Apatinib Inhibited Pancreatic Cell Migration. Furthermore, we examined the effects of apatinib on cell migration using the transwell assay. As shown in Figure 3(a), the migration effect was significantly reduced in cells treated with apatinib ($P < 0.01$). We found that apatinib significantly reduced cell migration in a concentration-dependent manner. The wound healing assay was performed to further validate the effect of apatinib on cell motility (Figure 3(b)).
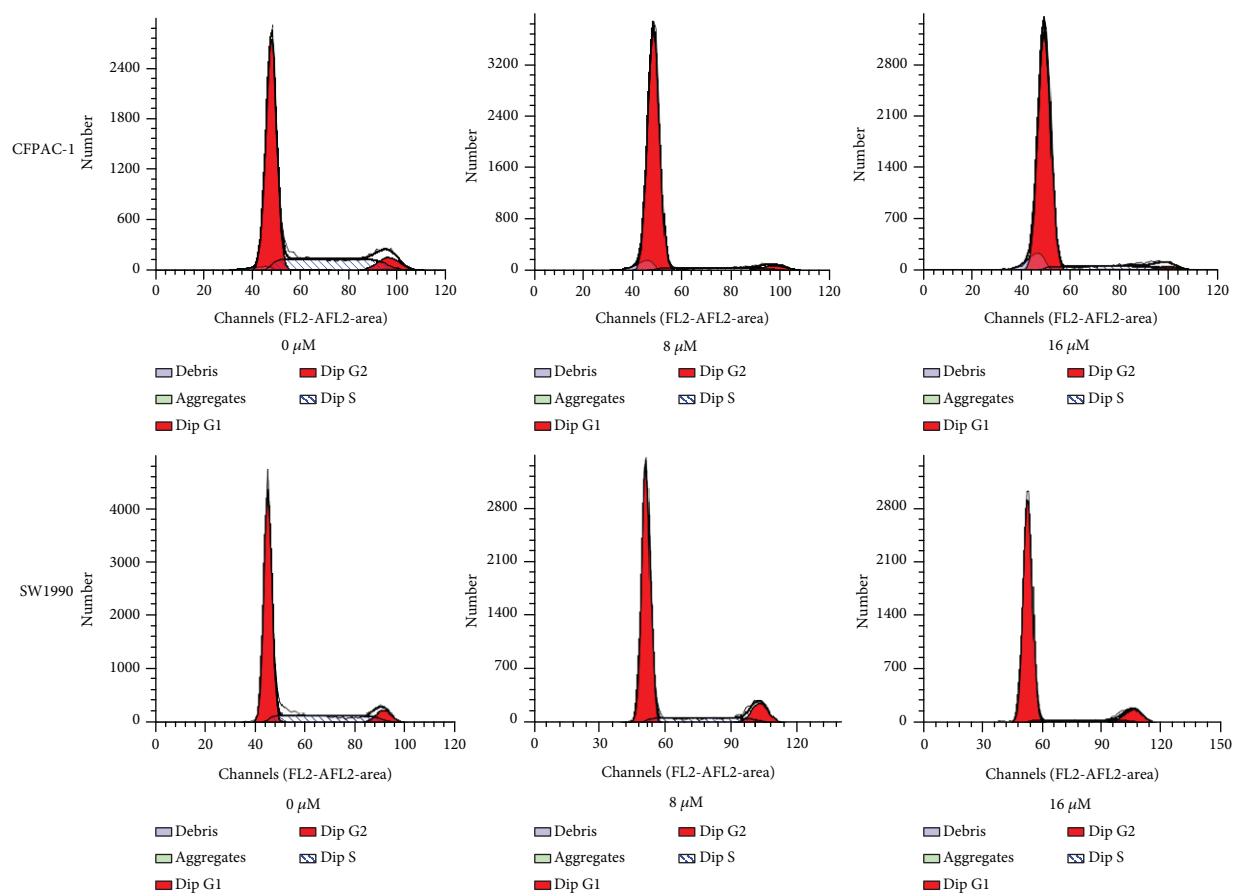
FIGURE 2: Apatinib promoted cell cycle arrest in a concentration-dependent manner. The cell cycle distributions of the CFPAC-1 and SW1990 cells after treatment with apatinib (0, 8, and 16 μM) for 24 h were determined through flow cytometry. All experiments were performed in triplicate.

Consistent with the aforementioned experimental results, treatment with apatinib depressed the mobility of pancreatic cancer cells. Furthermore, the inhibition ratio increased in a concentration-dependent manner. These evidences suggested that apatinib may be a promising antitumor and antimetastatic drug.

3.4. Apatinib Induced Apoptosis of Pancreatic Cancer Cells. Treatment with apatinib significantly increased the percentage of apoptotic cells in each cell (Figures 4(a) and 4(b)). In control cells, the percentages of apoptosis were $1.28 \pm 0.30\%$ and $9.21 \pm 0.65\%$, respectively. In cells treated with 8 μM apatinib, these values were $3.16 \pm 0.89\%$ and 21.46 ± 2.22 %, respectively. In cells treated with 16 μM apatinib, these values were $6.44 \pm 0.88\%$ and $30.02 \pm 1.91\%$, respectively. Both dosages significantly increased the proportion of apoptotic cells ($P < 0.05$). Furthermore, protein levels of Bcl-2, Bax, and caspase-3 related to apoptosis were detected by western blotting. As shown in Figure 4(c), the expression of Bcl-2 was decreased after treatment of CFPAC-1 and SW1990 cells with 8 μM apatinib, whereas those of Bax and cleaved caspase-3 were increased. These results suggested that apatinib promotes apoptosis in pancreatic cancer cells.

3.5. The Effects of Apatinib on the Generation of ROS. CFPAC-1 and SW1990 cells were treated with 8 μM apatinib for 24 h prior to staining with DCFH-DA. The generation of ROS was estimated by measuring the fluorescence intensity of DCFH-DA. The fluorescence of CFPAC-1 and SW1990 cells treated with apatinib was significantly increased compared with that observed for control cells (Figure 5). These results demonstrated that the increased levels of ROS after treatment with apatinib promoted apoptosis of the pancreatic cancer cell.

3.6. Apatinib Inhibited the Expression of HIF-1α and Its Downstream Genes. Subsequently, we attempted to identify the potential molecular mechanism involved in the promotion of apoptosis by apatinib. Hence, we measured the expression of HIF-1α, VEGF, AKT, pho-AKT, mTOR, and phospho-mTOR through western blotting, after we treated pancreatic cancer cells with apatinib for 24 h. Compared with the control cells, treated pancreatic cancer cells presented a significant decrease in the expression of HIF-1α and VEGF (Figure 6(a)). As shown in Figure 6(b), the expression of total AKT protein kept unchanged under all experimental concentrations. However, killing with apatinib (8 μM and 16 μM) resulted in a significant decrease

(a)

(b)
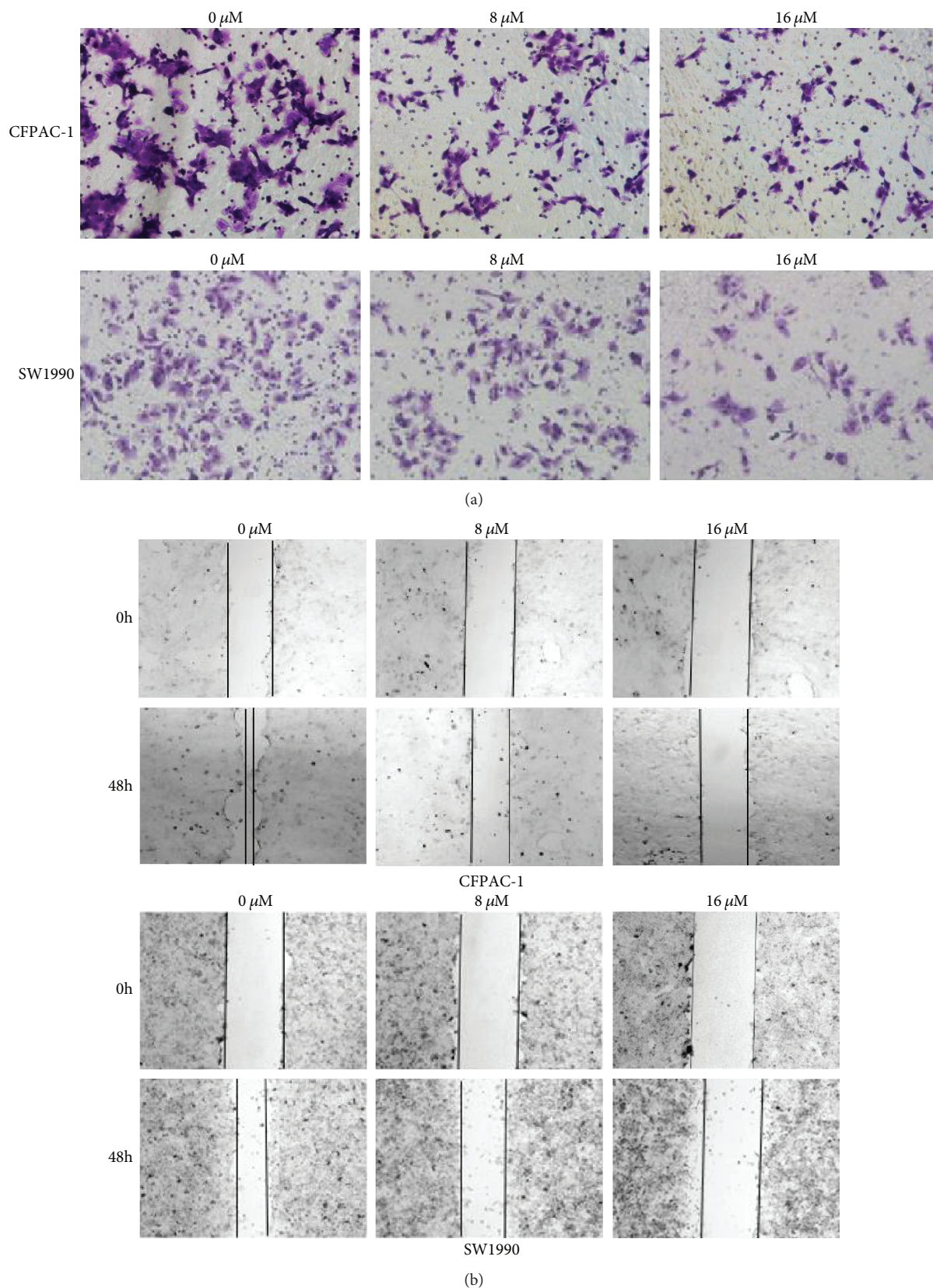
FIGURE 3: Apatinib inhibited the migration of pancreatic cancer cells. (a) The migration of CFPAC-1 and SW1990 cells after treatment with apatinib (0, 8, and 16 μM) for 30 h was assessed using the transwell assay. The migrated cells on the bottom surface of the filters were stained. (b) The movement ability of CFPAC-1 and SW1990 cells after treatment with apatinib (0, 8, and 16 μM) for 48 h was detected using scratch wound healing assays. All experiments were performed in triplicate.

(a)

(b)

(c)
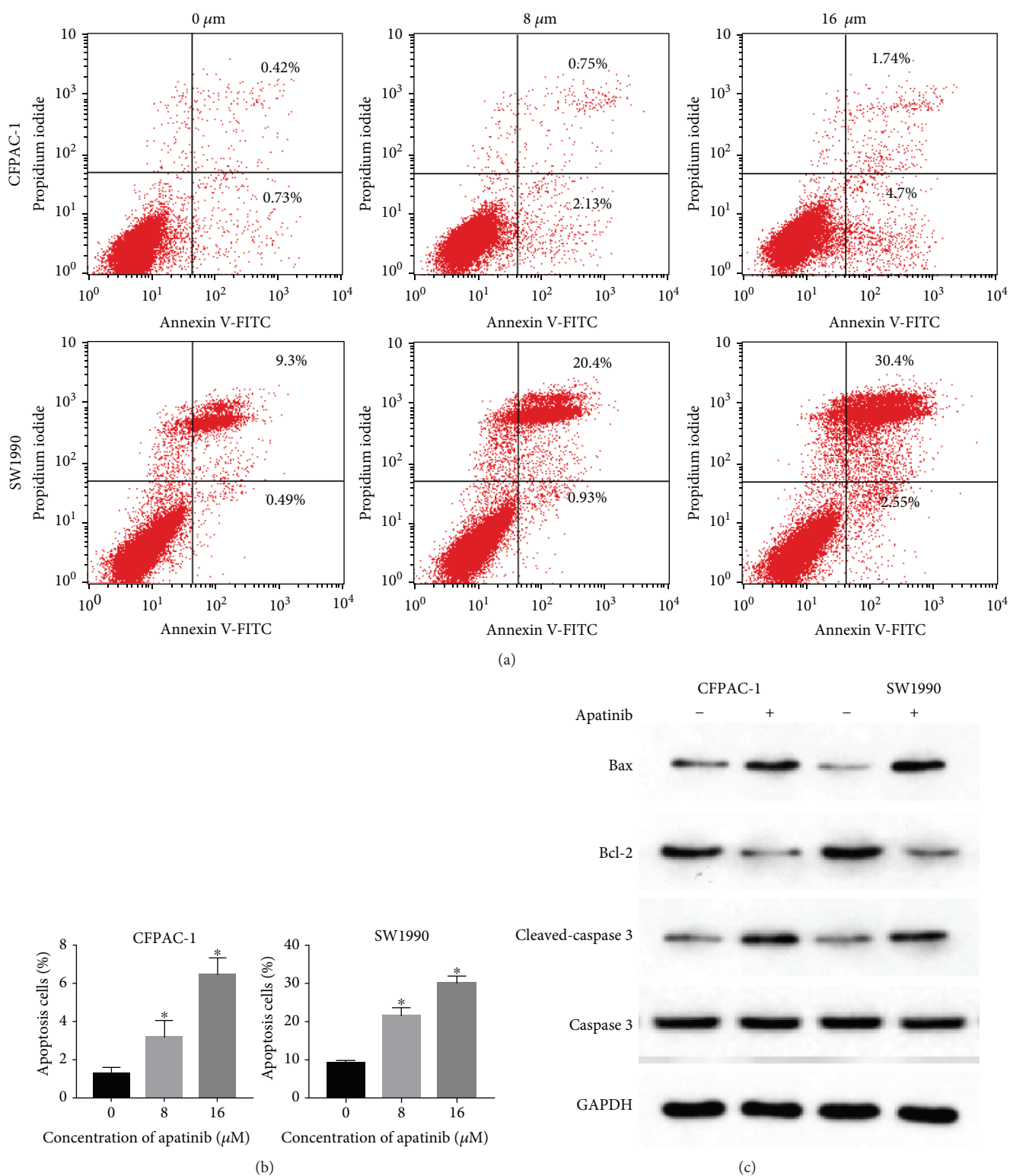
Figure 4: Apatinib induced apoptosis of pancreatic cancer cells. (a) Following the treatment of CFPAC-1 and SW1990 cells with various concentrations of apatinib (0, 8, and 16 μM) for 24 h, these cells were stained using annexin V-FITC/PI and assessed by FACS analysis. (b) The quantitative analysis of the apoptotic cell numbers is shown. (c) The protein levels of Bcl-2, Bax, caspase-3, and cleaved caspase-3 are shown. All experiments were performed in triplicate. The bars represent mean ± standard deviation; $*P < 0.05$.

in the levels of phospho-AKT protein in each cell line. Concurrently, compared with those observed in control cells, the levels of phospho-mTOR protein of apatinib-treated pancreatic cancer cells were depressed. These findings suggested that cell apoptosis and growth inhibition induced by apatinib may be closely related to the
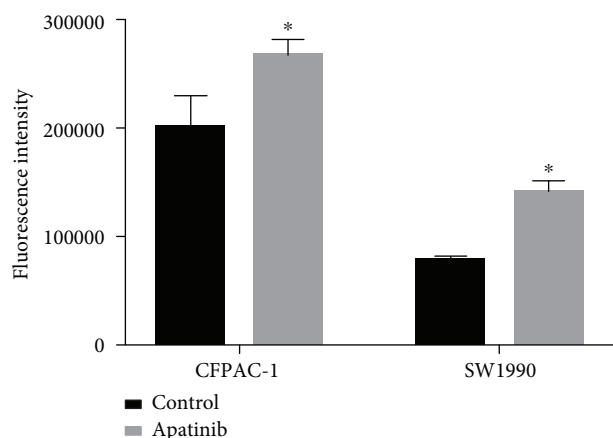
Figure 5: Apatinib induced apoptosis through an elevation of the levels of ROS. After treatment for 24 h, CFPAC-1 and SW1900 cells were stained using DCFH-DA. The fluorescence intensities of apatinib-treated and control cells are shown. All experiments were performed in triplicate. The bars represent mean ± standard deviation; $^*P < 0.05$.

downregulation of HIF-1α and VEGF. The downregulation of the AKT/mTOR pathway may also be partly involved in apoptosis. Moreover, the levels of light chain 3- (LC3-) II in apatinib-treated cells were found to be significantly higher than those reported in the control cells (Figure 6(b)). This increase in the level of LC3-II suggests the activation of autophagy after treatment of pancreatic cancer cells with apatinib.

4. Discussion

Although pancreatic cancers are resistant to certain inhibitors of the VEGF pathway, we found that the proliferation and migration of pancreatic cancer cells were inhibited by apatinib in a concentration-dependent manner. In this study, we also showed that apatinib was cytotoxic to pancreatic cancer cells and the treatment induced apoptosis and loss of cell viability. Furthermore, we indicated that apatinib played a great inhibitory role in the migration of pancreatic carcinoma cells, in a concentration-dependent manner. This phenomenon was consistent with the clinical implications of apatinib, so as to be an effective option for further treatment in pancreatic cancer patients.

In China, apatinib is considered the new generation of oral antiangiogenesis drugs. Moreover, it is a potential third-line selection for the treatment of refractory gastric carcinoma [20]. Currently, clinical trials have been unable to provide definitive conclusions. However, in massively pretreated patients, the survival ratios including overall survival and progression-free survival were improved [21]. Angiogenesis refers to the formation of new blood vessels from previously existing vessels. Antiangiogenesis has been identified as an important treatment for several tumors, such as gastric and colon cancer.

Recently, a case report demonstrated a positive response to treatment with apatinib in a patient diagnosed with metastatic pancreatic cancer [22]. Moreover, another case report showed achievement of a progression-free survival > 11 months after administration of apatinib in a patient with pancreatic cancer-mediated malignant ascites [23]. It was popular in the therapy to incorporate antiangiogenesis factors with VEGF pathway inhibitors. Apatinib—a VEGFR-2 inhibitor—may inhibit endothelial cell migration and proliferation stimulated by VEGF, while simultaneously decreasing the tumor microvascular density. Therefore, it was approved as a promising VEGFR-2 inhibitor for the prevention of tumor-induced angiogenesis [24, 25].

Regarding the antitumor mechanism of apatinib, the currently available studies are mostly focused on antiangiogenesis [26, 27]. Interestingly, our work revealed that treatment with apatinib may inhibit the expression of HIF-1α and increase the levels of ROS. It has been reported that HIF-1α is highly expressed in pancreatic cancer tissues and cell lines, assisting tumor cells in adapting to hypoxic stress. Thus, HIF-1α plays a regulatory role in tumor angiogenesis and energy metabolism. In this study, we found that expressions of HIF-1α and its downstream gene VEGF were both significantly decreased in apatinib-treated cells versus those observed in control cells. In addition, we further discovered that the ROS levels of apatinib-treated cells were significantly higher than those reported in control cells. It was hypothesized that apatinib may inhibit the expression of HIF-1α in pancreatic cancer cells, thereby attenuating their ability to adapt to oxidative stress. Consequently, the levels of ROS were increased and eventually led to apoptosis. Another important factor promoting apoptosis in pancreatic cancer cells may be the inhibition of the AKT/mTOR signaling pathway. Our study showed that the expressions of p-AKT and p-mTOR in apatinib-treated cells were lower than those observed in control cells.

Interestingly, we showed that in apatinib-treated cells the protein level of the autophagy marker LC3-II was elevated, whereas that of LC3-I was decreased. Previous studies have reported that the intracellular levels of ROS may lead to mitochondrial dysfunction, promoting autophagy [28]. This is consistent with the present results we observed in vitro. Autophagy has been recognized as an important catabolic process since the 1960s [29]. The key function of autophagy is to reduce the accumulation of toxic products or meet the change of energy requirement through recovering and redistributing cellular components [17, 30, 31]. It has been established that the Akt/mTOR signaling pathway is a significant regulator of apoptosis and autophagy [32]. The Ulk1 autophagic complex is negatively regulated by mTORC1 activation in the process of autophagy, consequently promoting autophagy and apoptosis [33, 34]. These results suggest that apatinib may be a potential candidate for the treatment of pancreatic cancer.

In summary, our present work revealed that apatinib plays a significant role in the biological function of pancreatic carcinoma cells. We provided new insight into the regulatory molecular mechanism of apatinib on apoptosis in pancreatic

(a)

(b)
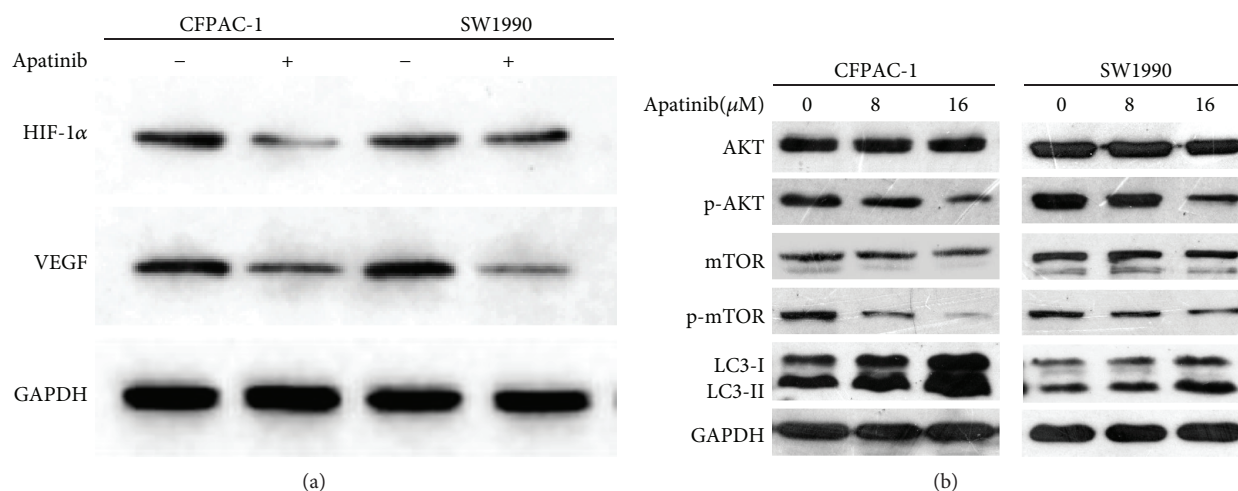
FIGURE 6: Apatinib inhibited the expression of HIF-1α and the AKT/mTOR pathway. (a) CFPAC-1 and SW1990 cells were treated with apatinib (0 or 16 μM) for 24 h, and alterations in the expression of HIF-1α and VEGF were determined through western blotting. GAPDH was included as a loading control. (b) CFPAC-1 and SW1990 cells were treated with different concentrations of apatinib (0, 8, and 16 μM) for 24 h, and the levels of phosphorylated AKT, mTOR, and LC3 were determined through western blotting. GAPDH was used as a loading control. All experiments were performed in triplicate.

cancer cells. The results provide a promising new therapeutic option for pancreatic carcinoma patients. Nevertheless, further animal studies and clinical trials are warranted to confirm these findings. Moreover, research should focus on combinations of chemotherapy drugs.

Data Availability

The data used to support the findings of this study are available from the corresponding author upon request.

Conflicts of Interest

The authors have no conflicts of interest to report in relation to this study.

Authors' Contributions

Ke He, Lu Wu, and Qianshan Ding equally contributed to this study.

Acknowledgments

References

[1] R. L. Siegel, K. D. Miller, and A. Jemal, "Cancer statistics, 2016," *CA: A Cancer Journal for Clinicians*, vol. 66, no. 1, pp. 7–30, 2016.

[2] E. P. Balaban, P. B. Mangu, A. A. Khorana et al., "Locally advanced, unresectable pancreatic cancer: American Society of Clinical Oncology clinical practice guideline," *Journal of Clinical Oncology*, vol. 34, no. 22, pp. 2654–2668, 2016.

[3] T. Kamisawa, L. D. Wood, T. Itoi, and K. Takaori, "Pancreatic cancer," *The Lancet*, vol. 388, no. 10039, pp. 73–85, 2016.

[4] P. P. Adiseshaiah, R. M. Crist, S. S. Hook, and S. E. McNeil, "Nanomedicine strategies to overcome the pathophysiological barriers of pancreatic cancer," *Nature Reviews Clinical Oncology*, vol. 13, no. 12, pp. 750–765, 2016.

[5] S. Chatterjee, L. C. Heukamp, M. Siobal et al., "Tumor VEGF: VEGFR2 autocrine feed-forward loop triggers angiogenesis in lung cancer," *The Journal of Clinical Investigation*, vol. 123, no. 4, pp. 1732–1740, 2013.

[6] C. Fontanella, E. Ongaro, S. Bolzonello, M. Guardascione, G. Fasola, and G. Aprile, "Clinical advances in the development of novel VEGFR2 inhibitors," *Annals of Translational Medicine*, vol. 2, no. 12, p. 123, 2014.

[7] G. C. Jayson, R. Kerbel, L. M. Ellis, and A. L. Harris, "Antiangiogenic therapy in oncology: current status and future directions," *The Lancet*, vol. 388, no. 10043, pp. 518–529, 2016.

[8] E. Chu, "An update on the current and emerging targeted agents in metastatic colorectal cancer," *Clinical Colorectal Cancer*, vol. 11, no. 1, pp. 1–13, 2012.

[9] G. Roviello, A. Ravelli, K. Polom et al., "Apatinib: a novel receptor tyrosine kinase inhibitor for the treatment of gastric cancer," *Cancer Letters*, vol. 372, no. 2, pp. 187–191, 2016.

[10] J. Ding, X. Chen, Z. Gao et al., "Metabolism and pharmacokinetics of novel selective vascular endothelial growth factor receptor-2 inhibitor apatinib in humans," *Drug Metabolism and Disposition*, vol. 41, no. 6, pp. 1195–1210, 2013.

[11] S. P. Ivy, J. Y. Wick, and B. M. Kaufman, "An overview of small-molecule inhibitors of VEGFR signaling," *Nature Reviews Clinical Oncology*, vol. 6, no. 10, pp. 569–579, 2009.

[12] J. Ding, X. Chen, X. Dai, and D. Zhong, "Simultaneous determination of apatinib and its four major metabolites in human plasma using liquid chromatography–tandem mass spectrometry and its application to a pharmacokinetic study," *Journal of Chromatography B*, vol. 895-896, pp. 108–115, 2012.

[13] A. J. Scott, W. A. Messersmith, and A. Jimeno, "Apatinib: a promising oral antiangiogenic agent in the treatment of multiple solid tumors," *Drugs of Today*, vol. 51, no. 4, pp. 223–229, 2015.

[14] H. S. Li, Y. N. Zhou, L. Li et al., "WITHDRAWN: Mitochondrial targeting of HIF-1α inhibits hypoxia-induced apoptosis independently of its transcriptional activity," *Free Radical Biology & Medicine*, 2018.

[15] M. Wang, M. Y. Chen, X. J. Guo, and J. X. Jiang, "Expression and significance of HIF-1α and HIF-2α in pancreatic cancer," *Journal of Huazhong University of Science and Technology [Medical Sciences]*, vol. 35, no. 6, pp. 874–879, 2015.

[16] J. Zhang, J. Xu, Y. Dong, and B. Huang, "Downregulation of HIF-1α inhibits the proliferation, migration and invasion of gastric cancer by inhibiting PI3K/AKT pathway and VEGF expression," *Bioscience Reports*, vol. 38, no. 6, 2018.

[17] J. Yang, S. Carra, W. G. Zhu, and H. H. Kampinga, "The regulation of the autophagic network and its implications for human disease," *International Journal of Biological Sciences*, vol. 9, no. 10, pp. 1121–1133, 2013.

[18] W. Lu, H. Ke, D. Qianshan, W. Zhen, X. Guoan, and Y. Honggang, "Apatinib has anti-tumor effects and induces autophagy in colon cancer cells," *Iranian Journal of Basic Medical Sciences*, vol. 20, no. 9, pp. 990–995, 2017.

[19] S. M. Huang, T. S. Chen, C. M. Chiu et al., "GDNF increases cell motility in human colon cancer through VEGF–VEGFR1 interaction," *Endocrine-Related Cancer*, vol. 21, no. 1, pp. 73–84, 2014.

[20] T. Aoyama and T. Yoshikawa, "Apatinib—new third-line option for refractory gastric or GEJ cancer," *Nature Reviews Clinical Oncology*, vol. 13, no. 5, pp. 268–270, 2016.

[21] G. Roviello, A. Ravelli, A. I. Fiaschi et al., "Apatinib for the treatment of gastric cancer," *Expert Review of Gastroenterology & Hepatology*, vol. 10, no. 8, pp. 887–892, 2016.

[22] C. M. Li, Z. C. Liu, Y. T. Bao, X. D. Sun, and L. L. Wang, "Extraordinary response of metastatic pancreatic cancer to apatinib after failed chemotherapy: a case report and literature review," *World Journal of Gastroenterology*, vol. 23, no. 41, pp. 7478–7488, 2017.

[23] L. Liang, L. Wang, P. Zhu et al., "Apatinib concurrent gemcitabine for controlling malignant ascites in advanced pancreatic cancer patient: a case report," *Medicine*, vol. 96, no. 47, article e8725, 2017.

[24] S. Tian, H. Quan, C. Xie et al., "YN968D1 is a novel and selective inhibitor of vascular endothelial growth factor receptor-2 tyrosine kinase with potent activity in vitro and in vivo," *Cancer Science*, vol. 102, no. 7, pp. 1374–1380, 2011.

[25] J. Li, X. Zhao, L. Chen et al., "Safety and pharmacokinetics of novel selective vascular endothelial growth factor receptor-2 inhibitor YN968D1 in patients with advanced malignancies," *BMC Cancer*, vol. 10, no. 1, p. 529, 2010.

[26] M. Chan, K. Sjoquist, and J. Zalcberg, "Clinical utility of ramucirumab in advanced gastric cancer," *Biologics: Targets and Therapy*, vol. 9, pp. 93–105, 2015.

[27] L. Fornaro, E. Vasile, and A. Falcone, "Apatinib in advanced gastric cancer: a doubtful step forward," *Journal of Clinical Oncology*, vol. 34, no. 31, pp. 3822-3823, 2016.

[28] L. Li, J. Tan, Y. Miao, P. Lei, and Q. Zhang, "ROS and autophagy: interactions and molecular regulatory mechanisms," *Cellular and Molecular Neurobiology*, vol. 35, no. 5, pp. 615–621, 2015.

[29] J. Ahlberg and H. Glaumann, "Uptake—microautophagy—and degradation of exogenous proteins by isolated rat liver lysosomes: effects of pH, ATP, and inhibitors of proteolysis," *Experimental and Molecular Pathology*, vol. 42, no. 1, pp. 78–88, 1985.

[30] B. Levine and G. Kroemer, "Autophagy in the pathogenesis of disease," *Cell*, vol. 132, no. 1, pp. 27–42, 2008.

[31] N. Mizushima, B. Levine, A. M. Cuervo, and D. J. Klionsky, "Autophagy fights disease through cellular self-digestion," *Nature*, vol. 451, no. 7182, pp. 1069–1075, 2008.

[32] S. Wullschleger, R. Loewith, and M. N. Hall, "TOR signaling in growth and metabolism," *Cell*, vol. 124, no. 3, pp. 471–484, 2006.

[33] J. Kim, M. Kundu, B. Viollet, and K. L. Guan, "AMPK and mTOR regulate autophagy through direct phosphorylation of Ulk1," *Nature Cell Biology*, vol. 13, no. 2, pp. 132–141, 2011.

[34] J. Liu, L. Fan, H. Wang, and G. Sun, "Autophagy, a double-edged sword in anti-angiogenesis therapy," *Medical Oncology*, vol. 33, no. 1, p. 10, 2016.

Research Article

Purple Sweet Potato Color Attenuates Kidney Damage by Blocking VEGFR2/ROS/NLRP3 Signaling in High-Fat Diet-Treated Mice

Gui-Hong Zheng [iD],[1,2] **Qun Shan** [iD],[1,2] **Jing-Jing Mu**,[1,2] **Yong-Jian Wang**,[1,2] **Zi-Feng Zhang**,[1,2] **Shao-Hua Fan**,[1,2] **Bin Hu**,[1,2] **Meng-Qiu Li**,[1,2] **Jun Xie**,[1,2] **Ping Chen**,[3] **Dong-Mei Wu** [iD],[1,2] **Jun Lu** [iD],[1,2] **and Yuan-Lin Zheng** [iD][1,2]

[1]*Key Laboratory for Biotechnology on Medicinal Plants of Jiangsu Province, School of Life Science, Jiangsu Normal University, Xuzhou, 221116 Jiangsu Province, China*
[2]*College of Health Sciences, Jiangsu Normal University, Xuzhou, 221116 Jiangsu Province, China*
[3]*Key Laboratory of Biology and Genetic Improvement of Sweet Potato, Ministry of Agriculture, Jiangsu Xuzhou Sweet Potato Research Center, Xuzhou, 221131 Jiangsu Province, China*

Correspondence should be addressed to Dong-Mei Wu; wdm8610@jsnu.edu.cn, Jun Lu; lu-jun75@163.com, and Yuan-Lin Zheng; ylzheng@jsnu.edu.cn

Received 30 June 2018; Revised 26 September 2018; Accepted 10 October 2018; Published 22 January 2019

Guest Editor: Ziqing Hei

Our preliminary data showed that VEGFR2 upregulation promoted renal ROS overproduction in high-fat diet- (HFD-) treated mice. Given that ROS-induced NLRP3 activation plays a central role in the pathogenesis of type 2 diabetic kidney injury, we evaluate whether VEGFR2 upregulation induces type 2 diabetic kidney injury via ROS-mediated NLRP3 activation and further explore the underlying mechanism. Our results showed that VEGFR2 knockdown decreased ROS overproduction, blocked NLRP3-dependent inflammation, and alleviated kidney damage in HFD-treated mice. Treatment with α-lipoic acid, a scavenger of ROS, lowered ROS overproduction and alleviated NLRP3-triggered kidney injury of HFD-treated mice. Collectively, the VEGFR2/ROS/NLRP3 signal is a critical therapeutic strategy for the kidney injury of HFD-treated mice. Purple sweet potato color (PSPC), a natural anthocyanin, can exert renal protection by inhibiting ROS in HFD-treated mice. Here, we provide a novel mechanism of PSPC against renal damage in HFD-treated mice by downregulating VEGFR2 expression.

1. Introduction

In recent years, type 2 diabetes mellitus (T2DM) has become more prevalent worldwide mainly due to excess calorie intake and low physical activity [1, 2]. Diabetic nephropathy (DN) is one of the major complications of T2DM and its pathological mechanism is still not clear [3]. Several lines of evidence have showed that oxidative stress and inflammation are the main pathological mechanisms of DN [4–7]. Further evidence shows that ROS-induced NLRP3 activation plays a key role in the pathological damage of DN [8]. Vascular endothelial growth factor receptor (VEGFR), a tyrosine kinase receptor, has been reported to trigger ROS generation and inflammation in many kinds of pathological angiogenesis in cancer, atherosclerosis, and diabetic retinopathy [9, 10].

Our preliminary data also found that upregulation of VEGFR2 promoted excessive ROS production in the kidney of high-fat diet- (HFD-) treated mice, but the underlying mechanism of the pathophysiologic process has not been fully elucidated. As a specific and high-affinity receptor for proinflammatory VEGF, VEGFR2 is originally recognized for many biological properties in vascular permeability, extracellular matrix degeneration, vascular endothelial cell migration, proliferation, and blood vessel formation [11, 12]. Based on our previous finding that ROS-induced NLRP3 activation accelerated the kidney damage in HFD-treated mice, we hypothesize that VEGFR2 may be involved in the renal pathological injury via ROS-activated NLRP3 inflammatory signaling in HFD-treated mice. Next, we confirm this hypothesis and

explore the underlying mechanism of VEGFR2 mediating the renal injury in the HFD-treated mice.

PSPC, a natural compound of flavonoids obtained from *Ipomoea batatas*, possesses multiple biological functions for preventing various diseases, such as cancers, atherosclerosis, and nonalcoholic fatty liver disease [8, 13–16]. Our previous data demonstrated that PSPC could prevent the pathological damage of the brain, liver, and kidney via antioxidative stress, anti-inflammation, and antiapoptosis in various animal models [8, 13, 16]. Recently, Shan et al. have found that PSPC relieves kidney damage by inhibiting NLRP3-induced inflammation [8]. In addition, various flavonoids have been shown to inhibit VEGFR2 expression and its downstream signaling in the pathological angiogenesis of tumors and diabetic retinopathy [17, 18]. Given our preliminary evidence showing that VEGFR2 stimulated ROS overproduction, the current study aims at investigating whether PSPC alleviates kidney injury by downregulating VEGFR2-mediated oxidation stress and inflammation and further explaining the pathological mechanism underlying kidney damage in HFD-treated mice.

2. Materials and Methods

2.1. Animal Administration. All experimental protocols and euthanasia procedures were approved by the Institutional Animal Care and Use Committee of Jiangsu Normal University (permit number: 16-0050, 6 March 2016). Eighty 8-week-old male ICR mice were purchased from Beijing Vital River Laboratory Animal Technology Co. Ltd. (Beijing, China). Mice were acclimated to laboratory conditions for 1 week before experimentation. Animals were housed at $23 \pm 1°C$ and $55 \pm 5\%$ humidity, with free access to food and water. After acclimatization for 1 week, the mice were divided into two groups of 40 animals each: the chow diet (CD, control) group and the HFD group. Both received separate treatments for 20 weeks. Mice in the control group ate the chow diet (10% of energy as fat; D12450; Research Diets Inc., New Brunswick, NJ, USA), while mice in the HFD group ate the HFD diet (60% of energy as fat; D12492; Research Diets Inc., New Brunswick, NJ, USA) [19].

2.2. Adeno-Associated Virus (AAV) Infection and VEGFR2 Short Hairpin RNA (shRNA) Knockdown. Adeno-associated viral (AAV2/9) vectors encoding short hairpin RNAs (shRNAs) were purchased from HannBio Technology Co. (Shanghai, China). AAV2/9 infection was performed as previously described [20]. In brief, vectors expressed shRNAs containing VEGFR2 (5′-GCGATGAACTCACCATCATGG-3′), negative control (5′-GGAAGTCGTGAGAAGTAGAAT-3′) target sequences under the control of the human U6 promoter. In addition, the vectors also expressed enhanced GFP (EGFP) as a reporter to allow for visualization of transduced kidney cells. Kidney-specific VEGFR2 knockdown experiments were performed 16 weeks after HFD administration. For a knockdown experiment, each mouse was injected $10 \mu L$ of each vector (1×10^{12}) in phosphate-buffered saline (PBS) into the right kidney via microinjection as described (using a $2 \mu L$ Hamilton syringe, 0.25 mL/min, injecting at 5 points on the sagittal plane

1.5 mm deep into the kidney). A schematic representation of the AAV2/9 used in this study is shown in Figure 1(a). The mice were sacrificed for subsequent experiments three weeks after injection.

2.3. α-Lipoic Acid Administration. Mice were fed with CD or HFD for 16 weeks (20 mice per group), then orally administrated 150 mg/kg α-lipoic acid daily for 4 weeks (α-lipoic acid was dissolved in the corn oil) as described in previous literature [21]. Additional HFD-treated and CD-treated mice (10 mice per group) received the same dose of the solvent, corn oil (Sigma-Aldrich, St. Louis, Missouri, USA). After 4 weeks of α-lipoic acid treatment, blood and kidneys were obtained from the sacrificed mice for further experiments [21].

2.4. PSPC Administration. PSPC was purchased from Qingdao Pengyuan Natural Pigment Research Institute (Qingdao, China). Its major components are six acetylated anthocyanins, all of which are flavonoids (purity > 90%). The detailed components of PSPC have been previously described [16]. Based on the pilot experiment (see Supplementary Figure 2), forty 8-week-old male ICR mice were randomly divided into four groups of 10 animals each: chow diet (CD, control) group, HFD group, HFD + PSPC group, and CD + PSPC group. They received the following treatments for 20 weeks: Mice in the HFD + PSPC and CD + PSPC groups were orally administered 700 mg/kg/d of PSPC in distilled water containing 0.1% Tween 80 daily for 20 weeks according to our previous and pilot results. An equal volume of distilled water containing 0.1% Tween 80 was administered to mice in the CD groups. The dosage of PSPC used in this study was according to data in our previous reports and preliminary experiments (see Supplementary Figure 2) [8]. At the end of the experiment, blood and kidneys were obtained from the sacrificed mice for further experiments.

The experimental procedures are shown in Supplementary Figure 3.

2.5. Quantitative Real Time Polymerase Chain Reaction (qPCR). Total mRNA was extracted with TRIzol (Invitrogen, Carlsbad, CA, USA), according to the manufacturer's instructions. Single-stranded cDNAs were amplified using the following primers: VEGFR2 (sense 5′-TACACAATTCA GAGCGATGTGTGGT-3′, antisense 5′-CTGGTTCCTCC AATGGGATATCTTC-3′) and glyceraldehyde 3-phosphate dehydrogenase (GAPDH) (sense 5′-GTCTTCCTGGGCAA GCAGTA-3′, antisense 5′-CTGGACAGAAACCCCACTT C-3′) (Sangon Biotech, Shanghai, China). VEGFR2 mRNA levels were analyzed by qPCR using BeyoFast™ SYBR Green qPCR Mix (2x, High ROX, Beyotime, Nantong, China) in a StepOnePlus instrument (Applied Biosystems, Carlsbad, CA, USA). Amplification was performed using an initial denaturation step at 95°C for 3 min, 40 cycles of 95°C for 15 s and 60°C for 30 s, and a final incubation at 72°C for 30 s. The relative levels of VEGFR2 mRNA were normalized to GAPDH mRNA and were analyzed by the comparative cycle threshold (Ct) method.

(a)

(b)

(c)

(d)

(e)

(f)

(g)

FIGURE 1: Continued.

(h)

(i)
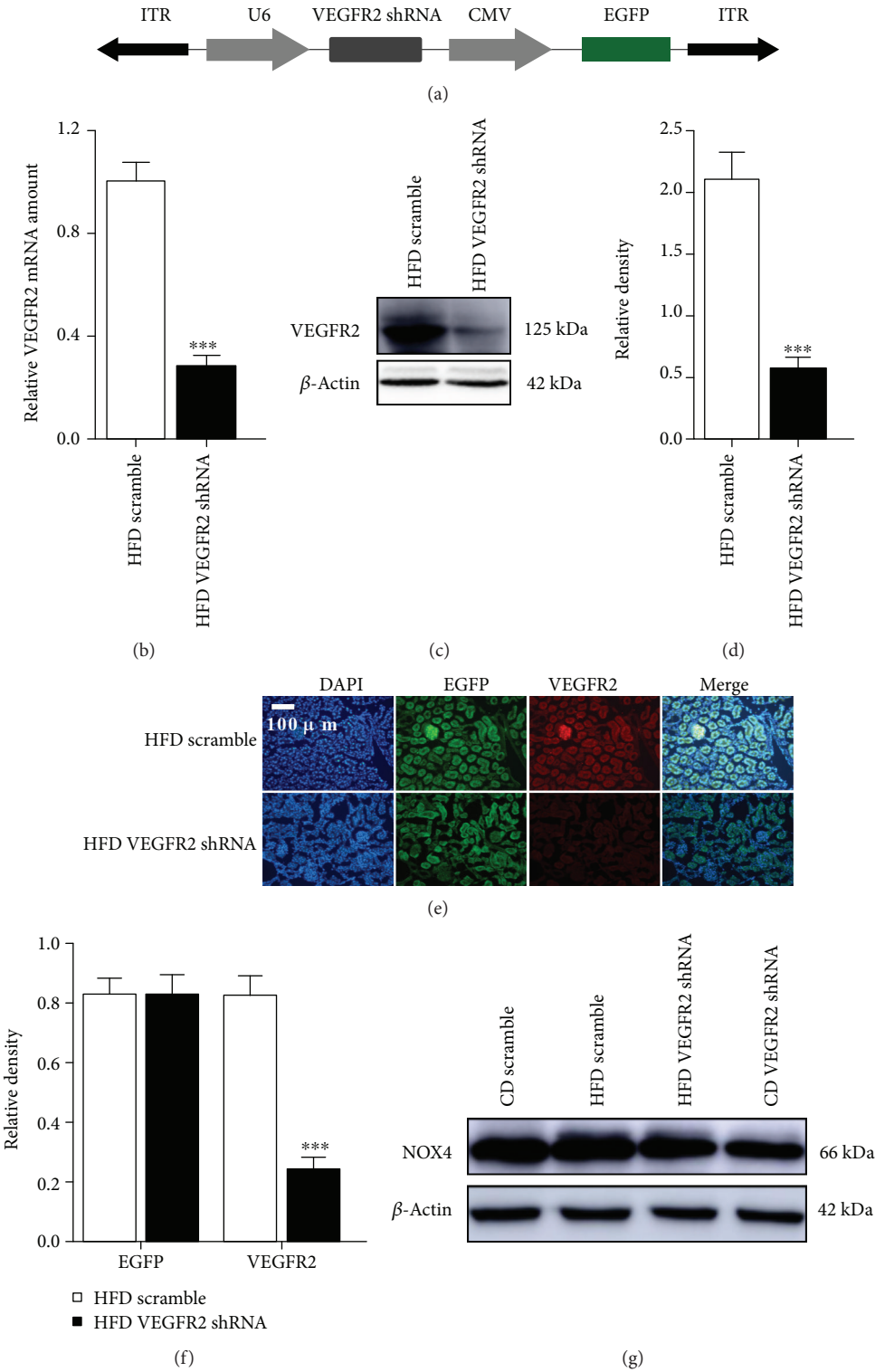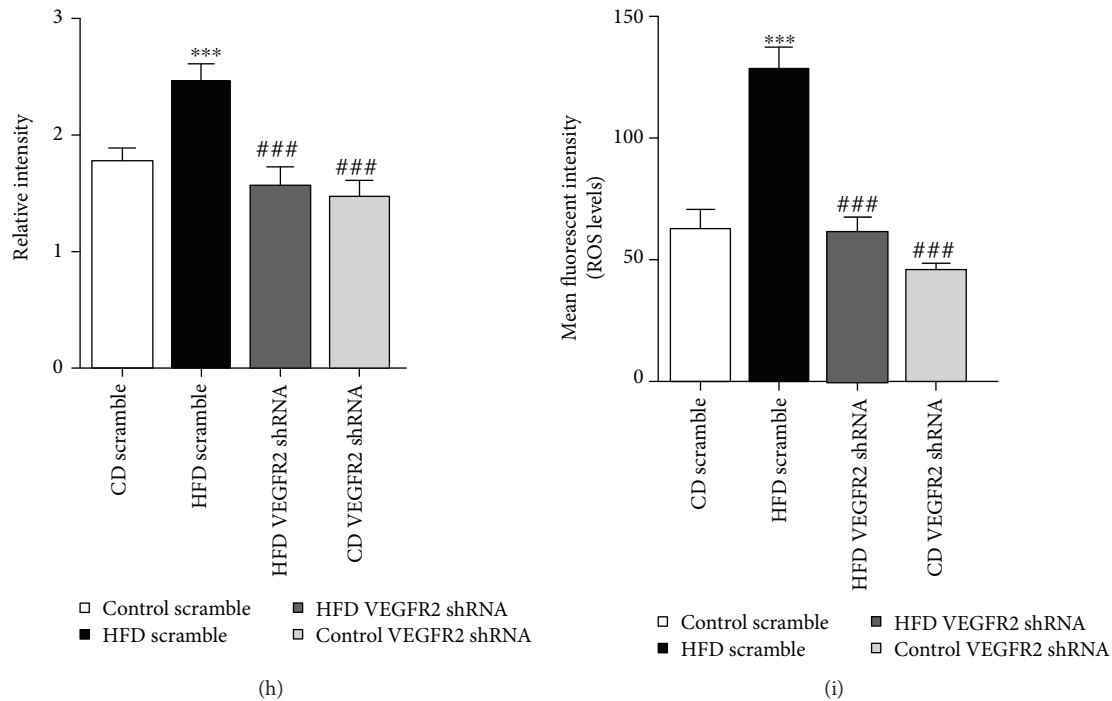
Figure 1: Kidney-specific VEGFR2 knockdown inhibits renal oxidative stress of the HFD-treated mice. (a) Schematic representation of the AAV used in this study. (b) VEGFR2 mRNA were determined by real time qPCR. Values are expressed as the ratio of VEGFR2 to GAPDH. $^{***}p < 0.001$ *vs.* the HFD scramble group. (c) Representative immunoblots for VEGFR2 and β-actin. (d) Relative density analysis of VEGFR2 protein bands. Relative densities are expressed as the ratio of VEGFR2 to β-actin. $^{***}p < 0.001$ *vs.* the HFD scramble group. (e) Kidney sections were stained with EGFP and CY3 (green) and VEGFR2 (red) to visualize AAV2/9-infective cells, respectively (200x, scale bar, 100 μm). (f) Analysis of the relative intensity of EGFP-positive and VEGFR2-positive cells in the kidney sections, $^{***}p < 0.001$ *vs.* the HFD scramble group. (g) Representative immunoblots for NOX4 and β-actin. (h) Relative density analysis of NOX4 protein bands. Relative densities are expressed as the ratio of NOX4 to β-actin. $^{***}p < 0.001$ *vs.* the CD scramble group, and $^{###}p < 0.001$ *vs.* the HFD scramble group. (i) ROS levels were assessed by $2',7'$-dichlorofluorescein diacetate (DCF-DA). All values are expressed as mean $\pm$ SEM ((b–i), $n = 5$). $^{***}p < 0.001$ *vs.* the CD scramble group, and $^{###}p < 0.001$ *vs.* the HFD scramble group.

2.6. Tissue Homogenates.

At the end of experiment, mice were deeply anesthetized and sacrificed. Kidney was promptly dissected and homogenized in 1:5 (w/v) 50 mM (pH 7.4) ice-cold Tris-buffered saline (TBS) containing a protease inhibitor cocktail (Sigma-Aldrich, MO, USA) with 10 strokes at 1200 rpm in a Teflon-glass Potter-Elvehjem homogenizer (Kontes Glass Inc., Vineland, NJ, USA). Homogenates were centrifuged at 12,000 ×g for 10 min, and the supernatant was used for the ROS assay and western blot analysis.

2.7. Assay of ROS.

ROS was determined as described previously, based on the oxidation of $2',7'$-dichlorodihydrofluorescein diacetate (DCFH-DA) to $2',7'$-dichlorofluorescein (DCF) (Jiancheng Institute of Biotechnology, Nanjing, China) [15, 16]. Briefly, each renal supernatant was diluted into a 1% tissue homogenate in 1 × PBS and the supernatant was obtained by centrifugation at 12,000 ×g and 4°C. Samples or hydrogen peroxide standard (50 μL) were mixed with 100 μL of 10 μM DCFH-DA in 96-well plates and incubated for 20 min at 37°C in the dark. Fluorescence was measured at 480 nm excitation/530 nm emission on a Synergy H4 Hybrid Multi-Mode Microplate Reader (Biotek, Winooski, Vermont, USA). ROS formation was quantified from a DCF-standard curve. Data are expressed as pmol of DCF formed/min/mg protein.

2.8. Biochemical Analysis.

At the end of experiment, the blood was obtained by caudal venipuncture. Each sample was divided into 2 parts: one for measuring serum creatinine and another for determining blood urea nitrogen concentrations using a commercial creatinine and urea nitrogen determination kit (Jiancheng Institute of Biotechnology, Nanjing, China) according to the manufacturer's protocols.

2.9. Isolation of Cytoplasmic and Nuclear Proteins.

The isolation of cytoplasmic and nuclear proteins was performed using commercial nuclear protein-cytoplasmic protein extraction kits (Thermo Scientific, Waltham, MA, USA), according to the manufacturer's protocols. Briefly, weighed fresh kidneys were added to hypotonic buffer (3 mL/g), homogenized with a ball mill instrument (Retsch GmbH, Haan, Germany), incubated on ice for 15 min, and centrifuged for 10 min at 850 ×g at 4°C. The supernatants and pellets contained the cytoplasmic and nuclear fractions, respectively. The nuclear pellets were resuspended in 50 μL Complete Lysis Buffer and vortexed, then incubated for 30 min at 4°C on a rocking platform at 150 rpm. After vortexing, the supernatant was obtained by centrifugation for 10 min at 14,000 ×g.

2.10. Western Blot Analysis.

Western blot was conducted as in previously published articles [8, 22]. Total proteins (30 μg)

were separated by sodium dodecyl sulfate-polyacrylamide gel electrophoresis and transferred to polyvinylidene difluoride membranes (Bio-Rad, Hercules, CA, USA). Nonspecific antigen binding sites were blocked with 5% skim milk in Tris-buffered saline containing 0.1% Tween 20 (TBST) for 1 h at $22 \pm 2°C$. Primary antibodies used included rabbit anti-VEGFR2 (ab39256, 1 : 5000, Abcam, Cambridge, USA), rabbit anti-NADPH oxidase 4 (NOX4, BM4135, 1 : 400, Boster Biological Technology Ltd., Wuhan, China), rabbit anti-NLRP3 (BM4490, 1 : 400, Boster Biological Technology Ltd., Wuhan, China), rabbit anti-tumor necrosis factor (TNF) α (PB0270, 1 : 1000, Boster Biological Technology Ltd., Wuhan, China), rabbit anti-interleukin- (IL-) 6 (BA4339, 1 : 1000, Boster Biological Technology Ltd., Wuhan, China), rabbit anti-inducible nitric oxide synthase (iNOS, BA0362, 1 : 400, Boster Biological Technology Ltd., Wuhan, China), rabbit anti-pro-IL1β (BM0962, 1 : 400, Boster Biological Technology Ltd., Wuhan, China), rabbit anti-cleaved IL1β (16806-1-AP, 1 : 4000, Proteintech, Wuhan, China), mouse anti-nuclear factor- (NF-) κB p65 (Bsm-33059M, 1 : 2000, Bioss, Beijing, China), anti-rabbit procaspase 1 (22915-1-AP, 1 : 1000, Proteintech, Wuhan, China), and anti-rabbit cleaved caspase 1 (22915-1-AP, 1 : 1000, Proteintech, Wuhan, China). Membranes were incubated with primary antibodies overnight at 4°C, rinsed with TBST three times for 10 min, and then incubated with horseradish peroxidase-conjugated anti-rabbit or anti-mouse secondary antibodies (SA00001-1/2, 1 : 5000, Proteintech, Wuhan, China) for 1 h. After washing, proteins were visualized on an Amersham Imager 600 (GE Healthcare UK Limited, UK) using LumiGLO® Reagent and Peroxide (Cell Signaling Technology, Beverly, MA, USA). The optic density (OD) values of detected bands were measured with the Scion Image analysis software (Scion, Frederick, MD, USA) and were normalized to mouse anti-β-actin (66009-1, 1 : 5000, Proteintech, Wuhan, China) or mouse anti-histone H3 (Bsm-33042M, 1 : 5000, Bioss, Beijing, China) as internal controls (OD detected protein/OD internal control). The specificity of each of the primary antibodies was evaluated by preincubation in the presence or absence of the corresponding blocking peptides or by omission of the primary antibodies.

2.11. Collection of Kidney Slices. At the end of experiment, mice were euthanized and perfused with sterile PBS to remove their blood. Kidneys were immediately fixed in 4% phosphate-buffered paraformaldehyde, dehydrated in 30% sucrose (Amresco, Ohio, USA), and then sectioned with a freezing microtome (Leica CM3050S, Biosystems, Nussloch, Germany) and stored at −80°C (DW-86L578J, Haier BioMedical, Qingdao, China) for dihydroethidium (DHE) staining, hematoxylin and eosin (HE) staining, and immunofluorescence.

2.12. Immunofluorescence Staining. Immunofluorescence staining of renal sections were conducted as previously described [8]. First, antigens were retrieved by boiling in citric acid buffer (pH 6.0) for 15 min. Nonspecific antigens were blocked with 5% bovine serum albumin for 1 h at room temperature. Samples were incubated with rabbit anti-VEGFR2 antibody (ab2349, 1 : 500, Abcam, Cambridge, UK) at 4°C overnight, and then goat anti-rabbit DyLight 488 Antibody

(1031-02, 1 : 20,000, Vector Laboratories, Burlingame, CA, USA) or anti-rabbit CY3 antibody (CY-1300-1, 1 : 2000, Vector Laboratories, Burlingame, CA, USA) was added for 1 h. Subsequently, DAPI was applied for 8 min. Stained sections were imaged at 200x on a fluorescence microscope (Leica DM4000B, Leica Microsystems, Wetzlar, Germany), and quantitative analysis was performed using Image-Pro Plus 6.0 (IPP; Media Cybernetics, Rockville, MD, USA) [21].

2.13. HE Staining. Mice were euthanized and perfused with sterile PBS to remove their blood. Kidney were immediately fixed in 4% phosphate-buffered paraformaldehyde, dehydrated in 30% sucrose (Amresco, Ohio, USA), and then sectioned with a freezing microtome (Leica CM3050S, Biosystems, Nussloch, Germany) and stored at −80°C (DW-86L578J, Haier Biomedical, Qingdao, China). To assess renal morphology, 10 μm sections were stained with HE (Sigma-Aldrich, St. Louis, MO, USA). Detailed staining procedures have been previously described [8]. Pathological changes in kidney tissues were observed under a light microscope, and renal damage was evaluated in a double-blind fashion by two kidney pathologists [23].

2.14. DHE Staining. DHE staining was used to detect the ROS production in the kidney sections. Simply, 10 μm-thick frozen renal sections were removed from −80°C storage and dried at 37°C for 30 min in an electric thermostatic incubator (Incucell, Germany), and then incubated in $1 \times PBS$ for 15 min. Next, sections were incubated with 10 mol/L fluorescent-labeled DHE (Molecular Probes, Invitrogen, Carlsbad, CA, USA) in a lucifugal-humidified chamber at 37°C for 30 min, then stained with $4', 6'$-diamidino-2-phenylindole (DAPI, Abcam, Cambridge, CA, USA). Images were obtained at 200x on a fluorescence microscope (Leica DM4000B, Leica Microsystems, Wetzlar, Germany). The average DHE fluorescence intensity was measured using IPP. Results were expressed as the ratio of the DHE-positive area and the DAPI.

2.15. Statistical Analysis. All statistical analyses were performed using SPSS version 11.5 (SPSS Inc., Chicago, IL, USA). Data were analyzed by one-way analysis of variance followed by Tukey's honest significant difference test. Data are expressed as the mean ± standard error of mean (SEM). Statistical significance was set at $p < 0.05$.

3. Results

3.1. Kidney-Specific VEGFR2 Knockdown Inhibits Renal Oxidative Stress of HFD-Treated Mice. The immunofluorescence density of EGFP expressed by AAV2/9 reached a peak after a three-week transfection in the kidney of HFD-treated mice (Supplementary Figure 1(a)–1(c)). So, an experiment of kidney-specific VEGFR2 knockdown was conducted after a three-week injection (Figures 1(b)–1(f)). Then, we evaluated the knockdown effect of VEGFR2 by qPCR, western blot, and immunofluorescence (Figures 1(b)–1(f)). In comparison with the HFD scramble group, VEGFR2 mRNA in the HFD VEGFR2 shRNA group was remarkably reduced to less than 70% (Figure 1(b)). Similar results were obtained from

western blot and immunofluorescence analysis of VEGFR2 protein (*vs*. the HFD scramble group, Figures 1(c)–1(f)). However, no significantly different EGFP expression was observed between scramble and VEGFR2 shRNA in the kidney of HFD-treated mice (Figures 1(e) and 1(f)). These results indicated that the VEGFR2 gene was successfully knocked down in the kidney of mice (*vs*. the HFD scramble group, Figures 1(b)–1(f)). Further, NOX4 protein expression and ROS production were markedly suppressed by VEGFR2 knockdown in the kidney of HFD-treated mice (*vs*. the HFD scramble group, Figures 1(g)–1(i)). However, no remarkable differences of NOX4 protein expression and ROS levels were observed between CD VEGFR2 shRNA and scramble in CD-treated mice (Figures 1(g)–1(i)). These results demonstrated that ROS overproduction was induced by VEGFR2 upregulation in the kidney of HFD-treated mice.

3.2. Kidney-Specific VEGFR2 Knockdown Alleviates NRLP3-Dependent Inflammation in the Kidney of the HFD-Treated Mice. Next, to verify whether VEGFR2 upregulation induced NRLP3-dependent inflammatory response, and ultimately resulting in kidney injury in the HFD-treated mice, we investigated the NRLP3 activation, NF-κB p65 nuclear translocation, and its inflammatory cascade protein expression. Western blot analysis showed that kidney-specific VEGFR2 knockdown notably inhibited NRLP3 activation and remarkably decreased the ratio of cleaved to procaspase and cleaved to pro-IL1β induced by HFD adminstration in the mice (*vs*. the HFD scramble group, Figures 2(a) and 2(b)). Additionally, further data showed that kidney-specific VEGFR2 knockdown markedly reduced the nuclear NF-κB p65, TNFα, IL6, and iNOS expression (*vs*. the HFD scramble group, Figures 2(c)–2(f)). However, no significant difference was observed in NRLP3 activation, NF-κB p65 nuclear translocation, TNFα, IL6, and iNOS expression, and the ratio of cleaved to procaspase 1 and cleaved to pro-IL1β between the HFD VEGFR2 shRNA and CD scramble group. These results indicated that kidney-specific VEGFR2 knockdown alleviated NRLP3-dependent inflammation in the kidney of the HFD-treated mice.

3.3. Kidney-Specific VEGFR2 Knockdown Alleviates Kidney Injury of HFD-Treated Mice. Then, to explore whether VEGFR2 upregulation accelerated kidney injury in the HFD-treated mice, we assessed kidney function by HE staining and determination of serum creatinine and blood urea nitrogen concentrations (Figures 3(a)–3(f)). HE staining showed that VEGFR2 knockdown obviously improved loosened kidney structure, glomerulus hypertrophy, swelled tubules, severe inflammatory cell accumulation, and thickened basement-membranes induced by HFD (*vs*. the HFD scramble group, Figures 3(a)–3(e)). Moreover, the enhancements of the glomerulus and Bowman's capsule diameter, tubule diameter, glomerulus and Bowman's capsule area, tubulointerstitial lesion score, and serum creatinine and blood urea nitrogen levels induced by HFD were remarkably depressed by VEGFR2 knockdown (*vs*. the HFD scramble group, Figures 3(a)–3(f)). In addition, no obvious

changes were displayed in the aforementioned parameters between the CD VEGFR2 shRNA and CD scramble group (Figures 3(a)–3(f)). These results suggested that kidney VEGFR2 upregulation significantly deteriorated the kidney injury in the HFD-treated mice.

3.4. α-Lipoic Acid Decreases ROS-Triggered NRLP3-Dependent Inflammation in the Kidney of HFD-Treated Mice. To explore whether ROS triggered NRLP3-dependent inflammation stimulated by VEGFR2 upregulation in the kidney of HFD-treated mice, we determined the effect of α-lipoic acid on ROS production, NRLP3 activation, and nuclear NF-κB and its downstream inflammatory protein expression. DHE staining showed that α-lipoic acid significantly inhibited ROS production in the kidney of HFD-treated mice (*vs*. HFD + α-lipoic acid, Figures 4(a) and 4(b)). Further western blot analysis showed that α-lipoic acid markedly depressed the NRLP3 activation and reduced the ratio of cleaved to procaspase 1 and cleaved to pro-IL1β in the kidney of HFD-treated mice (*vs*. HFD + α-lipoic acid, Figures 4(c) and 4(d)). In addition, α-lipoic acid significantly blocked NF-κB p65 nuclear translocation and its downstream TNFα, IL6, and iNOS expression in the kidney of HFD-treated mice (*vs*. HFD + α-lipoic acid, Figures 4(e)–4(h)). However, no significant variations of ROS levels and the abovementioned protein expression were observed between the CD + α-lipoic acid and CD + vehicle group. Thus, ROS was confirmed to be a mediator of VEGFR2-stimulated NRLP3 activation and its dependent inflammation in the kidney of HFD-treated mice.

3.5. α-Lipoic Acid Alleviates NRLP3-Dependent Kidney Injury in HFD-Treated Mice. Additionally, we explored whether α-lipoic acid alleviates NRLP3-dependent kidney injury in the HFD-treated mice. We determined the kidney function by HE staining and serum creatinine and blood urea nitrogen determination (Figures 5(a)–5(f)). HE staining showed that α-lipoic acid significantly improved loosened kidney structure, glomerular hypertrophy, swelled tubules, abundant inflammatory cell accumulation, thicker basement-membranes, and tubulointerstitial lesion score of HFD-treated mice (*vs*. the HFD + vehicle group, Figures 5(a)–5(e)). Moreover, further analysis showed that α-lipoic acid significantly lowered the glomerulus and Bowman's capsule diameter, tubule diameter, the glomerulus and Bowman's capsule area, tubulointerstitial lesion score, and serum creatinine and blood urea nitrogen levels of HFD-treated mice (*vs*. the HFD + vehicle group, Figures 5(a)–5(f)). However, no noticeable changes were disclosed in the abovementioned indicators between the CD + α-lipoic acid and CD + vehicle group (Figures 5(a)–5(f)). These results suggested that α-lipoic acid alleviates NRLP3-dependent kidney injury in HFD-treated mice.

3.6. PSPC Administration Inhibits ROS-Triggered NRLP3 Inflammation in HFD-Treated Mice. Furthermore, to estimate whether PSPC administration alleviates ROS-triggered NRLP3 inflammation by inhibiting VEGFR2 upregulation in HFD-treated mice, we determined the VEGFR2, NOX4, NRLP3 expression, and ROS levels.

(a)

(b)

(c)

(d)

(e)

(f)
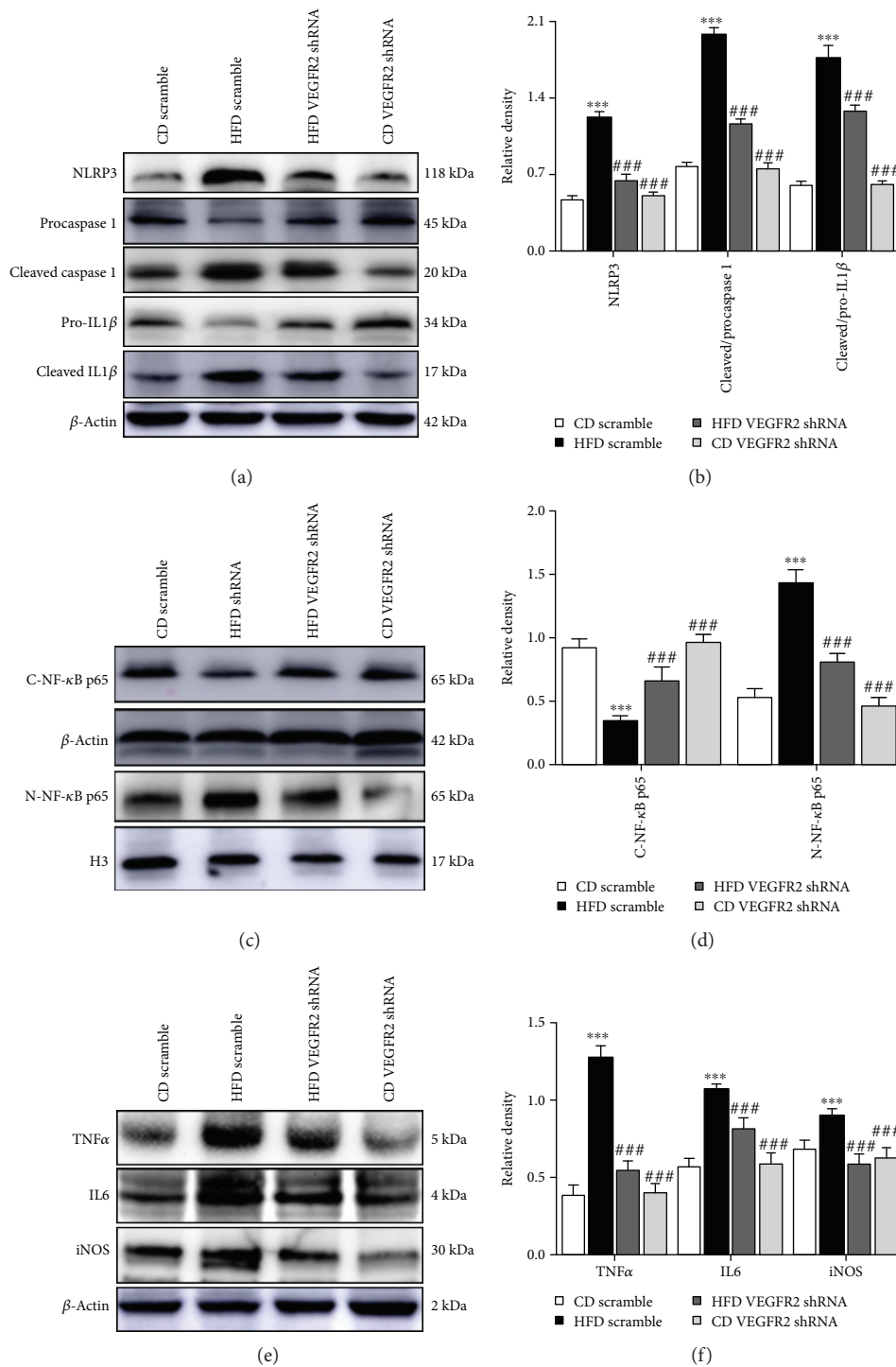
FIGURE 2: Kidney-specific VEGFR2 knockdown alleviates NRLP3-dependent inflammation in the kidney of the HFD-treated mice. (a) Representative immunoblots for NLRP3, procaspase 1, cleaved caspase 1, pro-IL1β, cleaved IL1β, and β-actin. (b) Relative density analysis of the NLRP3, cleaved caspase 1, and cleaved IL1β protein bands. Relative densities are expressed as the ratio of NRLP3 to β-actin, cleaved caspase 1 to procaspase 1 (expressed as cleaved/procaspase 1), and cleaved IL1β to pro-IL1β (expressed as cleaved/pro-IL1β). (c) Representative immunoblots for cytoplasmic NF-κB p65 (C-NF-κB p65), nuclear NF-κB p65 (N-NF-κB p65), β-actin, and histone H3 (H3). (d) Relative density analysis of the C-NF-κB p65 and N-NF-κB p65 protein bands. Relative densities are expressed as the ratio of C-NF-κB p65 to β-actin and N-NF-κB p65 to H3. (e) Representative immunoblots for TNFα, IL6, iNOS, and β-actin. (f) Relative density analysis of the TNFα, IL6, and iNOS protein bands. Relative densities are expressed as the ratio of TNFα, IL6, and iNOS to β-actin. All values are expressed as mean $\pm$ SEM ((a–f), $n = 5$). $^{**}p < 0.01$ and $^{***}p < 0.001$ $vs.$ the CD scramble group, and $^{##}p < 0.01$ and $^{###}p < 0.001$ $vs.$ the HFD scramble group.
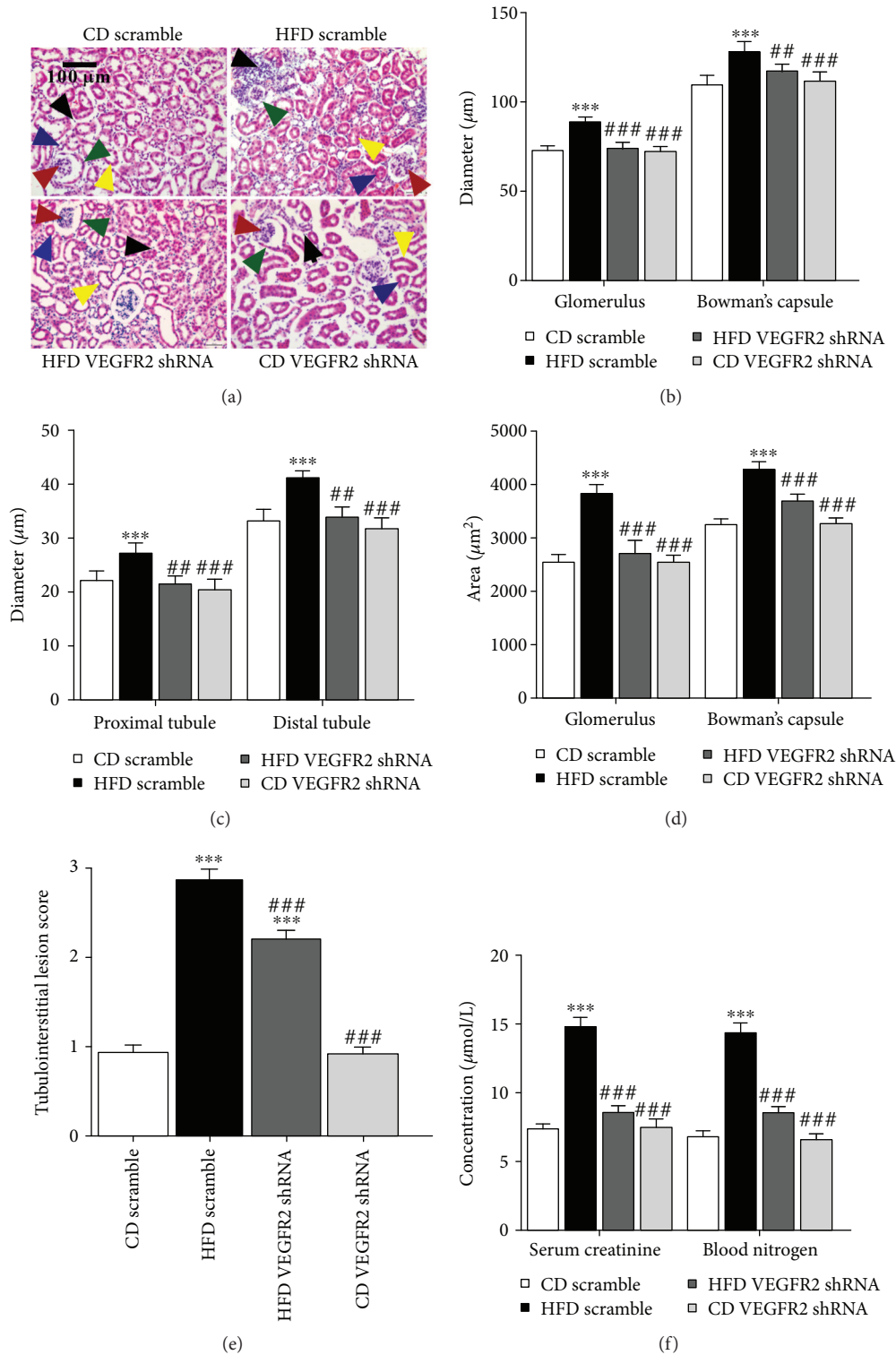
FIGURE 3: Kidney-specific VEGFR2 knockdown alleviates the kidney injury of HFD-treated mice. (a) Kidney sections were stained by hematoxylin-eosin; the black arrow represents the accumulation of inflammatory cells (200x, scale bar, 100 μm). (b) Glomerulus and Bowman's capsule diameter; the red arrow represents blood glomerulus, and the green arrow represents Bowman's capsule. (c) Tubule diameter; the blue arrow represents proximal tubules, and the yellow arrow represents the distal tubules. (d) Glomerulus and Bowman's capsule area. (e) Tubulointerstitial lesion score. (F) Serum creatinine and blood urea nitrogen determination. All values are expressed as mean $\pm$ SEM ((a–e), $n = 5$). ***$p < 0.001$ *vs.* the CD scramble group, and ##$p < 0.01$ and ###$p < 0.001$ *vs.* the HFD scramble group.

Immunofluorescence analysis showed that PSPC significantly reduced the VEGFR2-positive staining area in the kidney of HFD-treated mice (vs. CD group, Figures 6(a) and 6(b)). Further results showed that PSPC administration markedly inhibited NOX4 expression and ROS production in the kidney of HFD-treated mice (vs. the CD group, Figures 6(c)–6(e)). Moreover, western blot analysis showed that PSPC notably reduced NLRP3 expression and the ratio of cleaved to procaspase 1 and cleaved to pro-IL1β in the HFD-treated mice (vs. the CD group, Figures 6(f) and 6(g)). However, no marked difference of these indicators was observed between the CD + PSPC group and CD group. These results indicated that PSPC administration inhibits ROS-triggered NRLP3 activation by inhibiting VEGFR2 upregulation in HFD-treated mice.

Finally, to explore whether PSPC administration relieved NRLP3-dependent kidney injury in HFD-treated mice, we estimated the kidney function by HE staining and determination of serum creatinine and blood urea nitrogen concentrations. HE staining showed that PSPC administration significantly improved loosened kidney structure, glomerulus hypertrophy, swelled tubules, severe inflammatory cells, and the thickened basement-membranes induced by HFD (vs. the CD group, Figures 6(h)–6(l)). Moreover, the increment of glomerulus diameter, Bowman's capsule diameter, tubule diameter, glomerulus and Bowman' capsule area, and serum creatinine and blood urea nitrogen induced by HFD were markedly inhibited by PSPC administration in the HFD + PSPC group (vs. the CD group, Figures 6(h)–6(l)). However, no significant difference in these biomarkers was found between the CD + PSPC and CD group. These results indicated that PSPC administration remarkably alleviated kidney injury by inhibiting VEGFR2 expression in the HFD-treated mice.

4. Discussion

Oxidative stress and inflammation induced by HFD have been reported to cause renal damage in the T2DM [24, 25], but the potential regulatory mechanism is still obscure. The present findings show that VEGFR2 upregulation in the kidney of HFD-treated mice promotes ROS overproduction, consequently induces NLRP3-dependent inflammatory responses, and ultimately leads to kidney damage.

Initially, experimental observation found that VEGFR2 upregulation increased the NOX4 expression and ROS levels in the kidney of HFD-treated mice, which agree with previous evidence that VEGF induced ROS overproduction in the pathological angiogenesis [9]. NOX4 is a member of the NADPH oxidase family, and a main source for generating ROS in multiple physiological and pathological processes, such as cellular signaling, cell proliferation, neurodegeneration, and diabetes mellitus [26, 27]. Many studies have shown that NOX4 is activated by various growth factors and cytokines, and it aggravates renal injury in the DN, which is similar to the findings in our present study [27–31]. Additionally, NOX4 is an important mediator for VEGF-mediated feedback reduction of ROS overproduction in pathological angiogenesis and inflammations [9, 10, 32].

Given that ROS is a major trigger for NRLP3-dependent signaling, further results showed that NF-κB p65 nuclear translocation and the expression of NRLP3, IL1β, TNFα, IL6, and iNOS protein were markedly enhanced by VEGFR2 upregulation in the kidney of the HFD-treated mice compared with the CD-treated mice. The NRLP3 inflammasome is known as NLRP3 or cryopyrin, and it belongs to the leucine-rich-containing family, pyrin domain-containing-3 [33]. It could sense a metabolic dangerous stressor and initiates the recruitment of mature caspase 1, which activates IL1β release. As previous studies reported that excessive ROS is an effective activator for NRLP3 activation in many inflammatory diseases, such as in cancers and autoimmune diseases [32–35], this study obtained highly consistent results. In addition, NRLP3 has been reported as an initiator for inflammation in obesity-related disorders such as diabetic neurodegenerative disease, diabetic nonalcoholic fatty liver, and DN [33], and chronic inflammation is the key link for the etiopathogenesis of obesity and T2DM [34]. Based on the aforementioned literature, further studies demonstrated that VEGFR2 upregulation aggravated kidney injury by increasing the glomerulus, Bowman's capsule, and tubule diameter, as well as serum creatinine and blood urea nitrogen levels. Thus, a comprehensive assessment of serum creatinine levels, blood urea nitrogen levels, and pathological changes could provide a reliable reference for evaluating kidney injury in chronic and acute kidney diseases [35]. These results indicated that VEGFR2 induces kidney injury at least partly via ROS-mediated NLRP3 activation.

Additionally, to further verify whether VEGFR2 upregulation stimulated NLRP3 activation via excessive ROS in the kidney of HFD-treated mice, the effect of α-lipoic acid, a stronger ROS scavenger, on the kidney was determined after 4 weeks of administration at a dose of 150 mg/kg per day in the HFD-treated mice. Results showed that α-lipoic acid attenuated the kidney injury by reducing ROS levels, NLRP3 activation, NF-κB p65 nuclear translocation, and expression of its downstream inflammatory cytokines, such as IL1β, TNFα, IL6, and iNOS. Similar to these findings, previous studies also indicated that α-lipoic acid strongly reversed oxidative stress by directly or indirectly reacting to ROS in various disease models related to oxidative stress such as neurodegeneration, diabetes mellitus, and ischemic injury [19], and that the ROS scavenger effectively blocked NRLP3 activation, NF-κB nuclear translocation, and downstream inflammatory cytokine expression [36, 37]. As an important inflammatory transduction factor, NF-κB activation promotes proinflammatory gene translocation in numerous renal diseases such as systemic lupus erythematosus, ischemic nephropathy, aged nephropathy, and DN [38, 39], which is consistent with our present results. Moreover, the ROS scavenger has been shown to significantly decrease serum creatinine and blood urea nitrogen levels and to markedly relieve the glomerular hypertrophy and aggregation of inflammatory cells [40]. Therefore, scavenging of ROS by α-lipoic acid reduced the kidney injury by not only blocking NLRP3 activation, but also inhibiting NF-κB nuclear translocation and downstream inflammatory cytokine expression in the kidney of HFD-treated mice.

(a)

(b)

(c)

(d)

(e)

(f)

(g)

(h)
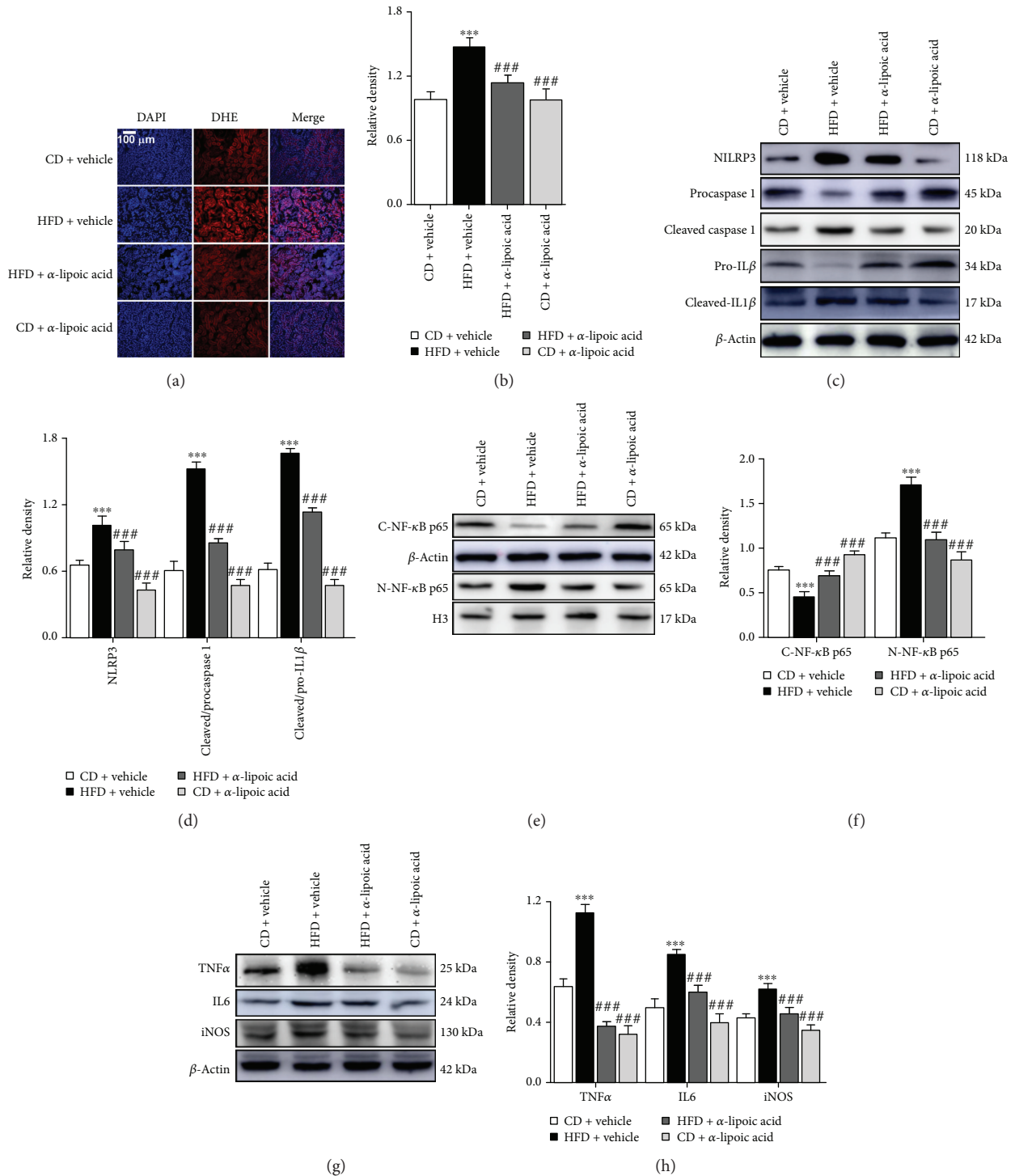
FIGURE 4: α-Lipoic acid decreases ROS-triggered inflammation in the kidney of HFD-treated mice. (a) ROS levels were assessed by dihydroethidium (DHE) staining. (b) DHE fluorescence intensity was measured by the IPP, and results are expressed by the ratio of the integrated optical density of the DHE-positive area to the DAPI. (c) Representative immunoblots for NLRP3, procaspase 1, cleaved caspase 1, pro-IL1β, cleaved IL1β, and β-actin. (d) Relative density analysis of NLRP3, cleaved caspase 1, and cleaved IL1β protein bands. Relative densities are expressed as the ratio of NRLP3 to β-actin, cleaved caspase 1 to procaspase 1 (expressed as cleaved/procaspase 1), and cleaved IL1β to Pro-IL 1β (expressed as cleaved/pro-IL1β). (e) Representative immunoblots for cytoplasmic NF-κB p65 (C-NF-κB p65), nuclear NF-κB p65 (N-NF-κB p65), β-actin, and histone H3 (H3). (f) Relative density analysis of the C-NF-κB p65 and N-NF-κB p65 protein bands. Relative densities are expressed as the ratio of C-NF-κB p65 to β-actin and N-NF-κB p65 to H3. (g) Representative immunoblots for TNFα, IL6, iNOS, and β-actin. (h) Relative density analysis of TNFα, IL6, and iNOS protein bands. Relative densities are expressed as the ratio of TNFα, IL6, and iNOS to β-actin. All values are expressed as mean ± SEM ((a–h), $n = 5$). ***$p < 0.001$ vs. the CD vehicle group, and ###$p < 0.001$ vs. the HFD vehicle group.

(a)

(b)

(c)

(d)

(e)

(f)
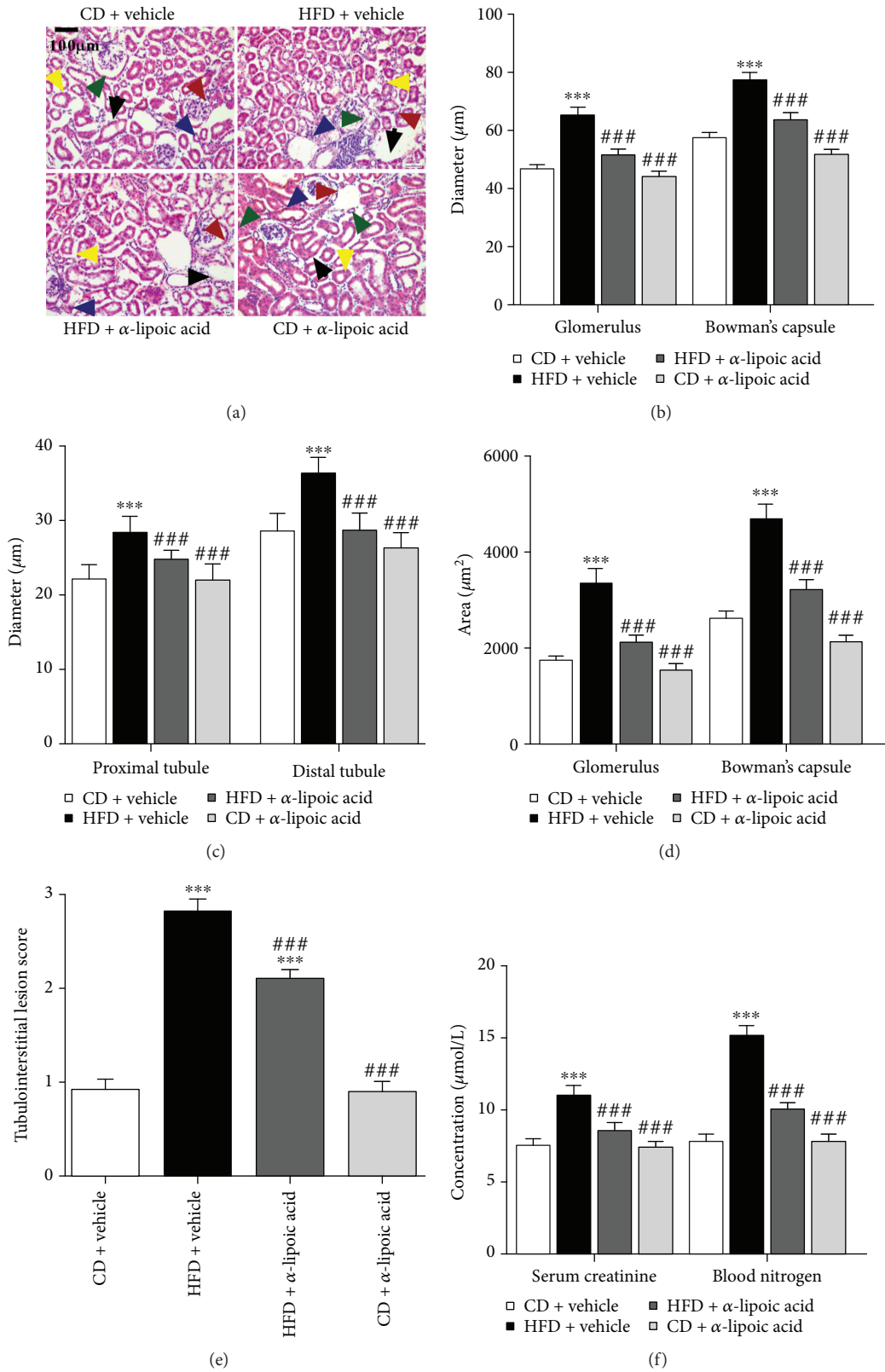
FIGURE 5: α-Lipoic acid alleviates NRLP3-dependent kidney injury in HFD-treated mice. (a) Kidney sections were stained by hematoxylin-eosin; the black arrow represents the accumulation of inflammatory cells (200x, scale bar, 100 μm). (b) Glomerulus and Bowman's capsule diameter; the red arrow represents blood glomerulus, and the green arrow represents Bowman's capsule. (c) Tubule diameter; the blue arrow represents proximal tubules, and the yellow arrow represents the distal tubules. (d) Glomerulus and Bowman's capsule area. (e) Tubulointerstitial lesion score. (f) Serum creatinine and blood urea nitrogen determination. All values are expressed as mean ± SEM ((a–e), $n = 5$). ***$p < 0.001$ $vs.$ the CD vehicle group, and ###$p < 0.001$ $vs.$ the HFD vehicle group.

(a)

(b)

(c)

(d)

(e)

(f)

(g)

(h)

(i)

FIGURE 6: Continued.

(j)

(k)

(l)

(m)

Figure 6: PSPC administration inhibits ROS-triggered NRLP3 inflammation in HFD-treated mice. (a) Kidney sections were stained with FITC to visualize VEGFR2-positive cell staining (green) (200x, scale bar, 100 μm). (b) Analysis of the relative intensity of VEGFR2-positive cells in the kidney sections. (c) Representative immunoblot for NOX4 and β-actin. (d) Relative density analysis of the NOX4 protein bands. Relative densities are expressed as the ratio of NOX4 to β-actin. (e) The ROS levels were assessed by 2′,7′-dichlorofluorescein diacetate (DCF-DA) in the kidney of HFD-treated mice. (f) Representative immunoblots for NLRP3, procaspase 1, cleaved caspase 1, pro-IL1β, cleaved IL1β, and β-actin. (g) The relative density analysis of the NLRP3, cleaved caspase 1, and cleaved IL1β protein bands. The relative densities are expressed as the ratio of NRLP3 to β-actin, cleaved caspase 1 to procaspase 1 (expressed as cleaved/procaspase 1), and cleaved IL1β to pro-IL1β (expressed as cleaved/pro-IL1β). All values are expressed as mean ± SEM ((a–g), $n = 5$). ***$p < 0.001$ vs. the CD group, and ###$p < 0.001$ vs. the HFD group. (h) Kidney sections were stained by hematoxylin-eosin; the black arrow represents the accumulation of inflammatory cells in the kidney (200x, scale bar, 100 μm). (i) Glomerulus and Bowman's capsule diameter were determined by Image-Pro Plus (IPP); the red arrow represents blood glomerulus, and the green arrow represents Bowman's capsule. (j) Tubule diameter was measured by IPP; the blue arrow represents proximal tubules, and the yellow arrow represents the distal tubules. (k) Glomerulus and Bowman's capsule area were determined by IPP. (l) Serum creatinine and blood urea nitrogen determination. (m) Schematic diagram of PSPC on VEGFR2/ROS/NRLP3 signaling in the kidney of HFD-treated mice. All values are expressed as mean ± SEM ((a–e), $n = 5$). ***$p < 0.001$ vs. the CD group, and ###$p < 0.001$ vs. the HFD group.

PSPC, a natural anthocyanin extracted from purple sweet potato, has been demonstrated to possess many biofunctions, such as antioxidative stress, antiapoptosis, and anti-inflammation, against cognitive disorders, nonalcoholic fatty liver disease, atherosclerosis, and DN [8, 13–16]. Based on our previous study of the protective effect of PSPC on kidney injury by reducing excessive ROS-mediated NLRP3 activation in HFD-treated mice [8], the present study was aimed at investigating the protective action of PSPC on kidney injury by targeting VEGFR2 via ROS-mediated NLRP3 activation inflammatory signaling. Our main observation disclosed that PSPC alleviated the kidney injury by downregulating the VEGFR2 expression. We also observed the inhibition of

ROS-mediated NLRP3 activation, as well as the decrease of NF-κB p65 nuclear translocation and its downstream inflammatory cascades.

Although our results clearly demonstrated potential molecular mechanisms underlying the HFD-induced and PSPC-alleviated kidney injury in HFD-treated mice, there are some limitations. Studies in food chemistry showed that PSPC is a multicomponent mixture of anthocyanins [41]. We were not able to determine which anthocyanins protected against kidney injury induced by HFD and in what ways and with what molecular mechanisms. Indeed, the pharmacological functions of detailed anthocyanins of PSPC depressing kidney injury induced by HFD and the

underlying molecular mechanisms are still obscure. Therefore, the separation of every anthocyanin in PSPC and the elucidation of the pharmacological mechanisms underlying the protective effects of every anthocyanin of PSPC on kidney injury induced by high-fat diet will be regarded as the focus of further research. Moreover, the relationships between VEGFR2/ROS/NRLP3 upregulation and injuries of renal intrinsic cells, such as endothelial cells, mesangial cells, podocytes, and renal tubular epithelial cells, remain unclear. Therefore, further experiments will explore these molecular mechanisms.

In summary, our study provides compelling evidence that the kidney VEGFR2 knockdown alleviated kidney injury by inhibiting inflammation in HFD-treated mice. Furthermore, PSPC relieved renal damage at least partly via the VEGFR2/ROS/NRLP3 signaling axis, which suggested that VEGFR2 may be a potential target for PSPC preventing or treating kidney injury induced by high-fat diet (Figure 6(m)).

Abbreviations

HFD:	High-fat diet
CD:	Chow diet
PSPC:	Purple sweet potato color
VEGF:	Vascular endothelial growth factor
ROS:	Reactive oxygen species
NLRP3:	NLR family pyrin domain-containing 3
PSPC:	Purple sweet potato color
DN:	Diabetic nephropathy
GAPDH:	Glyceraldehyde-3-phosphate dehydrogenase
shRNA:	Short hairpin RNA
qPCR:	Quantitative real time polymerase chain reaction
DCFH-DA:	Dichlorodihydrofluorescein diacetate
OD:	Optic density
DHE:	Dihydroethidium
EGFP:	Enhanced green fluorescent protein
NOX4:	Nicotinamide adenine dinucleotide phosphate (NADPH) oxidase 4
TNFα:	Tumor necrosis factor alpha
IL6:	Interleukin 6
iNOS:	Inducible nitric oxide synthase
pro-IL1β:	Prointerleukin 1β
cleaved-IL1β:	Cleaved interleukin 1β
NF-κB p65:	Nuclear translocation factor 65 subunit
IPP:	Image-Pro Plus
IOD:	Integrated optical density
AAV:	Adeno-associated virus.

Data Availability

All data used to support the findings of this study are included within the article and the supplementary information file. All authors firmly support and endorse the FAIR Guiding Principles for scientific data management and stewardship. All data used to support the findings of this study are available in the open database.

Conflicts of Interest

The authors have declared that no competing interests exist.

Supplementary Materials

Figure S1: (a) the transfection efficiency of AAV2/9 in the kidney of HFD-treated mice and (b) EGFP expression determined by immunofluorescence staining after AAV2/9 transfection in mouse kidney (Supplementary Figure S1(a): 10x, scale bar, 2 mm; Supplementary Figure S1(b): 200x, scale bar, 100 μm). (c) Relative intensity analysis of EGFP-positive cells in the kidney sections. All values are expressed as the mean $\pm$ SEM ($n = 5$). ***$p < 0.001$ vs. values at 1 week, ###$p < 0.001$ vs. values at 2 weeks. Figure S2: purple sweet potato color (PSPC) dosage selection. (a) HE staining (200x, scale bar, 100 μm). (b) Glomerulus and Bowman's capsule diameter were determined. (c) Tubule diameter was measured. (d) Glomerulus and Bowman's capsule area were determined. (e) Serum creatinine and blood urea nitrogen determination. (f) Representative immunoblots for VEGFR2 and β-actin. (g) Relative densities of VEGFR2 are expressed as the ratio to β-actin. All values are expressed as the mean $\pm$ SEM (A–G, $n = 5$). ***$p < 0.001$ vs. the CD group, and ###$p < 0.001$ vs. the HFD group. Figure S3: the flow chart of animal processing. Mice were 8 weeks old when obtained from the supplier. (a) Kidney-specific VEGFR2 knockdown inhibits renal oxidative stress of HFD-treated mice. (b) α-Lipoic acid decreases ROS-triggered NRLP3-dependent inflammation in the kidney of HFD-treated mice. (c) PSPC administration inhibits ROS-triggered NRLP3 inflammation in HFD-treated mice. (Supplementary Materials)

References

[1] D. R. Whiting, L. Guariguata, C. Weil, and J. Shaw, "IDF diabetes atlas: global estimates of the prevalence of diabetes for 2011 and 2030," *Diabetes Research and Clinical Practice*, vol. 94, no. 3, pp. 311–321, 2011.

[2] F. B. Hu, "Globalization of diabetes: the role of diet, lifestyle, and genes," *Diabetes Care*, vol. 34, no. 6, pp. 1249–1257, 2011.

[3] J. M. Forbes and M. E. Cooper, "Mechanisms of diabetic complications," *Physiological Reviews*, vol. 93, no. 1, pp. 137–188, 2013.

[4] A. A. Elmarakby and J. C. Sullivan, "Relationship between oxidative stress and inflammatory cytokines in diabetic nephropathy," *Cardiovascular Therapeutics*, vol. 30, no. 1, pp. 49–59, 2012.

[5] H. L. Hutton, J. D. Ooi, S. R. Holdsworth, and A. R. Kitching, "The NLRP3 inflammasome in kidney disease and autoimmunity," *Nephrology*, vol. 21, no. 9, pp. 736–744, 2016.

[6] A. Abderrazak, T. Syrovets, D. Couchie et al., "NLRP3 inflammasome: from a danger signal sensor to a regulatory node of oxidative stress and inflammatory diseases," *Redox Biology*, vol. 4, pp. 296–307, 2015.

[7] P. Gao, X. F. Meng, H. Su et al., "Thioredoxin-interacting protein mediates NALP3 inflammasome activation in podocytes during diabetic nephropathy," *Biochimica et Biophysica Acta-Molecular Cell Research*, vol. 1843, no. 11, pp. 2448–2460, 2014.

[8] Q. Shan, Y. Zheng, J. Lu et al., "Purple sweet potato color ameliorates kidney damage via inhibiting oxidative stress mediated NLRP3 inflammasome activation in high fat diet mice," *Food and Chemical Toxicology*, vol. 69, pp. 339–346, 2014.

[9] Y. M. Kim, S. J. Kim, R. Tatsunami, H. Yamamura, T. Fukai, and M. Ushio-Fukai, "ROS-induced ROS release orchestrated by Nox4, Nox2, and mitochondria in VEGF signaling and angiogenesis," *American Journal of Physiology-Cell Physiology*, vol. 312, no. 6, pp. C749–C764, 2017.

[10] T. Maraldi, C. Prata, C. Caliceti et al., "VEGF-induced ROS generation from NAD(P)H oxidases protects human leukemic cells from apoptosis," *International Journal of Oncology*, vol. 36, no. 6, pp. 1581–1589, 2010.

[11] M. Ushio-Fukai and Y. Nakamura, "Reactive oxygen species and angiogenesis: NADPH oxidase as target for cancer therapy," *Cancer Letters*, vol. 266, no. 1, pp. 37–52, 2008.

[12] M. Simons, E. Gordon, and L. Claesson-Welsh, "Mechanisms and regulation of endothelial VEGF receptor signalling," *Nature Reviews Molecular Cell Biology*, vol. 17, no. 10, pp. 611–625, 2016.

[13] Z.-F. Zhang, S.-H. Fan, Y.-L. Zheng et al., "Purple sweet potato color attenuates oxidative stress and inflammatory response induced by D-galactose in mouse liver," *Food and Chemical Toxicology*, vol. 47, no. 2, pp. 496–501, 2009.

[14] C. Sun, S. Fan, X. Wang et al., "Purple sweet potato color inhibits endothelial premature senescence by blocking the NLRP3 inflammasome," *Journal of Nutritional Biochemistry*, vol. 26, no. 10, pp. 1029–1040, 2015.

[15] J. Lu, D. M. Wu, Y. L. Zheng, B. Hu, W. Cheng, and Z. F. Zhang, "Purple sweet potato color attenuates domoic acid-induced cognitive deficits by promoting estrogen receptor-α-mediated mitochondrial biogenesis signaling in mice," *Free Radical Biology & Medicine*, vol. 52, no. 3, pp. 646–659, 2012.

[16] J. Lu, D.-m. Wu, Y.-l. Zheng, B. Hu, and Z.-f. Zhang, "Purple sweet potato color alleviates D-galactose-induced brain aging in old mice by promoting survival of neurons via PI3K pathway and inhibiting cytochrome *c*-mediated apoptosis," *Brain Pathology*, vol. 20, no. 3, pp. 598–612, 2010.

[17] R. N. Gacche, H. D. Shegokar, D. S. Gond, and R. J. Meshram, "Abstract 1006. Structural peculiarities of flavonoids influence anti-angiogenic, cytotoxic and antioxidant effects: experimental and insilico analysis," *Cancer Research*, vol. 74, Supplement 19, p. 1006, 2014.

[18] D. Ravishankar, K. A. Watson, S. Y. Boateng, R. J. Green, F. Greco, and H. M. I. Osborn, "Exploring quercetin and luteolin derivatives as antiangiogenic agents," *European Journal of Medicinal Chemistry*, vol. 97, pp. 259–274, 2015.

[19] E. J. Henriksen, "Exercise training and the antioxidant α-lipoic acid in the treatment of insulin resistance and type 2 diabetes," *Free Radical Biology & Medicine*, vol. 40, no. 1, pp. 3–12, 2006.

[20] G.-H. Zheng, Y.-J. Wang, X. Wen et al., "Silencing of SOCS-1 and SOCS-3 suppresses renal interstitial fibrosis by alleviating renal tubular damage in a rat model of hydronephrosis," *Journal of Cellular Biochemistry*, vol. 119, no. 2, pp. 2200–2211, 2018.

[21] S. B. Hong, W. H. Uhm, W. C. Joo, M. S. Nam, S. W. Lee, and J. H. Song, "Plasma markers of oxidative stress, inflammation and endothelial cell injury in diabetic patients with overt nephropathy administered alpha-lipoic acid and angiotensin II receptor blocker," *Molecular & Cellular Toxicology*, vol. 6, no. 2, pp. 179–185, 2010.

[22] J. Lu, D. M. Wu, Y. L. Zheng et al., "Quercetin activates AMP-activated protein kinase by reducing PP2C expression protecting old mouse brain against high cholesterol-induced neurotoxicity," *Journal of Pathology*, vol. 222, no. 2, pp. 199–212, 2010.

[23] T. W. C. Tervaert, A. L. Mooyaart, K. Amann et al., "Pathologic classification of diabetic nephropathy," *Journal of the American Society of Nephrology*, vol. 21, no. 4, pp. 556–563, 2010.

[24] F. Giacco and M. Brownlee, "Oxidative stress and diabetic complications," *Circulation Research*, vol. 107, no. 9, pp. 1058–1070, 2010.

[25] J. F. Navarro-Gonzalez and C. Mora-Fernandez, "The role of inflammatory cytokines in diabetic nephropathy," *Journal of the American Society of Nephrology*, vol. 19, no. 3, pp. 433–442, 2008.

[26] J. Rivera, C. G. Sobey, A. K. Walduck, and G. R. Drummond, "Nox isoforms in vascular pathophysiology: insights from transgenic and knockout mouse models," *Redox Report*, vol. 15, no. 2, pp. 50–63, 2010.

[27] K. Bedard and K. H. Krause, "The NOX family of ROS-generating NADPH oxidases: physiology and pathophysiology," *Physiological Reviews*, vol. 87, no. 1, pp. 245–313, 2007.

[28] J. C. Jha, S. P. Gray, D. Barit et al., "Genetic targeting or pharmacologic inhibition of NADPH oxidase Nox4 provides renoprotection in long-term diabetic nephropathy," *Journal of the American Society of Nephrology*, vol. 25, no. 6, pp. 1237–1254, 2014.

[29] C. E. Holterman, N. C. Read, and C. R. J. Kennedy, "Nox and renal disease," *Clinical Science*, vol. 128, no. 8, pp. 465–481, 2015.

[30] Y. Gorin and K. Block, "Nox4 and diabetic nephropathy: with a friend like this, who needs enemies?," *Free Radical Biology & Medicine*, vol. 61, pp. 130–142, 2013.

[31] M. Sedeek, R. Nasrallah, R. M. Touyz, and R. L. Hebert, "NADPH oxidases, reactive oxygen species, and the kidney: friend and foe," *Journal of the American Society of Nephrology*, vol. 24, no. 10, pp. 1512–1518, 2013.

[32] J. Oshikawa, S. J. Kim, E. Furuta et al., "Novel role of p66Shc in ROS-dependent VEGF signaling and angiogenesis in endothelial cells," *American Journal of Physiology-Heart and Circulatory Physiology*, vol. 302, no. 3, pp. H724–H732, 2012.

[33] B. Vandanmagsar, Y. H. Youm, A. Ravussin et al., "The NLRP3 inflammasome instigates obesity-induced inflammation and insulin resistance," *Nature Medicine*, vol. 17, no. 2, pp. 179–188, 2011.

[34] M. F. Gregor and G. S. Hotamisligil, "Inflammatory mechanisms in obesity," in *Annual Review of Immunology*, W. E. Paul, D. R. Littman, and W. M. Yokoyama, Eds., vol. 29, no. 1, pp. 415–445, 2011.

[35] R. G. Fassett, S. K. Venuthurupalli, G. C. Gobe, J. S. Coombes, M. A. Cooper, and W. E. Hoy, "Biomarkers in chronic kidney disease: a review," *Kidney International*, vol. 80, no. 8, pp. 806–821, 2011.

[36] Z. Gong, J. Zhou, H. Li et al., "Curcumin suppresses NLRP3 inflammasome activation and protects against LPS-induced septic shock," *Molecular Nutrition & Food Research*, vol. 59, no. 11, pp. 2132–2142, 2015.

[37] S. Qi, Y. Xin, Y. Guo et al., "Ampelopsin reduces endotoxic inflammation via repressing ROS-mediated activation of PI3K/Akt/NF-κB signaling pathways," *International Immunopharmacology*, vol. 12, no. 1, pp. 278–287, 2012.

[38] J. Castiblanco and J.-M. Anaya, "The IκBL gene polymorphism influences risk of acquiring systemic lupus erythematosus and Sjögren's syndrome," *Human Immunology*, vol. 69, no. 1, pp. 45–51, 2008.

[39] P. Burgos, C. Metz, P. Bull et al., "Increased expression of c-rel, from the NF-κB/Rel family, in T cells from patients with systemic lupus erythematosus," *Journal of Rheumatology*, vol. 27, no. 1, pp. 116–127, 2000.

[40] X. Yi, V. Nickeleit, L. R. James, and N. Maeda, "α-lipoic acid protects diabetic apolipoprotein E-deficient mice from nephropathy," *The Journal of Diabetic Complications*, vol. 25, no. 3, pp. 193–201, 2011.

[41] N. Terahara, T. Shimizu, Y. Kato et al., "Six diacylated anthocyanins from the storage roots of purple sweet potato, *Ipomoea batatas*," *Bioscience Biotechnology and Biochemistry*, vol. 63, no. 8, pp. 1420–1424, 2014.

Research Article

Hypoxia-Activated PI3K/Akt Inhibits Oxidative Stress via the Regulation of Reactive Oxygen Species in Human Dental Pulp Cells

Fei Liu ⓘ,[1,2,3] Xin Huang,[4] Zhenhua Luo,[5] Jingjun He,[3] Farhan Haider ⓘ,[6] Ci Song,[1] Ling Peng ⓘ,[1] Ting Chen ⓘ,[1] and Buling Wu ⓘ[1]

[1]*Department of Stomatology, Nanfang Hospital, Southern Medical University, Guangzhou 510515, China*
[2]*College of Stomatology, Southern Medical University, Guangzhou 510515, China*
[3]*International Medical Center, Guangdong Second Provincial General Hospital, Guangzhou 510317, China*
[4]*Department of Stomatology, Guangzhou Women and Children's Medical Center, Guangzhou Medical University, Guangzhou 510623, China*
[5]*Division of Gastroenterology, Hepatology and Nutrition, Cincinnati Children's Hospital Medical Center, Cincinnati, Ohio 45229, USA*
[6]*Department of Biochemistry, Zhongshan School of Medicine, Sun Yat-sen University, Guangzhou 510080, China*

Correspondence should be addressed to Ting Chen; 252199453@qq.com and Buling Wu; bulingwu@smu.edu.cn

In order to use stem cells as a resource for tissue regeneration, it is necessary to induce expansion *in vitro*. However, during culture, stem cells often lose functional properties and become senescent. Increasing evidence indicates that hypoxic preconditioning with physiological oxygen concentration can maintain the functional properties of stem cells *in vitro*. The purpose of the current study was to test the hypothesis that hypoxic preconditioning with physiological oxygen concentration can maintain the functional properties of stem cells in culture by reducing oxidative stress. *In vitro* studies were performed in primary human dental pulp cells (hDPCs). Reduced levels of oxidative stress and increased cellular "stemness" in response to physiological hypoxia were dependent upon the expression of reactive oxygen species (ROS). Subsequently, RNA-sequencing analysis revealed the increased expression of phosphoinositide 3-kinase (PI3K)/Akt signaling in culture, a pathway which regulates oxidative stress. Furthermore, we found evidence that PI3K/Akt signaling might affect intracellular ROS production by negatively regulating expression of the downstream protein Forkhead Box Protein O1 (FOXO1) and Caspase 3. Collectively, our data show that the PI3K/Akt pathway is activated in response to hypoxia and inhibits oxidative stress in a ROS-dependent manner. This study identified redox-mediated hypoxic preconditioning regulatory mechanisms that may be significant for tissue regeneration.

1. Introduction

Tissue regeneration requires the implantation of cellular adaptations to a wounded environment featuring a lesion. Because of their highly proliferative, multidifferentiation potential and low immunogenicity, hDPCs are considered to represent a promising source of stem cells for regenerative medicine and engineering tissue [1, 2]. However, stem cells

become aged during *in vitro* expansion, and the transplantation environment can often be extremely harsh for such cells, thus representing a significant challenge for regenerative medicine. An increasing number of studies pertaining to pretreatment strategies have attempted to improve the *ex vivo* expanded microenvironment and thus facilitate implantation, homing, and survivability [3–6]. Hypoxic preconditioning (HP) is a direct and effective strategy in which to promote

the *in vivo* survival and differentiation of transplanted stem cells; this is a vital factor for the success of stem cell-based tissue regeneration [7–9].

In recent years, hypoxia has also been found to play an important role in a number of physiological processes. Different levels of hypoxia are associated with various physiological behaviors and can regulate signal transduction in stem cell proliferation and differentiation during embryogenesis [10–12]. One of the advantages of living in a hypoxic niche is that stem cells can maintain a slowly circulating proliferation rate while avoiding tissue-related oxidative stress [13]. Essentially, all cells that undergo aerobic metabolism can produce ROS. This oxide can destroy DNA stability and induce oxidative stress in cells [13, 14]. The response of cells to ROS is highly dependent on other factors such as cell phenotype, cell differentiation status, or another stimulus state [15]. For example, hematopoietic stem cells (HSCs) have lower levels of ROS than differentiated hematopoietic cells [12]. There is a fine balance between ROS and hypoxia.

Physiological oxygen tension varies from 1% to 14% and is much lower when culturing *in vitro* [13]. Although there is no definitive experimental data for the measurement of physiological oxygen concentration in human dental pulp, a previous study using a rat animal model found that the oxygen concentration of incisor pulp tissue was approximately 3% [16]. The present literature relating to the effect of hypoxia on phenotypic changes in hDPCs shows that different oxygen-dependent concentrations are used for the treatment of hDPCs and that such changes are variable [17], especially in terms of cell differentiation and proliferation [18–20]. However, experiments have shown that the angiogenic ability of dental pulp cells after HP is significantly higher than that under normoxic conditions [21]. In addition, HP-treated cells exhibit increased levels of exosome secretion, which are effective in enhancing effector cell osteogenic and angiogenic capacity [22]. Contradictory reports of hypoxic preconditioning may be due to various conditions such as the degree of hypoxia, different cell lines, culture time, and donor's age.

To test the hypothesis that HP within the physiological range of oxygen concentration can maintain cell stemness by reducing oxidative stress in hDPCs, we investigated the effect of HP on the properties of oxidative stress and stemness. Our findings reveal that HP may effectively modulate oxidative stress in hDPCs via the PI3K/Akt pathway.

2. Material and Methods

2.1. Cell Identification and Culture. First, hDPCs were collected from the pulp tissues of extracted third molars (patient age: 15 to 25 years old). Cells from the first to the fifth passages were used in this study. All patients were informed, agreed to participate, and signed informed consent forms for scientific experiments involving tooth extraction. The study protocol was performed according to a standard protocol approved by the Ethics Committee of the Guangdong Provincial Second People's Hospital. Multidifferentiation of hDPCs was performed according to a procedure described previously [23]. Once cells had reached 80% confluency, hDPCs were allowed to differentiate in an osteogenic,

chondrogenic, and adipogenic induction medium. The induction medium was changed after every 2 days until the differentiated cells were harvested.

2.2. Cell Preconditioning. Hypoxic preconditioning was established using the Hypoxia Chamber 27310 (Stemcell, Vancouver, CA). All hypoxia experiments were performed at 3% oxygen concentration. The preconditioning of reoxygenation was first carried out under hypoxia for 2 d and then returned to normoxia for the remaining experimental duration. hDPCs were cultured in different oxygen concentrations and treated with 0.5 mM/L N-acetyl-L-cysteine (NAC), 100 μM/L hydrogen peroxide (H$_2$O$_2$), and 10 μM/L LY294002. NAC and LY294002 were provided by Selleck, Houston, USA. H$_2$O$_2$ was provided by Nanjing Jiancheng, China.

2.3. Cell Counting Kit 8 Assay. The viability of hDPCs was assessed by the cell counting kit 8 (CCK8, Dojindo, Kyushu island). Cells were seeded at a concentration of 2000 cells per well, and the culture procedure was performed according to the manufacturer's instructions. Optical density was measured by absorbance at 450 nm using an ELx800 microplate reader (BioTek Instruments Inc., Vermont, USA).

2.4. Cell Cycle Analysis. After culturing in different oxygen atmospheric environments, cells were harvested and fixed with 70% alcohol at 4°C overnight. The supernatant was completely removed and cells incubated in propidium iodide for 30 minutes at room temperature, in the dark. Cells were then analyzed by flow cytometry using a flow cytometer (Becton Dickinson, San Diego, CA).

2.5. Analysis of Cell Surface Markers. After pretreatment for 2 d, cells were washed and resuspended in staining medium (PBS containing 1% fetal bovine serum), then labelled with monoclonal antihuman STRO-1-FITC, CD34-PE, DO105-PE, CD133-PE, and OCT4-PE (Chemicon, Temecula, CA) for 30 minutes on ice. Cells were then washed twice and resuspended in stain buffer for analysis by flow cytometry.

2.6. Colony-Forming Assay. Cells were digested to a single-cell suspension, and 1000 cells were plated in a 6-well plate. After pretreatment for 10 days, hDPCs were fixed with 4% paraformaldehyde for 30 min at room temperature and then stained by crystal violet for 15 min. Cells were then observed under an optical microscope, and the number of colonies with more than 50 cells was counted.

2.7. Measurement of ROS Level. Levels of intracellular ROS were measured with a ROS assay kit (Nanjing Jiancheng, China) after treatment with different culture conditions. Cells were then stained with dihydrodichlorofluorescein diacetate (DCFDA) at a concentration of 10 μM for 45 min. Individual cells were measured by flow cytometry; 10,000 cells were analyzed for each sample.

2.8. Measurement of Apoptosis Ratio. An apoptosis assay was conducted using a KeyGEN apoptosis detection kit (KeyGEN Biotech Co., Nanjing, China) following the manufacturer's protocol. After pretreatment in each group, cells

were collected and resuspended in a 10x binding buffer. Cells were then incubated with annexin V-FITC/propidium iodide (PI). Finally, samples were analyzed by flow cytometry; 10,000 cells were analyzed for each sample.

2.9. *Measurement of Antioxidative Enzyme Activity.* Cells were cultured in normoxic and hypoxic conditions. Levels of superoxide dismutase (SOD), catalase (CAT), and glutathione peroxidase (GSH-PX) were all determined by commercial assay kits (Nanjing Jiancheng, China).

2.10. *Enzyme-Linked Immunosorbent Assay (ELISA).* Cells were cultured in normoxic and hypoxic conditions. Levels of IL-6 (interleukin-6) and IL-β1 (interleukin-β1) in culture supernatants were then assayed by enzyme-linked immunosorbent assay (ELISA; BioLegend) according to the manufacturer's instructions.

2.11. *Western Blotting Assay.* Cells were first collected using standard procedures. Total protein was then measured by the BCA Protein Assay Kit (Pierce Biotechnology, Rockford, IL), loaded for sodium dodecyl sulfate gel electrophoresis and transferred onto polyvinylidene fluoride membranes (Millipore, Billerica, MA). The membranes were then blocked with skimmed milk at room temperature for 1 hour and incubated at 4°C overnight with primary antibodies against HIF-1α (Santa Cruz, California, USA), PI3K (Abcam, Cambridge, UK), p-PI3K(Abcam, Cambridge, UK), Akt (Abcam, Cambridge, UK), p-Akt (Abcam, Cambridge, UK), Caspase 3 (Abcam, Cambridge, UK), and FOXO1 (Cell Signaling, Boston, USA). Total levels of GAPDH were used as a control. Densitometric analysis was performed using ImageJ Plus software (NIH, USA), and relative protein expression was calculated after normalization of the target total protein.

2.12. *Bioinformatic Analysis.* RNA-seq: hDPC gene expression profiling was performed using RNA deep sequencing by Annoroad Gene Technology Co. Ltd. (Beijing, China). Paired-end RNA-seq reads were mapped to the reference human genome (hg19) using HISAT2 (version 2.0.4). Read counts were calculated by HTSeq. Differential expression analysis was performed by DESeq2. For differential expression analysis, the fold-change cutoff was set at 2 or higher. Benjamini–Hochberg false discovery rate-adjusted p value less than 0.05 was considered statistically significant. Kyoto Encyclopedia of Genes and Genomes (KEGG) pathway analysis: 2-fold change, FDR-adjusted p value less than 0.05 genes was subjected to KEGG pathway analysis using ToppFun (https://toppgene.cchmc.org/enrichment.jsp) in the ToppGene toolbox (https://toppgene.cchmc.org/). Protein-protein interaction network analysis: protein-protein interactions among differentially expressed genes were retrieved from the STRING v10 database. The interaction network was generated by Cytoscape. Graph plotting: volcano plots and bar plots were generated by the ggrepel R package and GraphPad Prism 5, respectively. The heatmap was created by GENE-E software using expression profiles of 2-fold-changed genes in PI3K-Akt signaling pathways as input. The expression levels are displayed as z-score normalized counts per million (CPM) mapped fragment value. CPM values of each gene were z-score transformed normalized across all samples.

2.13. *Statistical Analysis.* All results are expressed as means ± standard deviation (SD). Statistical significance was determined using a t test or one-way analysis of variance (ANOVA). When $p < 0.05$, the difference was considered to be statistically significant.

3. Results

3.1. *Derivation of hDPCs from Mesenchymal Tissue with Multipotential Differentiation Potential.* To investigate the multidirectional differentiation potential of hDPCs, we first established hDPCs from pulp tissues of extracted third molars (patient age: 15 to 25 years). Cell surface marker identification experiments showed that hDPCs were derived from mesenchymal tissue and expressed mesenchymal specific surface markers (Figure 1(a)). Multidirectional differentiation experiments showed that hDPCs could differentiate into osteogenesis, cartilage, and adipocytes and express their corresponding specific markers (Figure 1(b)). Collectively, these data proved that hDPCs exhibit multidirectional differentiation potential.

3.2. *HP Improves the Stemness of hDPCs.* To investigate cellular responses to hypoxia in hDPCs, we investigated stemness and proliferation. The specific expression of hypoxia-inducible factor 1-alpha (Hif-1α) was enhanced when the hDPCs were under hypoxic conditions. The expression of HIF-1α reached maximal expression at 1 d, then slowly decreased (Figure 2(a)). The CCK-8 assay results revealed that HP treatment decreased cell viability for a certain period of time. Compared with the control group, the viability of the hypoxic group was slightly decreased. The late change of the reoxygenation group was similar to that of normoxia (Figure 2(b)). However, cell cycle experiments showed that HP can reduce the proportion of hDPCs in the G0/G1 phase and increase the proportion of cells in the S phase (Figure 2(c)) The ability for cell self-renewal was significantly improved after long-term hypoxia treatment (Figure 2(d)). Moreover, microscopical analysis showed that cells were smaller in size under hypoxic culture than under normoxia. The expression of the cell surface markers CD133 and CD34 was increased, while that of CD105 and OCT4 did not change significantly (Figure 2(e)). These results demonstrated that HP improves the stemness of hDPCs, especially during long-term processing.

3.3. *HP Reduces Oxidative Stress in hDPCs.* A ROS activity assay found that hypoxia reduced the release of ROS in hDPCs. Mean ROS activity in the reoxygenation group (hypoxia 2 d + normoxia 1 d) was higher than that in the hypoxic group but lower than that in the normoxia group (Figure 3(a)). After hypoxia treatment, expression of the inflammatory cytokine IL-6 and IL-1β was not statistically significant (Figure 3(b)). The proportion of apoptosis was lowest in the hypoxia group (Figure 3(c)). In the antioxidant enzyme experiment, HP-treated hDPCs showed an increased level of expression of the antioxidant enzyme GSH-PX,

(a)

(b)
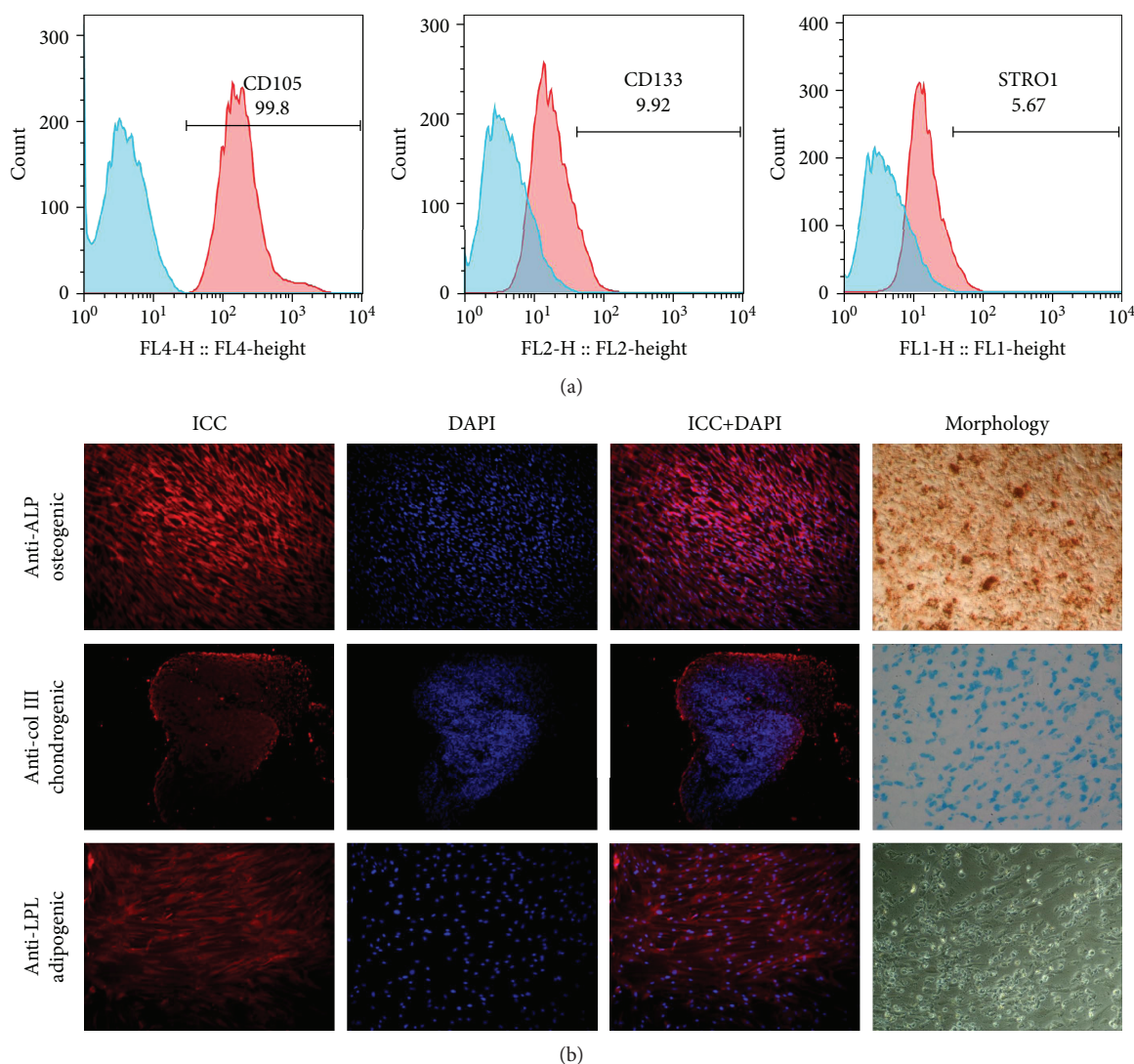
FIGURE 1: hDPC culture and identification of multidifferentiation ability: (a) identification of the mesenchymal stem cell surface markers CD105, CD133, and STRO1; (b) induced osteogenic, chondrogenic, adipogenic differentiation, and immunofluorescence staining of alkaline phosphatase (ALP), collagen type III (Col III), and lipoprotein lipase (LPL), respectively; nuclei were counterstained with $4'$,6-diamidino-2-phenylindole (DAPI) (magnification 10×10).

although there was no significant change in the levels of SOD and CAT (Figure 3(d)). These results indicated that HP slightly reduced oxidative stress in hDPCs.

3.4. Bioinformatic Analysis Revealed Activation of the PI3K/Akt Pathway under Hypoxic Conditions. To better understand the molecular mechanisms underlying hypoxia-induced changes, we performed whole transcriptome RNA-seq analysis in hDPCs. Differential expression analysis identified 1271 upregulated genes and 559 downregulated genes after hypoxia for 48 hours compared to normoxia. Importantly, we observed numerous protein-protein interactions among proteins encoded by differentially expressed genes (Supplementary Figure 1). These proteins formed a condensed interaction network with multiple hypoxia-induced proteins, such as ENO2, as hubs. To explore cellular signaling further, we conducted Kyoto Encyclopedia of

Genes and Genomes (KEGG) pathway analysis with the ToppGene tool. Downregulated genes in hypoxia showed enrichment of protein synthesis and metabolic pathways while glycolysis and cell cycle-related pathways were enriched in upregulated genes (Figures 4(a) and 4(b)). As expected, the HIF-1 signaling pathway was one of the top 10 enriched pathways in hypoxia (Figure 4(b)). We observed that the PI3K/Akt signaling pathway was also activated in hypoxia (Figure 4(b)). Notably, a substantial number of genes (32 genes) in the PI3K/Akt signaling pathway, including the cell cycle regulator, CDK2, are increased in hypoxia. Interestingly, we also found that 12 genes in this pathway are downregulated in hypoxia. This data seems to be paradoxical as we observed two sets of genes with opposite expression profiles in the same pathway, which also prompted us to experimentally investigate function of the PI3K/Akt pathway in hypoxia. Additionally, these data suggest that hDPCs
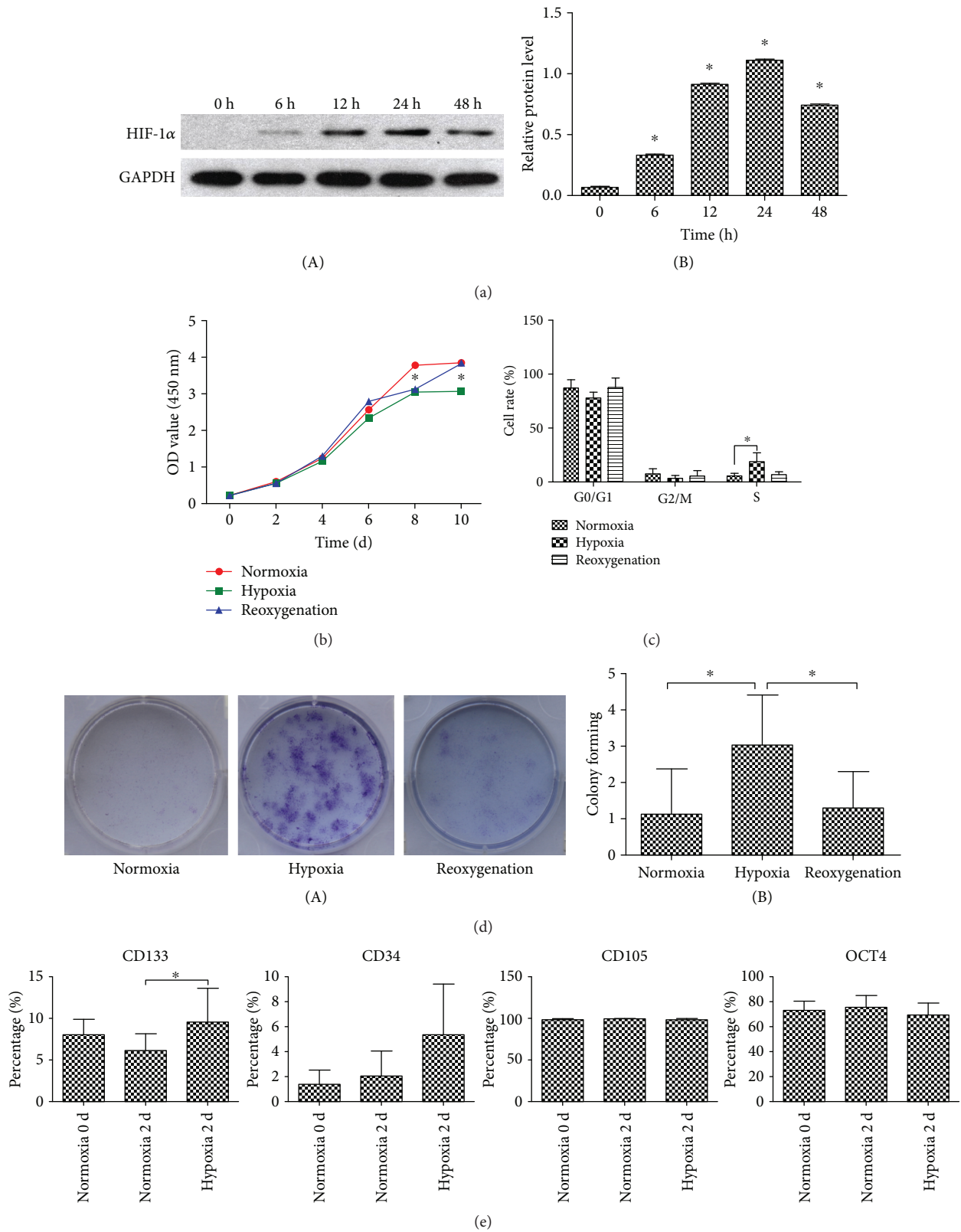
FIGURE 2: HP changed the cell phenotypes of hDPCs after culture under normoxia, hypoxia, and reoxygenation: (a) western blot assay and quantitative analysis of the expression of HIF-1α under normoxia and hypoxia at 0 h, 4 h, 8 h, 12 h, 24 h, and 48 h of culture; (b) proliferation ability of hDPCs in each group; (c) flow cytometry and quantitative analysis of cell cycle distribution in hDPCs after 3 d of culture under different oxygen concentrations; (d) colony-forming units and quantitative analysis in hDPCs after 10 d of culture; (e) expression of the mesenchymal stem cell surface markers CD133, CD34, CD105, and OCT4 in each group. Statistical significance is shown as $^*p < 0.05$.
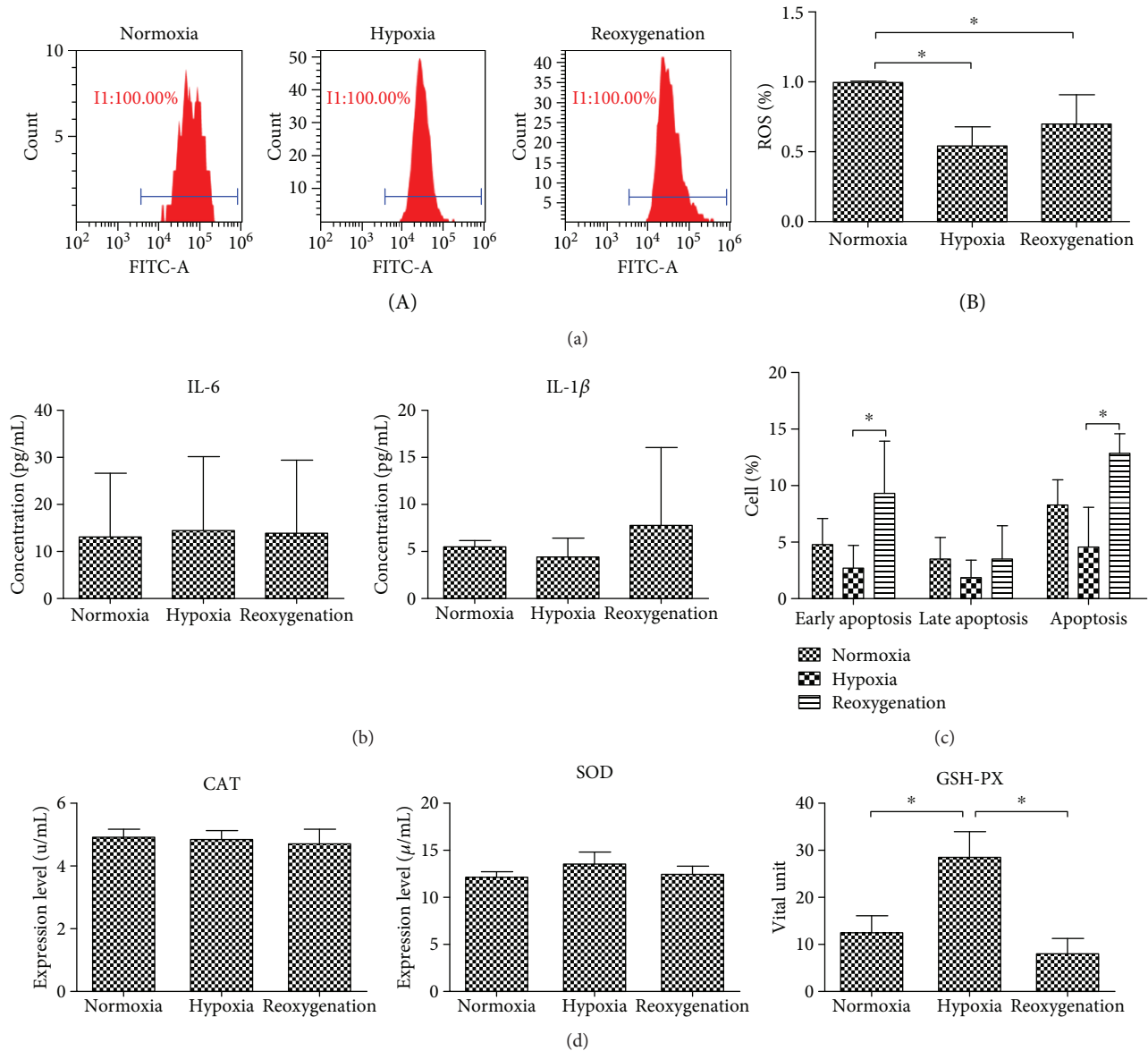
FIGURE 3: Effect of HP on oxidative stress in hDPCs after 3 d culture under normoxia, hypoxia, and reoxygenation: (a) HP-treated hDPCs were stained with $10\,\mu$M DCFDA and analyzed by flow cytometry; (b) the expression of inflammatory cytokines in each group, as analyzed by ELISA; (c) flow cytometry and quantitative analysis of cell apoptosis ratio in each group; (d) activity of the antioxidant enzymes SOD, CAT, and GSH-PX in hDPCs during culture at different oxygen concentrations. Statistical significance is expressed as $^{*}p < 0.05$.

may enhance cell proliferation and antioxidative stress in response to hypoxia stress.

3.5. PI3K/Akt Signaling Is Involved in the Regulation of Cellular Redox Status under Hypoxic Conditions. Given the essential roles of PI3K/Akt signaling in the response to hypoxia, we next examined whether inhibition of this pathway could change cellular phenotypes. LY294002, an inhibitor of the PI3K/Akt pathway, could enhance the expression of ROS and the apoptosis ratio in hDPCs (Figures 5(a) and 5(b)), although LY294002 has the same effect on ROS and apoptosis under normoxia or hypoxia. However, under hypoxia condition, the differences within the group

are more obvious. These results indicate that HP can effectively regulate the production of ROS in hDPCs through the PI3K/Akt pathway. Inhibitor-treated cells showed reduced expression of the inflammatory cytokine IL-6 and increased levels of IL-1β; however, there was no significant difference between hypoxia and normoxia (Figure 5(c)). It is suggested that the PI3K/Akt pathway may not be involved in the release of these two inflammatory factors pass by changed oxygen concentration. The expression of the antioxidant enzymes SOD and CAT did not change significantly, while the expression of GSH-PX decreased, indicating that the PI3K/Akt pathway is partially involved in the regulation of antioxidant enzyme expression levels (Figure 5(d)).
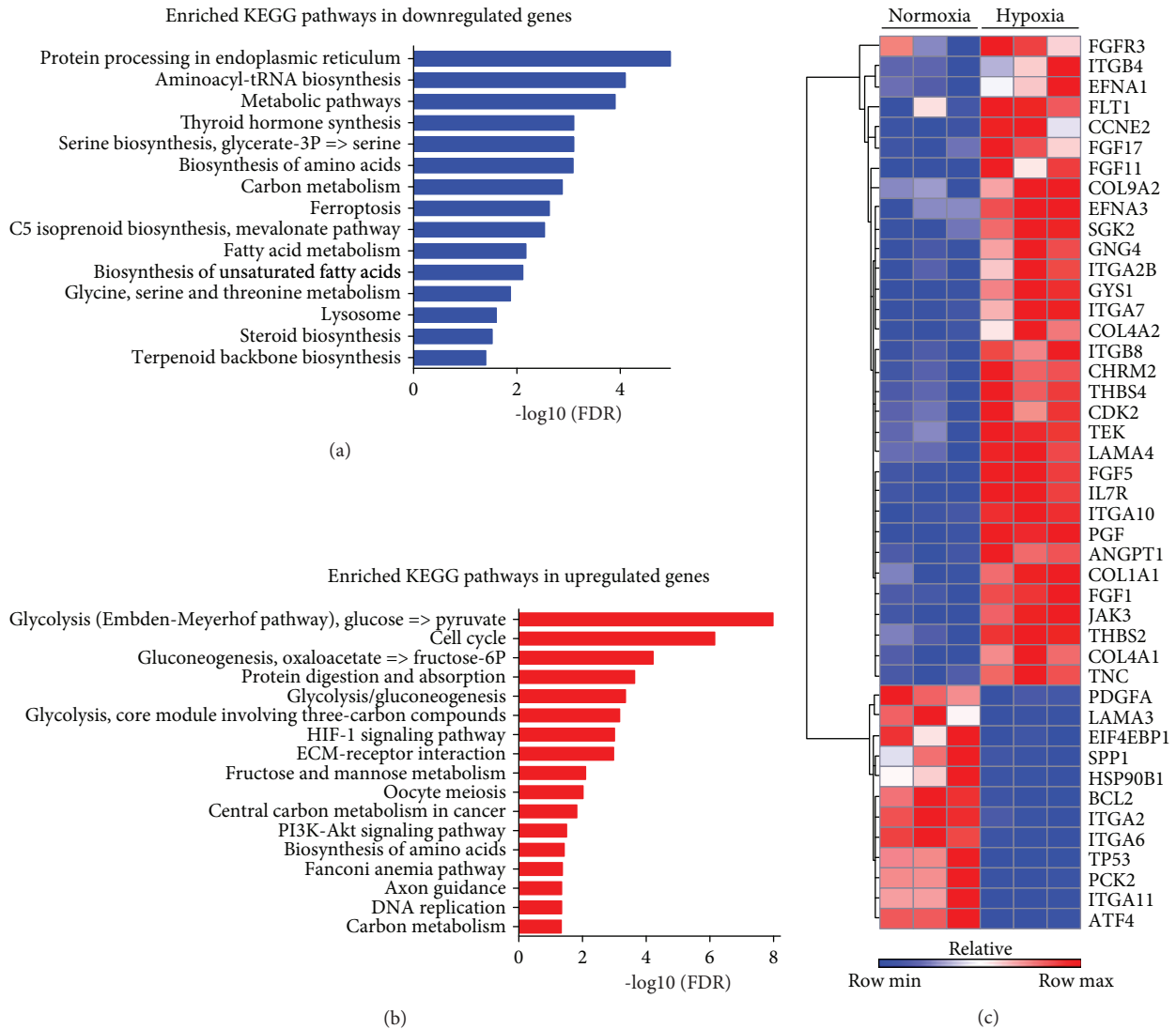
Figure 4: Differential expression analysis of hDPCs cultured between hypoxia and normoxia conditions: (a) top enriched pathways in downregulated genes of hypoxia condition; (b) top enriched KEGG pathways in upregulated genes of hypoxia condition; (c) heatmap shows expression of differentially expressed genes in the PI3K-Akt signaling pathway between hypoxia and normoxia conditions. Red indicates high expression, while blue indicates low expression.

Expression of phosphorylated PI3K and Akt was higher in the hypoxia group. The expression of phosphorylated PI3K and Akt in the NAC group was higher than that in the H₂O₂ and LY294002 group. The expression of Caspase 3 was similar to that of FOXO1 but in stark contrast to the expression of p-PI3K and p-Akt (Figure 5(e)). These findings are consistent with results arising from the bioinformatic analysis in that the treatment of hDPCs with HP activates phosphorylation of the PI3K/Akt pathway. The degree of phosphorylation in the PI3K/Akt pathway was decreased in cells under oxidative stress, and the effect of the inhibitor LY29004 was similar to H₂O₂. Moreover, Caspase 3 and FOXO1 may act downstream of the PI3K/Akt pathway, regulating the stress state of cells. PI3K/Akt signaling may affect intracellular ROS production by reverse regulating expression of the downstream protein FOXO1 and Caspase 3.

4. Discussion

Human dental pulp cells, as an adult stem cell, have not yet achieved widespread clinical applications, mainly because their source is limited, and because there have been issues with expansion and senescence during *in vitro* culture. Physiological hypoxia stimulates cells to adapt and increase their levels of glycolytic metabolism, thus reducing activity of the tricarboxylic acid (TCA) cycle and oxidative phosphorylation, which helps to reduce mitochondrial ROS production [10, 24]. ROS acts as a signaling molecule with low levels of homeostatic function or as a deleterious factor associated with high levels of tissue damage [10].

In the present study, we demonstrated that the HP treatment of hDPCs have a significant impact on cell self-renewal by reducing cell apoptosis ratio and ROS expression, while increasing colonial formation ability and the expression of

(a)

(b)

(c)

(d)

(e)
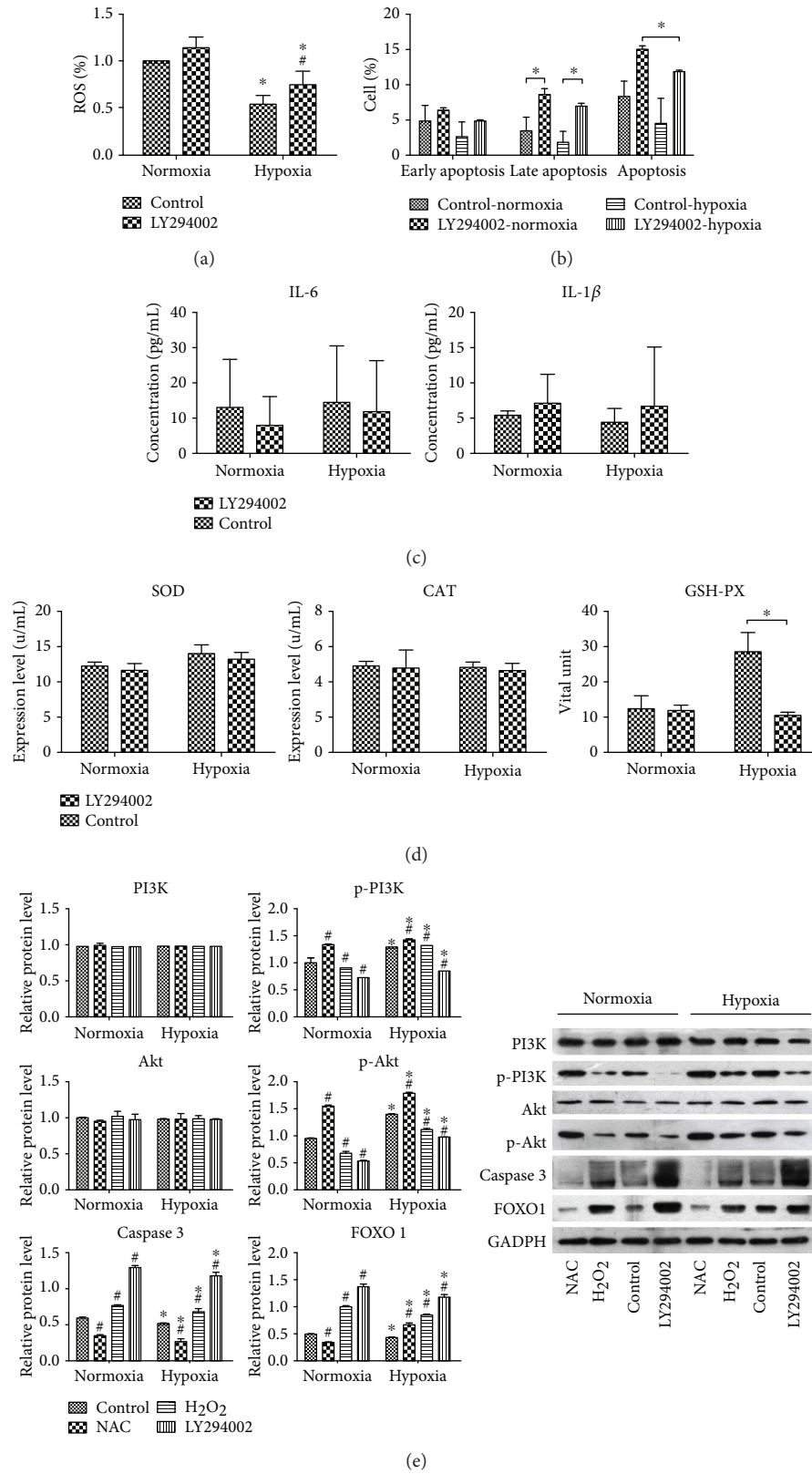
FIGURE 5: Inhibiting the PI3K/Akt pathway changed the redox status of hDPCs after 2 d of culture under normoxia and hypoxia: (a) hDPCs were stained with 10 μM of DCFDA and analyzed by flow cytometry; (b) flow cytometry and quantitative analysis of cell apoptosis ratio in different treatment groups; (c) levels of inflammatory cytokines secreted by each group, as determined by ELISA; (d) activity of the antioxidant enzymes SOD, CAT, and GSH-PX in hDPCs from each group; (e) western blot assay and quantitative expression of PI3K, p-PI3K, Akt, p-Akt, Caspase 3, and FOXO1 in different groups. Statistical significance is expressed as $^*p < 0.05$ versus *normoxia*; $^\#p < 0.05$ versus *control*.

the antioxidant enzyme GSH-PX. CD133, CD105, and OCT4 are considered to represent positive markers for mesenchymal stem cells. Evidence suggests that hypoxic preconditioning enhances the expression of these markers. In our experiment, the expression of CD133 was increased slightly after 2 days of hypoxic preconditioning. At the same time, the expression of CD34, a marker associated with hematopoietic function, was not statistically different and did not affect the qualitative properties of the hDPCs. The slight increase in expression may be related to a hypoxic function that promotes angiogenesis. In general, short-term hypoxic pretreatment (2 d) compared with long-term pretreatment (10 d) did not achieve a significant impact on cell phenotype.

In this study, oxygen-sensitive transcriptional programs in hDPCs were analyzed by bioinformatics tools, and their gene expression profiles were determined. Results showed that a variety of HIF-controlled genes, and genes encoding glycolytic enzymes and pentose phosphatase, were upregulated under two different low oxygen tension culture conditions. These experiments demonstrate the importance of using physiological hypoxic conditions, which mimic the anile environment of hDPCs to maintain pluripotency. Our data showed that the expression of PI3K/Akt was enhanced under hypoxic conditions. Many studies have reported that PI3K/Akt signaling can regulate the ROS expression, as well as the pathways involved in cellular oxidative stress [15, 25].

Further experimental results showed that the ratio of apoptotic cells and expression level of ROS increased after addition of the inhibitor LY294002. There was no significant change in the expression of the antioxidant enzymes and inflammatory cytokines, indicating that PI3K/Akt is not involved in the regulation of expression. Modulation of the expression of antioxidant enzymes and inflammatory cytokines may involve another molecular pathway simultaneously, such as APE-1/Ref-1 [26, 27] and Nrf2 signaling [28, 29]. However, there was significant change in GSH-PX levels, indicating that PI3K/Akt is involved in the upregulation of expression. Phosphorylated PI3K (p-PI3K) and Akt (p-Akt) expression increased and decreased after adding NAC and H_2O_2, respectively. It is suggested that PI3K/Akt signaling is involved in the expression of ROS under hypoxia. It has been reported that HIF-1α cannot translocate to the nucleus when Akt is inhibited, demonstrating that this may play an important role in the upstream regulation of HIF-1α [30]. Our study emphasizes that there might be a necessary connection between the two signaling pathways. The FOXO subfamily of Forkhead transcription factors are important regulators of cell survival in response to a variety of stress-related stimuli, such as hypoxia, DNA damage, and nutrient-poor conditions. The results of western blotting confirmed that PI3K/Akt negatively regulates the expression of FOXO1, a downstream regulatory target of the PI3K/Akt pathway [31–33]. We speculate that FOXO1 may be involved in hypoxia. However, further in-depth studies are now needed to verify the relationship between FOXO1 and hDPCs under hypoxia.

In summary, we have discovered a novel redox-mediated molecular mechanism for regulating the self-renewal and differentiation potential of hDPCs. The PI3K/Akt pathway was activated in response to hypoxia and inhibited oxidative stress in a ROS-dependent manner.

Data Availability

The RNA-seq data used to support the findings of this study are available from the corresponding author upon request.

Conflicts of Interest

The authors have no conflicts of interest to report in relation to this study.

Authors' Contributions

Fei Liu and Xin Huang contributed equally to this paper.

Supplementary Materials

Supplementary 1. Date 1: the fold changes of the ROS ratio and the detailed values of the statistical analysis, for both between-group and within-group comparisons.

Supplementary 2. Date 2: the fold changes of the apoptosis ratio and the detailed values of the statistical analysis, for both between-group and within-group comparisons.

Supplementary 3. Date 3: the fold changes and detailed values for the p-PI3K, p-Akt, Caspase 3, and FOXO1, for both between-group and within-group comparisons.

Supplementary 4. Figure 1: protein-protein interaction network analysis: protein-protein interactions among differentially expressed genes were retrieved from the STRING v10 database. Interaction network was generated by Cytoscape. We observed numerous protein-protein interactions among proteins encoded by differentially expressed genes. These proteins form a condensed interaction network with multiple hypoxia-induced proteins, such as ENO2, as hubs.

References

[1] S. Gronthos, M. Mankani, J. Brahim, P. G. Robey, and S. Shi, "Postnatal human dental pulp stem cells (DPSCs) in vitro and in vivo," *Proceedings of the National Academy of Sciences of the United States of America*, vol. 97, no. 25, pp. 13625–13630, 2000.

[2] M. Fujio, Z. Xing, N. Sharabi et al., "Conditioned media from hypoxic-cultured human dental pulp cells promotes bone healing during distraction osteogenesis," *Journal of Tissue Engineering and Regenerative Medicine*, vol. 11, no. 7, pp. 2116–2126, 2015.

[3] M. Pei, "Environmental preconditioning rejuvenates adult stem cells' proliferation and chondrogenic potential," *Biomaterials*, vol. 117, pp. 10–23, 2017.

[4] R. Narcisi, M. A. Cleary, P. A. J. Brama et al., "Long-term expansion, enhanced chondrogenic potential, and suppression of endochondral ossification of adult human MSCs via WNT signaling modulation," *Stem Cell Reports*, vol. 4, no. 3, pp. 459–472, 2015.

[5] M. Centola, B. Tonnarelli, S. Schären, N. Glaser, A. Barbero, and I. Martin, "Priming 3D cultures of human mesenchymal stromal cells toward cartilage formation via developmental pathways," *Stem Cells and Development*, vol. 22, no. 21, pp. 2849–2858, 2013.

[6] J. Li, K. C. Hansen, Y. Zhang et al., "Rejuvenation of chondrogenic potential in a young stem cell microenvironment," *Biomaterials*, vol. 35, no. 2, pp. 642–653, 2014.

[7] X. Zhi, J. Xiong, M. Wang et al., "Physiological hypoxia enhances stemness preservation, proliferation, and bidifferentiation of induced hepatic stem cells," *Oxidative Medicine and Cellular Longevity*, vol. 2018, Article ID 7618704, 10 pages, 2018.

[8] A. Moya, N. Larochette, J. Paquet et al., "Quiescence preconditioned human multipotent stromal cells adopt a metabolic profile favorable for enhanced survival under ischemia," *Stem Cells*, vol. 35, no. 1, pp. 181–196, 2017.

[9] I. Rosová, M. Dao, B. Capoccia, D. Link, and J. A. Nolta, "Hypoxic preconditioning results in increased motility and improved therapeutic potential of human mesenchymal stem cells," *Stem Cells*, vol. 26, no. 8, pp. 2173–2182, 2010.

[10] H. L. A. Vieira, P. M. Alves, and A. Vercelli, "Modulation of neuronal stem cell differentiation by hypoxia and reactive oxygen species," *Progress in Neurobiology*, vol. 93, no. 3, pp. 444–455, 2011.

[11] K. Wang, T. Zhang, Q. Dong, E. C. Nice, C. Huang, and Y. Wei, "Redox homeostasis: the linchpin in stem cell self-renewal and differentiation," *Cell Death & Disease*, vol. 4, no. 3, p. e537, 2013.

[12] T. Suda, K. Takubo, and G. L. Semenza, "Metabolic regulation of hematopoietic stem cells in the hypoxic niche," *Cell Stem Cell*, vol. 9, no. 4, pp. 298–310, 2011.

[13] A. Mohyeldin, T. Garzón-Muvdi, and A. Quiñones-Hinojosa, "Oxygen in stem cell biology: a critical component of the stem cell niche," *Cell Stem Cell*, vol. 7, no. 2, pp. 150–161, 2010.

[14] T.-S. Li and E. Marbán, "Physiological levels of reactive oxygen species are required to maintain genomic stability in stem cells," *Stem Cells*, vol. 28, no. 7, pp. 1178–1185, 2010.

[15] J. E. Le Belle, N. M. Orozco, A. A. Paucar et al., "Proliferative neural stem cells have high endogenous ROS levels that regulate self-renewal and neurogenesis in a PI3K/Akt-dependant manner," *Cell Stem Cell*, vol. 8, no. 1, pp. 59–71, 2011.

[16] C. Y. Yu, N. M. Boyd, S. J. Cringle, V. A. Alder, and D. Y. Yu, "Oxygen distribution and consumption in rat lower incisor pulp," *Archives of Oral Biology*, vol. 47, no. 7, pp. 529–536, 2002.

[17] N. E.-M. B. Ahmed, M. Murakami, S. Kaneko, and M. Nakashima, "The effects of hypoxia on the stemness properties of human dental pulp stem cells (DPSCs)," *Scientific Reports*, vol. 6, no. 1, p. 35476, 2016.

[18] S. B. Werle, P. Chagastelles, P. Pranke, and L. Casagrande, "The effects of hypoxia on in vitro culture of dental-derived stem cells," *Archives of Oral Biology*, vol. 68, pp. 13–20, 2016.

[19] V. G. Martinez, I. Ontoria-Oviedo, C. P. Ricardo et al., "Overexpression of hypoxia-inducible factor 1 alpha improves immunomodulation by dental mesenchymal stem cells," *Stem Cell Research & Therapy*, vol. 8, no. 1, p. 208, 2017.

[20] M. El Alami, J. Viña-Almunia, J. Gambini et al., "Activation of p 38, p21, and NRF-2 mediates decreased proliferation of human dental pulp stem cells cultured under 21% O_2," *Stem Cell Reports*, vol. 3, no. 4, pp. 566–573, 2014.

[21] A. M. F. Aranha, Z. Zhang, K. G. Neiva, C. A. S. Costa, J. Hebling, and J. E. Nör, "Hypoxia enhances the angiogenic potential of human dental pulp cells," *Journal of Endodontics*, vol. 36, no. 10, pp. 1633–1637, 2010.

[22] H. Gonzalez-King, N. A. García, I. Ontoria-Oviedo, M. Ciria, J. A. Montero, and P. Sepúlveda, "Hypoxia inducible factor-1α potentiates jagged 1-mediated angiogenesis by mesenchymal stem cell-derived exosomes," *Stem Cells*, vol. 35, no. 7, pp. 1747–1759, 2017.

[23] C. Y. Cui, Y. Bo, G. Chen et al., "Research on the effect of extract of dentin matrix on the differentiation of dental pulp cells," *Sichuan Da Xue Xue Bao Yi Xue Ban*, vol. 44, no. 4, pp. 657–661, 2013.

[24] U. Lendahl, K. L. Lee, H. Yang, and L. Poellinger, "Generating specificity and diversity in the transcriptional response to hypoxia," *Nature Reviews Genetics*, vol. 10, no. 12, pp. 821–832, 2009.

[25] H. Morimoto, K. Iwata, N. Ogonuki et al., "ROS are required for mouse spermatogonial stem cell self-renewal," *Cell Stem Cell*, vol. 12, no. 6, pp. 774–786, 2013.

[26] K. K. Bhakat, A. K. Mantha, and S. Mitra, "Transcriptional regulatory functions of mammalian AP-endonuclease (APE1/Ref-1), an essential multifunctional protein," *Antioxidants & Redox Signaling*, vol. 11, no. 3, pp. 621–637, 2009.

[27] G. M. Zou, M. H. Luo, A. Reed, M. R. Kelley, and M. C. Yoder, "Ape1 regulates hematopoietic differentiation of embryonic stem cells through its redox functional domain," *Blood*, vol. 109, no. 5, pp. 1917–1922, 2007.

[28] G. M. DeNicola, F. A. Karreth, T. J. Humpton et al., "Oncogene-induced Nrf2 transcription promotes ROS detoxification and tumorigenesis," *Nature*, vol. 475, no. 7354, pp. 106–109, 2011.

[29] C. E. Hochmuth, B. Biteau, D. Bohmann, and H. Jasper, "Redox regulation by Keap1 and Nrf2 controls intestinal stem cell proliferation in Drosophila," *Cell Stem Cell*, vol. 8, no. 2, pp. 188–199, 2011.

[30] M. Kanichai, D. Ferguson, P. J. Prendergast, and V. A. Campbell, "Hypoxia promotes chondrogenesis in rat mesenchymal stem cells: a role for AKT and hypoxia-inducible factor (HIF)-1α," *Journal of Cellular Physiology*, vol. 216, no. 3, pp. 708–715, 2008.

[31] W. J. Bakker, I. S. Harris, and T. W. Mak, "FOXO3a is activated in response to hypoxic stress and inhibits HIF1-induced apoptosis via regulation of CITED2," *Molecular Cell*, vol. 28, no. 6, pp. 941–953, 2007.

[32] L. Liao, X. Su, X. Yang et al., "TNF-α inhibits FoxO1 by upregulating miR-705 to aggravate oxidative damage in bone marrow-derived mesenchymal stem cells during osteoporosis," *Stem Cells*, vol. 34, no. 4, pp. 1054–1067, 2016.

[33] A. Eijkelenboom and B. M. T. Burgering, "FOXOs: signalling integrators for homeostasis maintenance," *Nature Reviews Molecular Cell Biology*, vol. 14, no. 2, pp. 83–97, 2013.

Research Article

Degradation of TRPML1 in Neurons Reduces Neuron Survival in Transient Global Cerebral Ischemia

Yang Wang,[1] **Shao-wei Jiang,**[1] **Xuan Liu,**[1] **Lei Niu,**[1] **Xiao-li Ge,**[1] **Jin-cheng Zhang,**[2] **Hai-rong Wang,**[1] **Ai-hua Fei,**[1] **Cheng-jin Gao** ⓘ**,**[1] **and Shu-ming Pan** ⓘ[1]

[1]*Department of Emergency, Xinhua Hospital, Shanghai Jiao Tong University School of Medicine, Shanghai 200092, China*
[2]*Department of Critical Care Medicine, Zhongshan Hospital, Fudan University, Shanghai 200032, China*

Correspondence should be addressed to Cheng-jin Gao; gaochengjin@xinhuamed.com.cn
and Shu-ming Pan; panshuming@xinhuamed.com.cn

Postcardiac arrest syndrome yields poor neurological outcomes, but the mechanisms underlying this condition remain poorly understood. Autophagy plays an important role in neuronal apoptosis induced by ischemia. However, whether autophagy is involved in neuron apoptosis induced by cardiac arrest has been less studied. This study found that TRPML1 participates in cerebral ischemic reperfusion injury. Primary neurons were isolated and treated with mucolipin synthetic agonist 1 (ML-SA1), as well as infected with the recombinant lentivirus TRPML1 overexpression vector *in vitro*. ML-SA1 was delivered intracerebroventricularly in transient global ischemia model. Protein expression levels were determined by western blot. Neurological deficit score and the infarct volume were analyzed for the detection of neuronal damage. We found that TRPML1 was significantly downregulated *in vivo* and *in vitro* ischemic reperfusion model. We also observed that TRPML1 overexpression or treatment with the ML-SA1 attenuated neuronal death in primary neurons and ameliorated neurological dysfunction *in vivo*. Our findings suggested that autophagy and apoptosis were activated after transient global ischemia. Administration of ML-SA1 before transient global ischemia ameliorated neurological dysfunction possibly through the promotion of autophagy and the inhibition of apoptosis.

1. Introduction

Neurological deficits after resuscitation contribute to high rates of mortality among patients after cardiac arrest [1–3]. Although recent advances in cardiopulmonary resuscitation techniques have significantly increased the rate of return of spontaneous circulation, few cardiac arrest victims achieve meaningful neurologic recovery [4–6]. Transient global cerebral ischemia (TGCI) is a clinical outcome related to cardiac arrest and other situations that deprive the oxygen and glucose in the brain during a short period. Severer neurologic deficits develop in the rare cases of survival from an unwitnessed cardiac arrest than in patients who have survived a witnessed cardiac arrest [7]. Therefore, the latent and persistent neurologic injuries that accompany TGCI may be the greatest obstacle to a full recovery from cardiac arrest, resulting in a broad range of neurological dysfunction [8–10].

Autophagy plays an important role in neuronal apoptosis induced by ischemia. As reported, autophagy protected the neurons from apoptosis both in the oxygen-glucose deprivation (OGD) model and the mouse cerebral ischemia model, via inhibiting neuronal apoptosis [11, 12]. Additionally, pharmacological induction of autophagy contributed to the neuron survival by suppressing apoptosis in the rat middle cerebral artery occlusion (MCAO) stoke model [13]. Furthermore, Wang et al. have demonstrated that deletion of β-arrestin-1, a vital scaffolding protein interacted with beclin-1 and Vps34 forming a proautophagic complex in neurons, hampered autophagosome formation and enhanced neural apoptosis [14]. However, whether autophagy is involved in neuron apoptosis induced by cardiac arrest has been less studied.

Transient receptor potential mucolipin-1 (TRPML1), also named MCOLN1, is widely expressed in mammalian cell

lysosomes or in the endosome membrane [15] and is the main channel for lysosome Ca^{2+} release and the key regulator for lysosomal storage and transportation [16, 17]. In addition, TRPML1 mutations can not only affect the activation of transcription factor EB (TFEB) but also the regulation of oxidative stress. Li et al. [18] determined TRPML1 is required for the activation of mammalian target of rapamycin complex 1 (mTORC1), which plays a fundamental role in autophagy regulation. TRPML1 has been also supposed to play a dual role in autophagosome membrane fusion and fission in the late endocytic pathways [15]. Further, impairment of autophagy has been reported in TRPML1$^{-/-}$ cells [19, 20]. Recently, Zhang et al. [17] showed TRPML1 could induce autophagy in a mTOR-independent way under stress conditions. Thus, TRPML1 is crucial for the regulation of autophagy [17, 21, 22].

However, the role of TRPML1 in cardiac arrest-induced ischemia is largely unknown. In this study, we hypothesize that TRPML1 is involved in ischemic reperfusion brain injury. Additionally, we aimed to assess the possible interaction between TRPML1 and neuronal injury. Furthermore, we attempt to describe a comprehensive mechanism of the effect of TRPML1 on ischemic reperfusion brain injury.

2. Materials and Methods

2.1. Animals. All animal experiments were performed in accordance with Xinhua Hospital Affiliated to Shanghai Jiao Tong University School of Medicine (Shanghai, China) guidelines for the use of experimental animals and the experimental protocols were approved by the Institutional Authority for Laboratory Animal Care of Xinhua Hospital Affiliated to Shanghai Jiao Tong University School of Medicine. All animal experiments were strictly followed with the guidelines of animal welfare in Xinhua Hospital Affiliated to Shanghai Jiao Tong University School of Medicine. The C57BL/6 mice were raised under standard laboratory conditions with food and water freely available. Humidity and temperature were kept constant at $60 \pm 5\%$ and $24 \pm 2°C$, respectively. Lights were on between 7:00 am and 7:00 pm.

2.2. Surgery for Mouse Models of Transient Global Cerebral Ischemia. The male C57BL/6 mice (8–10 weeks) were randomly assigned to the indicated groups and anesthetized with 4% isoflurane in 70% N_2O and 30% O_2. The transient bilateral common carotid artery occlusion (tBCCAO) surgery was performed as described previously [23] with minor modifications. Briefly, tBCCAO was initiated by occluding both common carotid arteries with microclips. After 40 min of ischemia, the clips were removed from both the arteries to allow for recirculation of the blood. The body temperature of mice was maintained at 37°C, and cerebral blood flow was examined during ischemia.

2.3. Triphenyl Tetrazolium Chloride (TTC) Staining. The mice were sacrificed and the brains were then dissected. The brain slices (2–3 mm) were made coronally and incubated with 2% TTC in 0.9% saline at 37°C for 15 min. After that, the TTC solution was replaced with PBS and the brain

slices were kept in 4% PFA. Infarct size was measured by an observer blinded to the experimental group assignment using the Image-Pro Plus. The infarct volume for each brain was calculated as IV% = (total volume of brain—normal volume of brain)/total volume of brain.

2.4. Neurological Deficit Score. The neurological deficit was determined using a 5-point-scale standard in a blinded fashion modified from described previously [24]: 0, no observable deficit; 1, torso flexion; 2, convulsion; 3, no spontaneous movement; 4, no forced movement; 5, death.

2.5. ML-SA1 Infusions. For ML-SA1 infusions, the reagent-infusion tubes were inserted into the lateral ventricles and fixed with the acrylic and dental cement. ML-SA1 was delivered intracerebroventricularly at a rate of $0.3 \mu l/min$ after 10-day recovery period. The coordinates of the lateral ventricles are AP −0.3 mm, ML ±1.0 mm, and DV −2.2 mm from bregma.

2.6. Isolation of the Adult Neurons and Astrocytes. The isolated mouse hippocampus or cortex was digested into cell suspension with Adult Brain Dissociation Kit (Miltenyi Biotec) following the vender protocol. The neurons or astrocytes were sorted by Neuron Isolation Kit (Miltenyi Biotec) or Anti-GLAST (ACSA-1) MicroBead Kit (Miltenyi Biotec), respectively, according to the manufacturer's instructions.

2.7. Cell Culture, Transfection. For hippocampal neuron culture, mouse hippocampus was isolated in cold PBS and then digested in 0.25% trypsin for 6 min at 37°C. After digestion termination by fetal bovine serum (FBS, Invitrogen), the cells were filtered through a $70 \mu m$ nylon strainer and then centrifuged at 800 rpm for 5 min. The cell pellets were resuspended in Dulbecco's modified Eagle's medium (DMEM, Invitrogen) supplemented with 20% FBS for 4 hr culture, and then the medium was replaced with Neurobasal (Invitrogen). After 3 days of culture, uridine ($17.5 \mu g/ml$) and 5-fluoro-2′-deoxyuridine ($7.5 \mu g/ml$) were added to the medium to limit the glia growth. For astrocyte culture, cerebral cortex was obtained from C57BL/6 mice between postnatal 1 and 3 days (P1-3) and cultured in DMEM supplemented with 10% FBS.

To package the TRPML1 lentivirus, the sequence containing TRPML1 cDNA (NCBI reference sequence: NM_053177.1) was cloned into pLenti-CMV-EGFP plasmid. The titers of lentivirus particles were between 5×10^8 and 1×10^9 units/ml. The hippocampal neuron culture was used for drug treatment after 48 hrs virus transfection.

2.8. OGD and Drug Treatment. For OGD, the culture medium of hippocampal neurons and astrocyte was replaced with glucose-free Earle's balanced salt solution purged by 5% CO2 and 95% N2 for 10 minutes. The cells were then kept with 5% CO2 and 95% N2 for another 0.5 or 1 hrs. ML-SA1 ($10 \mu M$), calpeptin ($10 \mu M$), DEVD ($10 \mu M$), or MG-132 ($5 \mu M$) was added into the culture medium before OGD.

2.9. MTT Assay. After OGD, the medium of the primary cultured hippocampal neurons or astrocytes was replaced

with 2 mg/ml MTT in PBS for 6 hr incubation at 37°C. After addition of DMSO, the plate was gently rotated for 20 minutes to solubilize the eventually formed formazan crystals. Finally, the absorbance value of 570 nm was measured using a microplate reader to determine the optic density.

2.10. RNA Isolation, Reverse Transcription, and qRT-PCR.

The primary cultured hippocampal neurons were harvested and lysed in TriZol (Sigma), and then the total RNA was extracted. 1 μg RNA was reverse-transcribed into cDNA using M-MLV reverse transcriptase following by the procedure: 10 min, 25°C; 60 min, 42°C; and 10 min, 70°C. The expression levels of TRPML1 and β-actin were quantified by Step One Plus Real-Time PCR System (ABI) with the two-step protocol (95°C, 10 min; 95°C, 10 s, and 60°C, 1 min for 40 cycles; 95°C, 15 s; 60°C, 1 min.).

Primers were listed as follows:
TRPML1.
Forward 5′-CAAGATCTTGGTGGTCACTGTGCAG-3′
Reverse 5′-GGTTGCTGAGCCCAAAGAGAATGAG-3′
β-Actin
Forward 5′-GGCTGTATTCCCCTCCATCG-3′
Reverse 5′-CCAGTTGGTAACAATGCCATGT-3′

2.11. Western Blot Analysis. The primary cultured hippocampal neurons/astrocytes and neurons/astrocytes sorted from the mouse brain tissues were harvested and lysed in 2% SDS lysis buffer. The total protein were T electrophoresed on SDS-8/12%PAGE and then transferred to polyvinyl difluoridine membranes. After blocking with 5% milk in PBS, the protein was incubated with the indicated antibody (TRPML1, 1 : 100; HA, 1 : 2000; LC3, 1 : 1000; NeuN, 1 : 1000; GFAP, 1 : 1000; cleaved caspase3, 1 : 500; and β-actin 1 : 5000) overnight at 4°C. The next day, the secondary antibodies (1 : 5000) were added after washing with PBS. The protein bands were visualized by Tanon 5200 (Tanon, China) using an ECL western blotting substrate kit, and the band density was analyzed by ImageJ.

2.11.1. Flow Cytometry. Apoptosis was analyzed using annexin V-FITC Apoptosis Detection Kit (BD Biosciences Pharmingen, San Diego, CA) and BD Biosciences FACSCalibur flow cytometry. Briefly, a total of 5^*10^5 cells were washed twice with cold PBS and resuspended with binding buffer and then stained with annexin V-FITC and propidium iodide (PI) for 15 min in the dark. Flow cytometry was analyzed using BD Biosciences FACSCalibur within 1 hour.

2.12. Drugs and Antibodies. Antibodies were used as follows: TRPML1 from Alomone Labs (acc-081), GFAP from Sigma (G3893), NeuN from Abcam (ab177487), HA from Sigma (H6908), LC3 from Abcam (ab192890), beclin-1 from Cell Signaling Technology (#3495), p62 from Proteintech (18420-1-AP), cleaved caspase3 from Cell Signaling Technology (#9661), and β-actin from Abcam (ab8227). Drugs were used as follows: ML-SA1 from Abcam (ab144622), MG-132 from Medchemexpress (HY-13259), DEVD from Medchemexpress (HY-12466), and calpeptin from Abcam (ab120804).

2.13. Statistical Analysis. All the data were presented as means ± SEM from at least three independent experiments. Two-tailed Student's t-test was performed to compare the differences between two groups and one-way ANOVA with Tukey's post hoc test performed to compare multiple groups using GraphPad Prism 5. Differences were considered to be significant when a P value is less than 0.05.

3. Results

3.1. TRPML1 Is Specifically Downregulated in Hippocampal Neurons through Proteasome in Ischemia. To investigate the role of TRPML1 in neuronal survival of ischemia reperfusion, the primary cultured hippocampal neurons were initially deprived of oxygen and glucose to mimic in vivo ischemia. As shown in Figures 1(a)–1(b), the protein expression of TRPML1 was greatly downregulated in the primary cultured hippocampal neurons 30 min after OGD and maintained its reduced level to one hour after OGD. In contrast, the protein level of TRPML1 in astrocytes was not changed 30 min or one hour after OGD (Figures 1(c)–1(d)).

We next studied the TRPML1 expression of hippocampal neurons in the tBCCAo model. Hippocampal neurons or astrocytes were isolated from the adult mouse hippocampus or total brain, respectively, and then verified by the expression of hexaribonucleotide binding protein-3 (NeuN), a marker for neurons and glial fibrillary acid protein (GFAP), a marker for astrocytes using western blotting (Figures 1(e)–1(f)). Consistent with the results from primary cultured hippocampal neurons, we found the neuronal TRPML1 protein was also downregulated in the mouse hippocampus after tBCCAo (Figures 1(g)–1(h)), while the protein expression of TRPML1 in astrocytes was not changed (Figures 1(i)–1(j)). Taken together, these findings suggest that TRPML1 is specifically reduced in hippocampal neurons in ischemia reperfusion.

To further explore the mechanism underlying the downregulation of TRPML1 of hippocampal neurons in ischemia reperfusion, we examined the TRPML1 mRNA level by quantitative real-time PCR (qRT-PCR). As shown in Figure 1(k), the mRNA level of TRPML1 in the primary cultured hippocampal neurons was not changed both 30 min and one hour after OGD. These results indicated that the downregulation of TRPML1 was probably regulated at its posttranscriptional level. As reported, protease calpain or caspase-3 plays an important role in protein cleavage and stability [25–27]. However, administration of calpeptin, the inhibitor of calpain or DEVD, the caspase-3 inhibitor did not prevent the TRPML1 degradation in hippocampal neurons (Figures 1(l)–1(m)). Notably, incubation of MG-132, the inhibitor of proteasome, significantly inhibited the reduction of TRPML1 level (Figures 1(l)–1(m)). Altogether, these observations indicated that proteasome mediates the TRPML1 degradation of hippocampal neurons in ischemia reperfusion.

3.2. TRPML1 Reduces the Hippocampal Neuron Death after OGD. To study the role of TRPML1 degradation in ischemia reperfusion, we next measured the hippocampal neuron

(a)

(b)

(c)

(d)

(e)

(f)

(g)

(h)

(i)

(j)

FIGURE 1: Continued.

(k) (l) (m)
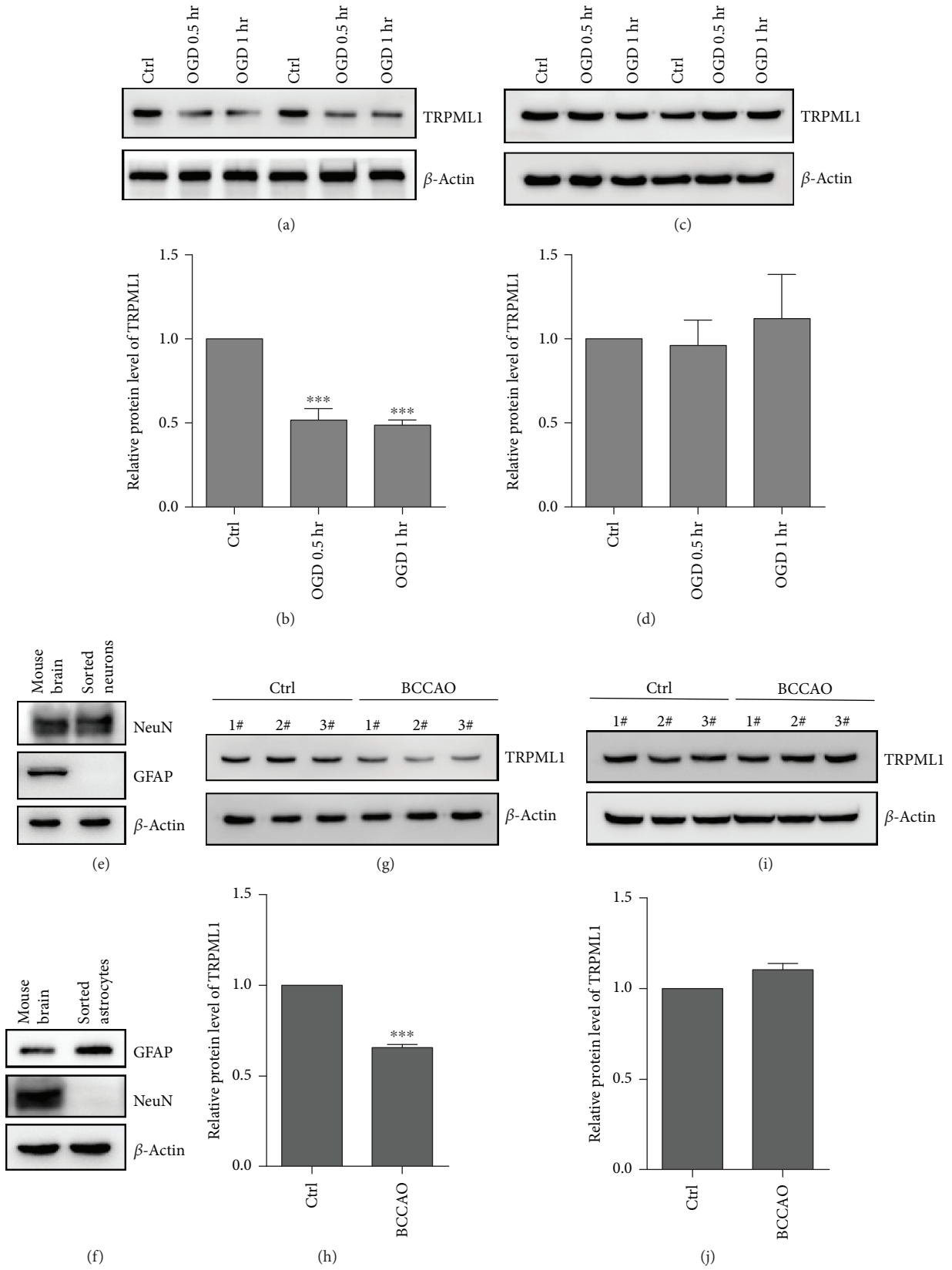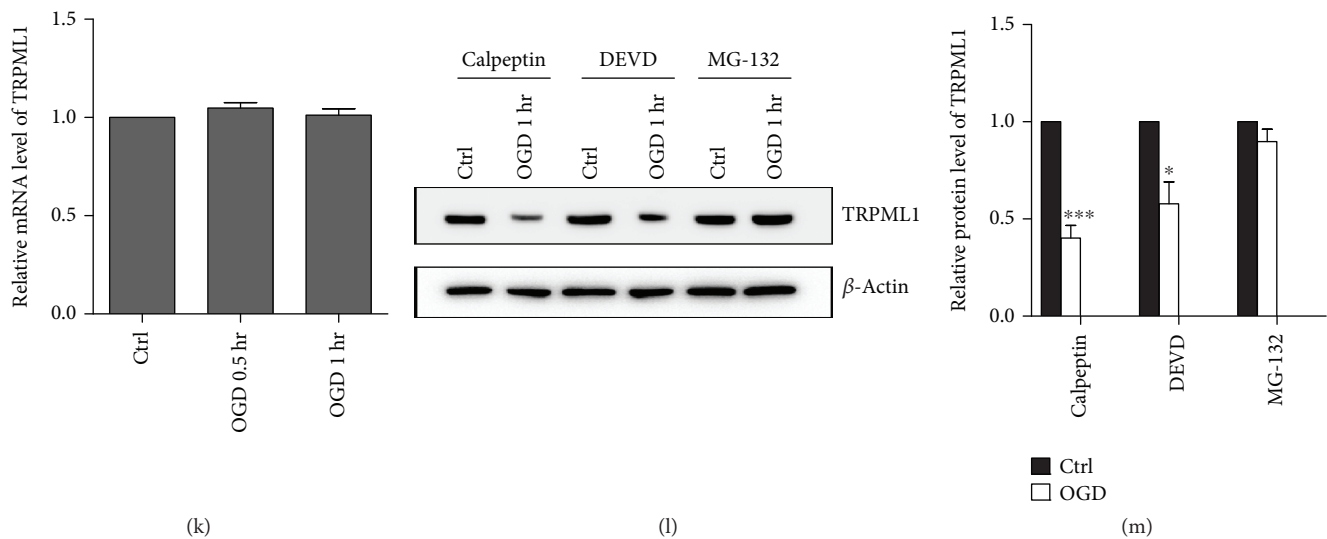
FIGURE 1: Proteasome-mediated degradation of TRPML1 of hippocampal neurons in ischemia. (a–d) Representative immunoblots of TRPML1 from cultured hippocampal neurons (a, $n = 4$) or astrocytes (c, $n = 4$) 0.5 or 1 hrs after OGD. (b) or (d) was the statistics for (a) or (c). (e, f) Immunoblots of analysis of the indicated marker expression in sorted neurons (e) and astrocytes (f) (GFAP: astrocyte marker, NeuN: neuron marker). (g–j) Representative immunoblots of TRPML1 from sorted neurons (g, $n = 9$) or astrocytes (i, $n = 9$) 40 min after tBCCAo. (h) or (j) was the statistics for (g) or (i). (k) Quantitative PCR analysis of TRPML1 mRNA levels in hippocampal neurons 1 hr after OGD ($n = 5$). (l, m) Representative immunoblots of TRPML1 from cultured hippocampal neurons ($n = 5$) incubated with/without calpeptin (10 μM), DEVD (10 μM), or MG132 (5 μM). (m) was the statistics for (l). β-Actin serves as a loading control. All data were presented as mean ± SEM. Comparisons between groups for statistical significance were performed with one-way analysis of variance (ANOVA) with Tukey's post hoc test (b, d, and k), Student's t-test, two tailed (h, j), or two-way ANOVA with Bonferroni post hoc test (m). $^{*}P < 0.05$, $^{***}P < 0.001$ versus Ctrl.

survival by MTT assay after OGD. The results in Figure 2(a) showed that the death rate of hippocampal neuron after OGD was about 60%. Incubation of ML-SA1, the TRPML1 agonist, significantly improved the neuron survival after OGD (Figure 2(a)). Furthermore, we engineered a hemagglutinin- (HA-) tagged TRPML1-2A-green fluorescent protein (GFP) lentivirus, which was well expressed in hippocampal neurons (Figure 2(b)). In accordance with the result of ML-SA1 treatment, the enhanced expression of TRPML1 also largely reduced the hippocampal neuron death after OGD (Figure 2(c)).

To further explore the apoptosis rate of hippocampal neurons in ischemia reperfusion, we examined the apoptosis rate by flow cytometry. The results in Figures 2(d)–2(g) showed the apoptosis rate was greatly increased after OGD. In addition, incubation of ML-SA1 significantly improved the neuron survival after OGD (Figures 2(d) and 2(f)). In accordance with the result of ML-SA1 treatment, the enhanced expression of TRPML1 also largely reduced the hippocampal neuron death after OGD (Figures 2(e) and 2(g)).

3.3. TRPML1 Activation Promotes Autophagy and Inhibits Apoptosis. The findings above suggested that TRPML1 degradation in ischemia reperfusion resulted in the death of hippocampal neurons. To explore the mechanism underlying it, we then studied the autophagy levels in the hippocampal neuron after TRPML1 degradation. As shown in Figures 3(a)–3(b), the expression level of autophagy markers beclin-1 and LC3B was greatly increased after

OGD. Moreover, incubation of ML-SA1 further potentiated the beclin-1 and LC3B expression in the hippocampal neurons (Figures 3(a)–3(b)). Additionally, the enhancement of TRPML1 expression also contributes to the elevation of beclin-1 and LC3B level in the hippocampal neurons (Figures 3(c)–3(d)). Analysis of p62 expression demonstrated that incubation of ML-SA1 or TRPML1 overexpression in OGD decreased the levels of p62. These results indicated that TRPML1 activation potentiated the autophagy level in ischemia reperfusion.

It has been reported that enhancement of autophagy level could prevent neuronal loss from apoptosis in ischemia [13]. To further study whether TRPML1-regulated autophagy could affect the neuronal loss, we examined the expression level of cleaved caspase-3 in the hippocampal neurons. The results in Figures 3(e)–3(f) showed that OGD induced the production of cleaved caspase-3 in the hippocampal neurons, which was remarkably inhibited by ML-SA1 treatment. Consistently, exogenous expression of TRPML1 also reduced the elevated expression of cleaved caspase-3 induced by OGD. As talked above, the results of flow cytometry after OGD showed the ameliorated apoptosis rate of neurons by either ML-SA1 treament or lentivirus overexpression (Figures 2(d)–2(e)). Taken together, downregulation of TRPML1 level in the hippocampal neurons inhibits autophagy and contributes to cell apoptosis.

3.4. TRPML1 Activation Prevents Brain Damage and Improves the Survival Rate in Transient GCI. To further

(a)   (b)   (c)

(d)

(e)

(f)   (g)
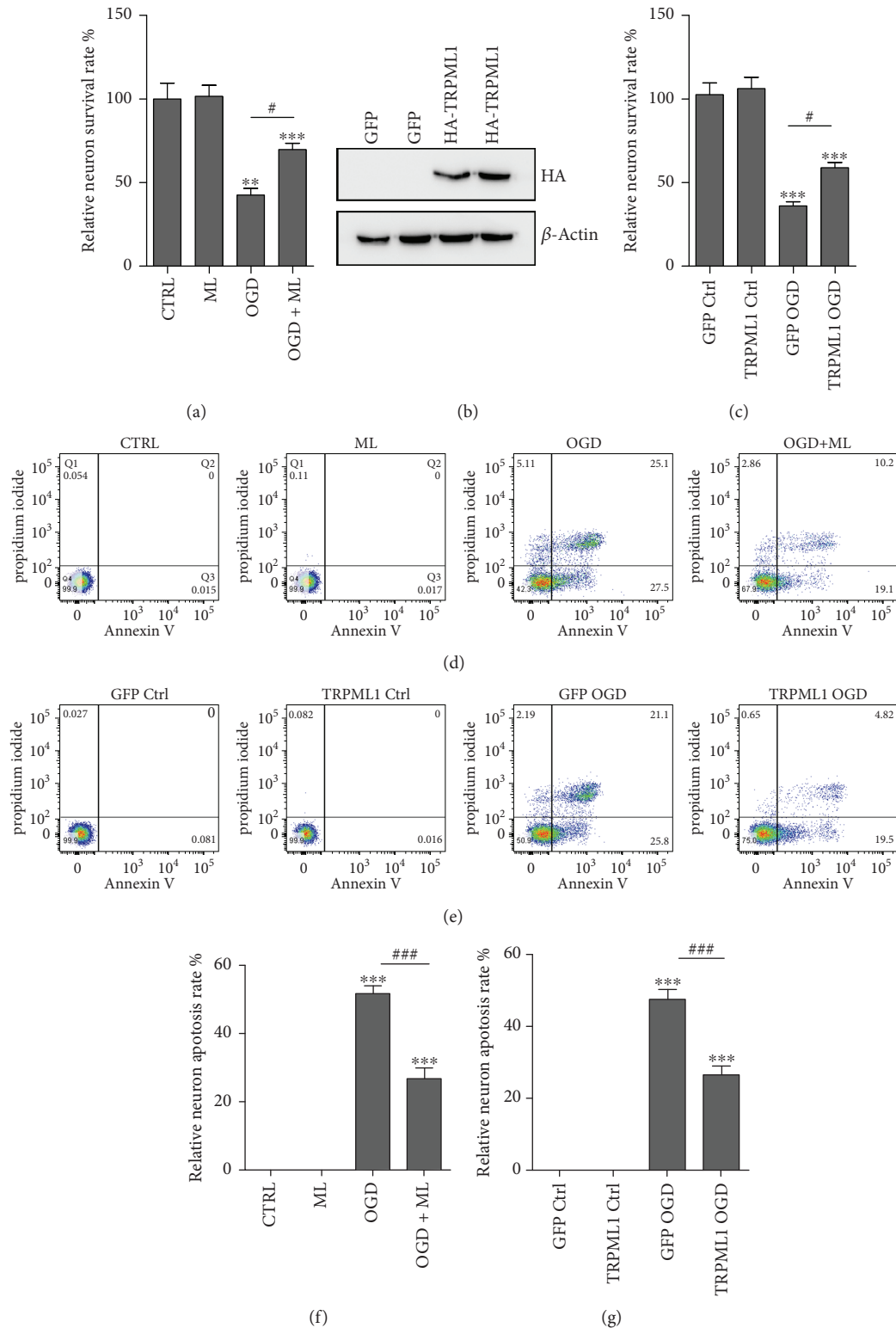
FIGURE 2: Reduction of neuron survival in OGD by TRPML1 degradation. (a) Hippocampal neuron survival rate determined by MTT assay after 3 hrs OGD in the preincubation with ML-SA1 (10 μM, $n = 4$). (b) Immunoblot analysis of HA-TRPML1 expression in hippocampal neuron. (c) The survival rate of hippocampal neuron transfected with TRPML1 lentivirus determined by MTT assay after 3 hrs OGD ($n = 5$). β-Actin serves as a loading control. (d, f) Hippocampal neuron apoptosis was analyzed by flow cytometry 3 hrs OGD in the preincubation with ML-SA1 (10 μM, $n = 4$). (e, g) The apoptosis of hippocampal neuron transfected with TRPML1 lentivirus was determined by flow cytometry after 3 hrs OGD ($n = 4$). All data were presented as mean ± SEM. All comparisons between groups for statistical significance were performed with one-way analysis of variance (ANOVA) with Tukey's post hoc test. $^{**}P < 0.01$, $^{***}P < 0.001$ versus Ctrl. $^{\#}P < 0.05$ versus OGD.

FIGURE 3: Continued.

(e)

(g)

(f)

(h)
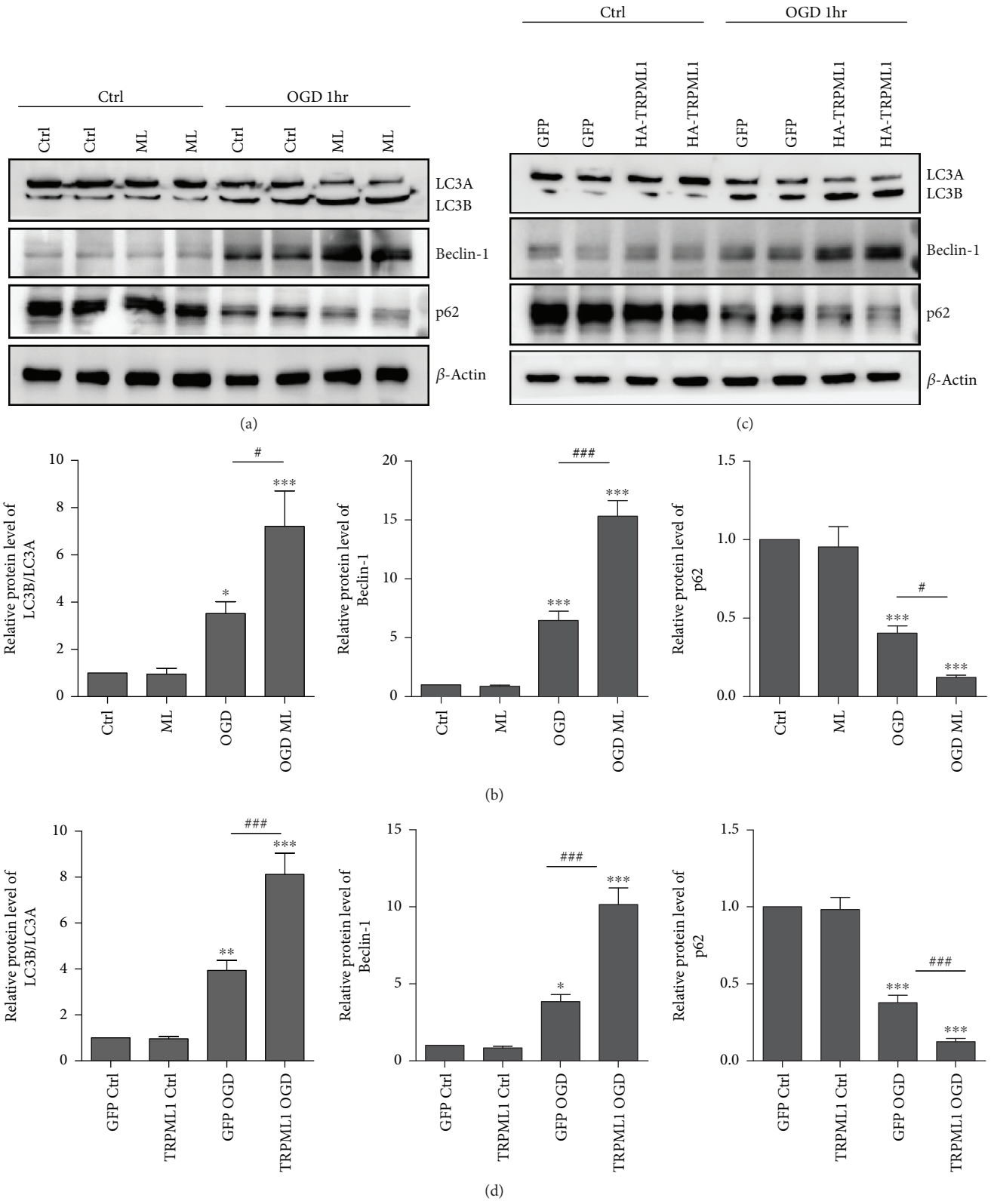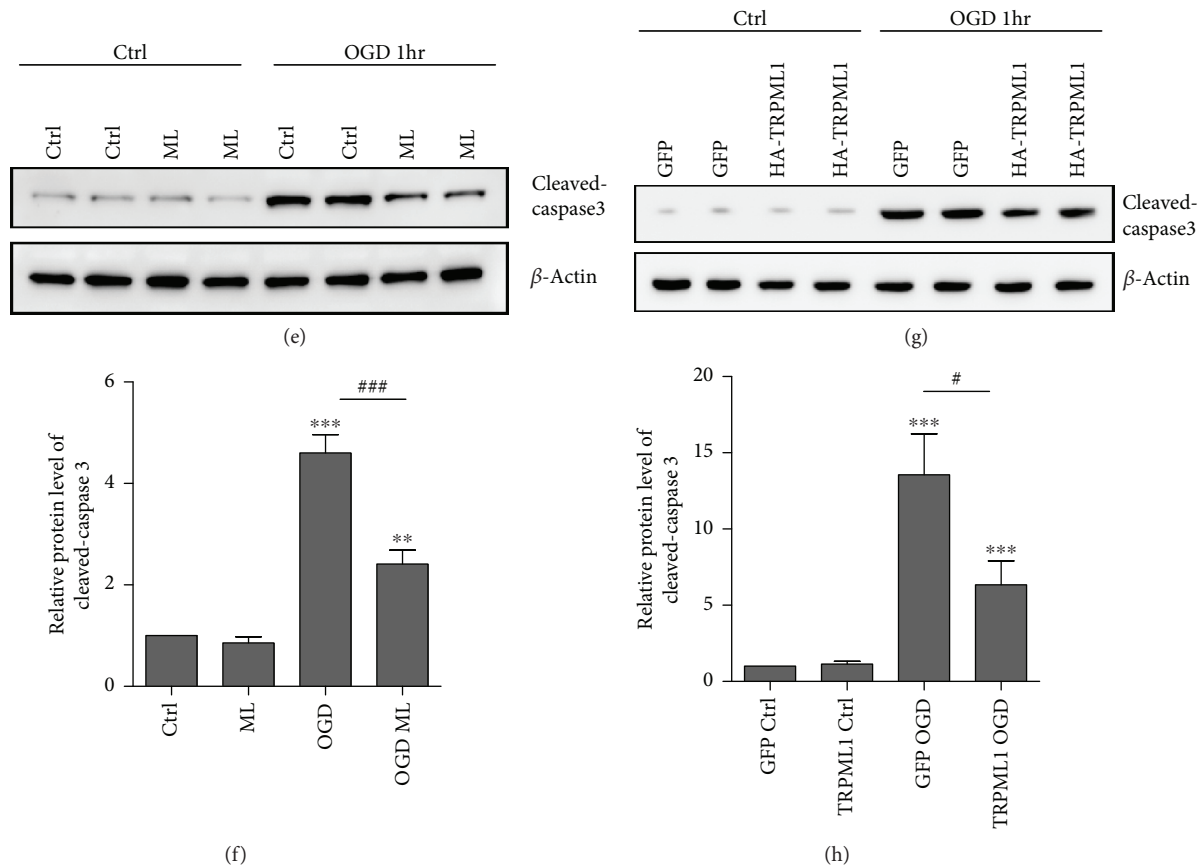
Figure 3: Autophagy enhancement and apoptosis inhibition by TRPML1 activation. (a–d) Representative immunoblots of beclin-1, LC3, and p62 from cultured hippocampal neurons preincubated with 10 μM ML-SA1 (a, $n = 6$) or transfected with TRPML1 lentivirus (c, $n = 6$) 1 hr after OGD. (b) or (d) was the statistics for (a) or (c). (e–h) Representative immunoblots of cleaved caspase3 from cultured hippocampal neurons preincubated with 10 μM ML-SA1 (e, $n = 6$) or transfected with TRPML1 lentivirus (g, $n = 6$) 1 hr after OGD. (f) or (h) was the statistics for (e) or (g). β-Actin serves as a loading control. All data were presented as mean ± SEM. All comparisons between groups for statistical significance were performed with one-way analysis of variance (ANOVA) with Tukey's post hoc test. $^*P < 0.05$, $^{**}P < 0.01$, $^{***}P < 0.001$ versus Ctrl. $^\#P < 0.05$, $^{\#\#\#}P < 0.001$ versus OGD.

explore the role of TRPML1 in the tBCCAO model, we delivered ML-SA1 into lateral ventricles of the mice. As shown by TTC staining in Figures 4(a) and 4(b), tBCCAO greatly induced the infarct volumes compared with control, while infusion of ML-SA1 significantly reduced the infarct volumes. Moreover, we measured the neurological deficits 24 hrs after tBCCAO and the mouse survival rate ten days after tBCCAO. Notably, ML-SA1 delivery remarkably improved the mouse behavior in neurological deficit score and increased the mouse survival rate (Figures 4(c)–4(d)). Collectively, our results above suggested that enhancement of TRPML1 activity in ischemia reperfusion protected the neurons from damage and reduced the mortality.

4. Discussion

Here, we found degradation of TRPML1 reduced neuron survival after ischemic reperfusion injury.

Several lines of evidence support this conclusion. First, the neuron protein level of TRPML1 was downregulated after ischemic reperfusion injury both in vivo and vitro. Furthermore, the decreased TRPML1 protein level could

be inhibited by proteasome inhibitor MG132. Second, upregulating TRPML1 by both agonist ML-SA1 and overexpression lentivirus could increase survival rate in neurons. Third, we found autophagy was enhanced and apoptosis was suppressed after TRPML1 activation. Lastly, upregulating TRPML1 in TGI mice could prevent brain damage, ameliorate neurological deficits, and reduce mortality. Taken together, our results provided that enhancement of TRPML1 in neurons can prevent neuronal death induced by ischemia.

The ubiquitin-proteasome system (UPS) is one of the most important pathways responsible for cellular homeostasis [28]. Previous studies showed that the UPS plays a complex and unambiguous role in the pathophysiology of cerebral ischemia-reperfusion injury [29]. Our results showed the protein degradation of TRPML1 in the neurons after ischemic reperfusion injury. However, the mRNA level of TRPML1 in the primary cultured hippocampal neurons was not changed both 30 min and one hour after OGD. Therefore, the downregulation of TRPML1 occurred at posttranscriptional level. Additionally, we found that the degradation of TRPML1 was significantly suppressed after MG132 treatment, indicating the involvement of UPS.

(a)

(b)

(c)

(d)
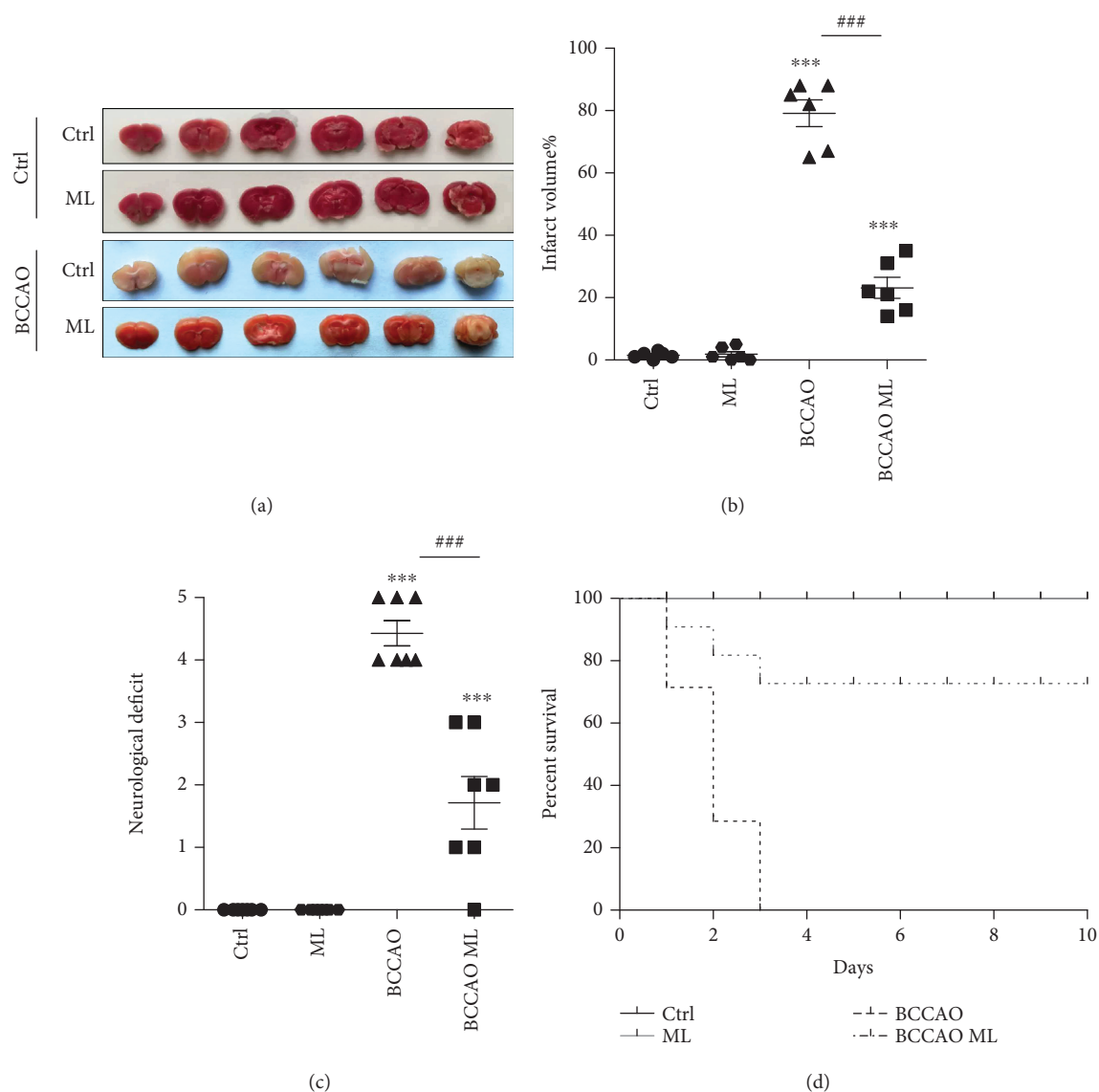
FIGURE 4: Reduction of the infarct volumes and mortality by TRPML1 activation. (a, b) Infarct volumes of mice infusion with or without $5\,\mu M$ ML-SA1after 12 hrs reperfusion ($n = 6$). (b) was the statistics for (a). (c) Evaluation of neurological deficit after 24 hrs reperfusion was evaluated in mice infusion with or without $5\,\mu M$ ML-SA1 ($n = 7$). (d) Evaluation of the survival rate in mice infusion with or without $5\,\mu M$ ML-SA1 after tBCCAO ($n = 8$). All data were presented as mean $\pm$ SEM. All comparisons between groups for statistical significance were performed with one-way analysis of variance (ANOVA) with Tukey's post hoc test. $^{***}P < 0.001$ versus Ctrl. $^{\#\#\#}P < 0.001$ versus OGD.

Evidence from a number of studies suggests that the important role of proteasome in ischemic reperfusion injury and proteasome inhibitors have been known to prevent brain ischemic damage, whose mechanisms are still largely unknown [30–32]. The ubiquitin E3 ligases, the critical components of this cascade, constitute the largest family of ubiquitin ligases with more than 600 predicted members. Zinc finger protein A20 was revealed as a ubiquitin ligase and attenuated the cerebral inflammatory injury in cerebral ischemia/reperfusion rats [33]. The HECT-domain E3 ligase Huwe1 (HECT, UBA, and WWE domain containing 1) involved in the ubiquitination, degradation of multiple proteins, was proven to interact with regulation of Gadd45 under oxygen-glucose deprivation and reperfusion injury in primary rat cortical neuronal cells [34]. Another ubiquitin E3 ligase TRAF6 was reported to be a key promoter of ischemic signaling cascades and neuronal death after cerebral ischemia reperfusion injury by ubiquitinating and activating Rac1 [35]. It is also reported that Siah1, parkin, and PARK2 act as an E3 ligase in cerebral ischemic reperfusion injury [36–40]. Therefore, identification of the E3 ligase of TRPML1 would further uncover the UPS function in cardiac arrest-induced ischemia.

ML-SA1, a structural analog of SF-51, can potently activate an inward rectifying TRPML1-dependent current similar to the one activated by phosphatidylinositol 3,5-bisphosphate ($PI_{3,5}P^2$) [41]. Recently ML-SA1 was identified to activate mammalian TRPML1 and shown to

alleviate lipid accumulation in lysosomes of cellular models of lysosome storage diseases [42]. Enhanced TRPML1 triggers lysosomal Ca^{2+} release, autophagy induction, and lysosome biogenesis [17]. In the present study, we demonstrated that ML-SA1 could significantly promote the autophagy, attenuate the apoptosis, and alleviate neuron survival and neurological dysfunction that occur after ischemic reperfusion injury. Diverse neuroprotective materials have been suggested as agents for protecting the brain from global ischemic injury during cardiac arrest; however, their application for clinical treatment is not satisfactory. Our findings above indicated that TRPML1 could be a novel target for preventing and treating ischemic reperfusion brain injury.

Several limitations of this work should be noted. First, we tested only one dose of ML-SA1. The optimal timing and dosage of ML-SA1 should be fully considered in future studies. Second, we used an intracerebroventricular pretreatment model for ML-SA1 administration; however, additional studies are needed in posttreatment settings and dosing site.

5. Conclusion

Taken together, our study provides evidence that TRPML1 participates in delayed neuronal damage after TGI. In addition, our data demonstrate that ML-SA1 pretreatment attenuates neuron injury *in vivo* and *in vitro*. These protective effects result from enhancing autophagy, the inhibition of apoptosis, and protein ubiquitination. Thus, the regulation of TRPML1 could be a novel strategy for preventing and treating ischemic reperfusion brain injury.

Data Availability

The data used to support the findings of this study are included within the article.

Disclosure

The manuscript was presented before as an abstract in "Annals of Emergency Medicine 2018" (doi:10.1016/j.annemergmed.2018.08.121).

Conflicts of Interest

The authors declare that there is no conflict of interests regarding the publication of this paper.

Authors' Contributions

Yang Wang and Shao-wei Jiang contributed equally to this manuscript.

Acknowledgments

References

[1] R. W. Neumar, J. P. Nolan, C. Adrie et al., "Post-cardiac arrest syndrome: epidemiology, pathophysiology, treatment, and prognostication. A consensus statement from the International Liaison Committee on Resuscitation (American Heart Association, Australian and New Zealand Council on Resuscitation, E)," *Circulation*, vol. 118, no. 23, pp. 2452–2483, 2008.

[2] X. P. Wang, Q. M. Lin, S. Zhao, S. R. Lin, and F. Chen, "Therapeutic benefits of mild hypothermia in patients successfully resuscitated from cardiac arrest: a meta-analysis," *World Journal of Emergency Medicine*, vol. 4, no. 4, pp. 260–265, 2013.

[3] B. S. Allen and G. D. Buckberg, "Studies of isolated global brain ischaemia: I. Overview of irreversible brain injury and evolution of a new concept - redefining the time of brain death," *European Journal of Cardio-thoracic Surgery*, vol. 41, no. 5, pp. 1132–1137, 2012.

[4] S. L. Gogela, Y. M. Gozal, B. Zhang et al., "Severe carotid stenosis and delay of reperfusion in endovascular stroke treatment: an Interventional Management of Stroke-III study," *Journal of Neurosurgery*, vol. 128, no. 1, pp. 94–99, 2018.

[5] V. M. Nadkarni, G. L. Larkin, M. A. Peberdy et al., "First documented rhythm and clinical outcome from in-hospital cardiac arrest among children and adults," *JAMA*, vol. 295, no. 1, pp. 50–57, 2006.

[6] J. P. Nolan, S. R. Laver, C. A. Welch, D. A. Harrison, V. Gupta, and K. Rowan, "Outcome following admission to UK intensive care units after cardiac arrest: a secondary analysis of the ICNARC Case Mix Programme Database," *Anaesthesia*, vol. 62, no. 12, pp. 1207–1216, 2007.

[7] T. N. Chung, J. H. Kim, B. Y. Choi et al., "Effect of adipose-derived mesenchymal stem cell administration and mild hypothermia induction on delayed neuronal death after transient global cerebral ischemia," *Critical Care Medicine*, vol. 45, no. 5, pp. e508–e515, 2017.

[8] K. S. Sunnerhagen, O. Johansson, J. Herlitz, and G. Grimby, "Life after cardiac arrest; a retrospective study," *Resuscitation*, vol. 31, no. 2, pp. 135–140, 1996.

[9] C. A. Anderson and D. B. Arciniegas, "Cognitive sequelae of hypoxic-ischemic brain injury: a review," *NeuroRehabilitation*, vol. 26, no. 1, pp. 47–63, 2010.

[10] A. Peskine, C. Rosso, C. Picq, E. Caron, and P. Pradat-Diehl, "Neurological sequelae after cerebral anoxia," *Brain Injury*, vol. 24, no. 5, pp. 755–761, 2010.

[11] P. Wang, Y. F. Guan, H. Du, Q. W. Zhai, D. F. Su, and C. Y. Miao, "Induction of autophagy contributes to the neuroprotection of nicotinamide phosphoribosyltransferase in cerebral ischemia," *Autophagy*, vol. 8, no. 1, pp. 77–87, 2012.

[12] B. Wu, H. Luo, X. Zhou et al., "Succinate-induced neuronal mitochondrial fission and hexokinase II malfunction in ischemic stroke: therapeutic effects of kaempferol," *Biochimica et Biophysica Acta (BBA) - Molecular Basis of Disease*, vol. 1863, no. 9, pp. 2307–2318, 2017.

[13] B. Lv, F. Li, J. Han et al., "Hif-1α overexpression improves transplanted bone mesenchymal stem cells survival in rat MCAO stroke model," *Frontiers in Molecular Neuroscience*, vol. 10, p. 80, 2017.

[14] P. Wang, T. Y. Xu, K. Wei et al., "ARRB1/β-arrestin-1 mediates neuroprotection through coordination of BECN1-dependent autophagy in cerebral ischemia," *Autophagy*, vol. 10, no. 9, pp. 1535–1548, 2014.

[15] X. Cheng, D. Shen, M. Samie, and H. Xu, "Mucolipins: intracellular TRPML1-3 channels," *FEBS Letters*, vol. 584, no. 10, pp. 2013–2021, 2010.

[16] X. Li, A. G. Garrity, and H. Xu, "Regulation of membrane trafficking by signalling on endosomal and lysosomal membranes," *Journal of Physiology*, vol. 591, no. 18, pp. 4389–4401, 2013.

[17] X. Zhang, X. Cheng, L. Yu et al., "MCOLN1 is a ROS sensor in lysosomes that regulates autophagy," *Nature Communications*, vol. 7, p. 12109, 2016.

[18] R. J. Li, J. Xu, C. Fu et al., "Regulation of mTORC1 by lysosomal calcium and calmodulin," *Elife*, vol. 5, 2016.

[19] K. Venkatachalam, A. A. Long, R. Elsaesser, D. Nikolaeva, K. Broadie, and C. Montell, "Motor deficit in a Drosophila model of mucolipidosis type IV due to defective clearance of apoptotic cells," *Cell*, vol. 135, no. 5, pp. 838–851, 2008.

[20] C. Curcio-Morelli, F. A. Charles, M. C. Micsenyi et al., "Macroautophagy is defective in mucolipin-1-deficient mouse neurons," *Neurobiology of Disease*, vol. 40, no. 2, pp. 370–377, 2010.

[21] M. Li, W. K. Zhang, N. M. Benvin et al., "Structural basis of dual Ca2+/pH regulation of the endolysosomal TRPML1 channel," *Nature Structural & Molecular Biology*, vol. 24, no. 3, pp. 205–213, 2017.

[22] X. Zhang, L. Yu, and H. Xu, "Lysosome calcium in ROS regulation of autophagy," *Autophagy*, vol. 12, no. 10, pp. 1954-1955, 2016.

[23] S. R. Lee, K. Tsuji, S. R. Lee, and E. H. Lo, "Role of matrix metalloproteinases in delayed neuronal damage after transient global cerebral ischemia," *Journal of Neuroscience*, vol. 24, no. 3, pp. 671–678, 2004.

[24] P. Li, Y. Gan, B. L. Sun et al., "Adoptive regulatory T-cell therapy protects against cerebral ischemia," *Annals of Neurology*, vol. 74, no. 3, pp. 458–471, 2013.

[25] D. E. Goll, V. F. Thompson, H. Li, W. Wei, and J. Cong, "The calpain system," *Physiological Reviews*, vol. 83, no. 3, pp. 731–801, 2003.

[26] Y. Ono, T. C. Saido, and H. Sorimachi, "Calpain research for drug discovery: challenges and potential," *Nature Reviews Drug Discovery*, vol. 15, no. 12, pp. 854–876, 2016.

[27] X. M. Sun, M. Butterworth, M. Macfarlane, W. Dubiel, A. Ciechanover, and G. M. Cohen, "Caspase activation inhibits proteasome function during apoptosis," *Molecular Cell*, vol. 14, no. 1, pp. 81–93, 2004.

[28] I. Dikic, "Proteasomal and autophagic degradation systems," *Annual Review of Biochemistry*, vol. 86, no. 1, pp. 193–224, 2017.

[29] M. V. Caldeira, I. L. Salazar, M. Curcio, L. M. T. Canzoniero, and C. B. Duarte, "Role of the ubiquitin-proteasome system in brain ischemia: friend or foe?," *Progress in Neurobiology*, vol. 112, no. 1, pp. 50–69, 2014.

[30] L. Tong, Z. Wu, M. Ran et al., "The role of SUMO-conjugating enzyme Ubc9 in the neuroprotection of isoflurane preconditioning against ischemic neuronal injury," *Molecular Neurobiology*, vol. 51, no. 3, pp. 1221–1231, 2015.

[31] M. Ahmad and S. H. Graham, "Inflammation after stroke: mechanisms and therapeutic approaches," *Translational Stroke Research*, vol. 1, no. 2, pp. 74–84, 2010.

[32] X. Chen, X. Zhang, Y. Wang et al., "Inhibition of immunoproteasome reduces infarction volume and attenuates inflammatory reaction in a rat model of ischemic stroke," *Cell death & disease*, vol. 6, no. 1, article e1626, 2015.

[33] J. Zhan, W. Qin, Y. Zhang et al., "Upregulation of neuronal zinc finger protein A20 expression is required for electroacupuncture to attenuate the cerebral inflammatory injury mediated by the nuclear factor-kB signaling pathway in cerebral ischemia/reperfusion rats," *Journal of Neuroinflammation*, vol. 13, no. 1, p. 258, 2016.

[34] G. Q. He, W. M. Xu, J. F. Li et al., "Huwe1 interacts with Gadd45b under oxygen-glucose deprivation and reperfusion injury in primary rat cortical neuronal cells," *Molecular Brain*, vol. 8, no. 1, p. 88, 2015.

[35] T. Li, J. J. Qin, X. Yang et al., "The ubiquitin E3 ligase TRAF6 exacerbates ischemic stroke by ubiquitinating and activating Rac1," *The Journal of Neuroscience : the Official Journal of the Society for Neuroscience*, vol. 37, no. 50, pp. 12123–12140, 2017.

[36] X. Zhang, Y. Yuan, L. Jiang et al., "Endoplasmic reticulum stress induced by tunicamycin and thapsigargin protects against transient ischemic brain injury: involvement of PARK2-dependent mitophagy," *Autophagy*, vol. 10, no. 10, pp. 1801–1813, 2014.

[37] T. Mengesdorf, P. H. Jensen, G. Mies, C. Aufenberg, and W. Paschen, "Down-regulation of parkin protein in transient focal cerebral ischemia: a link between stroke and degenerative disease?," *Proceedings of the National Academy of Sciences of the United States of America*, vol. 99, no. 23, pp. 15042–15047, 2002.

[38] C. Li, J. J. Feng, Y. P. Wu, and G. Y. Zhang, "Cerebral ischemia-reperfusion induces GAPDH S-nitrosylation and nuclear translocation," *Biochemistry*, vol. 77, no. 6, pp. 671–678, 2012.

[39] S. Galbán and C. S. Duckett, "XIAP as a ubiquitin ligase in cellular signaling," *Cell Death & Differentiation*, vol. 17, no. 1, pp. 54–60, 2010.

[40] D. Zhang, N. Zhao, B. Ma et al., "Procaspase-9 induces its cleavage by transnitrosylating XIAP via the thioredoxin system during cerebral ischemia-reperfusion in rats," *Scientific Reports*, vol. 6, no. 1, article 24203, 2016.

[41] X.-p. Dong, D. Shen, X. Wang et al., "PI(3,5)P$_2$ controls membrane trafficking by direct activation of mucolipin Ca^{2+} release channels in the endolysosome," *Nature Communications*, vol. 1, no. 4, pp. 1–11, 2010.

[42] X. Feng, J. Xiong, Y. Lu, X. Xia, and M. X. Zhu, "Differential mechanisms of action of the mucolipin synthetic agonist, ML-SA1, on insect TRPML and mammalian TRPML1," *Cell Calcium*, vol. 56, no. 6, pp. 446–456, 2014.

Review Article

The Dual Role of Inducible Nitric Oxide Synthase in Myocardial Ischemia/Reperfusion Injury: Friend or Foe?

Xin Yu,[1] **Liang Ge,**[2] **Liang Niu,**[3] **Xin Lian,**[4] **Haichun Ma** (ID),[2] **and Lei Pang** (ID)[2]

[1]*Department of Hand Surgery, The First Hospital of Jilin University, Jilin, China*
[2]*Department of Anesthesiology, The First Hospital of Jilin University, Jilin, China*
[3]*Department of Operating Room, The First Hospital of Jilin University, Jilin, China*
[4]*Department of Urology, The First Hospital of Jilin University, Jilin, China*

Correspondence should be addressed to Lei Pang; polly_sd@sina.com

Nitric oxide synthases (NOSs) are a family of enzymes that are responsible for the synthesis of nitric oxide (NO) from the amino acid L-arginine in the body. Among the three key NOSs, the expression of inducible NOS (iNOS) can only be induced by inflammatory stimuli and contribute to the large amount of NO production. iNOS-derived NO plays an important role in various physiological and pathophysiological conditions, including the ischemic heart disease. Nowadays, the development of specific iNOS inhibitors and the availability of iNOS knockout mice have provided substantial evidence to support the role of iNOS/NO signaling in the myocardium. Nevertheless, the role of iNOS/NO signaling in the myocardial ischemic reperfusion injury is very complex and highly perplexing; both detrimental and beneficial effects of iNOS have been described. Thus, this review will aim at providing basic insights into the current progress of the role of iNOS in myocardial ischemia reperfusion injury. A better understanding of the dual role of iNOS in details may help facilitate the development of more effective therapies for the management of ischemic heart diseases.

1. Introduction

Myocardial ischemic heart disease has been recognized as one of the main causes of death in the elderly in the industrialized world [1, 2]. It is characterized by insufficient blood supply to regions of the myocardium, which results in myocardial infarction, and further develops other disease states, such as hypertension, atherosclerosis, hyperlipidemia, diabetes, and heart failure. Timely reperfusion is one highly efficient treatment of this condition with mortality rate approximately half of hospitalized patients [3]. This procedure allows the rapid return of blood flow to the ischemic zone of the myocardium. However, reperfusion itself may lead to a consequence of tissue damage and pathological remodeling such as diminished cardiac contractile function, metabolic dysfunction, impairment of endothelial function, necrosis, and apoptosis [3]. All above complications further aggravate the degree of myocardial ischemia and eventually results in ischemia reperfusion injury [3, 4].

Nitric oxide (NO) is recognized as an important intracellular and intercellular biological active molecule that acts diverse physiological and pathophysiological functions in the body, including cardiac contractility and regulation of vasodilation [5]. However, the role of NO in myocardial damage and dysfunction during ischemia reperfusion remains controversial. The induction of inducible nitric oxide synthase (iNOS) produces excessive NO accompanied by increased production of reactive oxygen species (ROS), including peroxynitrite (OONO−) and superoxide, which are detrimental to the heart [6]. The expression of iNOS was also proved to correlate positively with the severity of cardiac dysfunction and expression of proinflammatory cytokines [7]. Nevertheless, endogenous NO production by NOSs may play a pivotal role for initiating and mediating the delayed role of ischemic preconditioning protection [8]. Clinical pretreatment with drugs, such as statins, certain calcium antagonists, angiotensin-converting enzyme (ACE) inhibitors, or dexamethasone, has been additionally reported

to increase the release of NO and protect the myocardium against ischemia reperfusion injury [9]. Administration of NO or NO donors prior to ischemia also attenuates the consequences of myocardial ischemia reperfusion, including reduction of infarct size and endothelial dysfunction [10, 11]. Therefore, in this review, the focus will cover both damaging and protective effects of iNOS and its consequent NO production in myocardial ischemia reperfusion injury.

2. NO and NOS

NO is an inorganic free radical gas and a very small compound. Its function on vascular biology was discovered in the 1980s [12, 13]. In mammalian organism, NO is synthesized endogenously by converting L-arginine into L-citrulline. Overall oxidative reaction involves two separate mono-oxygenation steps that molecular oxygen utilizes NADPH as an electron donor and heme proteins, flavin mononucleotide (FMN), flavin adenine dinucleotide (FAD), and (6R-)5,6,7,8-tetrahydrobiopterin (BH4) as cofactors. NOSs are a family of enzymes that catalyze the production of NO from L-arginine in the body [14, 15]. There are three different isoforms of the NOS, which are referred to as neuronal NOS (nNOS or NOS I), inducible NOS (iNOS or NOS II), and endothelial NOS (eNOS or NOS III). Two enzymes, nNOS and eNOS, are also designated as constitutive NOS (cNOS) that generate and release NO mainly in resting cells, such as nerve cells and endothelial cells, thereby maintaining long-term regulation of synaptic transmission as well as the regulation of microvascular tone in vivo. In contrast to cNOS that can be activated by calcium and calmodulin (CaM) in healthy states, iNOS can only be induced by inflammatory stimuli including immunostimulatory cytokines, bacterial products, or infection in different types of cells, not in resting cells but in endothelium, monocytes, mast cells, macrophages, and smooth muscle cells [7, 15, 16].

Both nNOS and eNOS produce small amounts of NO (<100 nM) in the heart and are tightly controlled at posttranscriptional level [9, 17]. In response to myocardial ischemia, the level of cardiac nNOS is upregulated and inhibits xanthine oxidoreductase, leading to the inhibition of superoxide generation [18]. Additionally, L-type calcium current is also downregulated by nNOS overexpression, attenuating calcium overload due to the cardiac ischemic insult, thereby protecting the heart against ischemia reperfusion injury [19, 20]. The cardiac eNOS level is upregulated within minutes during ischemia, but the expression of eNOS is reduced with the prolonged cardiac ischemia [17]. Multiple lines of evidence signify the cardioprotective role of eNOS during myocardial ischemia reperfusion injury. Deficiency of eNOS in mice exhibited worse systolic and diastolic function and mortality after myocardial infarction when compared to wild type mice [21]. Moreover, cardiac-specific overexpression of eNOS in mice strongly protects against ischemia reperfusion injury via high levels of NO/cyclic guanosine monophosphate (cGMP) [22].

In contrast, iNOS produces larger amounts of NO (>1 μM) and is primarily regulated at transcriptional level [9, 17]. The human iNOS gene is located at chromosome 17, around 37 kb with a high sequence similarity with nNOS and eNOS. The gene expression of iNOS and the subsequent mRNA translation are regulated by various stimuli, especially, lipopolysaccharide (LPS, endotoxin) and endogenous proinflammatory mediators, such as tumor necrosis factor-α (TNF-α), interleukin-1β (IL-1β), and interferon-γ (IFN-γ). Other stimulator, like hypoxia, is also demonstrated to be involved in the activation of iNOS gene expression [23]. One important intracellular signal transduction pathway of the above stimuli is the activation of NF-κB signaling. In addition, the janus tyrosine kinase (JAK)–signal transducers and activators of transcription (STAT) together with the mitogen-activated protein kinases (MAPK) pathways are also involved in the contribution of iNOS gene expression. Posttranscriptional regulation of iNOS gene expression predominantly occurs via mechanisms that influence iNOS mRNA stability and regulation of catalytic activity [24].

2.1. The Detrimental Effect of iNOS/NO on Ischemia Reperfusion Injury. NO could favor a detrimental role in myocardial ischemia reperfusion injury. Patel and his colleagues utilized in situ rabbit heart and demonstrated that pretreatment with an inhibitor of NO synthesis, L-NAME, significantly reduced infarct size following sustained coronary artery occlusion and reperfusion [25]. Mori's group later demonstrated that in dogs, NO production was enhanced in myocardial stunning and further aggravated cardiac damages through increased oxidative stress and the cytotoxicity. Such finding is the first time to report the detrimental role of NO in myocardial stunning in vivo [26]. During the reperfusion process, injury may occur in later stages associated with induction and activation of proinflammatory mediators, such as cytokines and iNOS [27, 28]. During the late phase of ischemia and reperfusion, high-output inducible iNOS/NO pathway was activated, which further aggravated left ventricular dysfunction and extent of myocardial infarct size. Whereas, continuous administration of aminoguanidine, a selective inhibitor of iNOS, can largely reduce infarct size and reverse myocardial injury [29]. Interestingly, during ischemia, overproduction of NO by upregulated iNOS for prolonged periods of time was suggested to act as a negative inotrope due to cardiac cGMP production [9, 30]. Increased iNOS activity also parallels the increment of intracellular cGMP through its subsequent production of NO. Of note, NO can prevent calcium (Ca^{2+}) influx through cGMP-dependent inhibition of Ca^{2+} channels, which depresses myofilament sensitivity to Ca^{2+} and subsequently attenuates cardiac contractile function [31, 32]. Thus, enhanced cGMP level due to activated iNOS/NO signaling could be one of the underlying mechanisms that result in further myocardial injury during ischemia reperfusion (Figure 1).

Besides the cGMP-dependent inhibition of Ca^{2+} channels, high levels of NO have also been proved to induce necrosis and apoptosis in cardiomyocytes after ischemia [33]. Under chronic isoproterenol stimulation, enhanced amount of NO induced by upregulated iNOS contributed to the formation of peroxynitrite, one byproduct of NO degradation, in the circulation system and heart, which subsequently leads to significantly severe myocardial apoptosis

Myocardial ischemia

iNOS/NO ↑

↑cGMP   Peroxynitrite ↑

Prevent Ca²⁺ influx   Enhanced oxidative stress   Pro-inflammatory responses
Attenuate cardiac function   Increased apoptosis

Ischemic myocardial injury
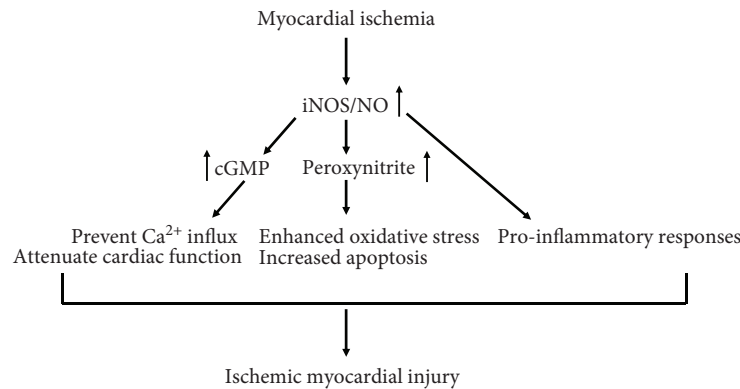
FIGURE 1: The detrimental effect of iNOS/NO on ischemia reperfusion injury. In response to myocardial ischemia, the upregulated iNOS-derived NO enhanced the level of intracellular cGMP, resulting in a decrease in Ca^{2+} influx, which depresses myofilament sensitivity to Ca^{2+} and subsequently attenuates cardiac contractile function. High levels of iNOS-derived NO also contribute to the formation of peroxynitrite, which subsequently leads to significantly increased oxidative stress and severe myocardial apoptosis. Together with iNOS/NO-mediated proinflammatory responses, these multiple actions of iNOS/NO exacerbate myocardial ischemia reperfusion injury.

and eventually leads to an enlarged myocardial infarction size [34]. The formation of peroxynitrite induced by high levels of NO has been early demonstrated to be one of the important causes in myocardial damage [35]. The expression of iNOS stimulated elevations of NO and peroxynitrite formation in the myocardium of left ventricular and resulted in decrease myocardial function and less of survival, while iNOS knockout mice showed better myocardial contractility and higher survival rate when compared to wild type mice [35]. Zhu et al. reported that autophagy is additionally involved in the modulation of cell migration, and apoptosis in ischemia reperfusion mediated upregulation of iNOS [36]. Results suggested that ischemia reperfusion-induced iNOS-mediated nitrative stress increased the migration and apoptosis of human umbilical vein endothelial cells and further was associated with elevated autophagy, while the iNOS-specific inhibitor L-NAME attenuated cell apoptosis and migration induced by ischemia reperfusion [36]. Most recently, Jeddi et al. further showed evidence that the toxic effects of iNOS-derived NO during ischemia were due to increased peroxynitrite formation associated with enhanced apoptosis marker Bax/Bcl2 expression ratio in the cardiomyocytes, which results in myocardial injury [37]. Thus, enhanced peroxynitrite formation due to activated iNOS/NO signaling could contribute to the severe NO-induced myocardial apoptosis during ischemia reperfusion (Figure 1).

Moreover, iNOS/NO signaling also plays a role in the modulation of the inflammatory responses caused by ischemia reperfusion [38]. Accumulating evidence indicated that the inflammatory response induces the release of inflammatory cytokines/chemokines which can recruit inflammatory cells like neutrophils and macrophages to migrate into the ischemic myocardium and produce more proinflammatory cytokines and chemokines, including TNF-α, IL-6, and MCP-1, which further exacerbate myocardial ischemia reperfusion injury [39]. Indeed, large amount of proinflammatory cytokines, such as IL-6 and TNF-α, are induced by stimulated iNOS after ischemia reperfusion, which lead to

the heart tissue damage and extent ischemic myocardial injury and apoptosis [32, 40, 41] (Figure 1).

2.2. The Beneficial Effect of iNOS/NO on Ischemia Reperfusion Injury. In the past decade, a number of studies have focused on the function of NO in myocardial ischemia and its role in modulating the severity of ischemia reperfusion injury in nonpreconditioned myocardium and proposed that iNOS/NO is harmful and aggravates myocardial ischemia reperfusion injury. However, overwhelming evidences have illustrated that NO overexpression by iNOS may actually have a protective role in mediating the antistunning and anti-infarct actions of ischemia-induced late preconditioning [42, 43].

Ischemic preconditioning is a well-described adaptive response of the heart that can protect against ischemia reperfusion injury through enhancing the ability to withstand a subsequent ischemic injury through a brief exposure to ischemic [44]. Study demonstrated that ischemic preconditioning upregulated iNOS expression in cardiomyocytes [45], and in conscious rabbits, the beneficial effects of late preconditioning against myocardial infarction were abrogated by the NOS inhibitor (N^w-nitro-L-arginine) and iNOS inhibitors (aminoguanidine and S-methylisothiourea) [10, 46], suggesting that iNOS is an essential mediator of such cardioprotective responses. Moreover, late preconditioning can also be induced by NO donors, adenosine A (1) receptor agonists stimulation *via* an iNOS-dependent pathway in the isolated working heart from mice [47]. The lacking of protective effect of adenosine A (1) receptor activation in iNOS knockout mice additionally suggested a direct cause-and-effect relationship of iNOS in adenosine-induced late cardioprotection [8].

Whereas the mechanism whereby iNOS/NO during ischemic preconditioning protects the myocardium against ischemia reperfusion injury remains unclear, many hypotheses have been put forth. The opening of mitochondrial ATP-sensitive K$^+$ (mitoKATP) channels has been demonstrated to play a significant role in delayed ischemic preconditioning

Ischemic preconditioning

↓

HIF-1α

↓

iNOS/NO

mitoKATP channel   TNF-α COX-2 dependent prostanoids

↓

Myocardial protection
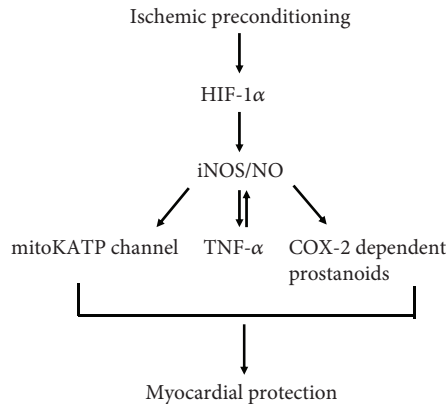
FIGURE 2: The beneficial effect of iNOS/NO on ischemia reperfusion injury. Enhanced iNOS-derived NO may be produced through HIF-1α signaling during ischemic preconditioning, resulting in the opening of mitoKATP channels and increased level of TNF-α and COX-2-dependent prostanoids, thereby mediating myocardial protection.

(protection appears 24 h later) [48]. The usage of the mito-KATP channel opener diazoxide in mouse heart significantly activated iNOS and eNOS proteins through Akt/PI3 kinase signaling, which contributes the improvement of cardiac function and reduced apoptosis after ischemia reperfusion, and diazoxide was totally ineffective in iNOS knockout mice, suggesting that mitoKATP channel is an end effector of cardioprotection during delayed ischemic preconditioning [48, 49] (Figure 2). Furthermore, in wild type mice, ischemic preconditioning reduced myocardial infarction size, while in TNF-α knockout mice, such protective effects were abrogated [50, 51]. Similar results were also observed in TNF-α receptor knockout mice that the delayed cardioprotection against myocardial ischemia disappeared [52, 53]. TNF-α administration can also mimic the ischemic preconditioning and reduce infarction size, although the protective effects of TNF-α may only occur with low doses, but not higher doses [54]. Interestingly, iNOS and TNF-α have been demonstrated to be mutually regulated. NOS inhibition completely abolished the increased myocardial TNF-α levels secondary to coronary microembolization in a dog [55]. Exogenous TNF-α can enhance iNOS expression and subsequently lead to NO production in macrophage [56], and in transgenic mice with cardiac-specific overexpression of TNF-α, researchers demonstrated that the expression of iNOS as well as its activity was increased when compared to the control group [57]. Since myocardial ischemic reperfusion induced the increment of iNOS expression and subsequently stimulated TNF-α production, it is thus likely that iNOS/TNF-α signaling mediates cardioprotection against ischemic/reperfusion injury (Figure 2). However, further studies are still necessary to clarify this mechanism.

In addition, cyclooxygenase 2 (COX-2) has also been proved to be a mediator of iNOS-mediated cardioprotection during ischemic preconditioning [58]. COX-2 acts as a major player in inflammatory reactions and has been demonstrated to be highly expressed in the cardiac tissue during myocardial ischemia [59, 60]. Indeed, COX-2 and COX-2-dependent

synthesis of prostanoids can mediate delayed preconditioning and play a role in cardioprotection [58]. In morphine-induced delayed cardioprotection model, the infarct-sparing effect after morphine administration was completely abolished by N-398 (COX-2-specific inhibitor). Furthermore, knockout of iNOS gene or administration of iNOS selective inhibitor (1400W) did not attenuate the increased expression of COX-2 protein after morphine pretreatment but completely abolished the upregulation of myocardial PGE$_2$ and 6-keto PGF1α, indicating that iNOS is essential for the enzymatic activity of newly synthesized COX-2 following morphine pretreatment [58]. Taken together, these findings suggested that COX-2 may be located downstream of iNOS signaling in the protective pathway of delayed cardioprotection induced by morphine [58] (Figure 2).

During myocardial ischemia, the enhanced iNOS expression could be a consequence of activation of Hypoxia-inducible factor 1α (HIF-1α) signaling. HIF-1α is an important regulator in myocardial ischemia reperfusion injury in healthy hearts and can augment the purine signaling to facilitate myocardial protection [61]. Natarajan and colleagues showed the evidence that preserved HIF-1 can attenuate cardiac ischemia reperfusion injury through an iNOS-dependent preconditioning effect. Results demonstrated that increasing transcriptional activity of HIF-1α under normoxic conditions potently preconditions hearts against ischemic stress, although HIF-1α was active in hypoxic/ischemic states [62]. In addition, increasing HIF-1α transcriptional activity and iNOS mRNA expression by inhibition of HIF-1α-prolyl-4 hydroxylase-2 (PHD2) gene expression significantly reduced myocardial infarction size in mice with ischemia reperfusion, suggesting that the activation of HIF-1α in hearts by PHD2 siRNA administration attenuated reperfusion injury through an iNOS-dependent pathway [62]. Thus, enhanced cardiac iNOS may be produced through HIF-1α pathway during ischemic preconditioning (Figure 2).

3. Conclusion

Activation of iNOS/NO signaling exerts both protective and detrimental effects during myocardial ischemia reperfusion injury. The apparent controversy is possibly due to the critical balance between NO and peroxynitrite (one byproduct of NO degradation due to decreased NO bioavailability). In particular, iNOS-derived NO plays a cardioprotective role *via* its antioxidant and vasodilator effects in normal physiological conditions. However, in response to myocardial ischemia, enhanced iNOS/NO production led to the formation of peroxynitrite and its associated oxidative stress, which mediated the detrimental effects of iNOS/NO, whereas ischemic preconditioning markedly enhances the ability of the heart to withstand a subsequent ischemic injury and is closely associated with the upregulation of antioxidant defense system, which eliminates the increased oxidative stress [63]. In particular, the ischemic preconditioning suppresses the subsequent overproduction of peroxynitrite and protects the heart. Thus, the enhanced iNOS expression in conjunction with the elimination of oxidative stress switches iNOS

from detrimental to protective NOS. In the future, with regard to the dual role of iNOS in myocardial ischemia reperfusion injury, a better understanding of iNOS/NO signaling is needed on how enhanced iNOS protects against ischemic heart disease without triggering unwanted side effects, with the aim to promote the development of more effective therapeutic approaches to treat ischemic heart diseases.

Conflicts of Interest

Authors declare no conflict of interest.

Acknowledgments

References

[1] A. Yazdanyar and A. B. Newman, "The burden of cardiovascular disease in the elderly: morbidity, mortality, and costs," *Clinics in Geriatric Medicine*, vol. 25, no. 4, pp. 563–577, 2009.

[2] A. J. Boyle, J. Hwang, J. Ye et al., "The effects of aging on apoptosis following myocardial infarction," *Cardiovascular Therapeutics*, vol. 31, no. 6, pp. e102–e110, 2013.

[3] P. Ferdinandy, R. Schulz, and G. F. Baxter, "Interaction of cardiovascular risk factors with myocardial ischemia/reperfusion injury, preconditioning, and postconditioning," *Pharmacological Reviews*, vol. 59, no. 4, pp. 418–458, 2007.

[4] P. Ferdinandy and R. Schulz, "Nitric oxide, superoxide, and peroxynitrite in myocardial ischaemia-reperfusion injury and preconditioning," *British Journal of Pharmacology*, vol. 138, no. 4, pp. 532–543, 2003.

[5] P. M. Vanhoutte, "Nitric oxide: from good to bad," *Annals of Vascular Diseases*, vol. 11, no. 1, pp. 41–51, 2018.

[6] K. Zhao, Z. Huang, H. Lu, J. Zhou, and T. Wei, "Induction of inducible nitric oxide synthase increases the production of reactive oxygen species in RAW264. 7 macrophages," *Bioscience Reports*, vol. 30, no. 4, pp. 233–241, 2010.

[7] F. Aktan, "iNOS-mediated nitric oxide production and its regulation," *Life Sciences*, vol. 75, no. 6, pp. 639–653, 2004.

[8] T. Zhao, L. Xi, J. Chelliah, J. E. Levasseur, and R. C. Kukreja, "Inducible nitric oxide synthase mediates delayed myocardial protection induced by activation of adenosine A_1 receptors: evidence from gene-knockout mice," *Circulation*, vol. 102, no. 8, pp. 902–907, 2000.

[9] R. Schulz, M. Kelm, and G. Heusch, "Nitric oxide in myocardial ischemia/reperfusion injury," *Cardiovascular Research*, vol. 61, no. 3, pp. 402–413, 2004.

[10] R. Bolli, S. Manchikalapudi, X. L. Tang et al., "The protective effect of late preconditioning against myocardial stunning in conscious rabbits is mediated by nitric oxide synthase: evidence that nitric oxide acts both as a trigger and as a mediator of the late phase of ischemic preconditioning," *Circulation Research*, vol. 81, no. 6, pp. 1094–1107, 1997.

[11] S. Kanno, P. C. Lee, Y. Zhang et al., "Attenuation of myocardial ischemia/reperfusion injury by superinduction of inducible nitric oxide synthase," *Circulation*, vol. 101, no. 23, pp. 2742–2748, 2000.

[12] R. F. Furchgott and J. V. Zawadzki, "The obligatory role of endothelial cells in the relaxation of arterial smooth muscle by acetylcholine," *Nature*, vol. 288, no. 5789, pp. 373–376, 1980.

[13] R. G. Knowles and S. Moncada, "Nitric oxide synthases in mammals," *Biochemical Journal*, vol. 298, no. 2, pp. 249–258, 1994.

[14] C. Nathan and Q.-W. Xie, "Nitric oxide synthases: roles, tolls, and controls," *Cell*, vol. 78, no. 6, pp. 915–918, 1994.

[15] U. Förstermann and W. C. Sessa, "Nitric oxide synthases: regulation and function," *European Heart Journal*, vol. 33, no. 7, pp. 829–837, 2012.

[16] Z. Xia and P. M. Vanhoutte, "Nitric oxide and protection against cardiac ischemia," *Current Pharmaceutical Design*, vol. 17, no. 18, pp. 1774–1782, 2011.

[17] V. W. Liu and P. L. Huang, "Cardiovascular roles of nitric oxide: A review of insights from nitric oxide synthase gene disrupted mice," *Cardiovascular Research*, vol. 77, no. 1, pp. 19–29, 2008.

[18] T. Damy, P. Ratajczak, E. Robidel et al., "Up-regulation of cardiac nitric oxide synthase 1-derived nitric oxide after myocardial infarction in senescent rats," *The FASEB Journal*, vol. 17, no. 13, pp. 1934–1936, 2003.

[19] N. Burkard, A. G. Rokita, S. G. Kaufmann et al., "Conditional neuronal nitric oxide synthase overexpression impairs myocardial contractility," *Circulation Research*, vol. 100, no. 3, pp. e32–e44, 2007.

[20] D. E. Burger, X. Lu, M. Lei et al., "Neuronal nitric oxide synthase protects against myocardial infarction-induced ventricular arrhythmia and mortality in mice," *Circulation*, vol. 120, no. 14, pp. 1345–1354, 2009.

[21] M. Scherrer-Crosbie, R. Ullrich, K. D. Bloch et al., "Endothelial nitric oxide synthase limits left ventricular remodeling after myocardial infarction in mice," *Circulation*, vol. 104, no. 11, pp. 1286–1291, 2001.

[22] F. Brunner, R. Maier, P. Andrew, G. Wölkart, R. Zechner, and B. Mayer, "Attenuation of myocardial ischemia/reperfusion injury in mice with myocyte-specific overexpression of endothelial nitric oxide synthase," *Cardiovascular Research*, vol. 57, no. 1, pp. 55–62, 2003.

[23] C. R. Ferreiro, A. C. P. Chagas, M. H. C. Carvalho et al., "Influence of hypoxia on nitric oxide synthase activity and gene expression in children with congenital heart disease: a novel pathophysiological adaptive mechanism," *Circulation*, vol. 103, no. 18, pp. 2272–2276, 2001.

[24] P. Lirk, G. Hoffmann, and J. Rieder, "Inducible nitric oxide synthase-time for reappraisal," *Current Drug Targets-Inflammation & Allergy*, vol. 1, no. 1, pp. 89–108, 2002.

[25] V. C. Patel, D. M. Yellon, K. J. Singh, G. H. Neild, and R. G. Woolfson, "Inhibition of nitric oxide limits infarct size in the in situ rabbit heart," *Biochemical and Biophysical Research Communications*, vol. 194, no. 1, pp. 234–238, 1993.

[26] E. Mori, N. Haramaki, H. Ikeda, and T. Imaizumi, "Intracoronary administration of L-arginine aggravates myocardial stunning through production of peroxynitrite in dogs," *Cardiovascular Research*, vol. 40, no. 1, pp. 113–123, 1998.

[27] M. S. Finkel, C. V. Oddis, T. D. Jacob, S. C. Watkins, B. G. Hattler, and R. L. Simmons, "Negative inotropic effects of cytokines on the heart mediated by nitric oxide," *Science*, vol. 257, no. 5068, pp. 387–389, 1992.

[28] R. Schulz, D. L. Panas, R. Catena, S. Moncada, P. M. Olley, and G. D. Lopaschuk, "The role of nitric oxide in cardiac depression induced by interleukin-1β and tumour necrosis factor-α," *British Journal of Pharmacology*, vol. 114, no. 1, pp. 27–34, 1995.

[29] S. M. Wildhirt, S. Weismueller, C. Schulze, N. Conrad, A. Kornberg, and B. Reichart, "Inducible nitric oxide synthase activation after ischemia/reperfusion contributes to myocardial dysfunction and extent of infarct size in rabbits: evidence for a late phase of nitric oxide-mediated reperfusion injury," *Cardiovascular Research*, vol. 43, no. 3, pp. 698–711, 1999.

[30] R. A. Kelly, J.-L. Balligand, and T. W. Smith, "Nitric oxide and cardiac function," *Circulation Research*, vol. 79, no. 3, pp. 363–380, 1996.

[31] S. M. Wildhirt, H. Suzuki, D. Horstman et al., "Selective modulation of inducible nitric oxide synthase isozyme in myocardial infarction," *Circulation*, vol. 96, no. 5, pp. 1616–1623, 1997.

[32] H. K. Saini, Y.-J. Xu, M. Zhang, P. P. Liu, L. A. Kirshenbaum, and N. S. Dhalla, "Role of tumour necrosis factor-alpha and other cytokines in ischemia-reperfusion-induced injury in the heart," *Experimental & Clinical Cardiology*, vol. 10, no. 4, pp. 213–222, 2005.

[33] B. Hofstaetter, G. Taimor, J. Inserte, D. Garcia-Dorado, and H. M. Piper, "Inhibition of apoptotic responses after ischemic stress in isolated hearts and cardiomyocytes," *Basic Research in Cardiology*, vol. 97, no. 6, pp. 479–488, 2002.

[34] A. Hu, X. Jiao, E. Gao et al., "Chronic β-adrenergic receptor stimulation induces cardiac apoptosis and aggravates myocardial ischemia/reperfusion injury by provoking inducible nitric-oxide synthase-mediated nitrative stress," *Journal of Pharmacology and Experimental Therapeutics*, vol. 318, no. 2, pp. 469–475, 2006.

[35] Q. Feng, X. Lu, D. L. Jones, J. Shen, and J. M. O. Arnold, "Increased inducible nitric oxide synthase expression contributes to myocardial dysfunction and higher mortality after myocardial infarction in mice," *Circulation*, vol. 104, no. 6, pp. 700–704, 2001.

[36] T. Zhu, Q. Yao, W. Wang, H. Yao, and J. Chao, "iNOS induces vascular endothelial cell migration and apoptosis via autophagy in ischemia/reperfusion injury," *Cellular Physiology and Biochemistry*, vol. 38, no. 4, pp. 1575–1588, 2016.

[37] S. Jeddi, A. Ghasemi, A. Asgari, and A. Nezami-Asl, "Role of inducible nitric oxide synthase in myocardial ischemia-reperfusion injury in sleep-deprived rats," *Sleep and Breathing*, vol. 22, no. 2, pp. 353–359, 2018.

[38] S. Cuzzocrea, P. K. Chatterjee, E. Mazzon et al., "Role of induced nitric oxide in the initiation of the inflammatory response after postischemic injury," *Shock*, vol. 18, no. 2, pp. 169–176, 2002.

[39] B. R. Slegtenhorst, F. J. M. F. Dor, H. Rodriguez, F. J. Voskuil, and S. G. Tullius, "Ischemia/reperfusion injury and its consequences on immunity and inflammation," *Current Transplantation Reports*, vol. 1, no. 3, pp. 147–154, 2014.

[40] P.-A. Bécherel, O. Chosidow, L. le Goff et al., "Inducible nitric oxide synthase and proinflammatory cytokine expression by human keratinocytes during acute urticaria," *Molecular Medicine*, vol. 3, no. 10, pp. 686–694, 1997.

[41] P. Kleinbongard, R. Schulz, and G. Heusch, "TNFα in myocardial ischemia/reperfusion, remodeling and heart failure," *Heart Failure Reviews*, vol. 16, no. 1, pp. 49–69, 2011.

[42] R. Bolli, "Cardioprotective function of inducible nitric oxide synthase and role of nitric oxide in myocardial ischemia and preconditioning: an overview of a decade of research," *Journal of Molecular and Cellular Cardiology*, vol. 33, no. 11, pp. 1897–1918, 2001.

[43] L. Xi, N. C. Jarrett, M. L. Hess, and R. C. Kukreja, "Essential role of inducible nitric oxide synthase in monophosphoryl lipid A–induced late cardioprotection: evidence from pharmacological inhibition and gene knockout mice," *Circulation*, vol. 99, no. 16, pp. 2157–2163, 1999.

[44] X. He, M. Zhao, X.-Y. Bi, X.-J. Yu, and W.-J. Zang, "Delayed preconditioning prevents ischemia/reperfusion-induced endothelial injury in rats: role of ROS and eNOS," *Laboratory Investigation*, vol. 93, no. 2, pp. 168–180, 2013.

[45] Y. Guo, W. K. Jones, Y. T. Xuan et al., "The late phase of ischemic preconditioning is abrogated by targeted disruption of the inducible NO synthase gene," *Proceedings of the National Academy of Sciences*, vol. 96, no. 20, pp. 11507–11512, 1999.

[46] H. Takano, S. Manchikalapudi, X.-L. Tang et al., "Nitric oxide synthase is the mediator of late preconditioning against myocardial infarction in conscious rabbits," *Circulation*, vol. 98, no. 5, pp. 441–449, 1998.

[47] M. Kudo, Y. Wang, M. Xu, A. Ayub, and M. Ashraf, "Adenosine A$_1$ receptor mediates late preconditioning via activation of PKC-δ signaling pathway," *American Journal of Physiology-Heart and Circulatory Physiology*, vol. 283, no. 1, pp. H296–H301, 2002.

[48] Y. Wang, N. Ahmad, M. Kudo, and M. Ashraf, "Contribution of Akt and endothelial nitric oxide synthase to diazoxide-induced late preconditioning," *American Journal of Physiology-Heart and Circulatory Physiology*, vol. 287, no. 3, pp. H1125–H1131, 2004.

[49] Y. Wang, M. Kudo, M. Xu, A. Ayub, and M. Ashraf, "Mitochondrial K(ATP) channel as an end effector of cardioprotection during late preconditioning: triggering role of nitric oxide," *Journal of Molecular and Cellular Cardiology*, vol. 33, no. 11, pp. 2037–2046, 2001.

[50] R. M. Smith, N. Suleman, J. McCarthy, and M. N. Sack, "Classic ischemic but not pharmacologic preconditioning is abrogated following genetic ablation of the TNFα gene," *Cardiovascular Research*, vol. 55, no. 3, pp. 553–560, 2002.

[51] Y. Ichikawa, T. Miura, A. Nakano et al., "The role of ADAM protease in the tyrosine kinase-mediated trigger mechanism of ischemic preconditioning," *Cardiovascular Research*, vol. 62, no. 1, pp. 167–175, 2004.

[52] B. Dawn, Y. Guo, A. Rezazadeh et al., "Tumor necrosis factor-α does not modulate ischemia/reperfusion injury in naïve myocardium but is essential for the development of late preconditioning," *Journal of Molecular and Cellular Cardiology*, vol. 37, no. 1, pp. 51–61, 2004.

[53] M. P. Flaherty, Y. Guo, S. Tiwari et al., "The role of TNF-α receptors p55 and p75 in acute myocardial ischemia/reperfusion injury and late preconditioning," *Journal of Molecular and Cellular Cardiology*, vol. 45, no. 6, pp. 735–741, 2008.

[54] S. Lecour, R. M. Smith, B. Woodward, L. H. Opie, L. Rochette, and M. N. Sack, "Identification of a novel role for sphingolipid signaling in TNF α and ischemic preconditioning mediated cardioprotection," *Journal of Molecular and Cellular Cardiology*, vol. 34, no. 5, pp. 509–518, 2002.

[55] M. Thielmann, H. Dörge, C. Martin et al., "Myocardial dysfunction with coronary microembolization: signal transduction through a sequence of nitric oxide, tumor necrosis

factor-α, and sphingosine," *Circulation Research*, vol. 90, no. 7, pp. 807–813, 2002.

[56] D. B. Sanders, D. F. Larson, K. Hunter, M. Gorman, and Bo Yang, "Comparison of tumor necrosis factor-α effect on the expression of iNOS in macrophage and cardiac myocytes," *Perfusion*, vol. 16, no. 1, pp. 67–74, 2016.

[57] H. Funakoshi, T. Kubota, Y. Machida et al., "Involvement of inducible nitric oxide synthase in cardiac dysfunction with tumor necrosis factor-α," *American Journal of Physiology-Heart and Circulatory Physiology*, vol. 282, no. 6, pp. H2159–H2166, 2002.

[58] X. Jiang, E. Shi, Y. Nakajima, and S. Sato, "COX-2 mediates morphine-induced delayed cardioprotection via an iNOS-dependent mechanism," *Life Sciences*, vol. 78, no. 22, pp. 2543–2549, 2006.

[59] K. Schrör, K. C. Zimmermann, and R. Tannhäuser, "Augmented myocardial ischaemia by nicotine–mechanisms and their possible significance," *British Journal of Pharmacology*, vol. 125, no. 1, pp. 79–86, 1998.

[60] S. C. Y. Wong, M. Fukuchi, P. Melnyk, I. Rodger, and A. Giaid, "Induction of cyclooxygenase-2 and activation of nuclear factor-κB in myocardium of patients with congestive heart failure," *Circulation*, vol. 98, no. 2, pp. 100–103, 1998.

[61] D. Wu, R. T. Huang, R. B. Hamanaka et al., "HIF-1α is required for disturbed flow-induced metabolic reprogramming in human and porcine vascular endothelium," *eLife*, vol. 6, article e25217, 2017.

[62] R. Natarajan, F. N. Salloum, B. J. Fisher, R. C. Kukreja, and A. A. Fowler III, "Hypoxia inducible factor-1 activation by prolyl 4-hydroxylase-2 gene silencing attenuates myocardial ischemia reperfusion injury," *Circulation Research*, vol. 98, no. 1, pp. 133–140, 2006.

[63] S. Hoshida, N. Yamashita, K. Otsu, and M. Hori, "The importance of manganese superoxide dismutase in delayed preconditioning: involvement of reactive oxygen species and cytokines," *Cardiovascular Research*, vol. 55, no. 3, pp. 495–505, 2002.

Research Article

Intravenous Anesthetic Protects Hepatocyte from Reactive Oxygen Species-Induced Cellular Apoptosis during Liver Transplantation *In Vivo*

Weifeng Yao [iD],[1] **Xue Han**,[2] **Yihan Zhang** [iD],[1] **Jianqiang Guan**,[1] **Mian Ge**,[1] **Chaojin Chen**,[1] **Shan Wu**,[1] **Jiaxin Chen**,[1] **Gangjian Luo**,[1] **Pinjie Huang** [iD],[1] **and Ziqing Hei** [iD][1]

[1]*Department of Anesthesiology, Third Affiliated Hospital, Sun Yat-sen University, Guangzhou, Guangdong 510630, China*
[2]*Department of Anesthesiology, Sun Yat-sen Memorial Hospital, Sun Yat-sen University, Guangzhou 510000, China*

Correspondence should be addressed to Pinjie Huang; hpjie@126.com and Ziqing Hei; heiziqing@sina.com

Background. Liver transplantation leads to liver ischemia/reperfusion (I/R) injury, resulting in early graft dysfunction and failure. Exacerbations of oxidative stress and inflammatory response are key processes in the development of liver I/R injury. Intravenous anesthetic propofol potent effects on free radical scavenging and protects livers against I/R injury. However, the role and mechanism of propofol-mediated hepatic protection in liver transplantation is poorly understood. The aim of this study was to evaluate the role of propofol postconditioning in the liver I/R injury after liver transplantation. *Methods*. Forty-eight rats were randomly divided into six groups: rats receiving either sham operation or orthotopic autologous liver transplantation (OALT) in the absence or presence of propofol (high dose and low dose) postconditioning or intralipid control or VAS2870 (Nox2 special inhibitor). Eight hours after OALT or sham operation, parameters of organ injury, oxidative stress, inflammation, and NADPH-associated proteins were assessed. *Results*. After OALT, severe liver pathological injury was observed that was associated with increases of serum AST and ALT, which were attenuated by propofol postconditioning. In addition, especially high dose of propofol postconditioning reduced TNF-α, IL-1β, IL-6, TLR4, and NF-κB inflammatory pathway, accompanied with decrease of neutrophil elastase activity, MPO activity, 8-isoprotane, p47^{phox} and gp91^{phox} protein expressions, and increase of SOD activity. Inhibition of Nox2 by VAS2870 conferred similar protective effects in liver transplantation. *Conclusion*. Liver transplantation leads to severe inflammation and oxidative stress with NADPH oxidase activation. Propofol postconditioning reduces liver I/R injury after liver transplantation partly via inhibiting NADPH oxidase Nox2 and the subsequent inflammation and oxidative stress.

1. Introduction

Liver transplantation has become the effective surgical treatment for patients with end-stage liver disease [1]. Liver ischemia reperfusion (I/R) injury is a severe postoperative complication during the early period after transplantation. It leads to early graft dysfunction and failure, which further results in acute and chronic rejection and irreversible death [2]. Characterized by uncontrolled inflammatory response, liver I/R injury promotes hypoxic hepatocyte reoxygenation and reactive oxygen species (ROS) formation, which result in neutrophil infiltration, robust ROS generation, and ultimately programmed death of hepatocytes [3]. To date, the

mechanisms accounted for liver injury, especially I/R injury during liver transplantation, are complicated and remained unclear; strategies for preventing I/R injury are still lacking. Hence, seeking protective intervention of I/R injury during perioperative period is regarded urgent and profound scientific significance and important clinical applications.

Propofol (2,6-diisopropylphenol) is widely used for anesthesia induction and maintenance during perioperation and sedation in intensive care unit (ICU) patients [4]. In addition to its clinical usages, propofol exerts anti-inflammatory and antioxidative effectiveness basing on the chemical group phenol [5]. In our previous study, we found that propofol pretreatment could attenuate pulmonary

oxidative stress induced by liver transplantation through activating Nrf2 nuclear translocation and upregulating its downstream of HO-1 antioxidant enzyme formation [6, 7]. However, in most clinical situations, propofol pretreatment is not feasible while treatment at the onset or after induction of reperfusion, termed as postconditioning, is more applicable [8], which has been proven as a promising therapeutic strategy against ischemia/reperfusion damage. Whether propofol postconditioning is crucial in reducing oxidative stress in liver I/R injury and the underline mechanism remains unknown.

Nicotinamide adenine dinucleotide phosphate (NADPH) oxidase (Noxs) is one of the major sources of cellular ROS, which has been identified to play an important role in liver I/R injury [9]. Nox2 and Nox4 are two predominant Nox isoforms existing in hepatocytes in liver parenchyma [10]. Nox2-deficient mice showed lower mortality rate than wild type group when subjected to hepatic I/R injury. Whether Nox2 is correlated to liver transplantation-induced hepatic oxidative stress and contributed to the antioxidant property of propofol need to be verified.

Therefore, the current study observed the effects of propofol postconditioning on liver I/R injury induced by liver transplantation and further explored the potential mechanism whether the protective effects provided by propofol postconditioning are associated with Nox2-related oxidative stress pathway.

2. Materials and Methods

2.1. Experimental Protocols. Male Sprague-Dawley rats (220–250 g, 8 weeks) obtained from Medical Experimental Animal Center of Guangdong Province (Guangzhou, China) were housed in the animal room of Zhongshan Medical School (Guangzhou, China). Rats were fasted for 8 hours prior to the study but were allowed to access tap water ad libitum. All the animal care and research protocols were approved by the Institutional Animal Care and Use Committee of Sun Yat-sen University (Guangzhou, China) and performed in accordance with National Institutes of Health guidelines for the use of experimental animals.

The orthotopic autologous liver transplantation (OALT) model was carried out according to our previous study [11, 12]. Rats were randomly divided into six groups ($n = 8$) as follows: sham-operated control (sham) and OALT, OALT treated with intralipid (OALT + INT), OALT treated with high dose of propofol (OALT + HPro), OALT treated with low dose of propofol (OALT + LPro), and OALT treated with VAS2870 (OALT + VAS). High dose (40 mg/kg/h) or low dose (20 mg/kg/h) of propofol [13] or the same volume of intralipid was administrated continuous via tail vein for 30 min at the onset of reperfusion. Some of the rats were treated with specific Nox2 inhibitor VAS2870 (2 mg/kg, Sigma, USA) [14] intravenously after reperfusion.

2.2. Sample Harvest. Blood and liver samples were harvested eight hours after reperfusion. Under general anesthesia, animals were euthanized by a lethal injection of sodium pentobarbital. The blood was collected from carotid artery into heparinized tubes and then centrifuged for 15 min at 2000 g (4°C). The supernatants were collected and stored at −80°C until measurement. Median hepatic lobes were immediately and promptly taken out (about 0.5 cm^3), washed in cold saline, fixed in 10% formalin solution, dehydrated in ascending grades of alcohol, and then embedded in paraffin. The residual parts of liver tissue were harvested and stored at −80°C until further measurement.

2.3. Serum Aspartate Aminotransferase (AST) and Alanine Aminotransferase (ALT) Levels. The activity of AST and ALT in serum, indicators of liver cellular damage, was measured by a clinical chemistry analyzer system.

2.4. Histological Examination of Liver Sections. Median hepatic lobes were fixed in 4% buffered formalin. After embedding and cutting of 4 μm slices, all samples were stained with hematoxylin/eosin. The staining sections were visualized and images were acquired using a microscope with 10x and 40x objectives. Histological evaluation was performed in a blinded manner. The severity of liver injury was graded with modified Suzuki criteria [15].

2.5. Assay of Inflammatory Cytokines and Oxidative Stress Markers. Part of the liver was homogenized with a Potter liver homogenizer at 500 g and centrifuged at 800 g for 10 min. The supernatant was pipetted into a fresh Eppendorf cup for the detection of cytokines. Inflammatory cytokines including TNF-α, IL-1β, and IL-6 in the liver were quantified with commercial ELISA kits (KeyGen BioTech, China). And the neutrophil elastase and 8-isoprostane were detected using ELISA kits (Cayman Chemical). Superoxide dismutase (SOD) and myeloperoxidase (MPO) activities were measured according to our previous methods [16].

2.6. Immunohistochemical Staining of p47^{phox}. Immunohistochemical staining was performed in a previous study [16]. Liver tissue sections were deparaffinized, hydrated, and incubated at 4°C overnight with a p47^{phox} primary antibody (Cell Signaling Technology, Danvers, USA, diluted 1 : 500), followed by incubation with a horseradish peroxidase-coupled anti-rabbit IgG secondary antibody at room temperature for 2 hours and then colored with diaminobenzidine (DAB) for 3 minutes. Phosphate-buffered saline (PBS) was used to replace primary antibody in the negative control. DAB staining intensity was observed under light microscope (Leica Microsystems Digital Imaging, Cambridge, UK) and assessed with a microscopic image analysis system (ImageJ, National Institutes of Health, USA).

2.7. TUNEL for DNA Fragmentation. The nuclear DNA fragmentation, a specific biochemical hallmark of apoptosis, was labeled by TUNEL staining with a Dead End Fluorometric TUNEL system kit (Promega Corp., Madison, Wisconsin, USA) according to the manufacturer's protocol and our previous study [17]. Liver sections were incubated with proteinase K solution (20 μg/ml in PBS) at room temperature for 10 minutes after deparaffinization and hydration. TUNEL labeling was conducted with a 100 μl mix of equilibration buffer, nucleotide mix, and recombinant terminal
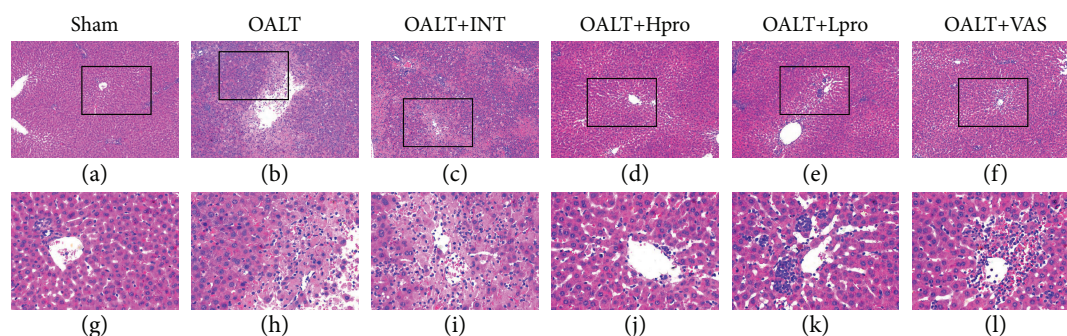
FIGURE 1: Representative photomicrographs of the livers after 8 hours of OALT. The liver tissue sections were stained with hematoxylin and eosin (H&E staining, 100x and 400x). $n = 8$ per group. $^{\#}P < 0.01$ vs. the sham group; $^{*}P < 0.05$ and $^{**}P < 0.01$ vs. the OALT group. HPro = high dose of propofol; LPro = low dose of propofol; INT = intralipid; VAS = VAS2870; OALT = orthotopic autologous liver transplantation.

deoxynucleotidyl transferase (rTdT) enzyme (the volume ratio was $45 : 5 : 1$) in a humidified, lucifugal chamber for 1 hour at 37°C, from which step to the end of experiment, the slides were protected from direct light. The reaction was terminated by immersing the slides in a $2 \times$ SSC buffer for 15 minutes at room temperature and then were rinsed with PBS. Nuclear was visualized by DAPI staining. The liver tissues were covered by an antifade solution and mounted by glass coverslips with clear nail polish sealing the edges. The slides were immediately analyzed by a fluorescence microscope and then stored at -20°C in dark if necessary.

2.8. Immunoblotting. Western blot analysis was performed in our previous studies [18]. In brief, the hepatic tissues were homogenized and nuclear proteins were extracted with a Nuclear-Cytosol Extraction kit (Applygen Technology Inc., Beijing, China) according to the manufacturer's instructions. The protein concentration had been determined by the BCA protein assay (Bio-Rad, Hemel Hempstead, Herts, UK). Sixty micrograms of each protein sample was subjected to Western blot analysis using the following primary antibodies incubated overnight at 4°C: anti-gp91$^{\text{phox}}$ at $1 : 8000$ dilution (Cell Signaling Technology Inc.), anti-p47$^{\text{phox}}$ at $1 : 1000$ dilution (Cell Signaling Technology Inc.), anti-Na/K-ATPase at $1 : 1000$ dilution (Cell Signaling Technology Inc.), anti-cleaved caspase-3 at $1 : 1000$ dilution (Cell Signaling Technology Inc.), anti-procaspase-3 at $1 : 1000$ dilution (Cell Signaling Technology Inc.), anti-nuclear factor kappa B (NF-κB) p65 at $1 : 1000$ dilution (Cell Signaling Technology Inc.), anti-Toll-like receptor 4 (TLR4) at $1 : 1000$ dilution (Santa Cruz Biotechnology Inc.), and anti-β-actin at $1 : 1500$ dilution (Merck Millipore, Germany). The secondary antibodies were goat anti-mouse or anti-rabbit IgG antibodies at $1 : 2000$ dilution (Thermo Fisher Scientific, Fremont, CA, USA). The enhanced chemiluminescence system was used to detect the protein-antibody complex (KGP1125, Nanjing KeyGEN Biotech. Co. Ltd.). The AlphaView software (Cell Biosciences, Santa Clara, CA) was used to measure the optical density of the interesting protein band signals which were correlated to the protein levels and normalized to those of β-actin.

2.9. Analysis of Data. Data were expressed as means $\pm$ SD. Statistical significance among groups was determined by one-way ANOVA followed by Newman-Keuls post hoc analysis using the GraphPad Prism 6 software (San Diego, CA, USA). Statistical significance was accepted at $P < 0.05$.

3. Results

3.1. Propofol Postconditioning Reduced Liver Injury after OALT. As shown in Figure 1, compared with the sham group, there was a massive cellular necrosis (Table 1) in the centrilobular regions of the livers at 8 hours after OALT, accompanied with severe cell ballooning and infiltration of inflammatory cell, which was assessed and scaled according to the modified Suzuki criteria ($P < 0.01$ vs. the sham group). Propofol postconditioning, especially administrated at high dose (40 mg/kg/h), significantly reduced the extent of necrosis, cell ballooning, and inflammatory cell infiltration ($P < 0.01$ vs. the OALT group or intralipid group). Similarly, the Nox2 inhibitor VAS2870 exerted the same protective effects in the livers against I/R injury following OALT, evidenced by ameliorated cell necrosis, cell ballooning, and inflammatory cell infiltration ($P < 0.05$ vs. the OALT group). Consisted with the pathological results, as shown in Figures 2(a) and 2(b), high dose of propofol dramatically attenuated AST and ALT levels compared with the OALT group or intralipid group. These results indicated that propofol postconditioning and Nox2 inhibition could both provide liver protection in the early stage of OALT.

3.2. Nox2 Inhibition Was Involved in the Protective Effects Conferred by Propofol Postconditioning. In order to test whether the antioxidative effect of propofol postconditioning was linked to Nox2, the Nox2 subunits p47$^{\text{phox}}$ on cell membrane and gp91$^{\text{phox}}$ in cytoplasm were detected. As shown in Figures 3(a)–3(d), OALT leads to upregulation of p47$^{\text{phox}}$ and gp91$^{\text{phox}}$ protein expressions, while propofol postconditioning significantly decreased these two Nox2 subunit protein expressions in the liver following OALT. Moreover, Nox2 specific inhibitor VAS2870 was used as a positive control showing dramatically inhibition of p47$^{\text{phox}}$ and gp91$^{\text{phox}}$ protein expressions after VAS2870 treatment.

TABLE 1: Histological score of liver injury by OALT.

Groups	Centrilobular cell death Grade				Average	Ballooning Grade				Average	Inflammation Grade				Average
	+3	+2	+1	0		+3	+2	+1	0		+3	+2	+1	0	
Sham	0	0	0	8 (100)	0	0	0	0	8 (100)	0	0	0	0	8 (100)	0
OALT	2 (25)	3 (38)	3 (38)	0 (0)	$1.9^{\#}$	3 (38)	3 (38)	2 (25)	0 (0)	$2.1^{\#}$	5 (63)	2 (25)	1 (13)	0 (0)	$2.5^{\#}$
OALT + INT	2 (25)	4 (50)	2 (25)	0 (0)	$2.0^{\#}$	2 (25)	4 (50)	2 (25)	0 (0)	$2.0^{\#}$	4 (50)	3 (38)	1 (13)	0 (0)	$2.4^{\#}$
OALT + HPro	0 (0)	1 (13)	6 (75)	1 (13)	1.0^{**}	0 (0)	1 (13)	7 (88)	0 (0)	1.1^{**}	0 (0)	2 (25)	5 (63)	1 (13)	1.1^{**}
OALT + LPro	0 (0)	1 (13)	7 (88)	0 (0)	1.1^{**}	0 (0)	2 (25)	6 (75)	0 (0)	1.3^{*}	0 (0)	4 (50)	4 (50)	0 (0)	1.5^{*}
OALT + VAS	0 (0)	2 (25)	6 (75)	0 (0)	1.3^{*}	0 (0)	2 (25)	5 (63)	1 (13)	1.1^{**}	0 (0)	3 (38)	4 (50)	1 (13)	1.3^{*}

Numbers of rats are shown, with percentages enclosed within parenthesis. Grade indication: no change (0), mild (1), moderate (2), and severe (3). $^{\#}P < 0.01$ vs. the sham group, $^{*}P < 0.05$ vs. the OALT group, and $^{**}P < 0.01$ vs. the OALT group.

(a)

(b)
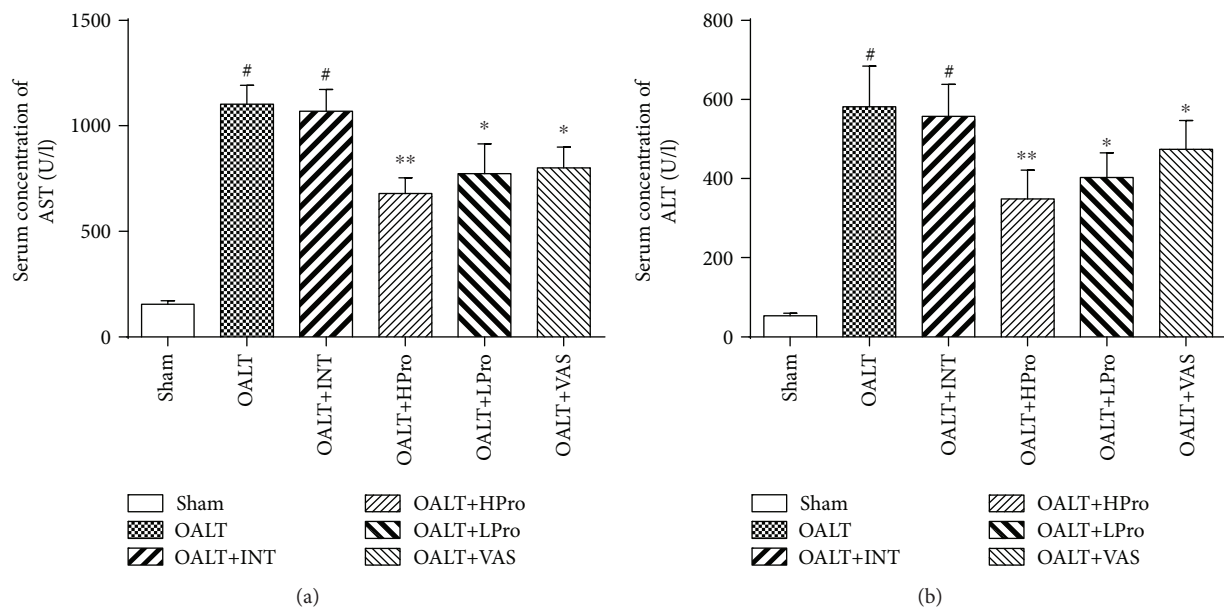
FIGURE 2: Serum alanine aminotransferase (ALT) (a) and aspartate aminotransferase (AST) (b) levels of experimental rats 8 hours after OALT. The results are expressed as the mean ± SD. $n = 8$ per group. $^{\#}P < 0.01$ vs. the sham group; $^{*}P < 0.05$ and $^{**}P < 0.01$ vs. the OALT group. HPro = high dose of propofol; LPro = low dose of propofol; INT = intralipid; VAS = VAS2870; OALT = orthotopic autologous liver transplantation.

Taken together, these results revealed that propofol post-conditioning may reduce hepatic oxidative stress via inhibiting NADPH oxidase Nox2 activity and the subsequent ROS generation.

3.3. Propofol Postconditioning Attenuated Liver Inflammatory Response following OALT. According to the pathological results, we found inflammatory infiltration during liver injury in the early stage of OALT; we then tested the inflammatory cytokines and inflammation-related TLR4/NF-κB pathway. As shown in Figures 4(a)–4(c), hepatic proinflammatory cytokines TNF-α, IL-1β, and IL-6 were all increased in the OALT group. Propofol postconditioning of both doses but not intralipid treatment significantly reduced the releases of proinflammatory cytokines compared to the OALT group. Treatment with Nox2 inhibitor

VAS2870 presented similar anti-inflammation effects with decrease of levels of cytokines TNF-α, IL-1β, and IL-6. Both propofol postconditioning and Nox2 inhibition could inhibit the TLR4/NF-κB inflammatory pathway, evidenced by reduced nuclear protein expressions of NF-κB p65 protein and downregulated total TLR4 expression (Figures 4(d)–4(f)) ($P < 0.05$ vs. OALT).

3.4. Propofol Postconditioning Mitigated Neutrophil Infiltration and Hepatic Oxidative Stress. ROS scavenging is one of the characteristics of propofol. In order to detect the antioxidative effects of propofol postconditioning on liver I/R injury after OALT, neutrophil infiltration and hepatic oxidative stress were measured. As shown in Figures 5(a) and 5(b), hepatic neutrophil elastase (NE) activity and MPO activity, both of which were associated with

(a)

(b)

(c)

(d)
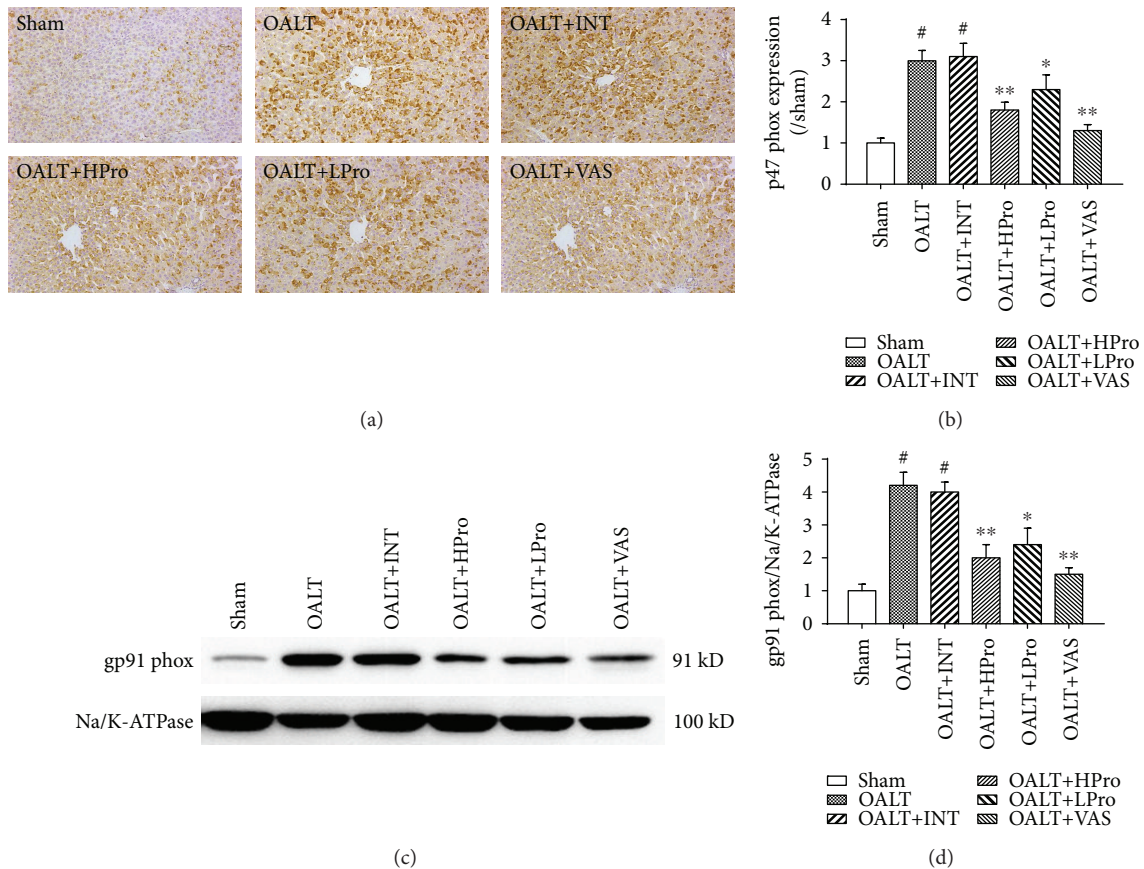
FIGURE 3: Hepatic NADPH oxidase expression changed due to OALT. Protein p47^{phox} expression was detected by immunohistochemistry method (a). The amount of protein p47^{phox} was calculated by gray scanning and was analyzed (b). Protein gp91^{phox} expression was detected by Western blot method (c). The amount of protein gp91^{phox} was calculated by gray scanning and was analyzed (d). The results are expressed as the mean ± SD. $n = 8$ per group. $^{\#}P < 0.01$ vs. the sham group; $^{*}P < 0.05$ and $^{**}P < 0.01$ vs. the OALT group. HPro = high dose of propofol; LPro = low dose of propofol; INT = intralipid; VAS = VAS2870; OALT = orthotopic autologous liver transplantation.

neutrophil infiltration, were significantly elevated in rats subjected to OALT. Both propofol postconditioning and VAS2870 treatment inhibited neutrophil infiltration caused by OALT and reduced lipid peroxidation product 8-isoprostane generation and increased SOD activity (Figures 5(c) and 5(d)) in the livers ($P < 0.05$ vs. OALT). These results indicated that propofol postconditioning and Nox2 inhibition protected the liver from oxidative stress via reduced neutrophil infiltration and ROS generation.

3.5. Propofol Postconditioning Protected Hepatocytes from Apoptosis. Oxidative stress and inflammation can finally lead to hepatocyte apoptosis or necrosis and cause liver I/R injury. As shown in Figures 6(a)–6(c), we identified a significant amount of cell apoptosis occurred in the liver following OALT compared to the sham group ($P < 0.01$ vs. the sham group). High dose of propofol postconditioning significantly reduced the number of apoptotic cells, which was consistent with the decrease of cleaved caspase-3/procaspase-3 ratio. Similarly, Nox2 inhibition by VAS2870 reduced hepatocyte apoptosis compared to the OALT group. These results indicated that propofol postconditioning reduced hepatocyte ROS generation and finally protected hepatocyte from apoptosis.

4. Discussion

In the current study, we demonstrated that propofol postconditioning reduced hepatocellular apoptosis after liver transplantation and its antioxidative property was related to inhibition of NADPH oxidase. We established an OALT model to mimic clinical liver transplantation and then detected the hepatic pathology, oxidative mediators, and inflammation response including TLR4/NF-κB signaling pathway. To further clarify the protective effects of propofol, VAS2870, a specific inhibitor of NADPH oxidase Nox2, was used as a positive control. Our results suggested that propofol postconditioning exerted protective effects against liver injury following OALT. And inhibition of Nox2 maybe a possible mechanism for liver protection conferred by propofol postconditioning (Figure 7).

Liver I/R injury has been identified as one of the most important factors to the etiology after liver transplantation, which contributes to early graft dysfunction and failure [19]. I/R processed is triggered when a donor liver is transiently deprived of oxygen and reoxygenation, leading to uncontrolled inflammatory response and reactive oxygen species release in the early stages of reperfusion [20]. In the present study, we found dramatically increased hepatic inflammatory
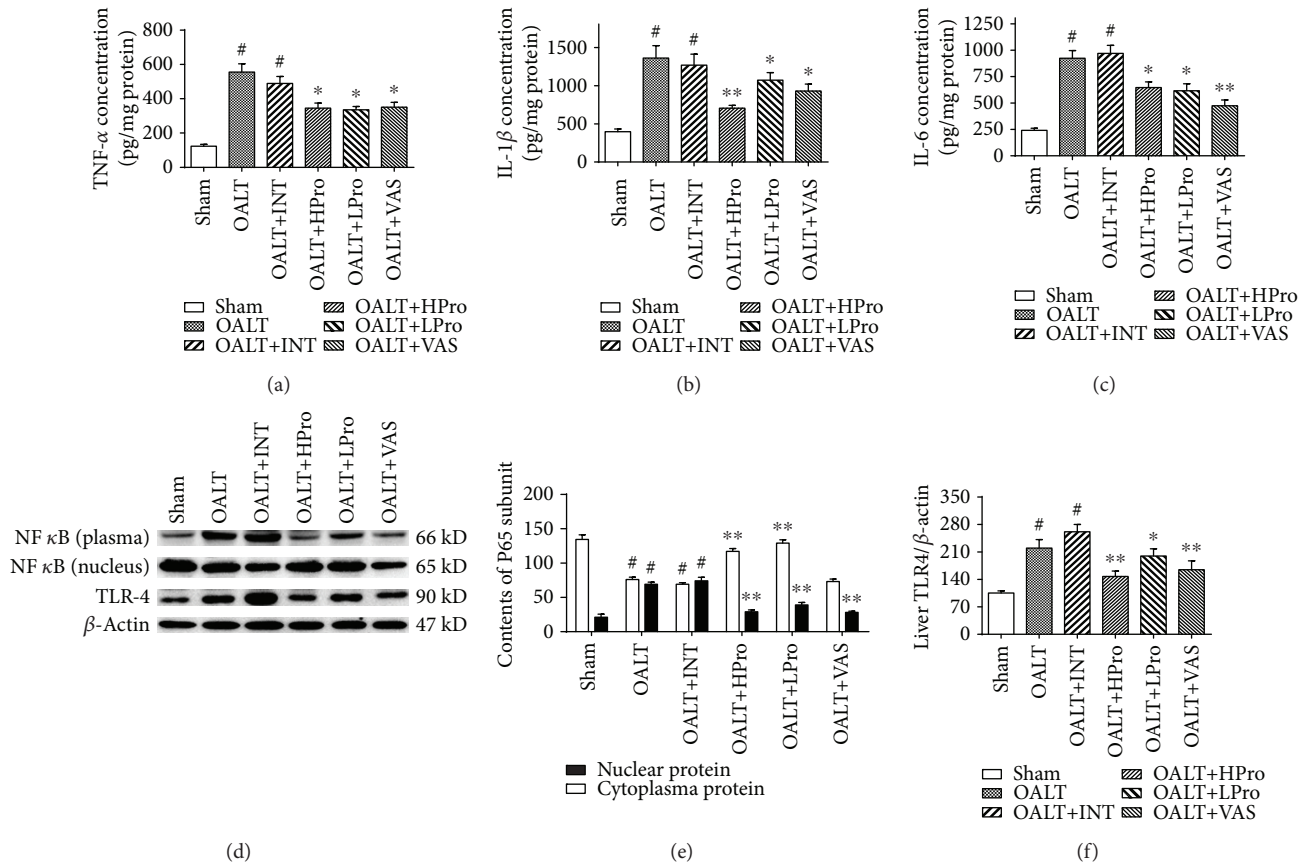
FIGURE 4: Hepatic inflammatory response after OALT. Proinflammatory cytokines TNF-α (a), IL-1β (b), and IL-6 (c) levels were measured by ELISA assay. Cytoplasm and nuclear NF-κB p65 and TLR4 proteins were detected by Western blot (d). The amount of target proteins NF-κB p65 (e) and TLR4 (f) was calculated by gray scanning and was analyzed. $n = 8$ per group. $^{\#}P < 0.01$ vs. the sham group; $^{*}P < 0.05$ and $^{**}P < 0.01$ vs. the OALT group. HPro = high dose of propofol; LPro = low dose of propofol; INT = intralipid; VAS = VAS2870; OALT = orthotopic autologous liver transplantation.

cytokines including TNF-α, IL-1β, and IL-6 as well as activated TLR4/NF-κB signaling pathway after OALT. These cytokines were proved to be vital to the initiation and propagation of liver I/R injury, whose main role was to recruit circulating neutrophils to the injured liver tissue during reperfusion [21]. In our study, hepatic MPO and neutrophil elastase were increased, which indicated that neutrophil extensively infiltrates the liver in the early stage of OALT. Along with neutrophil infiltration was excessive ROS generation and subsequent oxygen-derived product formation [22].

Strong evidences have illustrated the importance of ROS in pathogenesis of liver I/R injury [23, 24]. One of the currently promising intervention strategies is ischemic preconditioning (IPC), which is an intrinsic process whereby repeated short episode of ischemia to protect the liver against subsequent ischemia [25]. However, IPC may lead to potential vascular injury and thermogenesis [26]. We previously used propofol pretreatment during liver transplantation and found that propofol protected the lung from oxidative stress via enhancing antioxidant enzyme HO-1 expression. However, it takes several days to pretreat with propofol but most liver transplantations are emergency operations [6, 7]. Thus, we preferred propofol postconditioning and

demonstrated its protective function in reducing early liver damage after transplantation. In the model of rats' middle cerebral artery occlusion, it has proved that propofol postconditioning (20 mg/kg/h for 2 hours at the onset of reperfusion) led to long-term recovery of brain functions and upregulating the activity of the PKMζ/KCC2 pathway [27]. Li et al. found that propofol postconditioning enhanced cell viability and alleviated apoptosis to protect cardiomyocytes against hypoxia/reoxygenation injury through ERK signaling pathway [28]. Of interest, Li et al. found that alternative use of isoflurane and propofol conferred superior cardioprotection against postischemic myocardial injury and dysfunction, and this function was probably mediated through attenuating cardiac oxidative damage [29], which indicated that anesthesia may play an important role in organ protection during I/R injury.

NADPH oxidase activation and subsequent ROS formation are important upstream events which can activate hepatocytes and amplify the production of multiple proinflammatory cytokines, such as TNF-α or interlukin-1β [30]. Hepatic NADPH oxidase activation and the ROS production have been implicated as critical regulators of liver I/R injury [23]. Although propofol has been shown to reduce oxidative stress

(a)

(b)

(c)

(d)
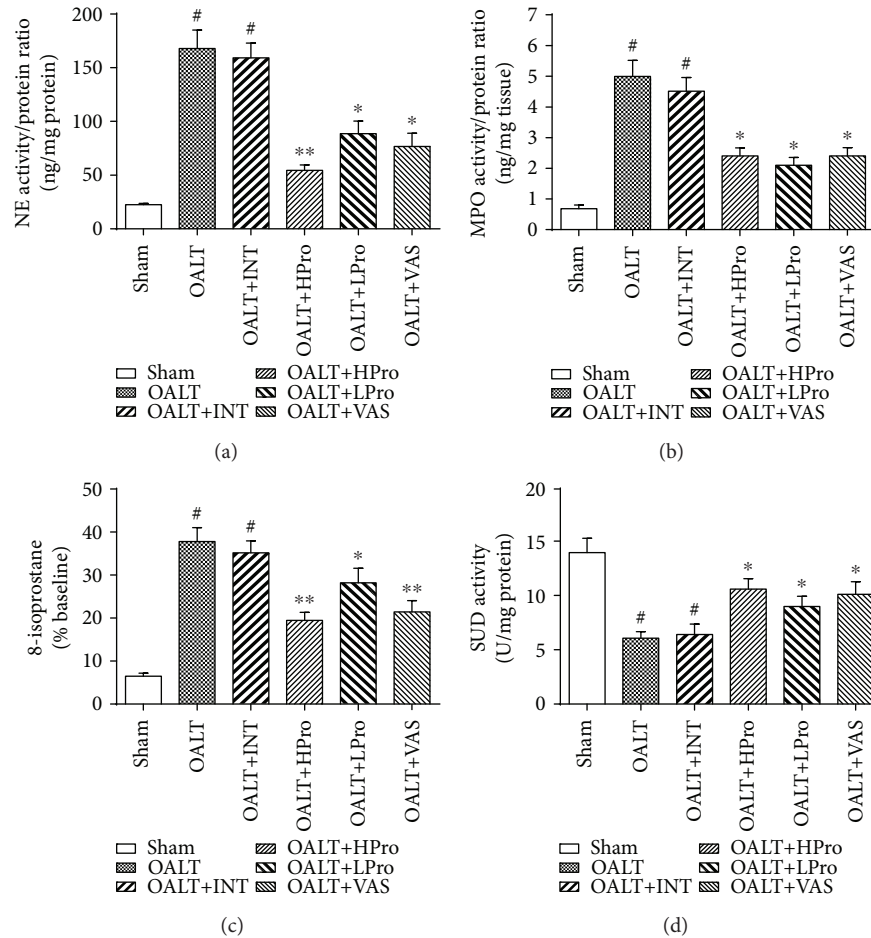
Figure 5: Neutrophil infiltration and oxidative stress in the liver. Neutrophil elastase (NE) (a) and myeloperoxidase (MPO) (b) activities reflected neutrophil infiltration. 8-Isoprostane (c) and superoxide dismutase (SOD) (d) were detected to reflect hepatic oxidative stress level. $n = 8$ per group. $^{\#}P < 0.01$ vs. the sham group; $^{*}P < 0.05$ and $^{**}P < 0.01$ vs. the OALT group. HPro = high dose of propofol; LPro = low dose of propofol; INT = intralipid; VAS = VAS2870; OALT = orthotopic autologous liver transplantation.

as an ROS scavenger, the current study shows that propofol can also suppress Nox2 to reduce the consequent production of ROS. Notably, propofol downregulated the hepatic expression of the NADPH oxidase membrane components p47^{phox} and glycosylated subunit gp91^{phox} after OALT. We speculated that this may be an important mechanism of propofol actions. Luo et al. showed that siRNA silencing of p22^{phox} significantly attenuated the protective effects of propofol [31]. Recent studies have also identified other receptors as potential molecular targets of propofol including nicotinic and M1 muscarinic receptors [32, 33]. Whether these receptors act as upstream regulators, NADPH oxidase remains to be determined.

Of note, in the current study, the OALT model is superior in mimicking the pathophysiological variation during liver ischemia/reperfusion in liver transplantation and ischemia/reperfusion-mediated liver injury without interference of immunoactivities between grafts and hosts. However, as the cold ischemia time in this model is about 20 minutes, so it is not able to represent the long (6 to 8 hours) cold preservation time that occurs in the liver graft before being transplanted. Propofol postconditioning was performed at the onset of

reperfusion with continuous infusion for 30 min and proved to be protective against liver I/R injury. However, whether the dose and the duration we chose was the best intervention required further investigation. Moreover, although we have confirmed that the protective effect of propofol postconditioning was related to Nox2 activity inhibition, whether it acts on the other NADPH oxidase subunit such as Nox4 also remains unknown. It is also still unclear that how propofol acts on Nox2, directly or indirectly. Those questions remain unanswered. More studies will be involved to clarify these mechanisms and make this intervention more safe and reliable.

In summary, liver transplantation leads to severe inflammation and oxidative stress accompanied with NADPH oxidase Nox2 activation. Propofol postconditioning exerted prominently protective function against the I/R injury after liver transplantation, which presented as lower levels of inflammatory mediators and oxidative products accompanied with less neutrophil filtration and weaker induction of Nox2. Collectively, propofol postconditioning had been proved to reduce liver inflammation and oxidative stress probably via inhibiting NADPH oxidase Nox2.

(a)

(b)

(c)
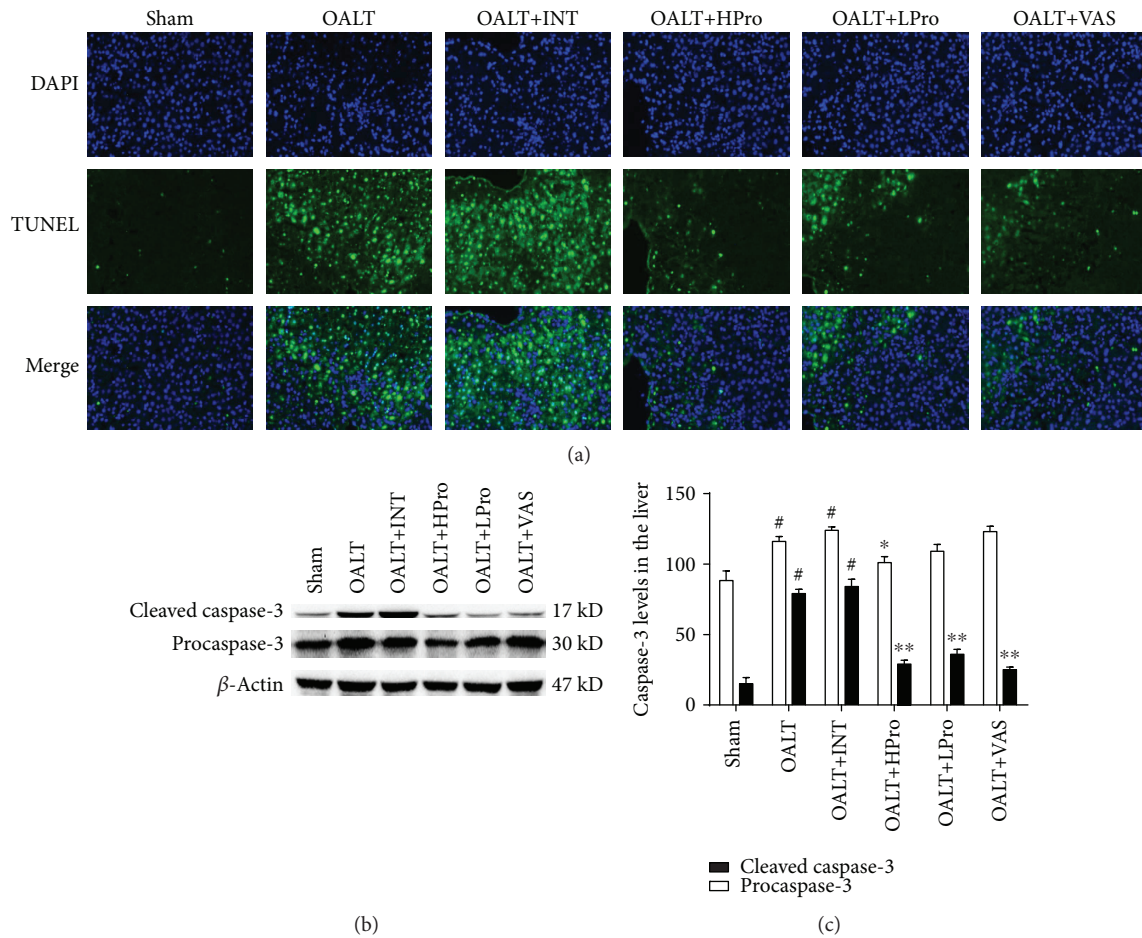
FIGURE 6: Propofol postconditioning protected hepatocyte from apoptosis. Fluorescent TUNEL staining of liver tissue (40x) (a). Cleaved caspase-3 and procaspase-3 proteins were detected by Western blot method (b). The amount of target proteins cleaved caspase-3 and procaspase-3 was calculated by gray scanning and was analyzed (c). The results are expressed as the mean ± SD. $n = 8$ per group. [#]$P < 0.01$ vs. the sham group; [*]$P < 0.05$ and [**]$P < 0.01$ vs. the OALT group. HPro = high dose of propofol; LPro = low dose of propofol; INT = intralipid; VAS = VAS2870; OALT = orthotopic autologous liver transplantation.
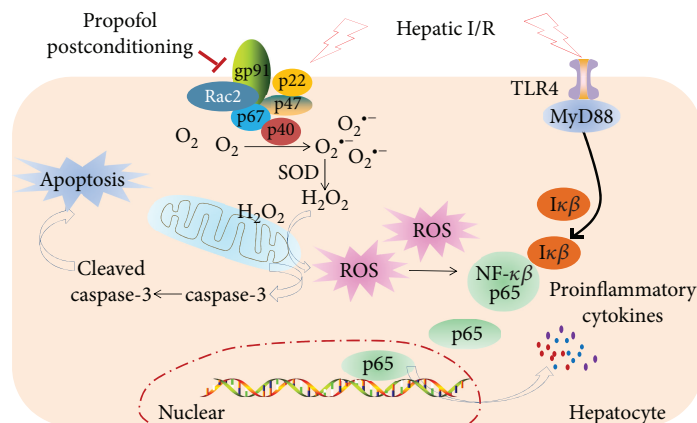
FIGURE 7: Propofol postconditioning reduces liver injury and the possible mechanisms. Under hepatic I/R condition, NADPH oxidase and TLR4/NF-κB pathway are activated. Endogenously, ROS were generated due to NADPH oxidase activation, resulting in the caspase-3-related apoptosis pathway as well as NF-κB pathway activation. Amount of proinflammatory cytokines was produced after NF-κB p65 pathway activation. Propofol postconditioning inhibited Nox2 (gp91[phox] and p47[phox]) which could lead to downregulation of ROS generation and finally reduced hepatic I/R injury.

Data Availability

The data used to support the findings of this study are available from the corresponding author upon request.

Conflicts of Interest

The authors declare that they have no competing interests.

Authors' Contributions

Weifeng Yao and Xue Han contributed equally to this study. Weifeng Yao, Ziqing Hei, and Pinjie Huang conceived and designed the experiments. Weifeng Yao, Xue Han, Yihan Zhang, Jianqiang Guan, Mian Ge, Chaojin Chen, Shan Wu, Jiaxin Chen, Gangjian Luo, and Pinjie Huang performed the experiments. Weifeng Yao analyzed the data. Xue Han contributed the reagents/materials/analysis tools. Weifeng Yao wrote the paper. All authors read and approved the manuscript.

Acknowledgments

References

[1] F. Durand, "How to improve long-term outcome after liver transplantation?," *Liver International*, vol. 38, Supplement 1, pp. 134–138, 2018.

[2] R. F. Saidi and S. K. H. Kenari, "Liver ischemia/reperfusion injury: an overview," *Journal of Investigative Surgery*, vol. 27, no. 6, pp. 366–379, 2014.

[3] J. Li, R. J. Li, G. Y. Lv, and H. Q. Liu, "The mechanisms and strategies to protect from hepatic ischemia-reperfusion injury," *European Review for Medical and Pharmacological Sciences*, vol. 19, no. 11, pp. 2036–2047, 2015.

[4] P. Tang and R. Eckenhoff, "Recent progress on the molecular pharmacology of propofol," *F1000Res*, vol. 7, p. 123, 2018.

[5] I. Vasileiou, T. Xanthos, E. Koudouna et al., "Propofol: a review of its non-anaesthetic effects," *European Journal of Pharmacology*, vol. 605, no. 1-3, pp. 1–8, 2009.

[6] M. Ge, W. Yao, Y. Wang et al., "Propofol alleviates liver oxidative stress via activating Nrf2 pathway," *The Journal of Surgical Research*, vol. 196, no. 2, pp. 373–381, 2015.

[7] W. Yao, G. Luo, G. Zhu et al., "Propofol activation of the Nrf2 pathway is associated with amelioration of acute lung injury in a rat liver transplantation model," *Oxidative Medicine and Cellular Longevity*, vol. 2014, Article ID 258567, 9 pages, 2014.

[8] D. Bracco, "Post-conditioning: promising answers and more questions," *Critical Care*, vol. 16, no. 6, p. 180, 2012.

[9] H. Harada, I. N. Hines, S. Flores et al., "Role of NADPH oxidase-derived superoxide in reduced size liver ischemia and reperfusion injury," *Archives of Biochemistry and Biophysics*, vol. 423, no. 1, pp. 103–108, 2004.

[10] S. H. Ellmark, G. J. Dusting, M. N. T. Fui, N. Guzzo-Pernell, and G. R. Drummond, "The contribution of Nox4 to NADPH oxidase activity in mouse vascular smooth muscle," *Cardiovascular Research*, vol. 65, no. 2, pp. 495–504, 2005.

[11] W. Yao, H. Li, G. Luo et al., "SERPINB1 ameliorates acute lung injury in liver transplantation through ERK1/2-mediated STAT3-dependent HO-1 induction," *Free Radical Biology & Medicine*, vol. 108, pp. 542–553, 2017.

[12] C. Luo, D. Yuan, X. Li et al., "Propofol attenuated acute kidney injury after orthotopic liver transplantation via inhibiting gap junction composed of connexin 32," *Anesthesiology*, vol. 122, no. 1, pp. 72–86, 2015.

[13] A. G. Hudetz, X. Liu, S. Pillay, M. Boly, and G. Tononi, "Propofol anesthesia reduces Lempel-Ziv complexity of spontaneous brain activity in rats," *Neuroscience Letters*, vol. 628, pp. 132–135, 2016.

[14] Y. H. Tuo, Z. Liu, J. W. Chen et al., "NADPH oxidase inhibitor improves outcome of mechanical reperfusion by suppressing hemorrhagic transformation," *Journal of NeuroInterventional Surgery*, vol. 9, no. 5, pp. 492–498, 2017.

[15] A. Naiki-Ito, M. Asamoto, T. Naiki et al., "Gap junction dysfunction reduces acetaminophen hepatotoxicity with impact on apoptotic signaling and connexin 43 protein induction in rat," *Toxicologic Pathology*, vol. 38, no. 2, pp. 280–286, 2010.

[16] X. Huang, W. Zhao, D. Hu et al., "Resveratrol efficiently improves pulmonary function via stabilizing mast cells in a rat intestinal injury model," *Life Sciences*, vol. 185, pp. 30–37, 2017.

[17] W. Yao, H. Li, X. Han et al., "MG53 anchored by dysferlin to cell membrane reduces hepatocyte apoptosis which induced by ischaemia/reperfusion injury in vivo and in vitro," *Journal of Cellular and Molecular Medicine*, vol. 21, no. 10, pp. 2503–2513, 2017.

[18] M. Ge, W. Yao, D. Yuan et al., "Brg1-mediated Nrf2/HO-1 pathway activation alleviates hepatic ischemia-reperfusion injury," *Cell Death & Disease*, vol. 8, no. 6, article e2841, 2017.

[19] M. Mendes-Braz, M. Elias-Miro, M. B. Jimenez-Castro, A. Casillas-Ramirez, F. S. Ramalho, and C. Peralta, "The current state of knowledge of hepatic ischemia-reperfusion injury based on its study in experimental models," *Journal of Biomedicine & Biotechnology*, vol. 2012, Article ID 298657, 20 pages, 2012.

[20] M. Abu-Amara, S. Y. Yang, N. Tapuria, B. Fuller, B. Davidson, and A. Seifalian, "Liver ischemia/reperfusion injury: processes in inflammatory networks-a review," *Liver Transplantation*, vol. 16, no. 9, pp. 1016–1032, 2010.

[21] K. M. Quesnelle, P. V. Bystrom, and L. H. Toledo-Pereyra, "Molecular responses to ischemia and reperfusion in the liver," *Archives of Toxicology*, vol. 89, no. 5, pp. 651–657, 2015.

[22] H. Jaeschke, "Reactive oxygen and mechanisms of inflammatory liver injury: present concepts," *Journal of Gastroenterology and Hepatology*, vol. 26, Suppl 1, pp. 173–179, 2011.

[23] H. Jaeschke and B. L. Woolbright, "Current strategies to minimize hepatic ischemia-reperfusion injury by targeting reactive oxygen species," *Transplantation Reviews*, vol. 26, no. 2, pp. 103–114, 2012.

[24] H. Jaeschke, "Mechanisms of liver injury. II. Mechanisms of neutrophil-induced liver cell injury during hepatic ischemia-reperfusion and other acute inflammatory conditions,"

American Journal of Physiology-Gastrointestinal and Liver Physiology, vol. 290, no. 6, pp. G1083–G1088, 2006.

[25] S. Yan, L. M. Jin, Y. X. Liu, L. Zhou, H. Y. Xie, and S. S. Zheng, "Outcomes and mechanisms of ischemic preconditioning in liver transplantation," Hepatobiliary & Pancreatic Diseases International, vol. 9, no. 4, pp. 346–354, 2010.

[26] R. S. Koti, A. M. Seifalian, and B. R. Davidson, "Protection of the liver by ischemic preconditioning: a review of mechanisms and clinical applications," Digestive Surgery, vol. 20, no. 5, pp. 383–396, 2003.

[27] C. Y. Yang, S. Y. Liu, H. Y. Wang et al., "Neuroprotection by propofol post-conditioning: focus on PKMζ/KCC2 pathway activity," Cellular and Molecular Neurobiology, vol. 38, no. 3, pp. 691–701, 2018.

[28] H. Li, J. Tan, Z. Zou, C. G. Huang, and X. Y. Shi, "Propofol post-conditioning protects against cardiomyocyte apoptosis in hypoxia/reoxygenation injury by suppressing nuclear factor-kappa B translocation via extracellular signal-regulated kinase mitogen-activated protein kinase pathway," European Journal of Anaesthesiology, vol. 28, no. 7, pp. 525–534, 2011.

[29] T. Li, W. Wu, Z. You et al., "Alternative use of isoflurane and propofol confers superior cardioprotection than using one of them alone in a dog model of cardiopulmonary bypass," European Journal of Pharmacology, vol. 677, no. 1-3, pp. 138–146, 2012.

[30] K. Kimura, K. Shirabe, T. Yoshizumi et al., "Ischemia-reperfusion injury in fatty liver is mediated by activated NADPH oxidase 2 in rats," Transplantation, vol. 100, no. 4, pp. 791–800, 2016.

[31] T. Luo, J. Wu, S. V. Kabadi et al., "Propofol limits microglial activation after experimental brain trauma through inhibition of nicotinamide adenine dinucleotide phosphate oxidase," Anesthesiology, vol. 119, no. 6, pp. 1370–1388, 2013.

[32] S. S. Jayakar, W. P. Dailey, R. G. Eckenhoff, and J. B. Cohen, "Identification of propofol binding sites in a nicotinic acetylcholine receptor with a photoreactive propofol analog," The Journal of Biological Chemistry, vol. 288, no. 9, pp. 6178–6189, 2013.

[33] O. Murasaki, M. Kaibara, Y. Nagase et al., "Site of action of the general anesthetic propofol in muscarinic M1 receptor-mediated signal transduction," The Journal of Pharmacology and Experimental Therapeutics, vol. 307, no. 3, pp. 995–1000, 2003.

Research Article

Exosomes Derived from miR-214-Enriched Bone Marrow-Derived Mesenchymal Stem Cells Regulate Oxidative Damage in Cardiac Stem Cells by Targeting CaMKII

Yan Wang [iD],[1] **Ranzun Zhao,**[1] **Debin Liu,**[2] **Wenwen Deng** [iD],[1] **Guanxue Xu,**[1] **Weiwei Liu,**[1] **Jidong Rong,**[1] **Xianping Long,**[1] **Junbo Ge,**[3] **and Bei Shi** [iD][1]

[1]*Department of Cardiology, Affiliated Hospital of Zunyi Medical College, Zunyi 563000, China*
[2]*Department of Cardiology, Shantou Glory Hospital, Shantou 515041, China*
[3]*Department of Cardiology, Shanghai Institute of Cardiovascular Diseases, Zhongshan Hospital, Fudan University,
 Shanghai 200032, China*

Correspondence should be addressed to Bei Shi; shibei2147@163.com

Cardiac stem cells (CSCs) have emerged as one of the most promising stem cells for cardiac protection. Recently, exosomes from bone marrow-derived mesenchymal stem cells (BMSCs) have been found to facilitate cell proliferation and survival by transporting various bioactive molecules, including microRNAs (miRs). In this study, we found that BMSC-derived exosomes (BMSC-exos) significantly decreased apoptosis rates and reactive oxygen species (ROS) production in CSCs after oxidative stress injury. Moreover, a stronger effect was induced by exosomes collected from BMSCs cultured under hypoxic conditions (Hypoxic-exos) than those collected from BMSCs cultured under normal conditions (Nor-exos). We also observed greater miR-214 enrichment in Hypoxic-exos than in Nor-exos. In addition, a miR-214 inhibitor or mimics added to modulate miR-214 levels in BMSC-exos revealed that exosomes from miR-214-depleted BMSCs partially reversed the effects of hypoxia-induced exosomes on oxidative damage in CSCs. These data further confirmed that miR-214 is the main effector molecule in BMSC-exos that protects CSCs from oxidative damage. miR-214 mimic and inhibitor transfection assays verified that CaMKII is a target gene of miR-214 in CSCs, with exosome-pretreated CSCs exhibiting increased miR-214 levels but decreased CaMKII levels. Therefore, the miR-214/ CaMKII axis regulates oxidative stress-related injury in CSCs, such as apoptosis, calcium homeostasis disequilibrium, and excessive ROS accumulation. Collectively, these findings suggest that BMSCs release miR-214-containing exosomes to suppress oxidative stress injury in CSCs through CaMKII silencing.

1. Introduction

The endogenous myocardial repair response to injury has been reported to be involved in the activation and differentiation of resident cardiac stem cells (CSCs) [1–3], and preclinical and clinical studies have provided abundant evidence for the ability of CSCs to improve cardiac function [4–8]. Despite this impressive cardiac repair capacity of CSCs, the poor survival and low retention of CSCs hinder functional improvements and cardiac outcomes [7, 9, 10]. The factors contributing to the poor survival of donor cells are complex and include inflammation, reactive oxygen species (ROS) release, Ca^{2+} homeostasis disruption, and activation of mitochondrial apoptosis and necrosis [8, 11–13]. Thus, exploring powerful strategies that facilitate CSC-based therapy in the ischemic myocardium is critical.

Over the past few years, several experimental studies have demonstrated that bone marrow-derived mesenchymal stem cells (BMSCs) release specialized nanosized membranous vesicles, termed exosomes, that improve cardiac function in the damaged heart [14]. These membrane-bound vesicles with a 30–100 nm diameter are released from many cell types and deliver many bioactive molecules, including microRNAs (miRs) and long noncoding RNAs (lncRNAs) as well as
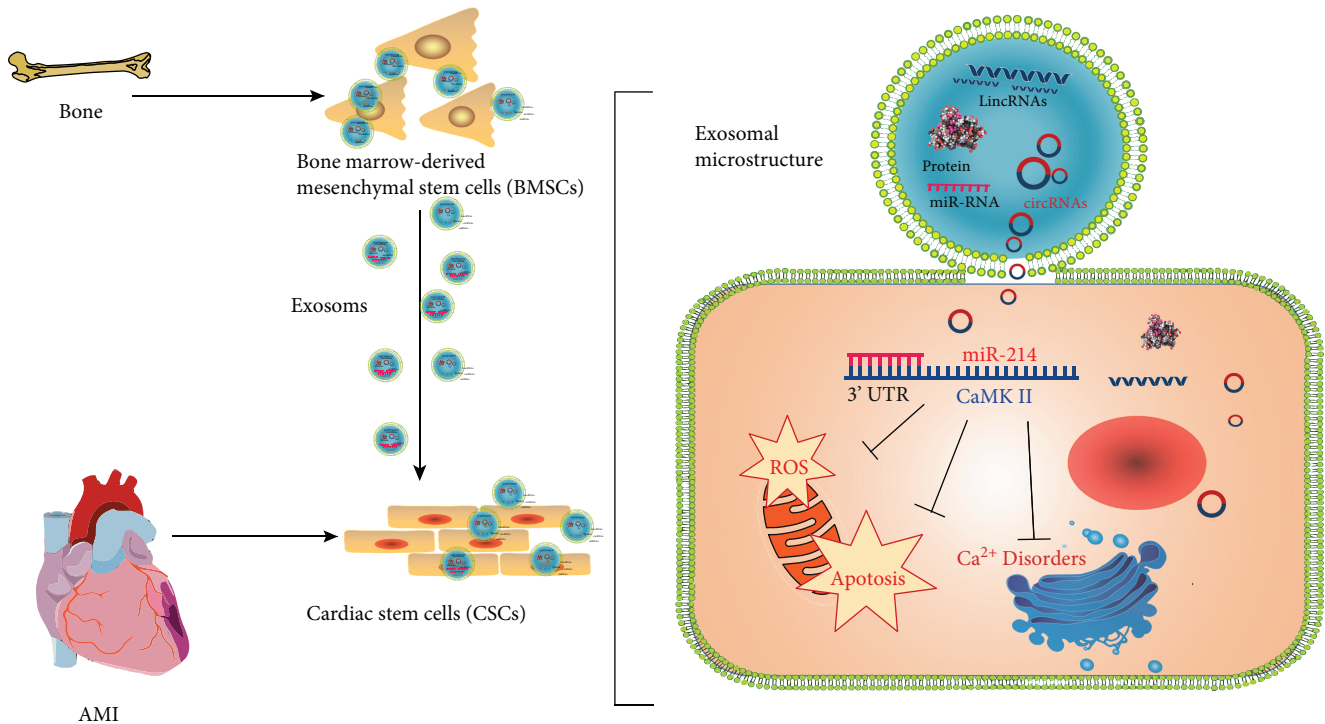
FIGURE 1

nutritional elements. As intracellular messengers, exosomes play an important role in cell-to-cell communication, ensuring that information is transferred from donor cells to recipient cells and enabling cells to react to environmental changes [15]. Recently, an increasing number of studies have suggested that the predominant role of paracrine secretion is to release exosomes from BMSCs (called BMSC-exos), which can improve cardiac function after myocardial infarction (MI) [15, 16]. In addition, exosomes can stimulate the proliferation, migration, and angiogenic potency of CSCs in vitro and in vivo, and miRs shuttled by exosomes may play an important role in these processes [17].

miRs are endogenous, single-stranded noncoding RNAs that consist of 20–22 nucleotides and have key roles in inhibiting translation or promoting the mRNA degradation of target genes [18, 19]. An increasing number of studies show that exosomes can serve as vehicles for miR transfer and mediate intercellular communication [20]. However, exosomal miRs vary widely across different cell types and pathological conditions because of preconditioning or genetic manipulation of parent BMSCs [21, 22], and these changes in exosomes might completely reverse the fate of target cells. Exosomes derived from stem cells cultured under hypoxic conditions have a greater reparative capacity than exosomes from normal cells, and microarray and principle component analyses of exosomes secreted by hypoxic medium strongly suggest that exosomal miRs are responsible for altering physiological effects [23]. Nonetheless, very few studies have focused on the regulatory ability of BMSC-exos pretreated with hypoxia to protect against oxidative damage in CSCs under conditions of oxidative stress. In addition, the systemic

regulation and function of exosomal miRs in protecting CSCs under H_2O_2-induced oxidative stress are poorly understood.

Many studies have shown that miR-214 is sensitive to cardiac stress and is upregulated in cardiac injury, and this upregulation of miR-214 has been reported to protect cardiac myocytes from H_2O_2-induced injury [24]. Importantly, endothelial cell-secreted exosomes promote endothelial cell migration and angiogenesis in vitro and in vivo through miR-214 transfer by repressing mutated ataxia telangiectasia (AT) expression in recipient cells [25]. Additionally, one study confirmed that miR-214 suppresses both NCX1 and proapoptotic effectors of Ca^{2+} signaling pathways such as calcium/calmodulin-dependent protein kinase II (CaMKII), cyclophilin D (CypD), and BIM [11]. Among these factors, CaMKII has emerged as an MI- and a ROS-activated signaling molecule that regulates apoptotic gene expression after MI [26, 27]. Furthermore, an apoptotic pathway involved in ROS overproduction via CaMKII activation was recently discovered [28, 29].

Considering the potential role of BMSC-exos in cardioprotection and the effects of miR-214 on regulating oxidative stress-mediated injury at the translational level in many cell types, we focused on investigating whether miR-214 expression in BMSC-exos is sensitive to hypoxic stimulation and whether miR-214-enriched exosomes play a protective role against H_2O_2-induced CSC apoptosis and ROS production and participate in Ca^{2+} homeostasis by targeting CaMKII. The findings provide new insight into the molecular basis of cell therapy in ischemic cardiomyopathy (Figure 1).

(In brief, bone marrow-derived mesenchymal stem cells shed exosomes containing MiR-214 which targets on

CaMKII mRNA $3'$UTR to downregulate gene expression in recipient cardiac stem cells that ultimately results in suppressing oxidative stress as well as apoptosis).

2. Materials and Methods

2.1. Animals. Sprague-Dawley rats (male and female, approximately 3 weeks old, 45–60 g) were purchased and fed at Zunyi Medical College (Zunyi, China). All experimental procedures were performed according to the "Guide for the Care and Use of Laboratory Animals" in China and were approved by the local Experimental Animal Care and Use Committee.

2.2. Materials. Collagenase type II was from Sigma (USA). Trypsin was from Gibco (USA). Penicillin and streptomycin were from Solarbio (China). Ham's/F-12 medium and fetal bovine serum (FBS) were purchased from HyClone (USA). Low-glucose Dulbecco's modified Eagle's medium (L-DMEM) was from Gibco (USA). Fibroblast growth factor was obtained from PeproTech (USA). Leukocyte inhibitory factor was produced by Gibco (USA). The rabbit anti-rat c-kit$^+$ primary antibody was supplied by Biorbyt (UK). M-280 beads conjugated to a sheep anti-rabbit secondary antibody were from Dynal Biotech (Norway). PE-conjugated anti-CD34 and anti-CD45, anti-CD63, anti-CD9, and anti-Alix antibodies were purchased from Abcam (USA). DiI was from Invitrogen (USA). miR-214 mimics, inhibitors, and scrambled controls were synthesized by Ribo-Bio (China). Lipofectamine 2000 was from Invitrogen (USA). The primers, miR reverse transcription kit, and qRT-PCR kit were from Sangon Biotech (China). Anti-pro Caspase-3, anti-cleaved Caspase-3, anti-CaMKII, anti-Bax, anti-Bcl-2, anti-β-actin, anti-GAPDH primary antibodies, and other secondary antibodies were obtained from Boster (China). Synthesized siRNA against CaMKII (siRCaMKII), CaMKII and negative control RNA were from GeneCopoeia (MD). Lentiviruses and empty vectors were synthesized by Hanbio (China). The ROS assay kit was from Sigma (USA), and the Annexin V-FITC apoptosis detection kit was from Solarbio (China). Fluo-8 was purchased from AAT Bioquest (USA). Superoxide dismutase (SOD) and malondialdehyde (MDA) commercial kits were from Jiancheng Bioengineering Institute (China). The in situ cell death detection kit was purchased from Sigma (USA), and unlisted reagents were of analytical grade.

2.3. Isolation and Culture of C-Kit$^+$ CSCs and Establishment of the H_2O_2 Oxidative Stress Model. CSCs were isolated [17] and purified [30] using our previously published methods. The rats were deeply anesthetized with sevoflurane, and the atrial appendage was sliced and digested with 0.1% collagenase type II (Sigma, USA). After approximately 40 minutes (min) of digestion at 37°C, the cells were collected by sedimentation at 1200 rpm for 5 min. Then, the cells from the atrial appendage were incubated in a humid chamber in Ham's/F12 medium containing 10% FBS, 1% penicillin and streptomycin, 1% L-glutamine, 20 ng/ml human recombinant fibroblast growth factor, 20 ng/ml leukocyte inhibitory factor, and 10 ng/ml epidermal growth factor (EGF). When

the cells reached > 90% confluence, they were suspended by trypsinization. Then, CSCs were incubated with a rabbit anti-c-kit antibody (1 : 250 in F12 medium) for 1 hour (h) and sorted with anti-rabbit secondary antibody conjugated to 2.8 μm magnetic beads (Dynal Biotech, Norway) for 30 min according to the manufacturer's protocols. The purified c-kit$^+$ CSCs were cultured in F12 medium. Flow cytometry (FCM) was used to confirm the surface markers on the c-kit$^+$ CSCs. The cells were incubated with the following fluorochrome-conjugated primary antibodies and anti-c-kit IgG-APC secondary antibody (all from BioLegend, USA): anti-CD34-PE, anti-CD45-PE, and anti-c-kit. The CSCs were exposed to 100 μM H_2O_2 for 2 h to establish oxidative stress conditions for subsequent experiments.

2.4. BMSC Isolation, Purification, and Hypoxia Preconditioning. Total bone marrow cells were flushed from the femurs and tibias of rats (2- to 4-month-old) with culture medium; the rats were sacrificed via sevoflurane overdose as previously described [31]. Complete L-DMEM containing 15% FBS, 100 U/ml penicillin, and 100 U/ml streptomycin was used to resuspend the BMSCs, and then, the BMSCs were incubated in a humid chamber. At 48 h, the first medium change was performed to remove the nonadherent cells. When the cells reached 90% confluence, they were harvested with 0.25% trypsin (Sigma) and passaged at a ratio of 1 : 2. FCM was performed to assess the BMSC surface markers. The cells were incubated with the following fluorochrome-conjugated primary antibodies (all from BioLegend, USA): anti-CD90-PE, anti-CD29-APC, and anti-CD45-PE. BMSCs from passage (P) 3 to P5 were used for subsequent experiments.

The cells were stimulated with hypoxia, and cell viability was detected [32]. Approximately 5×10^5 BMSCs suspended in L-DMEM were plated in 150 mm-diameter culture dishes. The cells were then separately cultured under the conditions below for 12, 24, 48, 72, 96, or 120 h: 10% exosome-free FBS with hypoxia (94% N_2, 5% CO_2, and 1% O_2 gas mixture). BMSC viability was analyzed with CCK-8 assays. Briefly, adherent cells were digested with 0.05% trypsin and collected for CCK-8 assay according to the manufacturer's instructions.

2.5. Purification and Identification of BMSC-Exos. The BMSC-exo extraction procedures were as previously described [33]. The BMSCs were cultured in L-DMEM supplemented with 10% FBS that had been previously centrifuged at 100,000 to 110,000g for 8 to 10 h to eliminate preexisting bovine-derived exosomes [9]. Conditioned culture medium (50 ml) containing 10% exosome-free FBS was used to culture BMSCs for 48 h; the BMSCs were grown to 90% confluence and allowed to become quiescent for 12 h. The plated cells were subjected to normoxic or hypoxic conditions for 48 h. After conditioning, the media were subjected to sequential centrifugation (Optima XPN-100 ultracentrifuge; Beckman Coulter SW 41 Ti rotor) at 10,000g for 35 min to remove cell debris and at 100,000g for 70 min, followed by 2 washes in phosphate-buffered saline (PBS) (100,000g for 70 min). The exosomes were

resuspended in 20 μl of PBS and stored at −80°C. The amount of BMSC-exos was detected by measuring the total protein content by using a bicinchoninic acid (BCA) protein assay kit (Pierce). The exosomes were observed directly under a transmission electron microscope (TEM, Hitachi H7500, Tokyo, Japan). In addition, the BMSC-exos were identified by Western blotting with anti-CD63, anti-CD9, and anti-Alix antibodies (all purchased from Abcam).

2.6. Nanoparticle Tracking Analysis.
The absolute exosome size distribution was analyzed using a NanoSight NS300 (Malvern, UK). With nanoparticle tracking analysis (NTA), the particles are automatically tracked and sized based on Brownian motion and the diffusion coefficient [34]. After isolation, the exosomes were diluted in 1 ml of filtered PBS. Control medium and filtered PBS were used as controls. The NTA measurement conditions were as follows: a temperature of $23.75 \pm 0.5°C$, 25 frames per second, and a measurement time of 60 s. The detection threshold was similar in all the samples. Three recordings were performed for each sample.

2.7. Internalization of DiI-Labeled Exosomes into CSCs.
CSCs were harvested, seeded in fibronectin-coated dishes, and maintained at 37°C overnight. Briefly, the BMSC-exos were labeled with 1 μg/ml DiI (Invitrogen, USA) as previously described [15]. Then, the BMSC-exos were washed in PBS with centrifugation at 100,000 ×g for 2 h to remove unbound DiI. DiI-labeled BMSC-exos (400 μg/ml) were added to CSC culture medium for 24 h. The CSCs were then washed in PBS, fixed in 4% paraformaldehyde, and stained with 1 mg/ml 40,6-diamidino-2-phenylindole (DAPI) (Invitrogen, USA) for 10 min. Finally, cell fluorescence was observed by using a fluorescence microscope (Olympus).

2.8. Transfection of miRs into CSCs and BMSCs.
miR-214 mimics, inhibitors, and negative control RNAs (RiboBio, China) were transfected with Lipofectamine 2000 (Life Technologies) according to an established protocol. To knock down miR-214 expression, a miR-214 inhibitor was added to the culture medium at a final concentration of 100 nM. To upregulate miR-214 expression, miR-214 mimics were added directly to the complexes at a final concentration of 50 nM. At 6 h posttransfection, the transfection medium was replaced by regular culture medium. After incubation for 48 h, the cells were harvested for total RNA and protein extraction. The efficiency of transfection of mimics or inhibitors was confirmed by RT-qPCR, and a negative control for miR-214 mimics and inhibitors was also used.

2.9. Construction of and Infection with CaMKII or siRCaMKII Lentiviral Vectors.
CaMKII with/without the $3'$ untranslated region ($3'$UTR) (Lv-CaMKII-EGFP) and siRCaMKII was constructed by, respectively, inserting the CaMKII and siRCaMKII coding sequences (GeneCopoeia, MD) into a lentiviral EGFP vector using BamHI (FD0054) and EcoRI (N41890) restriction sites, all obtained from Invitrogen (Thermo Fisher Scientific Inc.). The lentiviral particles were prepared using a calcium phosphate method as previously described [31, 35]. The CSCs were transfected with Lv-CaMKII-EGFP, Lv-siRCaMKII-EGFP, or Lv-EGFP in the presence of 2 μg/ml polybrene (Sigma-Aldrich) at a multiplicity of infection (MOI) of 20 for 48 h. After 48 h, EGFP was expressed in >90% of the infected cells as determined by fluorescence microscopy (Olympus).

2.10. Reverse Transcription and Real-Time PCR of miR-214 and CaMKII.
miR-214 and CaMKII mRNA levels were determined by using quantitative RT-PCR as previously reported [36, 37]. Briefly, total RNA was extracted from the exosomes by SeraMir (System Biosciences) following the manufacturer's instructions, and cell RNA was extracted by an RNAprep pure Cell/Bacteria kit (Tiangen, Beijing, China). miR-214 levels were quantified with a stem-loop real-time PCR miR kit (RiboBio, China). The miR primer was also purchased from RiboBio (China). The purity of the isolated RNA was determined by the OD260/280 ratio using a Nanodrop ND-1000 spectrophotometer (Thermo Scientific). Isolated RNAs were reverse transcribed using a PrimeScript RT Reagent kit (TaKaRa, Kusatsu, Shiga, Japan). cDNA was used for quantitative PCR on a Bio-Rad Real-Time PCR system (Bio-Rad, Hercules, CA, USA) using a SYBR kit (Bio-Rad, USA). Amplification was performed at 95°C for 5 min, followed by 40 cycles of 95°C for 10 s, and 55.7°C for 30 s. The difference in the expression levels between the treatments was then calculated using the following equation: relative gene expression = 2 − (ΔCt, sample − ΔCt, control). U6 and β-actin were used as internal controls for miR-21 and CaMKII mRNA quantitation, respectively.

2.11. Apoptosis Assay of CSCs by FCM.
CSCs were preincubated with the different treatments (2×10^9 particles/ml). CSC apoptosis levels were determined by FCM using Annexin V-FITC/propidium iodide (PI) staining assays, as reported elsewhere [38]. Phosphatidylserine levels on CSC surface were estimated with Annexin V-FITC and PI apoptosis detection kits from Solarbio (China) according to the manufacturer's instructions. CSC apoptosis was analyzed via a FACSCalibur flow cytometer (BD Biosciences, USA). The results are expressed as the percentage of apoptotic cells among all the cells. FCM was performed twice using CSCs from three independent experiments.

2.12. ROS Assay of CSCs by FCM.
Intracellular ROS production was determined by dihydroethidium (DHE) (Sigma) staining, followed by FCM [12, 39] according to the manufacturer's instructions. Briefly, cells were incubated with MitoSOX reagent (2.5 mmol/l, Invitrogen) for 30 min at 37°C, washed twice with PBS, trypsinized, and centrifuged. The cell fluorescence intensity was analyzed by FCM. FCM was performed twice using CSCs from three independent experiments.

2.13. Assessment of Intracellular SOD and MDA Levels In Vitro.
After treating CSCs with different conditions, respectively, the intracellular superoxide dismutase (SOD) activities and malondialdehyde (MDA) levels were evaluated by the assay kits based on colorimetric methods (Nanjing Jiancheng Bioengineering Institute, China). After treatment, CSCs were harvested by centrifugation and the supernatants were

removed. The remaining cells were washed with PBS twice and lysed in lysis buffer for 30 min at 4°C. Following centrifugation, the supernatant was used for detecting the activities of SOD and the levels of MDA by using different assay kits as mentioned in the protocols. BCA test was used for quantifying proteins.

2.14. Terminal Deoxynucleotidyl Transferase dUTP Nick End Labeling (TUNEL) and C-Kit Staining for the Detection of CSC Apoptosis Rate. An in situ cell death detection kit (Sigma, USA) was used to detect the percentage of apoptotic cells following the manufacturer's protocol. Cells were fixed with 4% paraformaldehyde and permeabilized by incubating with 1% Triton X-100. The cells were incubated in 50 μl TUNEL reaction mixture per slide (vial 1 : vial 2 = 1 : 9) at 37°C in the dark for 60 min in a humidified atmosphere and then blocked with 10% goat serum before being incubated with the anti-C-kit antibody. The cells were subsequently incubated with DyLight 594-conjugated secondary antibody. After washing, the nuclei were counterstained with DAPI. Immunofluorescence images were taken with a fluorescence microscope (Olympus, Japan). The percentage of TUNEL-positive cells was determined in random fields by fluorescence microscopy; each experiment was performed in triplicate (40x magnification, at least 6 fields per sample).

2.15. Determination of Ca^{2+} Homeostasis in CSCs by Confocal Laser Scanning Microscopy. Intracellular Ca^{2+} changes reflect Ca handling. To detect these changes, we performed Ca^{2+} imaging experiments. Intracellular calcium was detected using a dual-excitation fluorescence photomultiplier system (IonOptix, Milton, MA, USA) as previously described [40]. Briefly, CSCs were loaded with Fluo-8/AM (0.5 μM) solution for 10 min, and the fluorescence signal was detected using an IonOptix fluorescence system (IonOptix, Milton, MA, USA). After subtracting the background fluorescence, the 340/380 nm ratio was analyzed offline using the SoftEdge Myo-Cam® system (IonOptix, Milton, MA, USA). Fluorescence emission was detected from 480 to 520 nm, and the quantitative change in Fluo-8 fluorescence intensity (FFI) was obtained from the FFI ratio at the 2 wavelengths. Regarding baseline FFI, the ΔFFI (340/380) reflects the resting intracellular Ca^{2+} level, electrically stimulated increase in intracellular Ca^{2+} level, and transient attenuation rate of intracellular Ca^{2+}. A single exponential tau value is presented as an indicator of intracellular Ca^{2+} clearance.

2.16. Western Blotting. Western blot analysis of total protein from CSCs was performed as previously described [41]. The protein extracts were separated by SDS-polyacrylamide gel electrophoresis (SDS-PAGE) and transferred onto PVDF membranes. After blocking overnight in a nonfat milk solution, the membranes were probed with primary antibodies against CaMKII, Bcl-2, Bax, procaspase-3, cleaved caspase-3, β-actin, or GAPDH. The PVDF membranes were incubated with horseradish peroxidase-conjugated secondary antibodies for 1 h, followed by incubation with enhanced chemiluminescence reagent (Amersham Biosciences, USA). Immunoreactivity was visualized by a ChemiDoc MP system

(Bio-Rad, USA), and protein levels were normalized to those of β-actin or GAPDH.

2.17. Statistical Analysis. All data were analyzed by Student's t-tests or one-way ANOVA, followed by least significant difference (LSD) or Dunnett's T3 post hoc test for multiple comparisons. A P value lower than 0.05 was considered statistically significant. Data analyses were carried out using SPSS (v.19.0, IBM, USA). Data are presented as the mean ± SD.

3. Results

3.1. Internalization of DiI-Labeled Exosomes by CSCs. CSCs purified by using anti-rabbit secondary antibody-conjugated magnetic beads [5, 30] were stained with the anti-C-kit antibody and counterstained with DAPI to visualize nuclei. Immunofluorescence staining and double staining for C-kit$^+$ and DAPI were detected (Figure 2(a)). FCM analysis also revealed that 90.01% of the cells were positive for C-kit, 0.09% were positive for CD45, and 0.01% were positive for CD34 (Figure 2(b)). Ultra-high-speed centrifugation was used to obtain BMSC-exos. Then, the morphology and phenotype of the isolated particles were characterized according to the previously described characteristics of exosomes. The exosomes were round with a cup-like shape and approximately 30–100 nm in diameter, as directly observed by a TEM (Figure 2(c)). NTA revealed that the particles had an average diameter of 111 nm (Figure 2(d)), typical of exosomes in such analyses. The exosome surface markers CD63, CD9, and Alix were detected by Western blotting in BMSC-exos (Figure 2(e)). These data demonstrated that the BMSC-exos were successfully purified.

Exosome internalization by target cells is a prerequisite for subsequent RNA transfer. To determine whether BMSC-exos are internalized by CSCs, we labeled the exosomes with DiI. After the labeled BMSC-exos (400 μg/ml) were incubated with CSCs for 24 h and counterstained with DAPI to visualize the nuclei, fluorescence microscopy analysis revealed a strong red fluorescence in the CSC cytoplasm and blue nuclei (Figure 2(f)), suggesting that the DiI-labeled exosomes had been successfully internalized and transferred to the perinuclear CSC compartments.

3.2. Hypoxia Preconditioning Enhanced the Ability of BMSC-Exos to Protect CSCs from Oxidative Damage. To investigate the regulatory effects of exosomes in CSCs, we prepared exosomes from BMSCs cultured in normal medium (Nor-exos) or in medium under hypoxic conditions (Hypoxic-exos). Exosome-free medium (Free-exos), which was prepared by ultra-high-speed centrifugation to eliminate exosomes from normal medium for culturing BMSCs was used as a control. CSCs ($>1 \times 10^9$) were cultured with BMSC-exos (400 μg/ml) for 24 h and then exposed to H_2O_2 (100 μM) for 2 h to induce oxidative stress. The FCM results indicated significantly higher apoptosis rates and ROS production levels in the H_2O_2-treated group than in the normal group. The CSCs pretreated with exosomes exhibited a significantly decreased

(a)

(b)

(c)

(d)

(e)

(f)
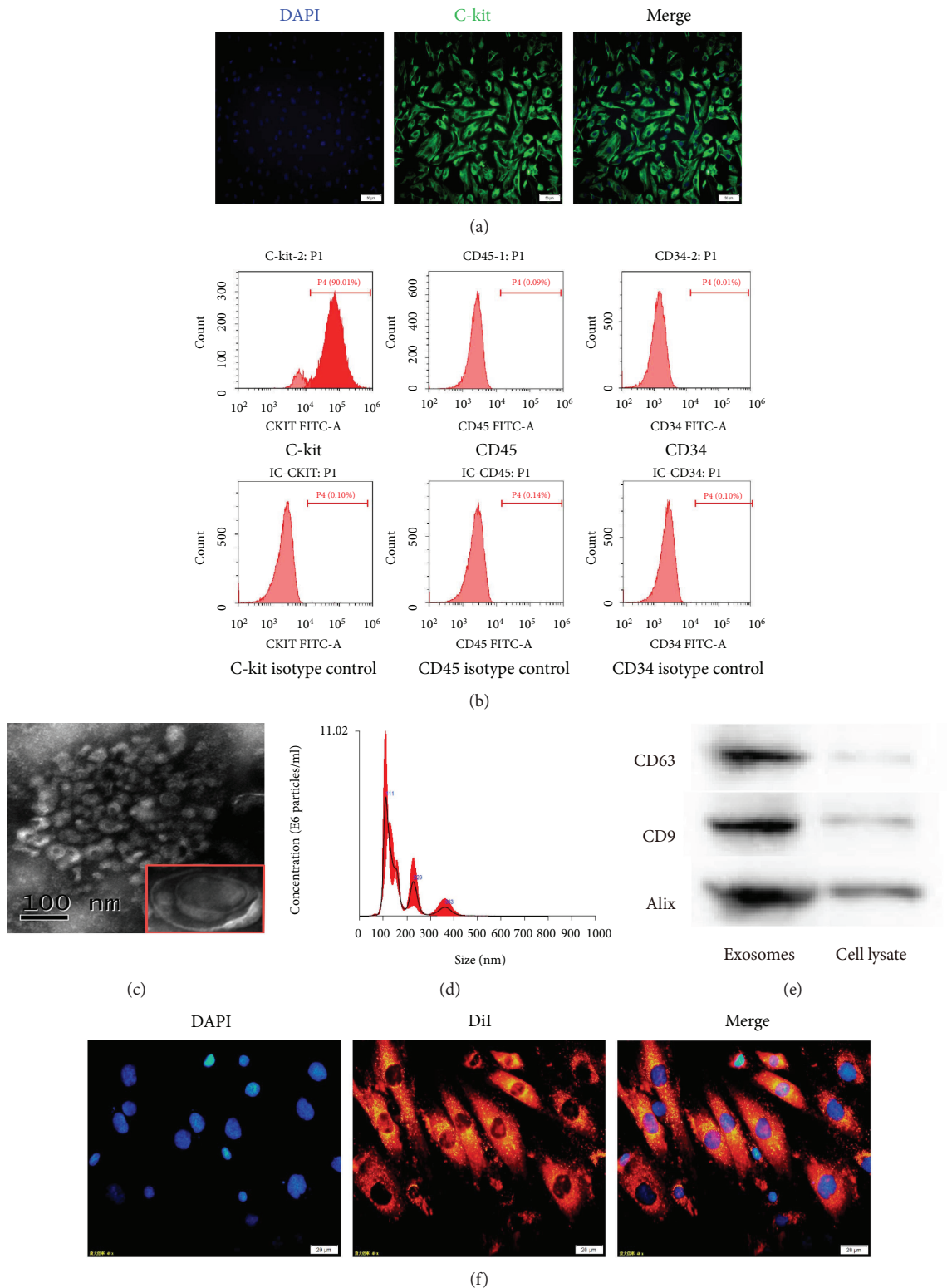
FIGURE 2: Characterization of C-kit$^+$ CSCs, exosomes, and cellular internalization. (a) Purified cells were double stained for c-kit (green) and DAPI (blue) and observed under a fluorescence microscope (Olympus, Japan). (b) Representative FCM characterization of C-kit$^+$ CSCs for typical surface antigens and isotype control after magnetic bead sorting. Surface expression of C-kit, and the absence of surface expression of CD45 and CD34. (c) Transmission electron microscopy analysis of BMSC-exos. Scale bar = 100 nm. (d) NTA of exosome diameter and concentration. (e) Western blotting of the exosome markers CD63, CD9, and Alix. (f) CSCs were incubated with DiI-labeled BMSC-exos (400 μg/ml) for 24 h. Fluorescence photomicrographs showed internalized DiI-labeled BMSC-exos (red) in DAPI-labeled CSCs (blue). Scale bar = 20 μm.

percentage of apoptotic cells and ROS production. Moreover, Hypoxic-exos induced more regulatory effects than did Nor-exos or Free-exos (Figures 3(a)–3(d)). The levels of cell apoptosis-related genes, such as procaspase-3, cleaved caspase-3, Bax, and Bcl-2 were also detected by Western blotting. Not surprisingly, compared with H_2O_2-treated cells, the cells treated with BMSC-exos displayed substantially decreased levels of cleaved caspase-3 and Bax increased levels of Bcl-2 (Figures 4(e) and 4(f)). Intracellular malondialdehyde (MDA) and superoxide dismutase (SOD) levels, which reflect oxidation levels, was also detected by assay kit. As exhibited in (Figures 4(g) and 4(h)), compared with H_2O_2 group, Hypoxic-exos inhibited MDA levels and increased SOD production. Next, we examined whether exosomes protected CSCs against H_2O_2-induced DNA fragmentation. As shown in (Figures 4(i) and 4(j)), the percentage of TUNEL-positive cells was significantly increased in the H_2O_2-treated group compared with that in the normal group. Furthermore, compared with the H_2O_2- or Nor-exo-treated group, the percentage of TUNEL-positive cells was significantly reduced in the Hypoxic-exo-treated group. Collectively, these results indicate that Hypoxic-exos might exert a strong protective effect against H_2O_2-induced oxidative damage in CSCs.

3.3. miR-214 Expression Increased in BMSC-Exos after Hypoxic Preconditioning and Was Potentially Involved in Protecting CSCs from Apoptosis.

It is important to investigate the content of miRs with potential biological functions in exosomes secreted under certain pathological conditions. The effect of hypoxia preconditioning on the miR-214 level in BMSC-exos was evaluated using RT-qPCR. Compared to that with Nor-exos, miR-214 expression was significantly upregulated with Hypoxic-exos (Figure 3(a)). This result provided a potential exosomal miR target that might affect oxidative stress injury in CSCs under conditions of oxidative stress. Furthermore, miR-214 levels were examined in H_2O_2-treated CSCs. Indeed, miR-214 levels were substantially downregulated in CSCs treated with H_2O_2 (Figure 3(b)), suggesting the existence of a possible negative connection between miR-214 and H_2O_2-induced oxidative damage in CSCs.

To verify the effects of miR-214 on CSCs and to further determine whether the effects of BMSC-exos on CSCs are miR-214 dependent, we treated CSCs with miR-214 inhibitors or mimics to modulate miR-214 levels. The miR-214 levels in Hypoxic-exos were also reduced after transfection of BMSCs with a miR-214 inhibitor, and the resulting exosomes were called inhibitor-exosomes (inhibitor-exos). RT-qPCR analysis of miR-214 expression revealed that CSCs pretreated with Hypoxic-exos or those transfected with miR-214 mimics had significantly rescued miR-214 levels, whereas miR-214 inhibitor-pretreated CSCs displayed a significant decrease in miR-214 expression under oxidative stress. Interestingly, CSCs pretreated with inhibitor-exos had significantly decreased miR-214 levels (Figure 3(b)), which indicated that miR-214 inhibitor could neutralize miR-214 upregulation in Hypoxic-exos. Next, the antiapoptosis and regulating oxidative stress effect were detected.

The results revealed that Hypoxic-exos or miR-214 mimics substantially downregulated CSC apoptosis and oxidative status (including ROS, SOD, and MDA), whereas the miR-214 inhibitor upregulated CSC apoptosis and oxidative status under oxidative stress, of course that transfected miR-214 inhibitor in Hypoxia-exos (inhibitor-exos) pretreated showed miR-214 inhibitor could partially neutralize the protective effect of Hypoxic-exos (Figures 3(c)–3(j)). Furthermore, procaspase-3, cleaved caspase-3, Bax, and Bcl-2 levels were detected by Western blotting. Quantification showed that cleaved caspase-3 and Bax expression levels were substantially decreased compared with cells treated with H_2O_2, in contrast, Bcl-2 expression was markedly increased in cells treated with Hypoxic-exos or miR-214 mimics. The miR-214 inhibitor or inhibitor-exos clearly increased cleaved caspase-3 and Bax expression but substantially decreased Bcl-2 expression in CSCs. However, inhibitor-exos also partially protected CSCs from oxidative stress-induced apoptosis (Figures 3(k) and 3(l)). These data confirmed the antioxidative stress function of miR-214 and suggested that rescuing downregulated miR-214 expression in CSCs with Hypoxic-exos is a potential strategy for protecting CSCs from oxidative stress injury.

3.4. miR-214 Derived from BMSC-Exos Decreased CaMKII Protein Expression.

Because miRs mainly target the mRNA $3'$UTR to regulate gene expression, we overexpressed the cDNA of CaMKII with or without the $3'$UTR to prove that CaMKII is a target gene of miR-214 in CSCs. Western blotting and RT-qPCR were employed to verify the effect of miR-214 mimics on CaMKII expression in CSCs. The results demonstrated that miR-214 mimics could significantly downregulate the expression of CaMKII with the $3'$UTR (CaMKII3$'$) at both mRNA and protein levels. However, miR-214 mimics had no effect on mRNA or protein levels of CaMKII without the $3'$UTR (Figures 5(a)–5(c)).

The effects of BMSC-exo-derived miR-214 on CaMKII expression in CSCs were also assessed. Compared with those in the normal group, CaMKII mRNA and protein levels were significantly upregulated in the H_2O_2 group and significantly downregulated in the Hypoxic-exos group (Figures 5(d)–5(f)), and inhibitor-exos failed to suppress CaMKII expression in CSCs. Furthermore, gain- and loss-of-function assays revealed that miR-214 inhibitors increased CaMKII mRNA or protein levels in CSCs under oxidative stress, whereas miR-214 mimics decreased these levels (Figures 5(d)–5(f)). These data indicated that exosomal miR-214 possibly inhibited CSC apoptosis by inhibiting CaMKII expression.

3.5. miR-214 Derived from BMSC-Exos Prevented CSCs from H_2O_2-Induced Oxidative Damage by Targeting CaMKII.

To examine the mechanisms responsible for the antiapoptotic effects of BMSC-exo-derived miR-214 in CSCs by targeting CaMKII, we overexpressed or inhibited CaMKII expression in CSCs, respectively, via lentiviruses expressing CaMKII containing the $3'$UTR (CaMKII3$'$) or SiRCaMKII containing the $3'$UTR (siRCaMKII3$'$). CaMKII3$'$ transfection

(a)

(b)

(c)

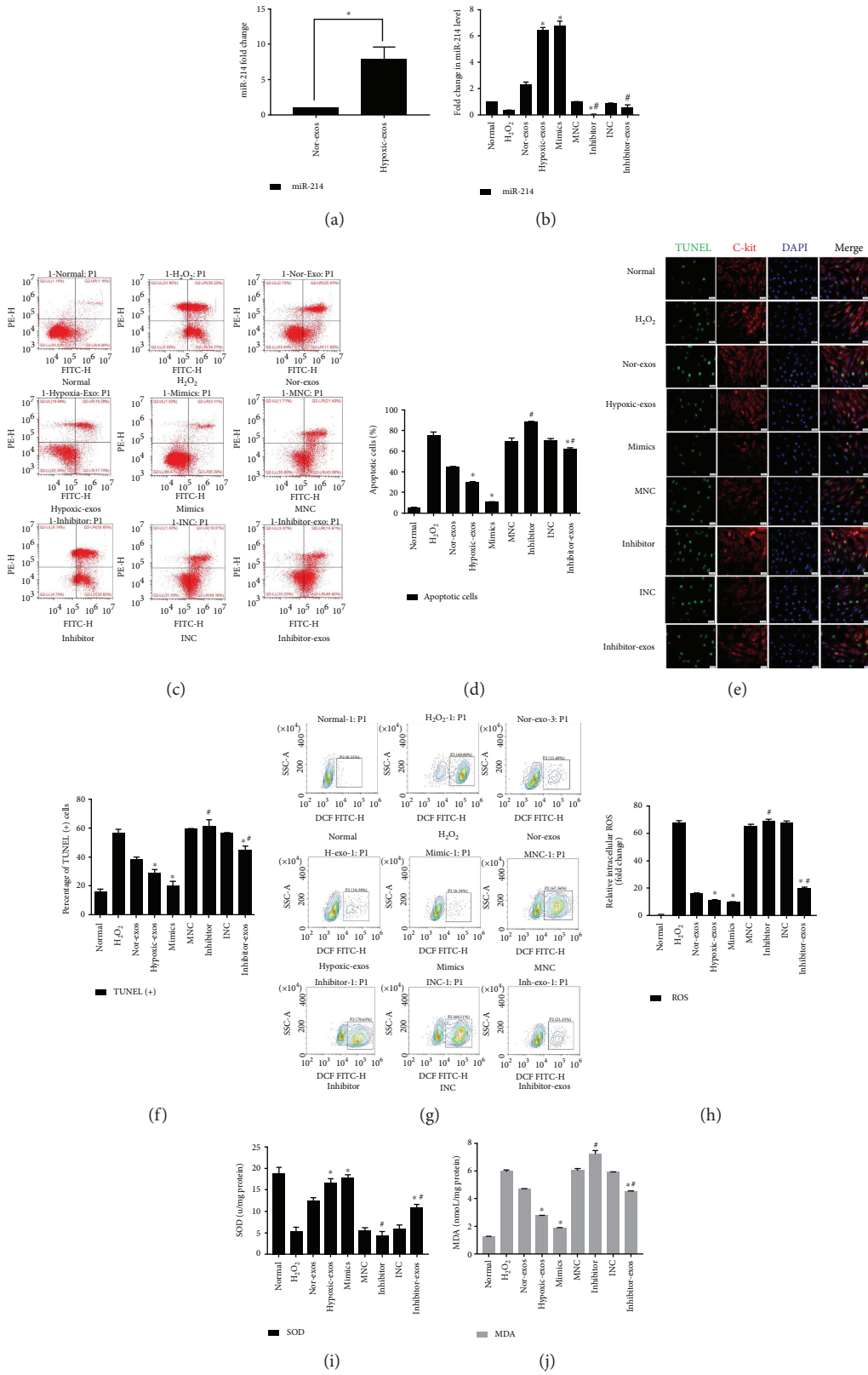(d)

(e)

(f)

(g)

(h)
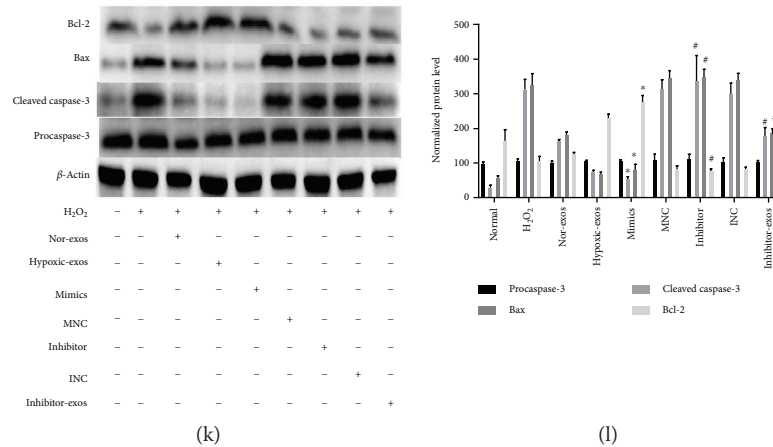

(i)

(j)

FIGURE 3: Continued.

(k)

(l)

FIGURE 3: Effect of miR-214 expression on CSC apoptosis under oxidative stress. Cells were treated with miR-214 mimics, inhibitors, or negative control RNA for 48 h and/or pretreated with BMSC-exos (400 μg/ml) for 24 h and then cultured with 100 μM H_2O_2 for 2 h for subsequent analyses. (a) RT-qPCR was used to analyze miR-214 expression in exosomes after normoxic or hypoxic preconditioning. Compared that in Nor-exos, miR-214 expression was significantly upregulated in Hypoxic-exos. (b) RT-qPCR analysis of miR-214 expression in CSCs after different treatments. Compared with that in the H_2O_2 group, miR-214 significantly upregulated in the Hypoxic-exos or miR-214 mimics group. Compared with the Hypoxic-exos group, the inhibitor-exos group displayed a significantly decreased miR-214 expression. (c) Representative dot plots of cell apoptosis after Annexin V/PI dual staining are shown. The upper left quadrant (% gated) shows necrotic cells (Annexin V−/PI+); the upper right quadrant (% fated) shows late apoptotic cells (Annexin V+/PI+); the left lower quadrant (% gated) shows live cells (Annexin V−/PI−); and the right lower quadrant (% gated) shows early apoptotic cells (Annexin V+/PI−). These cells were measured for comparison. (d) The percentage of apoptotic cells represents both early and late apoptotic cells. Compared with H_2O_2 or miR-214 inhibitor, Hypoxic-exos or miR-214 mimics decreased the percentage of apoptotic cells. In addition, the Hypoxic-exo-induced protective effect against CSC apoptosis under oxidative stress was partially suppressed by miR-214 inhibitors. (e) Representative immunofluorescence staining for TUNEL (green), C-kit (red), DAPI (blue), and merged images. Photos were randomly captured using a fluorescence microscope. Scale bar = 20 μm. (f) The panel shows the percentage of TUNEL-positive cells. Compared with H_2O_2 or miR-214 inhibitors, Hypoxic-exos or miR-214 mimics could significantly decrease the percentage of TUNEL-positive cells. In addition, compared with Hypoxic-exos, inhibitors-exos could partially increase the percentage of TUNEL-positive cells. (g) The intracellular ROS level was determined by FCM. The P2 percentage indicates the proportion of cells with increased ROS production, with signals above background DCF fluorescence levels. (h) Compared with that in CSCs treated with H_2O_2 or miR-214 inhibitors, the fluorescence intensity of intracellular ROS was decreased in CSCs treated with Hypoxic-exos or miR-214 mimics. Inhibitor-exos showed higher ROS fluorescence intensity than Hypoxic-exos. (i and j) Graph represents the SOD and MDA levels in CSCs, compared with H_2O_2 group, Hypoxic-exos or miR-214 mimics inhibited MDA levels and increased SOD production, while miR-214 inhibitors or inhibitor-exos increased MDA levels and suppressed SOD production. (k and l) The expression of apoptosis-related proteins, such as procaspase-3, cleaved caspase-3, Bax, and Bcl-2 were detected using immunoblotting. Compared with H_2O_2-treated cells, the cells treated with Hypoxic-exos or miR-214 mimics displayed substantially decreased cleaved caspase-3 and Bax expression and increased Bcl-2 expression. However, compared with Hypoxic-exos, miR-214 inhibitors or inhibitor-exos significantly increased cleaved caspase-3 and Bax expression but decreased Bcl-2 expression, $n = 3$; $^*P < 0.05$ compared with the H_2O_2 group; $^\#P < 0.05$ compared with the Hypoxic-exos group.

upregulated the CaMKII mRNA and protein levels in CSCs exposed to H_2O_2, whereas SiRCaMKII3′ transfection significantly downregulated CaMKII protein and mRNA levels in CSCs (Figures 6(a)–6(c)). Next, Annexin V/PI assays were used to detect the antiapoptotic effect of Hypoxic-exos via the CaMKII pathway. The percentage of apoptotic cells was higher in the CaMKII3′ group than in the Hypoxic-exos or SiRCaMKII3′ group. Interestingly, the percentage of apoptotic cells was increased in the Hypoxic-exos + Lv-CaMKII3′ group, whereas it was significantly decreased in the inhibitor-exos + SiRCaMKII3′ (Figures 6(d) and 6(e)). Besides, the percentages of TUNEL-positive cells in each group were in line with the apoptotic trend observed in Annexin V/PI assay (Figures 7(a) and 7(b)).

To detect intracellular ROS production, we exposed cells with different conditions and used FCM with H_2DCFDA, a fluorescent probe that reacts with several ROS. As anticipated, we detected a significant increase in fluorescence in the H_2O_2 group. The Hypoxic-exos and SiRCaMKII3′ groups displayed a significantly decreased ROS level. Intriguingly, CaMKII3′ overexpression induced a marked increase in CSC ROS fluorescence level. In addition, ROS fluorescence was upregulated in the Hypoxic-exos + Lv-CaMKII3′ group and downregulated in the inhibitor-exos + SiRCaMKII3′ group (Figures 6(f) and 6(g)). SOD and MDA were analyzed in CSCs as an indicator of activity of antioxidant enzymes. As shown in (Figure 7(e)), SOD in the H_2O_2-induced CSCs group was significantly lower than those of normal, whereas the SOD level of CSCs treated with Hypoxic-exos and siR-CaMKII3′ was higher than the H_2O_2 group. In addition, SOD level of cells transfected with CaMKII3′ was decreased compared with the Hypoxic-exos group. What is more, as
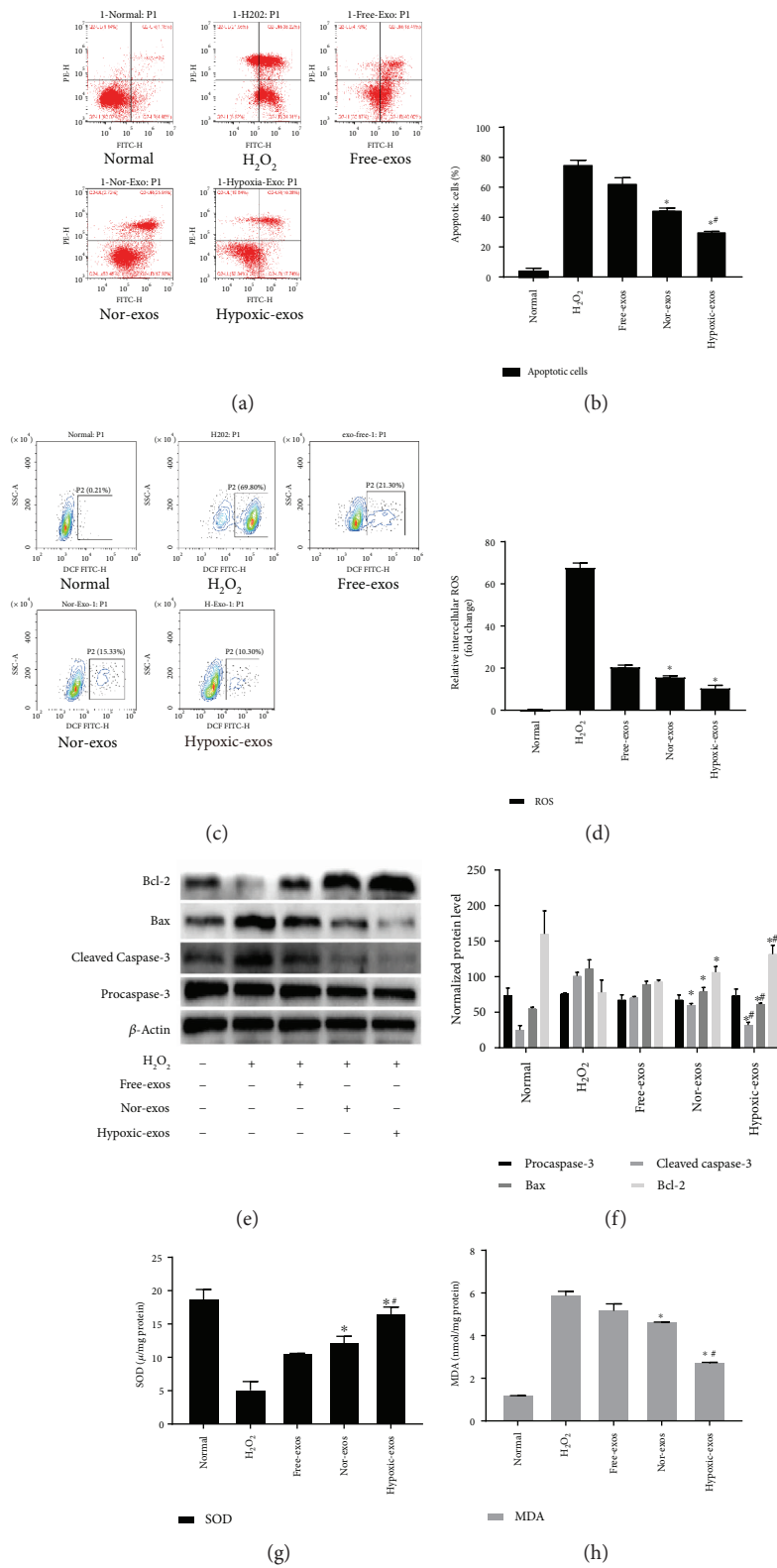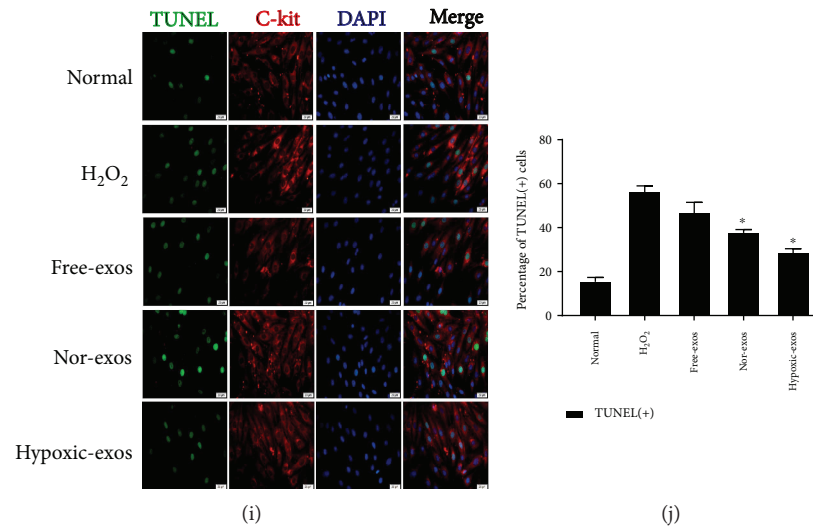
(a)

(b)

(c)

(d)

(e)

(f)

(g)

(h)

Figure 4: Continued.

(i)

(j)

FIGURE 4: Exosomes released from hypoxia-pretreated BMSCs protect CSCs from oxidative stress injury. CSCs cultured with $100\,\mu M$ H_2O_2 were pretreated with BMSC-exos ($400\,\mu g/ml$) for 24 h and then subjected to analysis. (a) Representative dot plots of cell apoptosis after Annexin V/PI dual staining are shown. The left upper quadrant (% gated) shows necrotic cells (Annexin V−/PI+); the upper right quadrant (% gated) shows late apoptotic cells (Annexin V+/PI+); the left lower quadrant (% gated) shows live cells (Annexin V−/PI−); and the right lower quadrant (% gated) shows early apoptotic cells (Annexin V+/PI−). These cells were measured for comparison. (b) The percentage of apoptotic cells represents both early and late apoptotic cells. Compared with the H_2O_2-treated group, the BMSC-exo-treated group displayed a decreased percentage of apoptotic cells. In addition, Hypoxic-exos more markedly decreased apoptosis than did Nor-exos or Free-exos. (c) The intracellular ROS level was determined by FCM. The P2 percentage indicates the proportion of cells with increased ROS production, with signals above background $2',7'$-dichlorofluorescein (DCF) fluorescence levels. (d) Compared with the H_2O_2-treated group, the BMSC-exo-treated group had a significantly decreased intracellular ROS fluorescence intensity. In addition, Hypoxic-exos decreased ROS fluorescence to a greater degree than did Nor-exos or Free-exos. (e and f) The effects of BMSC-exos on cell apoptosis-related genes, such as procaspase-3, cleaved caspase-3, Bax, and Bcl-2 were detected by immunoblotting. Compared with the H_2O_2-treated cells, the BMSC-exo-treated cells had substantially decreased levels of cleaved caspase-3 and Bax and increased levels of Bcl-2. Additionally, Hypoxic-exos more markedly affected these protein levels than did Nor-exos. (g and h) Graph represents the SOD and MDA levels in CSCs; compared with H_2O_2 group, Hypoxic-exos inhibited MDA levels and increased SOD production. (i) Representative immunofluorescence staining for TUNEL (green), C-kit (red), DAPI (blue), and merged images. Photos were randomly captured using a fluorescence microscope. Scale bar $= 20\,\mu m$. (j) The panel shows the percentage of TUNEL-positive cells. Compared with the H_2O_2-treated group, the BMSC-exo-treated group had significantly decreased percentage of TUNEL-positive cells. $n = 3$; $^*P < 0.05$ compared with the H_2O_2 group; $^\#P < 0.05$ compared with the Nor-exos group.

exhibited in (Figure 7(f)), induction of CSCs with H_2O_2 resulted in elevation of MDA, which was significantly different from Hypoxic-exos and siRCaMKII3$'$ group. However, the level of MDA in CSCs transfection with CaMKII3$'$ was significantly increased when compared with Hypoxic-exos group.

We also explored the expression of apoptosis-related proteins in CSCs by immunoblotting. Compared with Hypoxic-exos or CaMKII3$'$ silencing, CaMKII3$'$ overexpression substantially increased the expression of the proapoptotic proteins cleaved caspase-3 and Bax, then decreased the expression of the antiapoptotic protein Bcl-2. Notably, CaMKII3$'$ overexpression partially reversed the effect of Hypoxic-exos on caspase-3, Bax, and Bcl-2 expression, which was demonstrated by the increase in caspase-3 and Bax expression and the decrease in Bcl-2 expression. In addition, the inhibitor-exos + SiRCaMKII group displayed downregulated caspase-3 and Bax expression levels and upregulated Bcl-2 levels (Figures 7(c) and 7(d)). Considering the regulatory effects of CaMKII and miR-214 on Ca^{2+} homeostasis, we also detected Ca^{2+} fluorescence intensity in CSCs.

Compared with that in the H_2O_2 or CaMKII3$'$ group, the fluorescence intensity of intracellular Ca^{2+} was significantly decreased in the Hypoxic-exos or siRCaMKII3$'$ group (Figures 7(g) and 7(h)). Moreover, compared with inhibitor-exo + SIRCaMKII3$'$-treated CSCs, Hypoxic-exo + CaMKII3$'$-treated CSCs clearly displayed increased calcium fluorescence. These data indicated that under oxidative stress, Hypoxic-exos protected CSCs from apoptosis, ROS overproduction, and Ca^{2+} homeostasis disruption by suppressing CaMKII.

3.6. Exosomes Derived from miR-214-Modified BMSCs Protected CSCs from Apoptosis under Oxidative Stress via CaMKII. To further determine whether the effects of BMSC-exos on CSCs are dependent on miR-214, we transfected BMSCs with miR-214 mimics, inhibitors, or negative control RNA. At 48 h posttransfection, extracellular exosomes were isolated from BMSCs pretreated with hypoxia and added to CSCs under oxidative stress for 2 h. Clearly, compared with that in Hypoxic-exos, miR-214 was significantly upregulated in the miR-214 mimic-modified BMSC-
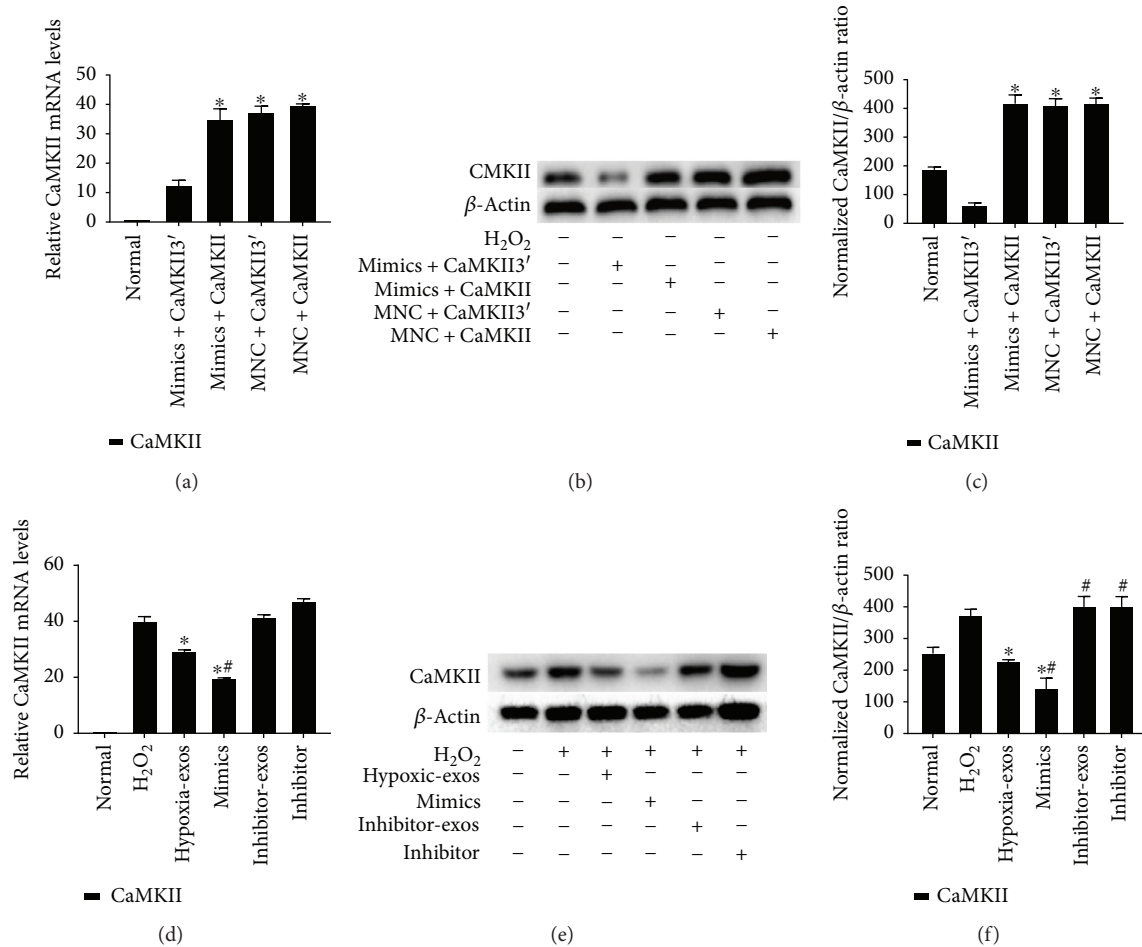
(a)

(b)

(c)

(d)

(e)

(f)

FIGURE 5: CaMKII is a target gene of miR-214 in CSCs. Cultured CSCs were transfected with CaMKII overexpression cDNA with or without the 3′UTR for 48 h. Subsequently, the cells were transfected with miR-214 mimics, inhibitors, or negative control RNA for 48 h. The cells were harvested and subjected to RT-qPCR or Western blotting analysis after treatment with BMSC-exos collected under different conditions for 24 h and/or cultured with 100 μM H_2O_2 for 2 h. (a) RT-qPCR analysis of CaMKII expression in CSCs after different treatments. After overexpressing cDNA for CaMKII containing the 3′UTR (CaMKII3′) in CSCs, CaMKII3′ mRNA levels dramatically decreased in response to treatment with miR-21 mimics as demonstrated by RT-qPCR. However, miR-214 mimics had no effect on mRNA levels of CaMKII without the 3′UTR. (b-c) CaMKII protein levels were detected by immunoblotting. miR-214 mimics could significantly downregulate the expression of CaMKII with the 3′UTR at protein levels. However, miR-214 mimics had no effect on the protein levels of CaMKII without the 3′UTR. $n = 3$; *$P < 0.05$ compared with the mimics + CaMKII3′ group. (d) RT-qPCR analysis of CaMKII expression in CSCs after different treatments. Compared with that in the normal group, the CaMKII mRNA level was significantly upregulated in the H_2O_2 group. Compared with H_2O_2, Hypoxic-exos or miR-214 mimics significantly suppressed CaMKII mRNA expression. (e-f) Western blotting was used to verify the effect of exosomal miR-214 on CaMKII expression in CSCs. CaMKII protein levels were dramatically decreased after Hypoxic-exo or mimic-exo (exosomes from miR-214-mimic-modified BMSCs) treatment relative to those with H_2O_2 treatment. However, compared with Hypoxic-exos, miR-214 inhibitors or inhibitor-exos upregulated CaMKII protein levels. $n = 3$; *$P < 0.05$ compared with the H_2O_2 group; #$P < 0.05$ compared with the Hypoxic-exos group.

exos (mimic-exos), while miR-214 was substantially down-regulated in inhibitor-exos (Figure 8(a)). Next, CaMKII mRNA or protein levels were detected by RT-qPCR or Western blotting. Compared with Hypoxic-exos or mimic-exos, inhibitor-exos upregulated CaMKII mRNA and protein levels in CSCs exposed to H_2O_2 (Figures 8(b)–8(d)).

Annexin V/PI assays were used to identify the antioxidative damage effect of mimic-exos. Compared with the H_2O_2 group, the Hypoxic-exos and mimic-exos groups displayed a substantially reduced apoptosis, whereas the inhibitor-exos group displayed elevated apoptosis (Figures 8(e) and

8(f)). As anticipated, the percentages of TUNEL-positive cells in each group were in line with the apoptotic trend observed in Annexin V/PI assay (Figures 8(g) and 8(h)). The production of ROS and intracellular levels of SOD and MDA was measured to confirm further the antioxidative ability of BMSCs-exos. In H_2O_2 group, the production of ROS and MDA was increased dramatically in comparison to that of Normal group, whereas, SOD level was extremely decreased. In contrast, While Hypoxic-exos and mimics-exos pretreatment significantly weakened this increase of ROS, MDA and decrease of
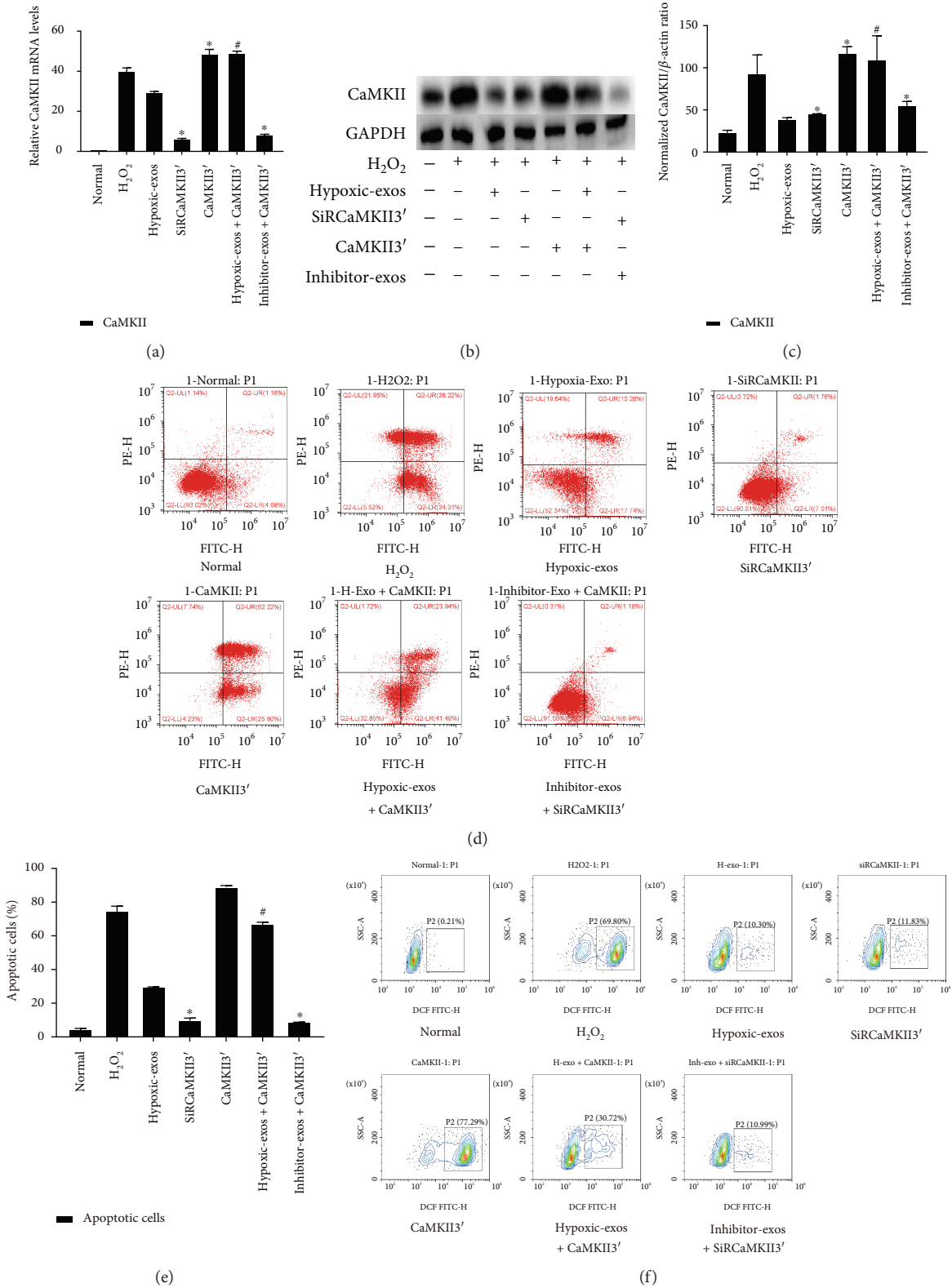
(a)

(b)

(c)
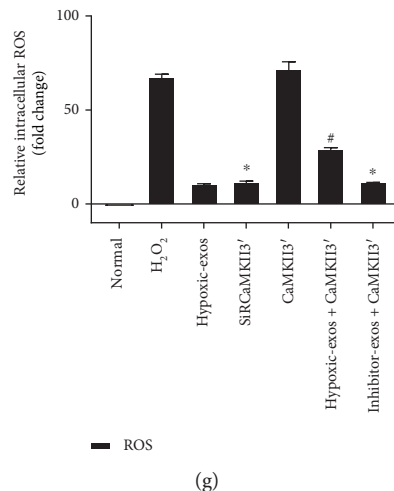
(d)

(e)

(f)

FIGURE 6: Continued.

(g)

FIGURE 6: Change in CaMKII expression during BMSC-exo-induced antiapoptotic effect in CSCs under oxidative stress. Cultured CSCs were transfected with CaMKII3′ overexpression cDNA or siRCaMKII3′ for 48 h. Then, the cells were treated with BMSC-exos under different conditions for 24 h and/or cultured with 100 μM H_2O_2 for 2 h. (a) RT-qPCR were carried out to detect CaMKII mRNA levels. Compared with other treatments, CaMKII3′ transfection significantly upregulated CaMKII expression, and SiRCaMKII3′ transfection significantly downregulated CaMKII mRNA levels in CSCs. (b-c) Western blotting revealed that compared with H_2O_2 treatment, CaMKII3′ transfection upregulated CaMKII protein levels, while SiRCaMKII3′ transfection downregulated CaMKII protein levels in CSCs. Additionally, compared with Hypoxic-exos, Hypoxic-exos + CaMKII3′ upregulated CaMKII protein levels. (d) Representative dot plots of cell apoptosis after Annexin V/PI dual staining are shown. The upper left quadrant (% gated) shows necrotic cells (Annexin V−/PI+); the upper right quadrant (% gated) shows late apoptotic cells (Annexin V+/PI+); the left lower quadrant (% gated) shows live cells (Annexin V−/PI−); and the right lower quadrant (% gated) shows early apoptotic cells (Annexin V+/PI-). These cells were measured for comparison. (e) The percentage of apoptotic cells represents both early and late apoptotic cells. Compared with the H_2O_2 group, the SiRCaMKII3′-transfected group displayed a decreased percentage of apoptotic cells. In addition, the Hypoxic-exo-induced protective effect on CSC apoptosis under oxidative stress was suppressed by CaMKII3′ overexpression. (f) Intracellular ROS level was determined by FCM. The P2 percentage indicates the proportion of cells with increased ROS production, with fluorescence levels above background DCF fluorescence levels. (g) Compared with that in H_2O_2-treated CSCs, fluorescence intensity of intracellular ROS was decreased in SiRCaMKII3′-treated CSCs. In addition, the Hypoxic-exo-induced protective effect on CSCs against oxidative stress injury was suppressed by CaMKII3′ overexpression. $n = 3$; $^*P < 0.05$ compared with the H_2O_2 group. $^\#P < 0.05$ compared with Hypoxic-exos group.

SOD. In addition, ROS and MDA was significantly increased in the inhibitor-exos group compared with Hypoxic-exos group. In contrast, Hypoxic-exos and mimics-exos dramatically increased SOD levels. Reversely, inhibitor-exos significantly inhibited SOD in CSCs (Figures 8(i), 8(j), and 8(m), 8(n)).

Apoptosis-related proteins were then detected by Western blotting. Indeed, compared with the H_2O_2-treated cells, mimics-exo-treated CSCs displayed substantially decreased expression of proapoptotic proteins cleaved caspase-3 and Bax and increased expression of the anti-apoptotic protein Bcl-2, while inhibitor-exo-treated cells displayed the opposite results, as demonstrated by increased caspase-3 and Bax levels and decreased Bcl-2 level (Figures 8(k) and 8(l)). Together, these data revealed that in vitro, the exosome-mediated stimulation of CSC apoptosis and oxidative status were dependent on miR-214 expression in exosome-producing cells, and miR-214 depletion reduced these functional effects in recipient cells.

4. Discussion

As CSCs have been shown to differentiate into myocardial cell types and to secrete a range of bioactive molecules

[2, 5], these cells are important candidates for cardiac regenerative therapy [4]. Accumulating experimental and clinical data has shown that CSC transplantation can effectively treat MI [8, 42]. However, after adoptive transfer, CSCs encounter various undesirable conditions including oxidative stress and inflammatory reactions [17, 43]. Pathological stimulation causes functional mitochondrial disruption and consequently results in excessive ROS generation; ROS, in turn, deteriorate mitochondrial dysfunction and amplify mitochondrial apoptosis activation in a positive feedback loop [44], decreasing cell viability and thereby compromising therapeutic activities. The paracrine effect of BMSCs has been considered a key mechanism of cardiac protection [14, 45]. Stress-activated exosome release is one of the crucial factors mediating the crosstalk among BMSCs and surrounding cells, which may be involved in maintaining stem cell homeostasis in situ and facilitating stem cell transplantation [15, 20, 46]. In the present study, we obtained round, double-membraned vesicles with a diameter of 30–100 nm from BMSC-conditioned medium by using ultra-high-speed centrifugation. These vesicles were determined to express specific exosome protein markers and to be internalized by CSCs, which indicated that these exosomes play roles in CSCs by transferring cargo.
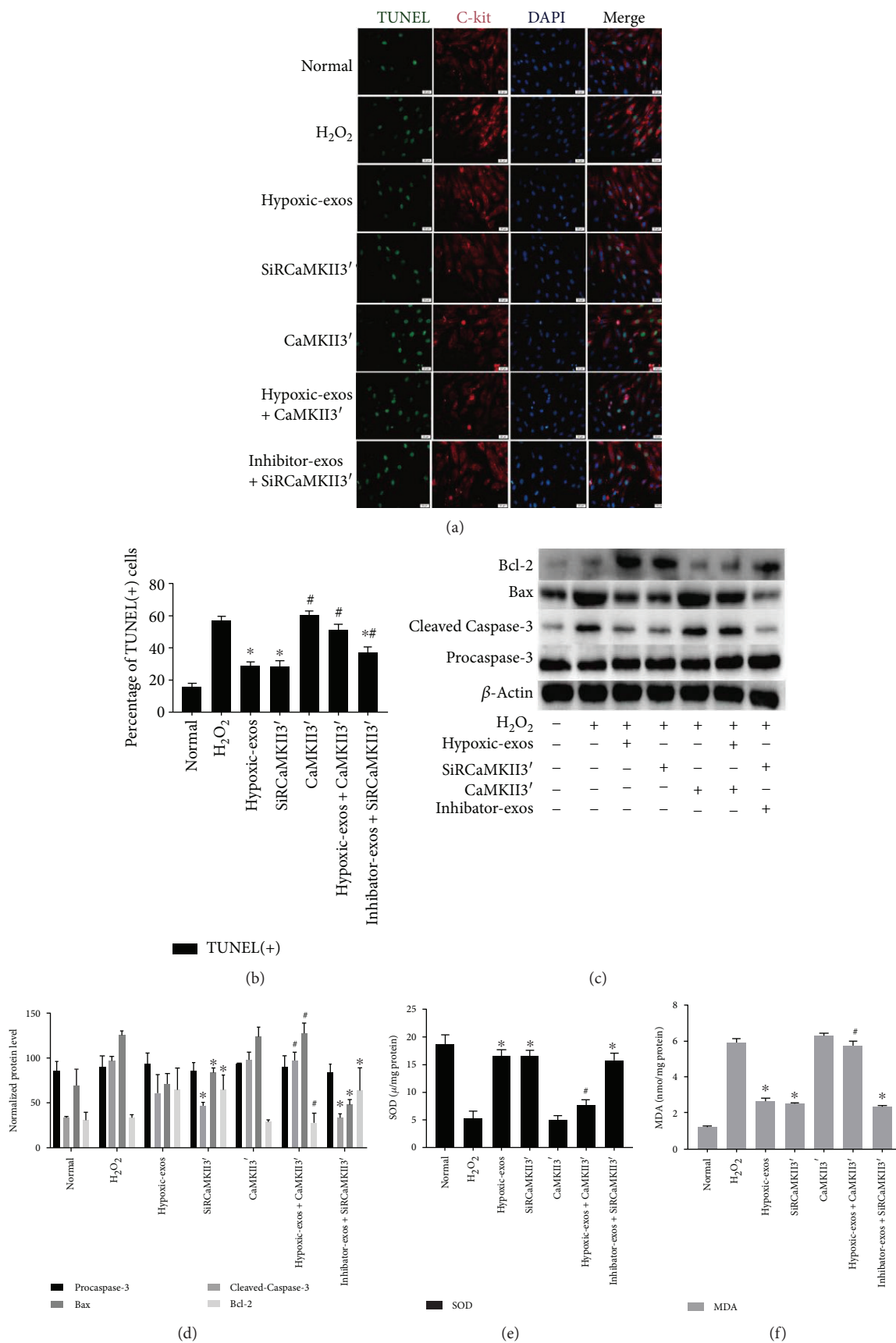
(a)

(b)

(c)

(d)

(e)

(f)

Figure 7: Continued.

Normal   H$_2$O$_2$ Hypoxic-exos   SiRCaMKII3$'$

CaMKII3$'$ Hypoxic-exos + CaMKII3$'$ Inhibator-exos + SiRCaMKII3$'$
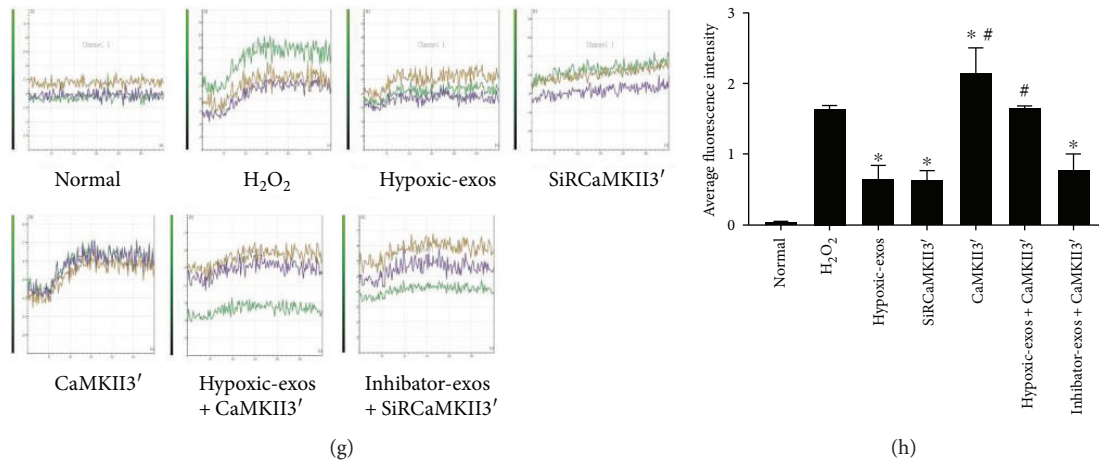
(g)

(h)

Figure 7: Change in CaMKII expression during BMSC-exo-induced antioxidative injury in CSCs under oxidative stress. Cultured CSCs were transfected CaMKII3$'$ overexpression cDNA or siRCaMKII3$'$ for 48 h. Then, the cells were treated with BMSC-exos under different conditions for 24 h and/or cultured with 100 μM H$_2$O$_2$ for 2 h. (a) Representative immunofluorescence staining for TUNEL (green), C-kit (red), DAPI (blue), and merged images. Photos were randomly captured using a fluorescence microscope. Scale bar = 20 μm. (b) The panel shows the percentages of TUNEL-positive cells. Compared with H$_2$O$_2$, SiRCaMKII3$'$ could significantly decreased the percentage of TUNEL-positive cells. Additionally, compared with Hypoxic-exos, CaMKII3$'$ could partially increase the percentage of TUNEL-positive cells. (c and d) The expression levels of procaspase-3, cleaved caspase-3, Bax, and Bcl-2 were detected by immunoblotting. Compared with Hypoxic-exos or SiRCaMKII3$'$ group, the CaMKII3$'$ group displayed substantially increased cleaved caspase-3 and Bax expression and decreased Bcl-2 expression. In addition, the Hypoxic-exo-induced protective effect against CSC apoptosis under oxidative stress was suppressed by CaMKII3$'$ overexpression. (e and f) Graph represents the SOD and MDA levels in CSCs; compared with H$_2$O$_2$ group, Hypoxic-exos or SiRCaMKII3$'$ inhibited MDA levels and increased SOD production, while CSCs were transfected with CaMKII3$'$ increased MDA levels and suppressed SOD production. (g) Transient intracellular Ca^{2+} measurement assays with Fluo-8/AM fluorescent labeling were used to detect Ca^{2+} concentration in CSCs exposed to different treatments. (h) Compared with that in the H$_2$O$_2$ or CaMKII3$'$ group, the fluorescence intensity of intracellular Ca^{2+} was significantly decreased in the Hypoxic-exos or siRCaMKII group. Furthermore, CaMKII3$'$ overexpression could suppress the Hypoxic-exo-induced protective effect against CSC oxidative stress injury. $n = 3$; $^*P < 0.05$ compared with the H$_2$O$_2$ group. $^\#P < 0.05$ compared with the Hypoxic-exos group.

In recent years, many studies have focused on the hypoxic BMSC niche. Hypoxic BMSC preconditioning can reduce hypoxia-induced cell death [47]. Some researchers have also found that BMSCs release exosomes under hypoxic conditions, resulting in neoangiogenesis in vitro and in vivo and enhanced cardiac function [15]. However, whether exosomes released by BMSCs after hypoxic preconditioning have increased beneficial effects on CSC regulation under oxidative stress conditions remains unknown. Oxidative stress originates mainly in the mitochondria from ROS and can be identified in the pathophysiology of the consequential clinical manifestations of cardiovascular diseases [48]. H$_2$O$_2$ induces oxidative stress, which may cause cell damage [49]. In this study, we found that H$_2$O$_2$ increased apoptosis rate and ROS production in CSCs. Additionally, CSCs pretreated with exosomes displayed a substantially alleviated response. Moreover, Hypoxic-exos had a greater regulatory effect than Nor-exos. This is likely a result of the alteration in miR expression profile in exosomes upon the in vitro exposure of BMSCs to pathological conditions [50]; the exosomal miR content is dynamically regulated after other types of stem cells are exposed to hypoxia, and this difference in the physiological response was not due to exosome size, total RNA content, or protein levels, since these values are similar among exosome in the different groups [23].

miRs are small, noncoding RNAs that block translation or induce mRNA degradation and thereby control gene expression patterns [18]. We focused on miR-214, which is expressed at low levels in CSCs after ROS production and has a role in antioxidation. Interestingly, we demonstrated that hypoxia not only increased the antiapoptotic effect of exosomes from conditioned BMSC culture medium but also changed exosomal miR-214 levels. Our results also demonstrated that oxidative stress decreased miR-214 levels in CSCs, indicating that miR-214 may be one of the key factors regulating CSC function under oxidative stress and suggesting that miR-214 enrichment may be an interesting area for future proregenerative studies. We established in vitro miR-214 gain- and loss-of-function models to assess the effect of miR-214 on apoptosis and found that upregulated miR-214 levels effectively decreased CSC apoptosis and ROS production. In addition, we discovered that the exosomes derived from hypoxia-treated BMSCs showed a strong ability to increase miR-214 levels in receptor cells. Interestingly, miR-214 depletion in BMSCs downregulates hypoxia-induced exosomal miR-214 levels. However, inhibitor-exos partially reversed the functional effects in recipient cells, likely because BMSC-exos contain various types of miRs, including miR-214. If miR levels are increased in Hypoxic-exos,

(a)
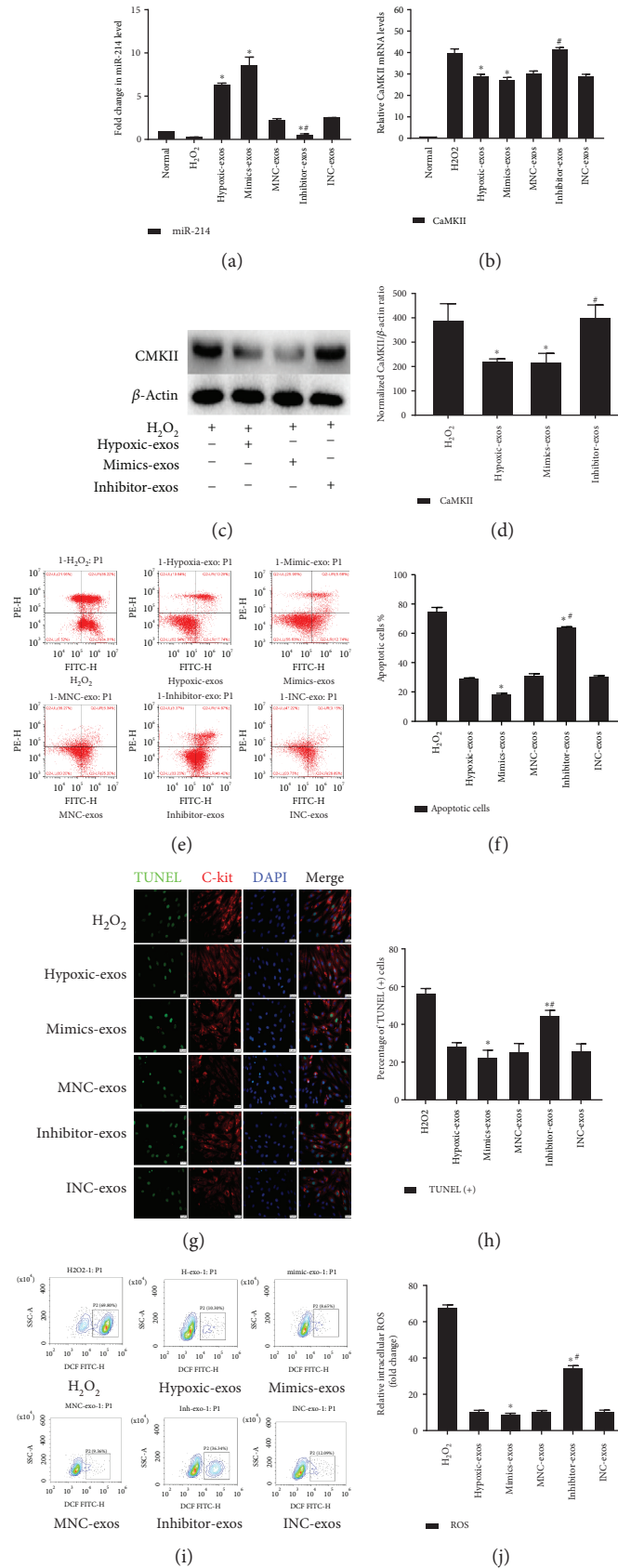
(b)

(c)

(d)

(e)

(f)

(g)
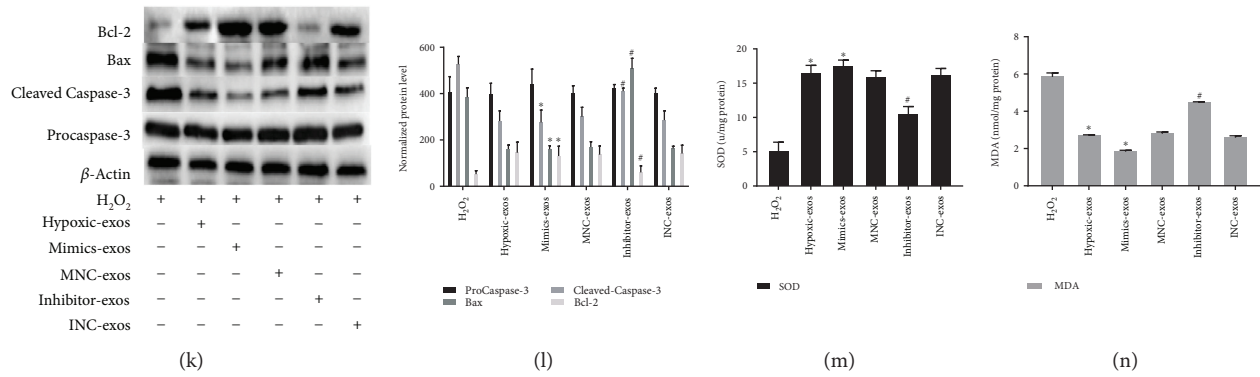
(h)

(i)

(j)

Figure 8: Continued.

FIGURE 8: Exosomes derived from miR-214-modified BMSCs exert an antiapoptotic effect on CSCs under oxidative stress. BMSCs were transfected with miR-214 mimics, inhibitors, or negative control RNA. At 48 h posttransfection, exosomes were isolated from BMSCs pretreated with hypoxia and then added to CSCs under oxidative stress for 2 h. (a) RT-qPCR analysis of miR-214 expression in CSCs after different treatments. Compared with that in the H_2O_2 group, miR-214 was significantly upregulated in mimic-exos group and substantially downregulated in the inhibitor-exos group. (b) RT-qPCR analysis of CaMKII mRNA expression in CSCs after different treatments. Compared with that in the H_2O_2 group, CaMKII mRNA was significantly downregulated in the mimic-exos group but substantially upregulated in the inhibitor-exos group. (c and d) Western blotting was carried out to detect CaMKII protein levels, which revealed that compared with those in H_2O_2-treated CSCs, CaMKII levels were significantly downregulated in Hypoxic-exo- or mimic-exo-treated CSCs, whereas CaMKII protein levels were significantly upregulated in inhibitor-exo-treated CSCs. (e) Representative cell apoptosis dot plots after Annexin V/PI dual staining are shown. The upper left quadrant (% gated) shows necrotic cells (Annexin V−/PI +); the upper right quadrant (% gated) shows late apoptotic cells (Annexin V+/PI+); the left lower quadrant (% gated) shows live cells (Annexin V−/PI−); and the right lower quadrant (% gated) shows early apoptotic cells (Annexin V+/PI−). These cells were measured for comparison. (f) The percentage of apoptotic cells represents both early and late apoptotic cells. Compared with the H_2O_2 group, the Hypoxic-exos or mimic-exos group displayed a decreased percentage of apoptotic cells. In addition, compared with Hypoxic-exos, inhibitor-exos increased the percentage of apoptotic cells. (g) Representative immunofluorescence staining for TUNEL (green), C-kit (red), DAPI (blue), and merged images. Photos were randomly captured using a fluorescence microscope. Scale bar = 20 μm. (h) The panel shows the percentage of TUNEL-positive cells. Compared with H_2O_2, Hypoxic-exos or mimic-exos could significantly decrease the percentage of TUNEL-positive cells. Additionally, compared with Hypoxic-exos, inhibitor-exos could partially increase the percentage of TUNEL-positive cells. (i) The intracellular ROS level was determined by FCM. The P2 percentage indicates the proportion of cells with increased ROS production, with signals above background DCF fluorescence levels. (j) Compared with that in H_2O_2-treated CSCs, the fluorescence intensity of intracellular ROS was decreased in Hypoxic-exo- or mimic-exo-treated CSCs. However, compared with Hypoxic-exos, inhibitor-exos decreased the fluorescence intensity of intracellular ROS in CSCs. (k and l) The expression levels of procaspase-3, cleaved caspase-3, Bax, and Bcl-2 were detected by immunoblotting. Compared with H_2O_2 or inhibitor-exos, Hypoxic-exos or mimic-exos substantially decreased cleaved caspase-3 and Bax expression and increased Bcl-2 expression. (m and n) Graph represents the SOD and MDA levels in CSCs; compared with H_2O_2 group, Hypoxic-exos or mimics-exos inhibited MDA levels and increased SOD production, while inhibitor-exos group increased MDA levels and suppressed SOD production. $n = 3$; $^*P < 0.05$ compared with the H_2O_2 group; $^{\#}P < 0.05$ compared with the Hypoxic-exos group.

these miRs will be transferred to recipient cells and promoted to play their biological role primarily through their target genes [23, 51, 52]. Therefore, our data indicated an intricate exosome-mediated crosstalk between BMSCs and CSCs that regulates oxidative damage, at least partly, via miR-214.

miR transfer between cells can activate recipient cells to produce a series of biological effects by inhibiting miR target genes. NCX1, CaMKII, CypD, and BIM are regulated by miR-214 in many cell types [11]. These genes are critical for regulating cell proliferation, apoptosis, and Ca^{2+} homeostasis [53]. In miR-214 knockout (KO) mice, increased CaMKII levels have been reported to contribute to additional cardiomyocyte loss. miR-214 is likely cardioprotective and targets CaMKII under a variety of stress conditions [11]. Interestingly, some studies have found that CaMKII may serve as a novel modulatory protein for enhancing cardiac progenitor cell survival in cardiac tissues [54]. To further confirm whether CaMKII is also a target gene of miR-214 in CSCs, we overexpressed cDNA of CaMKII with or

without the 3′UTR. Simultaneously, we overexpressed miR-214 mimics in these CSCs and found that miR-214 mimics could significantly downregulate the expression of CaMKII with the 3′UTR at both mRNA and protein levels. Nonetheless, miR-214 had no effect on mRNA or protein levels of CaMKII without the 3′UTR. The results indirectly verified that miR-214 mainly targets CaMKII mRNA the 3′UTR to regulate its gene expression. Furthermore, we performed gain- and loss-of-function studies and found that in CSCs, CaMKII mRNA and protein levels were upregulated in response to oxidative stress, and miR-214 inhibitors increased while miR-214 mimics decreased CaMKII mRNA and protein levels in CSCs. Importantly, CaMKII protein levels were significantly downregulated in the Hypoxic-exos group, whereas inhibitor-exos failed to suppress CaMKII expression in CSCs. Based on these results, upregulated miR-214 levels effectively decrease CSC apoptosis and oxidative stress, and CaMKII is negatively regulated by miR-214 expression in oxidative stress-induced CSCs.

To address whether CaMKII signaling is responsible for exosome-mediated antiapoptotic effects, we overexpressed CaMKII by synthesizing a CaMKII (containing the $3'UTR$) lentiviral vector and blocked CaMKII with CaMKII-targeting siRNA (containing the $3'UTR$) in CSCs after pretreating the cells with exosomes. We found that oxidative stress and apoptosis were decreased in Hypoxic-exo-pretreated or CaMKII-silenced CSCs. CaMKII overexpression partially reversed these Hypoxic-exo-induced antiapoptotic and oxidative stress effects. Clearly, inhibiting CaMKII prevented H_2O_2-induced injury in CSCs pretreated with inhibitor-exos. The CaMKII pathway is involved in inhibiting apoptosis, regulating Ca^{2+} homeostasis and promoting cell proliferation [53]. miR-214-mediated Ca^{2+} handling and gene signaling regulation are important contributors to the pathophysiology of a wide range of cardiac diseases [11]. Considering the effects of CaMKII on Ca^{2+} homeostasis regulation, we also detected Ca^{2+} fluorescence intensity in CSCs and found that Ca^{2+} fluorescence intensity was increased in response to oxidative stress in the presence of Nor-exos, and Hypoxic-exos and siRCaMKII decreased Ca^{2+} fluorescence intensity, consistent with antiapoptotic effects. CaMKII overexpression partially reversed the Hypoxic-exo-induced effects on Ca^{2+} homeostasis regulation. Moreover, inhibitor-exos reduced Ca^{2+} fluorescence intensity while blocking CaMKII levels. To further determine whether these effects of BMSC-exos on CSCs were miR-214-dependent, we cultured CSCs with mimic-exos. Compared with that in H_2O_2-treated cells, miR-214 expression was significantly upregulated in mimic-exo-treated cells. In contrast, miR-214 expression was substantially downregulated in the inhibitor-exo-exposed cells. Compared with Hypoxic-exos or mimic-exos, inhibitor-exos upregulated CaMKII mRNA and protein levels in CSCs exposed to H_2O_2. Furthermore, Hypoxic-exos and mimic-exos substantially decreased the percentage of apoptotic cells and oxidative stress level in CSCs, whereas inhibitor-exos induced the opposite effect. These findings strongly suggested that CaMKII is the underlying factor by which exosomal miR-214 mediates cellular protection.

It has been demonstrated that exosomes regulate cell-to-cell communication, such as crosstalk between stromal cells and breast cancer cells [55] and between mesenchymal stem cells and endothelial cells [56]. Regardless, our understanding of exosome biogenesis and endocytosis is incomplete, and whether exosomes specifically recognize their receptor cells still needs to be explored in depth. In our study, when CSCs were pretreated with BMSCs-exos, the exosomes were taken up with high efficiency, and exosomal miR-214 was transferred into CSCs and participated in cellular signaling pathways. This transfer successfully induced a downstream response and decreased CaMKII expression, cell apoptosis, oxidative stress, and Ca^{2+} homeostasis disruption in CSCs.

In conclusion, BMSC-exos pretreated with hypoxia effectively inhibit CSC apoptosis under oxidative stress by altering the miR-214/CaMKII pathway. Although our data suggest that BMSC-derived exosomal miR-214 plays a critical role in the apoptotic regulation of recipient cells, there are some limitations in this study. We cannot exclude the contribution of other exosomal cargo. Notably, BMSC-exos contain various types of miRs, including miR-214; in addition, miR-214 targets more than one gene, and CaMKII is not the only pathway downstream of miR-214.

Data Availability

The data used to support the findings of this study are available from the corresponding author upon request.

Ethical Approval

All experimental procedures were performed according to the "Guide for the Care and Use of Laboratory Animals" in China and were approved by the Experimental Animal Care and Use Committee of Zunyi Medical College.

Conflicts of Interest

The authors declare that no competing interests exist regarding the publication of this paper.

Authors' Contributions

Yan Wang and Ranzun Zhao contributed equally to this work.

Acknowledgments

References

[1] A. P. Beltrami, L. Barlucchi, D. Torella et al., "Adult cardiac stem cells are multipotent and support myocardial regeneration," *Cell*, vol. 114, no. 6, pp. 763–776, 2003.

[2] A. E. Mayfield, E. L. Tilokee, and D. R. Davis, "Resident cardiac stem cells and their role in stem cell therapies for myocardial repair," *The Canadian Journal of Cardiology*, vol. 30, no. 11, pp. 1288–1298, 2014.

[3] K. U. Hong and R. Bolli, "Cardiac stem cell therapy for cardiac repair," *Current Treatment Options in Cardiovascular Medicine*, vol. 16, no. 7, p. 324, 2014.

[4] R. Bolli, X. L. Tang, S. K. Sanganalmath et al., "Intracoronary delivery of autologous cardiac stem cells improves cardiac function in a porcine model of chronic ischemic cardiomyopathy," *Circulation*, vol. 128, no. 2, pp. 122–131, 2013.

[5] X. L. Tang, Q. Li, G. Rokosh et al., "Long-term outcome of administration of c-kit^POS cardiac progenitor cells after acute myocardial infarction: transplanted cells do not become cardiomyocytes, but structural and functional improvement and proliferation of endogenous cells persist for at least one year," *Circulation Research*, vol. 118, no. 7, pp. 1091–1105, 2016.

[6] S. Taghavi, T. E. Sharp III, J. M. Duran et al., "Autologous c-kit+ mesenchymal stem cell injections provide superior therapeutic benefit as compared to c-kit+ cardiac-derived stem cells in a feline model of isoproterenol-induced cardiomyopathy," *Clinical and Translational Science*, vol. 8, no. 5, pp. 425–431, 2015.

[7] K. U. Hong, Q. H. Li, Y. Guo et al., "A highly sensitive and accurate method to quantify absolute numbers of c-kit+ cardiac stem cells following transplantation in mice," *Basic Research in Cardiology*, vol. 108, no. 3, p. 346, 2013.

[8] K. Malliaras, R. R. Makkar, R. R. Smith et al., "Intracoronary cardiosphere-derived cells after myocardial infarction: evidence of therapeutic regeneration in the final 1-year results of the CADUCEUS trial (CArdiosphere-Derived aUtologous stem CElls to reverse ventricUlar dySfunction)," *Journal of the American College of Cardiology*, vol. 63, no. 2, pp. 110–122, 2014.

[9] J. A. Cho, Y. S. Lee, S. H. Kim, J. K. Ko, and C. W. Kim, "MHC independent anti-tumor immune responses induced by Hsp70-enriched exosomes generate tumor regression in murine models," *Cancer Letters*, vol. 275, no. 2, pp. 256–265, 2009.

[10] S. Hu, M. Huang, P. K. Nguyen et al., "Novel microRNA prosurvival cocktail for improving engraftment and function of cardiac progenitor cell transplantation," *Circulation*, vol. 124, no. 11, Supplement 1, pp. S27–S34, 2011.

[11] A. B. Aurora, A. I. Mahmoud, X. Luo et al., "MicroRNA-214 protects the mouse heart from ischemic injury by controlling Ca^{2+} overload and cell death," *The Journal of Clinical Investigation*, vol. 122, no. 4, pp. 1222–1232, 2012.

[12] J. Park, B. Kim, J. Han et al., "Graphene oxide flakes as a cellular adhesive: prevention of reactive oxygen species mediated death of implanted cells for cardiac repair," *ACS Nano*, vol. 9, no. 5, pp. 4987–4999, 2015.

[13] P. P. Gan, Y. Y. Zhou, M. Z. Zhong, Y. Peng, L. Li, and J. H. Li, "Endoplasmic reticulum stress promotes autophagy and apoptosis and reduces chemotherapy resistance in mutant p53 lung cancer cells," *Cellular Physiology and Biochemistry*, vol. 44, no. 1, pp. 133–151, 2017.

[14] B. Yu, H. W. Kim, M. Gong et al., "Exosomes secreted from GATA-4 overexpressing mesenchymal stem cells serve as a reservoir of anti-apoptotic microRNAs for cardioprotection," *International Journal of Cardiology*, vol. 182, pp. 349–360, 2015.

[15] S. Bian, L. Zhang, L. Duan, X. Wang, Y. Min, and H. Yu, "Extracellular vesicles derived from human bone marrow mesenchymal stem cells promote angiogenesis in a rat myocardial infarction model," *Journal of Molecular Medicine*, vol. 92, no. 4, pp. 387–397, 2014.

[16] R. C. Lai, F. Arslan, M. M. Lee et al., "Exosome secreted by MSC reduces myocardial ischemia/reperfusion injury," *Stem Cell Research*, vol. 4, no. 3, pp. 214–222, 2010.

[17] W. Deng, Y. Wang, X. Long et al., "miR-21 reduces hydrogen peroxide-induced apoptosis in c-kit$^+$ cardiac stem cells in vitro through PTEN/PI3K/Akt signaling," *Oxidative Medicine and Cellular Longevity*, vol. 2016, Article ID 5389181, 14 pages, 2016.

[18] E. M. Small, R. J. A. Frost, and E. N. Olson, "MicroRNAs add a new dimension to cardiovascular disease," *Circulation*, vol. 121, no. 8, pp. 1022–1032, 2010.

[19] C. Darido, S. R. Georgy, T. Wilanowski et al., "Targeting of the tumor suppressor GRHL3 by a miR-21-dependent proto-oncogenic network results in PTEN loss and tumorigenesis," *Cancer Cell*, vol. 20, no. 5, pp. 635–648, 2011.

[20] E. Cervio, L. Barile, T. Moccetti, and G. Vassalli, "Exosomes for intramyocardial intercellular communication," *Stem Cells International*, vol. 2015, Article ID 482171, 10 pages, 2015.

[21] M. Hulsmans and P. Holvoet, "MicroRNA-containing microvesicles regulating inflammation in association with atherosclerotic disease," *Cardiovascular Research*, vol. 100, no. 1, pp. 7–18, 2013.

[22] J. P. G. Sluijter, V. Verhage, J. C. Deddens, F. van den Akker, and P. A. Doevendans, "Microvesicles and exosomes for intracardiac communication," *Cardiovascular Research*, vol. 102, no. 2, pp. 302–311, 2014.

[23] W. D. Gray, K. M. French, S. Ghosh-Choudhary et al., "Identification of therapeutic covariant microRNA clusters in hypoxia-treated cardiac progenitor cell exosomes using systems biology," *Circulation Research*, vol. 116, no. 2, pp. 255–263, 2015.

[24] G. Lv, S. Shao, H. Dong, X. Bian, X. Yang, and S. Dong, "MicroRNA-214 protects cardiac myocytes against H_2O_2-induced injury," *Journal of Cellular Biochemistry*, vol. 115, no. 1, pp. 93–101, 2014.

[25] B. W. M. van Balkom, O. G. de Jong, M. Smits et al., "Endothelial cells require miR-214 to secrete exosomes that suppress senescence and induce angiogenesis in human and mouse endothelial cells," *Blood*, vol. 121, no. 19, pp. 3997–4006, 2013.

[26] H. Toko, H. Takahashi, Y. Kayama et al., "Ca^{2+}/calmodulin-dependent kinase IIδ causes heart failure by accumulation of p53 in dilated cardiomyopathy," *Circulation*, vol. 122, no. 9, pp. 891–899, 2010.

[27] B. Yoo, A. Lemaire, S. Mangmool et al., "β1-adrenergic receptors stimulate cardiac contractility and CaMKII activation in vivo and enhance cardiac dysfunction following myocardial infarction," *American Journal of Physiology-Heart and Circulatory Physiology*, vol. 297, no. 4, pp. H1377–H1386, 2009.

[28] F. D. Toledo, L. M. Pérez, C. L. Basiglio, J. E. Ochoa, E. J. Sanchez Pozzi, and M. G. Roma, "The Ca^{2+}-calmodulin-Ca^{2+}/calmodulin-dependent protein kinase II signaling pathway is involved in oxidative stress-induced mitochondrial permeability transition and apoptosis in isolated rat hepatocytes," *Archives of Toxicology*, vol. 88, no. 9, pp. 1695–1709, 2014.

[29] M. Federico, E. L. Portiansky, L. Sommese et al., "Calcium-calmodulin-dependent protein kinase mediates the intracellular signalling pathways of cardiac apoptosis in mice with impaired glucose tolerance," *The Journal of Physiology*, vol. 595, no. 12, pp. 4089–4108, 2017.

[30] B. Shi, Y. Wang, R. Zhao, X. Long, W. Deng, and Z. Wang, "Bone marrow mesenchymal stem cell-derived exosomal miR-21 protects C-kit$^+$ cardiac stem cells from oxidative injury through the PTEN/PI3K/Akt axis," *PLoS One*, vol. 13, no. 2, article e0191616, 2018.

[31] B. Shi, X. Long, R. Zhao, Z. Liu, D. Wang, and G. Xu, "Transplantation of mesenchymal stem cells carrying the human receptor activity-modifying protein 1 gene improves cardiac function and inhibits neointimal proliferation in the carotid angioplasty and myocardial infarction rabbit model," *Experimental Biology and Medicine*, vol. 239, no. 3, pp. 356–365, 2014.

[32] L. Wei, J. L. Fraser, Z. Y. Lu, X. Hu, and S. P. Yu, "Transplantation of hypoxia preconditioned bone marrow mesenchymal stem cells enhances angiogenesis and neurogenesis after cerebral ischemia in rats," *Neurobiology of Disease*, vol. 46, no. 3, pp. 635–645, 2012.

[33] M. Colombo, G. Raposo, and C. Thery, "Biogenesis, secretion, and intercellular interactions of exosomes and other

extracellular vesicles," *Annual Review of Cell and Developmental Biology*, vol. 30, no. 1, pp. 255–289, 2014.

[34] J. M. Vicencio, D. M. Yellon, V. Sivaraman et al., "Plasma exosomes protect the myocardium from ischemia-reperfusion injury," *Journal of the American College of Cardiology*, vol. 65, no. 15, pp. 1525–1536, 2015.

[35] N. Yin, R. Lu, J. Lin, S. Zhi, J. Tian, and J. Zhu, "Islet-1 promotes the cardiac-specific differentiation of mesenchymal stem cells through the regulation of histone acetylation," *International Journal of Molecular Medicine*, vol. 33, no. 5, pp. 1075–1082, 2014.

[36] S. Bobis-Wozowicz, K. Kmiotek, M. Sekula et al., "Human induced pluripotent stem cell-derived microvesicles transmit RNAs and proteins to recipient mature heart cells modulating cell fate and behavior," *Stem Cells*, vol. 33, no. 9, pp. 2748–2761, 2015.

[37] S. A. Fisher, C. Doree, A. Mathur, and E. Martin-Rendon, "Meta-analysis of cell therapy trials for patients with heart failure," *Circulation Research*, vol. 116, no. 8, pp. 1361–1377, 2015.

[38] C. Lv, Y. Hao, Y. Han et al., "Role and mechanism of microRNA-21 in H_2O_2-induced apoptosis in bone marrow mesenchymal stem cells," *Journal of Clinical Neuroscience*, vol. 27, pp. 154–160, 2016.

[39] T. Hao, J. Li, F. Yao et al., "Injectable fullerenol/alginate hydrogel for suppression of oxidative stress damage in brown adipose-derived stem cells and cardiac repair," *ACS Nano*, vol. 11, no. 6, pp. 5474–5488, 2017.

[40] S. Nakao, S. Wakabayashi, and T. Y. Nakamura, "Stimulus-dependent regulation of nuclear Ca^{2+} signaling in cardiomyocytes: a role of neuronal calcium sensor-1," *PLoS One*, vol. 10, no. 4, article e0125050, 2015.

[41] D. Mozaffarian, E. J. Benjamin, A. S. Go et al., "Heart disease and stroke statistics—2016 update: a report from the American Heart Association," *Circulation*, vol. 133, no. 4, pp. e38–e360, 2016.

[42] R. Bolli, A. R. Chugh, D. D'Amario et al., "Cardiac stem cells in patients with ischaemic cardiomyopathy (SCIPIO): initial results of a randomised phase 1 trial," *The Lancet*, vol. 378, no. 9806, pp. 1847–1857, 2011.

[43] N. Naftali-Shani, L. P. Levin-Kotler, D. Palevski et al., "Left ventricular dysfunction switches mesenchymal stromal cells toward an inflammatory phenotype and impairs their reparative properties via toll-like receptor-4," *Circulation*, vol. 135, no. 23, pp. 2271–2287, 2017.

[44] E. T. Chouchani, V. R. Pell, E. Gaude et al., "Ischaemic accumulation of succinate controls reperfusion injury through mitochondrial ROS," *Nature*, vol. 515, no. 7527, pp. 431–435, 2014.

[45] X. Cheng, G. Zhang, L. Zhang et al., "Mesenchymal stem cells deliver exogenous miR-21 via exosomes to inhibit nucleus pulposus cell apoptosis and reduce intervertebral disc degeneration," *Journal of Cellular and Molecular Medicine*, vol. 22, no. 1, pp. 261–276, 2018.

[46] D. G. Phinney, M. di Giuseppe, J. Njah et al., "Mesenchymal stem cells use extracellular vesicles to outsource mitophagy and shuttle microRNAs," *Nature Communications*, vol. 6, no. 1, p. 8472, 2015.

[47] X. Hu, Y. Xu, Z. Zhong et al., "A large-scale investigation of hypoxia-preconditioned allogeneic mesenchymal stem cells for myocardial repair in nonhuman primates: paracrine activity without remuscularization," *Circulation Research*, vol. 118, no. 6, pp. 970–983, 2016.

[48] M. D. Brand, R. L. S. Goncalves, A. L. Orr et al., "Suppressors of superoxide-H_2O_2 production at site I_Q of mitochondrial complex I protect against stem cell hyperplasia and ischemia-reperfusion injury," *Cell Metabolism*, vol. 24, no. 4, pp. 582–592, 2016.

[49] H. Sies, C. Berndt, and D. P. Jones, "Oxidative stress," *Annual Review of Biochemistry*, vol. 86, no. 1, pp. 715–748, 2017.

[50] W. H. Lee, W. Y. Chen, N. Y. Shao et al., "Comparison of non-coding RNAs in exosomes and functional efficacy of human embryonic stem cell- versus induced pluripotent stem cell-derived cardiomyocytes," *Stem Cells*, vol. 35, no. 10, pp. 2138–2149, 2017.

[51] A. G. E. Ibrahim, K. Cheng, and E. Marbán, "Exosomes as critical agents of cardiac regeneration triggered by cell therapy," *Stem Cell Reports*, vol. 2, no. 5, pp. 606–619, 2014.

[52] T. Umezu, H. Tadokoro, K. Azuma, S. Yoshizawa, K. Ohyashiki, and J. H. Ohyashiki, "Exosomal miR-135b shed from hypoxic multiple myeloma cells enhances angiogenesis by targeting factor-inhibiting HIF-1," *Blood*, vol. 124, no. 25, pp. 3748–3757, 2014.

[53] M. Harada, X. Luo, T. Murohara, B. Yang, D. Dobrev, and S. Nattel, "MicroRNA regulation and cardiac calcium signaling: role in cardiac disease and therapeutic potential," *Circulation Research*, vol. 114, no. 4, pp. 689–705, 2014.

[54] P. Quijada, N. Hariharan, J. D. Cubillo et al., "Nuclear calcium/calmodulin-dependent protein kinase II signaling enhances cardiac progenitor cell survival and cardiac lineage commitment," *The Journal of Biological Chemistry*, vol. 290, no. 42, pp. 25411–25426, 2015.

[55] B. Y. Nabet, Y. Qiu, J. E. Shabason et al., "Exosome RNA Unshielding couples stromal activation to pattern recognition receptor signaling in cancer," *Cell*, vol. 170, no. 2, pp. 352–366.e13, 2017.

[56] H. Gonzalez-King, N. A. García, I. Ontoria-Oviedo, M. Ciria, J. A. Montero, and P. Sepúlveda, "Hypoxia inducible factor-1α potentiates jagged 1-mediated angiogenesis by mesenchymal stem cell-derived exosomes," *Stem Cells*, vol. 35, no. 7, pp. 1747–1759, 2017.

Research Article

The Protective Role of Brain CYP2J in Parkinson's Disease Models

Yueran Li,[1] **Jinhua Wu,**[1] **Xuming Yu,**[1] **Shufang Na,**[1] **Ke Li,**[2] **Zheqiong Yang,**[1] **Xianfei Xie,**[1] **Jing Yang,**[1] **and Jiang Yue** ![ORCID] [1]

[1]*Department of Pharmacology, School of Basic Medical Sciences, Wuhan University, Wuhan 430071, China*
[2]*Demonstration Center for Experimental Basic Medicine Education, School of Basic Medical Sciences, Wuhan University, Wuhan 430071, China*

Correspondence should be addressed to Jiang Yue; yuejiang@whu.edu.cn

CYP2J proteins are present in the neural cells of human and rodent brain regions. The aim of this study was to investigate the role of brain CYP2J in Parkinson's disease. Rats received right unilateral injection with lipopolysaccharide (LPS) or 6-hydroxydopamine (6-OHDA) in the substantia nigra following transfection with or without the CYP2J3 expression vector. Compared with LPS-treated rats, CYP2J3 transfection significantly decreased apomorphine-induced rotation by 57.3% at day 12 and 47.0% at day 21 after LPS treatment; moreover, CYP2J3 transfection attenuated the accumulation of α-synuclein. Compared with the 6-OHDA group, the number of rotations by rats transfected with CYP2J3 decreased by 59.6% at day 12 and 43.5% at day 21 after 6-OHDA treatment. The loss of dopaminergic neurons and the inhibition of the antioxidative system induced by LPS or 6-OHDA were attenuated following CYP2J3 transfection. The TLR4-MyD88 signaling pathway was involved in the downregulation of brain CYP2J induced by LPS, and CYP2J transfection upregulated the expression of Nrf2 via the inhibition of miR-340 in U251 cells. The data suggest that increased levels of CYP2J in the brain can delay the pathological progression of PD initiated by inflammation or neurotoxins. The alteration of the metabolism of the endogenous substrates (e.g., AA) could affect the risk of neurodegenerative disease.

1. Introduction

Parkinson's disease (PD) is a progressive neurodegenerative disorder characterized by motor symptoms, including bradykinesia with resting tremor, rigidity, and gait disturbance. The major neuropathological findings of PD are the loss of dopaminergic (DA) neurons and the presence of α-synuclein-containing aggregates in the substantia nigra (SN). Although the underlying mechanisms remain unknown, putative factors in PD pathogenesis include oxidative stress, proteostasis imbalance, neuroinflammation, environmental toxins, and genetic variants.

Increasing evidence indicates that neuroinflammation is an important contributor to PD pathogenesis and that peripheral inflammation contributes to the initiation and/or progression of the disease by exacerbating and synergizing with neuroinflammation [1]. Astrocytes play vital roles in neuroinflammatory processes in PD [2]. They respond to inflammatory stimulation by producing proinflammatory cytokines both *in vitro* and *in vivo* [3, 4]. Astrocyte-specific overexpression of mutant α-synuclein causes widespread astrogliosis, microglial activation, and the degeneration of DA neuron in mice [5]. Reactive astrogliosis has been reported in PD animal models and in the affected brain regions of patients with PD [6]. Astrocytes amplify the inflammatory signals activated by microglia, and uncontrolled neuroinflammation ultimately contributes to neurodegeneration [3, 7]. The injection of lipopolysaccharide (LPS) into the SN induces the progressive, specific, and irreversible loss of DA neurons and the accumulation of α-synuclein [8]. The intranigral injection of LPS into the striatum and nigra causes no detectable damage to GABAergic or serotoninergic neurons, suggesting that DA neurons are selectively vulnerable to LPS [9].

In addition to neuroinflammation, oxidative stress is a critical neurotoxic event in the death of DA neurons [10].

Actually, the inflammation and oxidative stress are tightly linked and may be a positive reciprocal feedback loop in the pathophysiological processes of many chronic diseases including PD [11]. Nuclear factor erythroid 2-related factor 2 (Nrf2), a key regulator of the antioxidant system, has been shown to be a therapeutic target for PD. And the genetic association has been previously reported between functional polymorphisms of the Nrf2-encoding NFE2L2 gene and the risk of Parkinson's disease [12, 13]. The dopamine analog 6-hydroxydopamine (6-OHDA), a typical neurotoxin, produces high levels of reactive oxygen species and causes mitochondrial dysfunction [14]. The injection of 6-OHDA into the striatum causes the progressive loss of nigral DA neurons; however, no α-synuclein aggregates were observed in this model [15, 16].

Cytochrome P450 (CYP) is a superfamily responsible for the biotransformation of exogenous and endogenous compounds. The previous study has shown that CYP2J acts as an arachidonic acid (AA) epoxygenase, and epoxidation of AA produces four regioisomeric cis-epoxyeicosatrienoic acids (5,6-, 8,9-, 11,12-, and 14,15-EET) [17]. EETs are metabolized into dihydroxyeicosatrienoic acids by soluble epoxide hydrolase [18]. Immunohistochemistry experiments confirm the presence of CYP2J proteins in the neurons of human and rodent brain regions [19]. In the present study, we investigated the protective role of brain CYP2J and possible mechanisms of action in LPS and 6-OHDA PD models.

2. Methods

2.1. Animals.
Male adult Wistar rats weighing 250–300 g, supplied by the Experimental Animal Center (Hubei, China), were kept at room temperature (22°C–25°C) on a 12 h artificial light/dark cycle, with free access to food and water. Animals were allowed to habituate for 7 days prior to use. All procedures were approved by the Animal Care Committee of Wuhan University and complied with the recommendations of the International Association for the Study of Pain [20]. Rat CYP2J3 is the major isoform in the CYP2J subfamily, which shares a high identity of amino acid sequence with human CYP2J2 (>70%) [21].

2.2. Plasmid Construction.
The fragment encoding CYP2J2 was cloned into the pcDNA-3.1(+) vector (YouBio Biological Technology Co., Wuhan, China) after the digestion by BamHI/EcoRI (Thermo Scientific, Waltham, MA, USA). The fragment encoding CYP2J3 was cloned into the pHAGE-CMV-MCS-IZsGreen vector (Stargene SciTech Development Co., Wuhan, China) after the digestion by XhoI/HindIII (Thermo Scientific, Waltham, MA, USA). The fragment encoding primary miR-340 was cloned into the pcDNA-3.1(−) vector (Invitrogen, Carlsbad, CA, USA) after the digestion by NotI/BamHI (Thermo Scientific, Waltham, MA, USA). All final constructs were verified by DNA sequence analysis.

2.3. Lentiviral Vector (LV) Construction.
Recombinant lentiviruses were produced by transfecting 293T cells with a viral vector containing the enhanced green fluorescent protein (eGFP) gene, the CYP2J3 expression vector or a control vector, and packing and envelope plasmids (psPAX2 and pMD2.G; Addgene, Cambridge, MA, USA) using Lipofectamine 2000. The virus-containing medium was harvested after 48 and 72 h, then concentrated by a two-step ultracentrifugation procedure after filtration. Titers of the viral vectors used in this study ranged from 1 to 2×10^9 TU/ml.

2.4. Surgery and Treatment Procedure.
The procedure for implantation of i.c.v. guide cannula was conducted as previously described [22]. The rats were anesthetized by chloral hydrate (300 mg/kg, i.p.) and were secured in a stereotaxic frame (RWD Life Science, Shenzhen, China). The head was shaved, and a 1 mm hole was drilled using a high-speed drill (RWD Life Science, Shenzhen, China). A guide cannula (62003, RWD Life Science, Shenzhen, China) was implanted at 0.5 mm above the right substantia nigra pars compacta (SNpc) (Bregma coordinates: AP, 5.3 mm; ML, 2.0 mm; and DV, 7.8 mm). The insertion cannula for stereotaxic injection protruded 0.5 mm below the tip of the guide cannula. Guide cannula was fixed with acrylic dental cement and three stainless steel screws affixed to the skull. The incision was closed using 5-0 Dysilk. Animals were administered with benzylpenicillin (60 mg/kg, s.c.) after the operation and kept warm until they were awake. Body weights and clinical signs were monitored closely during postsurgical recovery.

Experiment I. A total of 60 rats were randomly divided into the following groups: control group, LPS group, LPS treatment following empty vector transfection, and LPS treatment following LV-CYP2J3 transfection ($n = 15$). LPS (from Escherichia coli, serotype O55:B5, Sigma, St. Louis, MO, USA), dissolved in sterile phosphate-buffed saline (PBS), was unilaterally injected (10 μg, 2 μl) into the right SNpc of rats at a rate of 0.2 μl/min by an automatic injector (CMA 402, CMA Microdialysis AB, Sweden) in the CMA 120 System for Freely Moving Animals (CMA Microdialysis AB) [23]. The syringe was left in situ for 5 min. Control animals were injected with sterile PBS. After injection, the syringe was left in situ for 5 min. Rats received unilateral injections of the empty vector or the LV-CYP2J3 vector 3 days before treatment with LPS. One microliter LV was injected for 5 min at a rate of 0.2 μl/min by an automatic injector. Using a fluorescent microscope, the expression of eGFP was used as a visual marker of the injection site and LV transduction.

Experiment II. A total of 40 rats were randomly divided into the following groups: control group, 6-OHDA group, 6-OHDA treatment following empty vector transfection, and 6-OHDA treatment following LV-CYP2J3 transfection ($n = 10$). 6-OHDA (Sigma, St. Louis, MO, USA) was dissolved in sterile saline with 0.2% vitamin C. For the 6-OHDA PD animal model, 6-OHDA (8 μg, 2 μl) was unilaterally injected into the right SNpc of rats. Control animals were injected with the vehicle. Rats received unilateral injections of the control vector or the LV-CYP2J3 vector 3 days before 6-OHDA treatment. One microliter of LV was injected for 5 min at a rate of 0.2 μl/min by an automatic injector. After injection, the syringe was left in situ for 5 min.

2.5. Rotational Behavior. The animals were tested for rotational behavior after treatment with the DA agonist apomorphine (0.5 mg/kg, s.c.) dissolved in sterile saline 12 and 21 days after LPS or 6-OHDA injections [24]. Rats were placed in a circular test arena. Rotational activity was measured for 30 min, beginning 5 min after injection, and the number of turns was counted [25].

2.6. Immunohistochemistry. Rats were deeply anesthetized and perfused with saline followed by cold 4% paraformaldehyde through the aorta. Brain tissues were quickly removed and postfixed with 4% paraformaldehyde. The samples were embedded in paraffin, and a series of $4 \mu m$ sections were cut. Four sections were selected from the SN, and sections from different groups were matched as closely as possible [26]. The sections were incubated with a polyclonal rabbit anti-rat antibody for tyrosine hydroxylase (TH, 1:200). After incubation with biotinylated anti-rabbit IgG (1:100), the antigen-antibody complex was visualized using the avidin-biotin complex technique (ABC kit, Vector Laboratories, Burlington, Ont., Canada) followed by a reaction with $3,3'$-diaminobenzidine and hydrogen peroxide (DAB kit, Vector Laboratories, Burlington, Ont., Canada). TH-positive cells in the lesioned and intact hemispheres were assayed using the ImageJ software to measure a gray scale value within the range of 0–200. Background staining was subtracted, and analysis was performed blinded. The data shown are the percentage of cells relative to the intact SN side.

2.7. Immunofluorescence. To investigate the effects of CYP2J on Nrf2 protein levels, brain tissues from both LPS and 6-OHDA PD models were fixed with 4% paraformaldehyde. The SN was embedded in paraffin and cut into $4 \mu m$. After deparaffinization and rehydration of the paraffin sections, antigen retrieval was performed with citrate buffer (0.1 M, pH 6.0) at 95°C for 10 min. The sections were blocked with 3% BSA for 1 h and incubated with a polyclonal rabbit anti-rat CYP2J antibody (1:400) and a monoclonal mouse anti-rat Nrf2 antibody (1:200). The samples were incubated with the secondary antibodies including a rhodamine-conjugated AffiniPure Goat anti-rabbit IgG for CYP2J (1:100) and a Cy3-conjugated AffiniPure Donkey anti-mouse IgG for Nrf2 (1:100). Images were analyzed using an Olympus BX51 fluorescent microscope (Olympus Corporation, Tokyo, Japan) equipped with an Olympus Micro DP72 camera. Identical illumination and camera settings were used within each data set.

To investigate the effects of CYP2J on α-synuclein accumulation, the SN from the LPS PD model was co-incubated with a monoclonal mouse anti-rat α-synuclein antibody (1:400) and a polyclonal rabbit anti-rat TH antibody (1:200). Then, the samples were incubated with the secondary antibodies which included a rhodamine-conjugated AffiniPure Goat anti-rabbit IgG for TH (1:100) and a Cy3-conjugated AffiniPure Donkey anti-mouse IgG for α-synuclein (1:100).

To investigate the effects of LPS on the p-CREB levels, U251 cells were pretreated with CLI-095 (1 μM) or ST 2825 (20 μM) for 1 h before LPS treatment (1 μg/ml, 24 h). The

cells were fixed and permeabilized with 0.5% Triton X-100. Fixed cells were blocked with 3% fetal calf serum for 30 min. The cells were incubated with monoclonal rabbit anti-human p-CREB (S133) antibody and goat anti-mouse alpha tubulin antibody overnight at 4°C. Samples were incubated with fluorescent-labeled goat anti-rabbit IgG and fluorescent-labeled goat anti-mouse IgG in PBS for 1 h at 37°C. Then, the cells were washed twice in PBS and incubated with 4,6-diamidino-2-phenylindole (DAPI) for 5 min.

2.8. Cell Culture and Treatment. Human glioma U251 cells were grown in Dulbecco's modified Eagle's medium containing 10% fetal bovine serum. To determine whether CYP2J or AA metabolite plays a role in oxidative stress, U251 cells were transfected with the CYP2J2 expression vector or treated with 14,15-EET (1 μM) and 12-(3-adamantan-1-yl-ureido)-dodecanoic acid (AUDA) (1 μM), an inhibitor of soluble epoxide hydrolase. To investigate the mechanism by which LPS regulates CYP2J, U251 cells were pretreated with a specific TLR4 inhibitor (CLI-095, 1 μM) or a specific MyD88 inhibitor (ST 2825, 20 μM) for 1 h before LPS treatment (1 μg/ml, 24 h).

2.9. Real-Time RT-PCR. Total RNA was isolated using the TRIzol reagent (Invitrogen, Carlsbad, CA, USA). cDNA was synthesized using a cDNA Synthesis Kit (Toyobo, Osaka, Japan) for first-strand synthesis. All real-time PCR reactions with SYBR Green (Toyobo, Osaka, Japan) were performed on a CFX connect real-time PCR detection system (Bio-Rad, Hercules, CA, USA). For miR-340 detection, a small RNA-specific stem-loop RT primer was used as follows: 5-GTCGTATCCAGTGCGTGTCGTGGA GTCGGCAATTGCACTGGATACGACAATCAG-3$'$. The primers for PCR are listed in Additional file 1 (Table S1). Human GAPDH was used for the normalization of relative expression levels, and U6 was used to normalize the relative expression of miR-340. Gene expression levels were calculated using the $2^{-\Delta\Delta CT}$ method relative to internal controls.

2.10. Immunoblotting. The pellets of cells were lysed using RIPA lysis buffer. For the detection of Nrf2 proteins, 20 μg of total proteins from U251 cells were separated by SDS-polyacrylamide gel electrophoresis (4% stacking and 10% resolving gels) and then transferred onto PVDF membranes. These membranes were incubated for 2 h with a polyclonal rabbit anti-human Nrf2 antibody (1:1000). The protein levels of Nrf2 were normalized to β-actin (1:1000) to control the loading efficiency. The immunoblots were visualized using chemiluminescence followed by exposure to autoradiography films and analyzed using Gel Documentation & Analysis Systems (Beijing Liuyi Instrument, Beijing, China). The relative density of each band was expressed in arbitrary density units after subtracting the background.

2.11. Chromatin Immunoprecipitation (ChIP) Assay. The ChIP kit (EpiGentek Group Inc., Brooklyn, NY, USA) was used to determine the binding profile of *CYP2J2* genes with p-CREB protein in cells pretreated with or without CLI-095 (1 μM) or ST 2825 (20 μM) for 1 h before LPS treatment

(1 μg/ml, 24 h). Briefly, the cross-linked chromatin from the nuclear fraction was sheared into fragments of the proper length by sonication according to the manufacturer's protocol. The chromatin concentration was measured, and approximately 10% of the chromatin was retained as input material. The chromatin solution was immunoprecipitated with rabbit anti-human p-CREB (S133) antibody (1 : 100) or non-immune mouse IgG as a negative control. The number of cycles used for PCR amplification were within the linear range (primers are listed in Table S1), and PCR products were resolved on a 2% agarose gel. The band intensities were quantified using an AutoChemi Imaging System (UVP LLC, Upland, CA, USA).

2.12. Materials. LPS (cat. number L2880) and 6-OHDA (cat. number H116) were purchased from Sigma (St. Louis, MO USA), 14,15-EET were purchased from Cayman Chemical Co. (cat. number 50651, Ann Arbor, MI), apomorphine (cat. number HY-12723A) and ST 2825 (cat. number HY-50937) were purchased from MedChem Express (Princeton, NJ, USA), and CLI-095 was purchased from InvivoGen (cat. number tlrl-cli95, San Diego, CA, USA).

Primary antibodies to TH (cat. number ab112), Nrf2 (cat. number ab89443), α-synuclein (cat. number ab1903), and p-CREB (S133) (cat. number ab32096) were purchased from Abcam (Cambridge, MA, USA). Primary antibodies to CYP2J were purchased from Merck Millipore (cat. number ABS1605, CA, USA). Primary antibodies to TH were purchased from GeneTex Inc. Irvine (cat. number GTX113016, CA, USA). Primary antibodies to alpha-tubulin were purchased from Proteintech (cat. number 66031-1-lg, Chicago, IL, USA). Primary antibodies to β-actin were purchased from Santa (cat. number sc-8432, Santa Cruz, CA, USA). Rhodamine-conjugated AffiniPure Goat anti-rabbit IgG was purchased from Kerui Biotechnology Co. (cat. number 100428, Wuhan, China) and DyLight 405 Donkey anti-mouse IgG was purchased from Antgene (cat. number ANT080, Wuhan, China). FITC-conjugated AffiniPure Goat anti-rabbit IgG (cat. number AS1110) and CY3-conjugated AffiniPure Goat anti-mouse IgG (cat. number AS1111) were purchased from Aspen Biological (Wuhan, China).

Dulbecco's modified Eagle's medium (DMEM) was purchased from HyClone (Rockford, IL, USA); reduced serum medium Opti-MEM was purchased from Gibco (Carlsbad, CA, USA). Lipofectamine 2000 was purchased from Invitrogen (Carlsbad, CA, USA). Fetal bovine serum (FBS) was purchased from Zhejiang Tianhang Biotechnology Co. (Zhejiang, China). Other materials were purchased from standard suppliers or as indicated in the text.

2.13. Statistical Analysis. All data are expressed as arithmetic mean with a standard error of the mean (SEM). The normalized mRNA levels of genes from cells and rat brain tissue were expressed as arbitrary density units. Results from the ChIP assay were expressed as arbitrary density units and normalized to input levels. Data were obtained from at least five separate experiments. One-way ANOVA was used to test for differences among the groups and was followed by the least significant difference post hoc test. A value of $p < 0.05$ was considered significant.

3. Results

3.1. LPS Downregulated CYP2J Levels via the TLR4-MyD88 Signaling Pathway in U251 Cells. Our previous study showed that brain CYP2J2 is the target gene of CREB in astrocytes [17]. Compared with controls, mRNA levels of CYP2J2 and CREB were decreased by 67.4% and 34.8%, respectively, after LPS treatment for 24 h (Figure 1(a)). The LPS-induced inhibition of CYP2J2 and CREB mRNA levels was abolished by CLI-095 (a specific TLR4 inhibitor) and partly attenuated by ST 2825 (a specific MyD88 inhibitor) compared with the LPS group. Immunofluorescence data showed that CLI-095 and ST 2825 attenuated LPS-induced decreases in the p-CREB protein level in cells (Figure 1(b)). ChIP data showed that p-CREB proteins bound to the CYP2J2 promoter at −1426 to −1405 bp. Compared with the control, binding of the p-CREB protein to the CYP2J2 promoter was decreased by 50% following LPS treatment; however, decreased binding of the p-CREB protein to the CYP2J2 promoter induced by LPS was attenuated by CLI-095 and ST 2825 (Figure 1(c)). These data suggest that the TLR4-MyD88 signaling pathway is involved in the regulation of CYP2J via CREB following treatment with LPS.

3.2. CYP2J-Dependent Metabolites Upregulated Antioxidative Genes via miR-340. Compared with controls, CYP2J2 overexpression significantly increased both the mRNA and protein levels of Nrf2 in U251 cells (Figures 2(a)–2(c)). The mRNA levels of genes related to mitochondrial oxidative defense (SOD1, CAT, and GPX1) in astrocytes were significantly elevated by CYP2J2 overexpression compared with controls; however, no changes were observed in the mRNA levels of genes related to endoplasmic reticulum stress, including MANF, PERK, IRE1α, and ATF6 (data not shown). Compared with controls, the level of miR-340 mRNA was significantly decreased following CYP2J2 overexpression (Figure 2(d)). Western blotting and real-time RT-PCR revealed that miR-340 targeted Nrf2 expression in astrocytes (Figures 2(e)–2(g)). Following 14,15-EET and/or AUDA (a soluble epoxide hydrolase inhibitor) treatment of U251 cells, miR-340 and Keap1 were downregulated; however, genes related to mitochondrial oxidative defense were upregulated including Nrf2, SOD1, CAT, and GPX1 (Figures 2(h)–2(m)).

3.3. CYP2J Transfection Protected Dopaminergic Neurons in the LPS PD Animal Model. The accumulation of α-synuclein was observed after LPS treatment for 12 and 21 days (Figure 3(a)); however, CYP2J transfection attenuated the LPS-induced accumulation of α-synuclein. Compared with the control, the number of DA neurons was decreased by 75.5% after stereotaxic injections of LPS for 21 days (Figures 3(b) and 3(c)); however, DA neurons remaining in the SNpc of rats transfected with the CYP2J expression vector were increased by 2.1-fold compared with the LPS group. Compared with LPS-treated rats, the number of
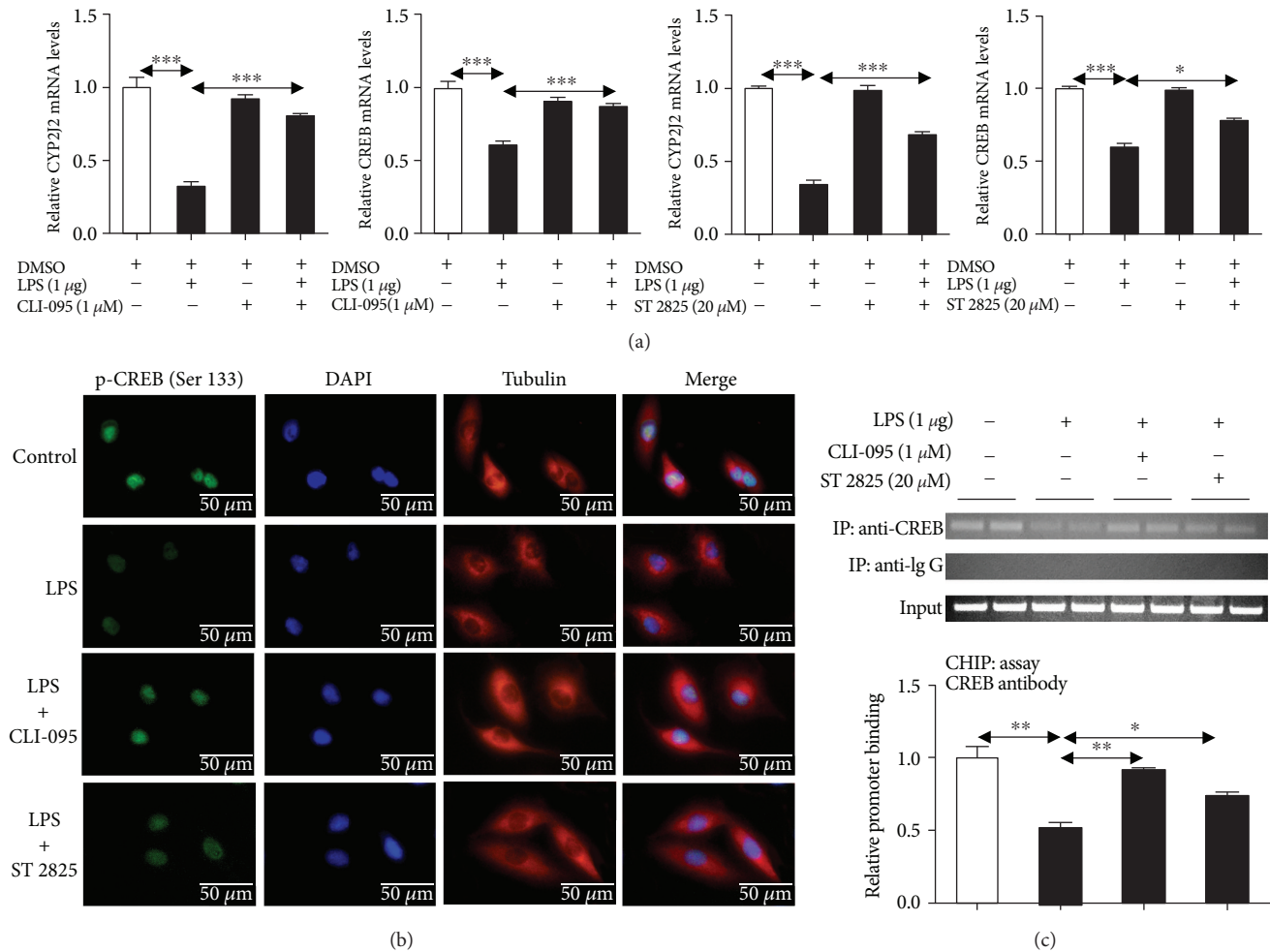
(a)

(b)

(c)

Figure 1: The TLR4-MyD88 signaling pathway was involved in the inhibition of CYP2J2 levels by LPS treatment in U251 cells. Compared with the control, LPS treatment decreased CYP2J and CREB mRNA levels in cells (a). The LPS-induced inhibition of CYP2J2 and CREB mRNA levels was abolished by CLI-095 and attenuated by ST 2825. Moreover, CLI-095 and ST 2825 attenuated the LPS-induced decrease in p-CREB protein levels in cells (b). ChIP data shows that the LPS-induced decrease of p-CREB protein binding to the *CYP2J2* promoter by LPS was attenuated by CLI-095 and ST 2825 (c). Data were analyzed by one-way ANOVA. The data are mean ± SEM; $n = 5$, $^{*}p < 0.05$, $^{**}p < 0.01$, and $^{***}p < 0.001$ compared with respective controls.

rotations in rats transfected with the CYP2J expression vector was decreased by 57.3% at day 12 and 47.0% at day 21 after LPS treatment (Figures 3(d) and 3(e)).

3.4. CYP2J Transfection Upregulated Genes Related to Mitochondrial Oxidative Defense in the LPS PD Animal Model. The effect of CYP2J expression on Nrf2 protein levels was investigated by fluorescent immunocytochemistry. Levels of Nrf2 protein were elevated in cells with high levels of CYP2J3 after LPS treatment for 12 and 21 days compared with the LPS group (Figures 4(a) and 4(b)). Compared with the control, mRNA levels of CREB and CYP2J3 in the SN were decreased by 31.0% and 45.6%, respectively, following LPS treatment for 21 days, but miR-340 mRNA levels were increased by 2.5-fold, and levels of genes related to mitochondrial oxidative defense were decreased. Compared with the LPS group, the mRNA levels of Nrf2, SOD1, CAT, and GPX1 in rat SN transfected with the CYP2J3 expression vector were increased by 6.0-, 2.6-, 3.2-, and 3.2-fold,

respectively, and miR-340 mRNA levels were decreased by 47.7% (Figures 4(c) and 4(d)).

3.5. CYP2J Transfection Protected Dopaminergic Neurons in the 6-OHDA PD Animal Model. Compared with the control, the number of DA neurons decreased by 74.8% after treatment with 6-OHDA for 21 days; however, in the SNpc of rats transfected with the CYP2J expression vector, the number of DA neurons increased by 2.4-fold compared with the 6-OHDA and pHAGE groups (Figures 5(a) and 5(b)). Compared with 6-OHDA-treated rats, rotations in rats transfected with the CYP2J3 expression vector were decreased by 59.6% at day 12 and 43.5% at day 21 after 6-OHDA treatment (Figures 5(c) and 5(d)).

3.6. CYP2J Transfection Upregulated Genes Related to Mitochondrial Oxidative Defense in the 6-OHDA PD Animal Model. Compared with the 6-OHDA group, Nrf2 protein levels were elevated in cells with high levels of CYP2J3 after

(a)   (b)   (c)   (d)   (e)

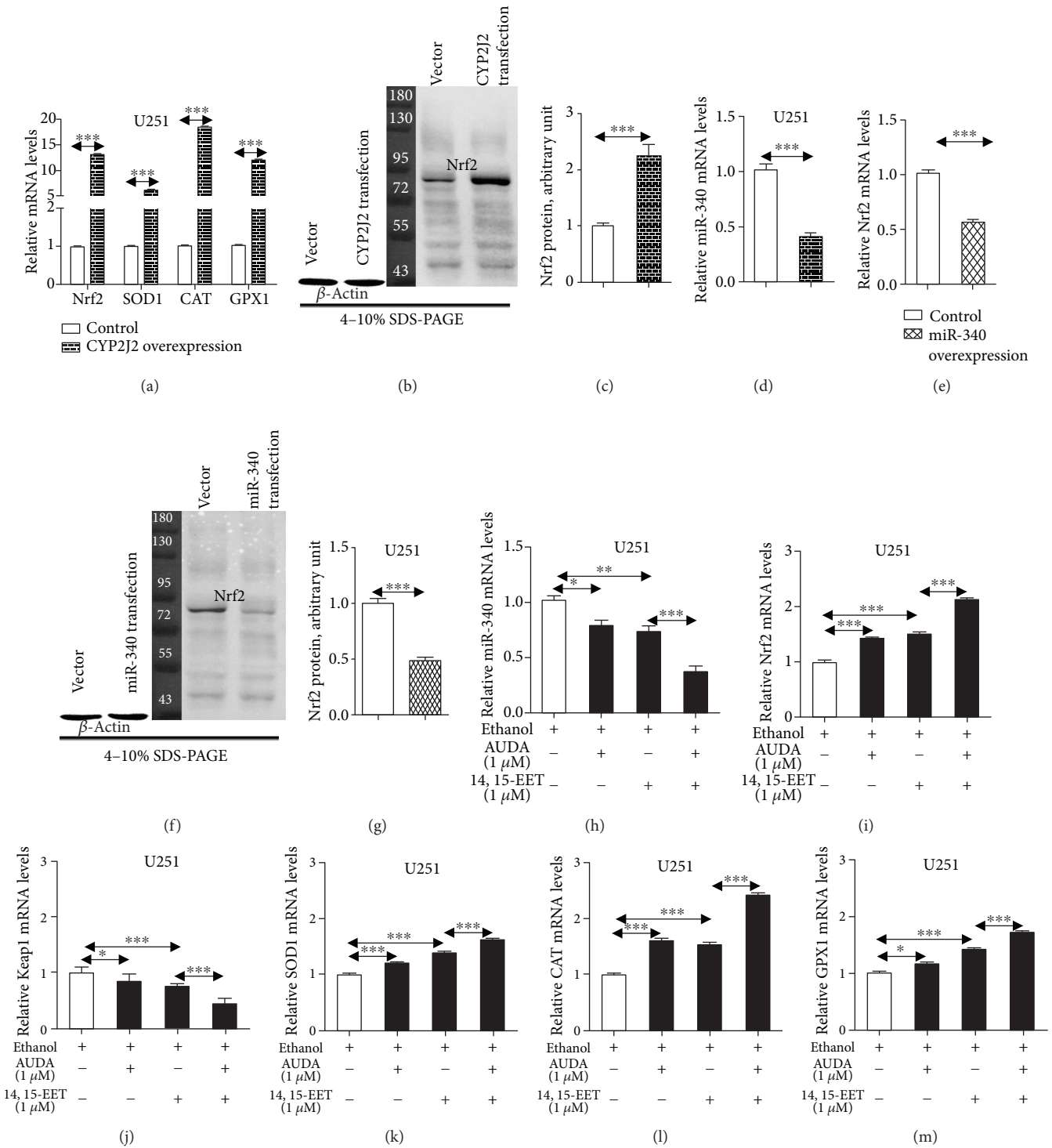(f)   (g)   (h)   (i)

(j)   (k)   (l)   (m)

FIGURE 2: Astrocytic CYP2J upregulated the antioxidative system via the inhibition of miR-340 in U251 cells. Compared with controls, mRNA levels of Nrf2, SOD1, CAT, and GPX1 were increased in cells following transfection with the CYP2J2 expression vector (a); moreover, Nrf2 protein levels were increased indicated by Western blotting (b and c). The level of miR-340 mRNA was decreased following transfection with CYP2J2 (d) compared with the control. Nrf2 mRNA (e) and protein (f and g) levels were decreased following miR-340 transfection. Compared with the controls, 14,15-EET and/or AUDA (a soluble epoxide hydrolase inhibitor) treatment decreased the mRNA levels of miR-340 (h) and Keap1 (j) but increased mRNA levels of Nrf2 (i), SOD1 (k), CAT (l), and GPX1 (m) in U251 cells. Data were analyzed by one-way ANOVA. The data are mean ± SEM; $n = 5$, $^{*}p < 0.05$, $^{**}p < 0.01$, and $^{***}p < 0.001$ compared with respective controls.
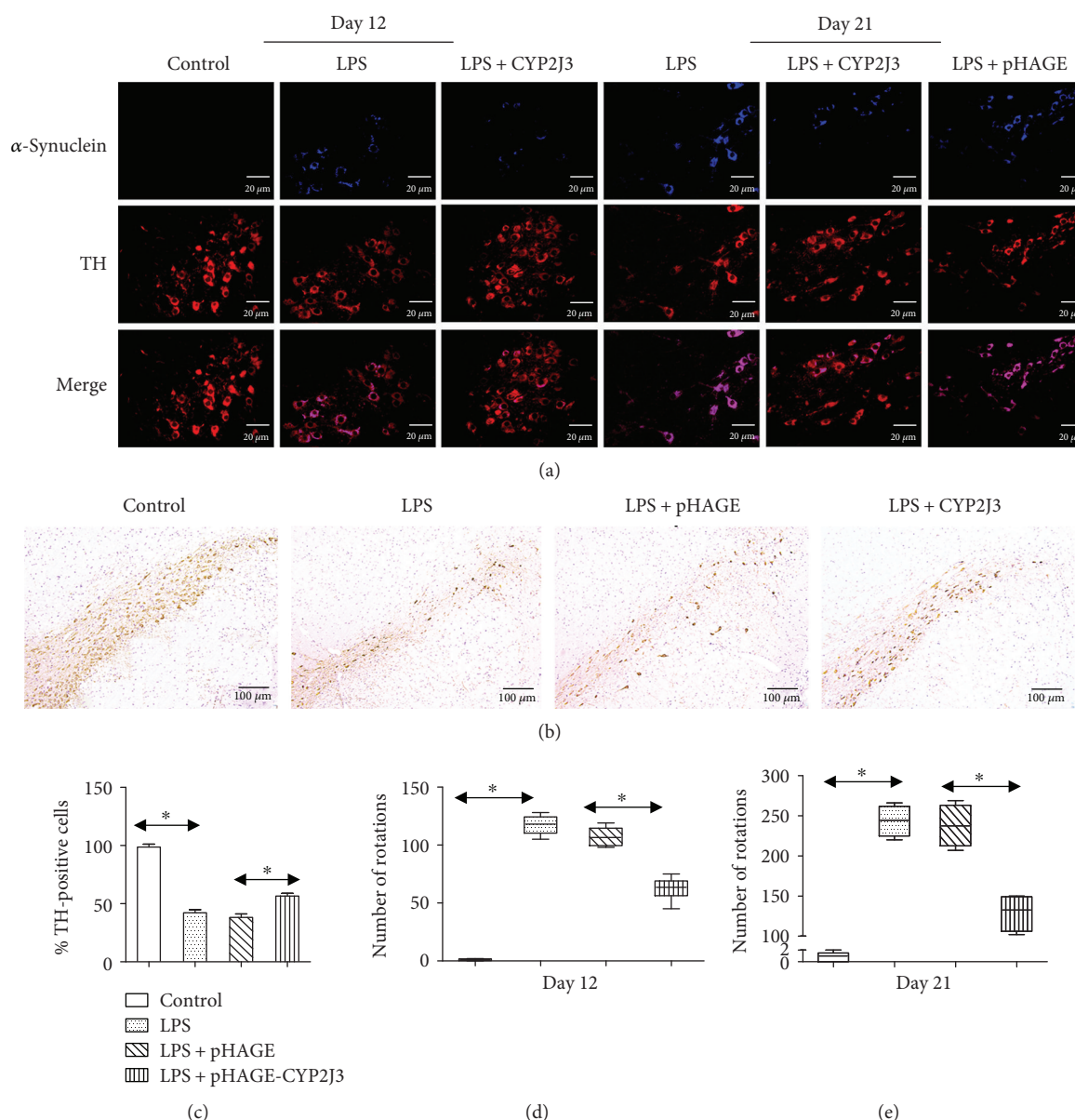
(a)

(b)

(c)

(d)

(e)

FIGURE 3: The effects of CYP2J transfection on the loss of dopaminergic (DA) neurons in the SN and behavioral impairment in the LPS PD animal model. Fluorescent immunocytochemistry data shows the accumulation of α-synuclein (blue) in tyrosine hydroxylase positive neurons (red) after LPS treatment for 12 and 21 days (a); however, CYP2J transfection attenuated the LPS-induced accumulation of α-synuclein. Immunohistochemistry staining shows the loss of DA neurons in the SN after LPS treatment (b). There were an increased number of DA neurons remaining in the SNpc of rats transfected with the CYP2J3 expression vector compared with the LPS group (c). Compared with LPS-treated rats, the number of rotations by rats with high CYP2J3 levels was decreased on day 12 (d) and day 21 (e) after LPS treatment. Data were analyzed by one-way ANOVA. The data are mean ± SEM; $n = 15$, $^*p < 0.05$ compared with respective controls.

6-OHDA treatment for 12 and 21 days indicated by fluorescent immunocytochemistry (Figures 6(a) and 6(b)). Compared with the control, CREB and CYP2J3 mRNA levels in the SN decreased by 16.5% and 55.2%, respectively, following 6-OHDA treatment (Figure 6(c)). However, the 6-OHDA-induced inhibition of genes related to mitochondrial oxidative defense was attenuated by transfection with CYP2J3. Compared with the control, mRNA levels of Nrf2, SOD1, CAT, and GPX1 in rat SN transfected with the CYP2J3 expression vector were increased by 8.7-, 4.9-, 12.9-, and 6.5-fold,

respectively, and miR-340 mRNA levels were decreased by 48.8% (Figure 6(d)).

4. Discussion

This is the first demonstration that brain CYP2J plays a protective role in PD models induced by inflammation or oxidative stress. We showed that (i) CYP2J3 transfection significantly attenuated LPS- or 6-OHDA-induced behavioral impairment and the loss of DA neurons in the SN; (ii)
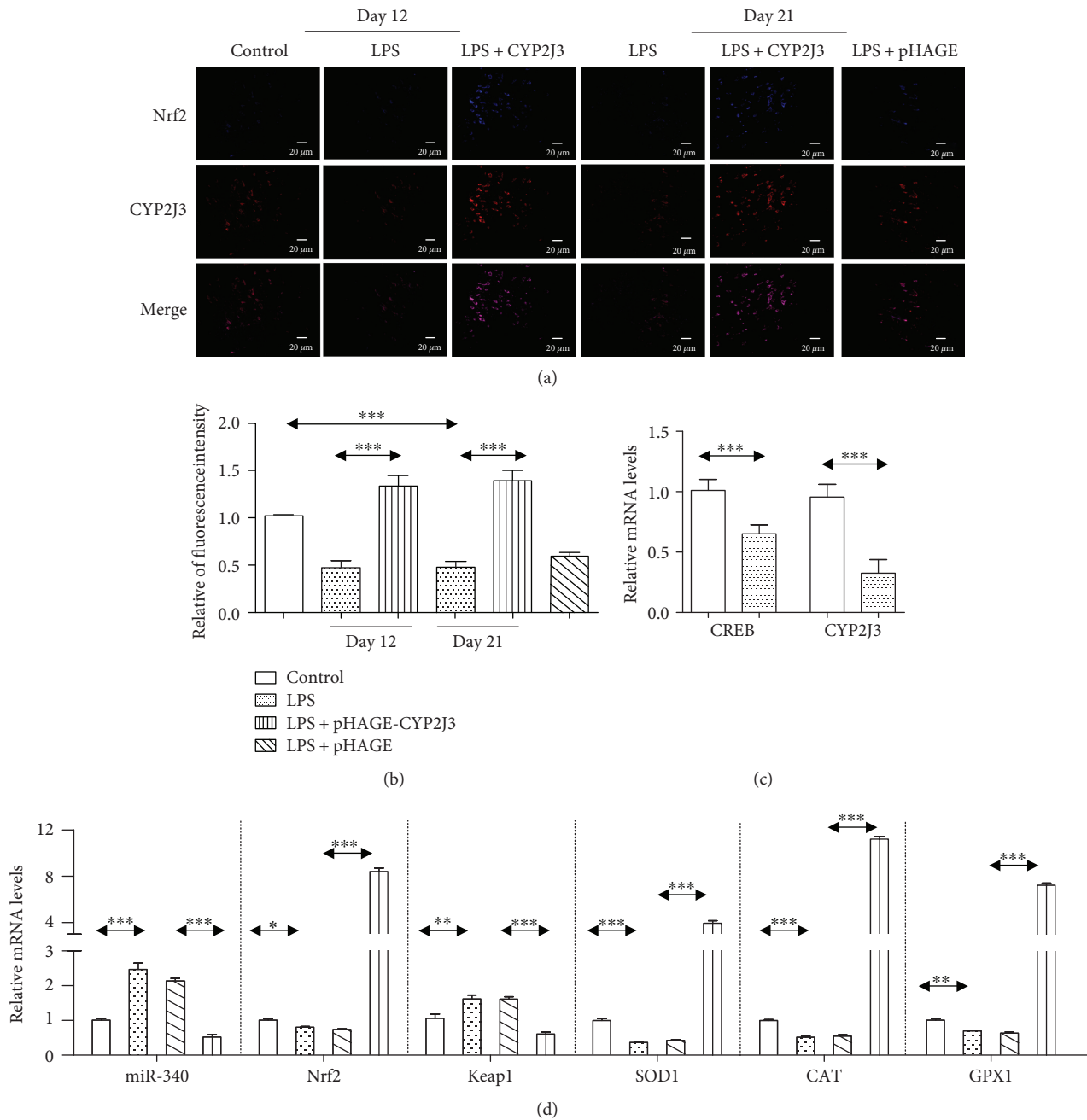
(a)

(b)

(c)

(d)

Figure 4: Changes in genes related to mitochondrial oxidative defenses in the LPS PD animal model. Fluorescent immunocytochemistry data shows reduced levels of Nrf2 (blue) and CYP2J3 (red) protein in rats treated with LPS for 12 and 21 days (a). Nrf2 protein levels were increased following transfection with the CYP2J3 expression vector (b). Compared with the control, mRNA levels of CREB and CYP2J3 were decreased following LPS treatment (c) but miR-340 mRNA levels were increased (d). Compared with the LPS group, the LPS-induced inhibition of Nrf2, SOD1, CAT, and GPX1 mRNA levels was attenuated by transfection with CYP2J3 (d). Data were analyzed by one-way ANOVA. The data are mean ± SEM; $n = 5$, $^*p < 0.05$, $^{**}p < 0.01$, and $^{***}p < 0.001$ compared with respective controls.

the TLR4-MyD88 signaling pathway was involved in the downregulation of brain CYP2J induced by LPS; and (iii) both CYP2J transfection and 14,15-EET activated the Nrf2-antioxidant response element (ARE) pathway via the inhibition of miR-340. These data indicate that AA metabolites catalyzed by brain CYPs may affect the mitochondrial oxidative defense system.

A growing body of basic research shows that the Nrf2-ARE pathway plays a protective role in both toxin-induced and transgenic mouse models of PD [27]. Following oxidative stress, Nrf2 is released from Keap1, translocates into the nucleus, and binds with the ARE of antioxidant genes. Our data showed the activation of the Nrf2-ARE pathway by 14,15-EET treatment in astrocytes, which is
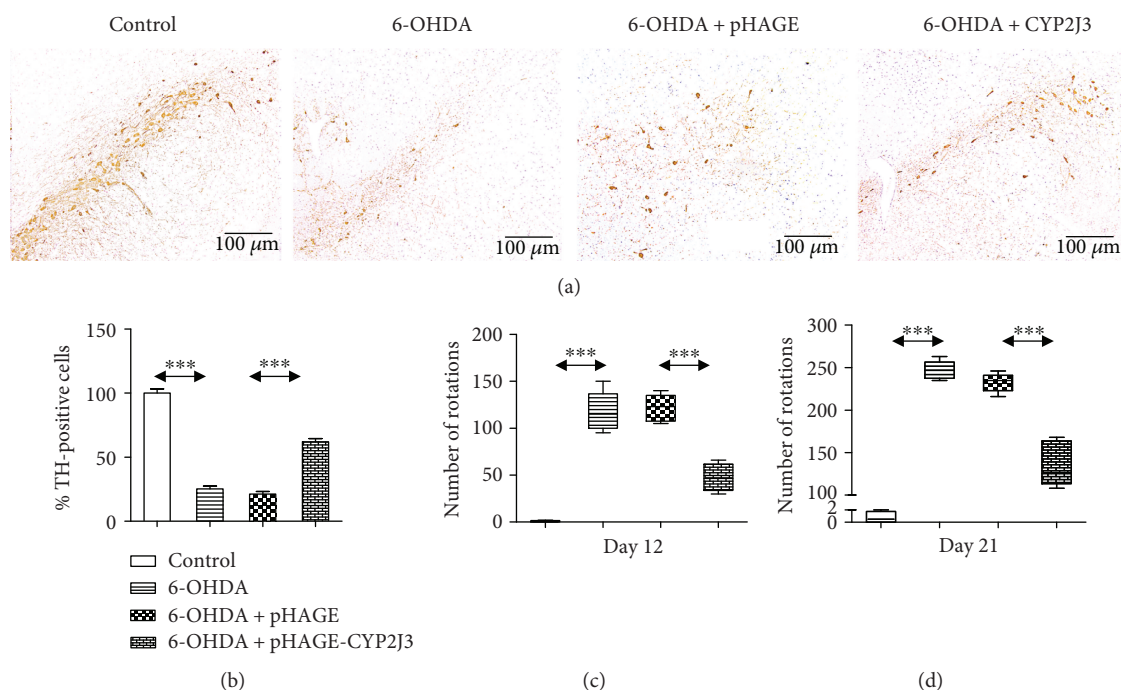
(a)

(b)

(c)

(d)

Figure 5: The effects of CYP2J3 transfection on the loss of dopaminergic (DA) neurons in the SN and behavioral impairment in the 6-OHDA PD animal model. Immunohistochemistry staining showed the loss of DA neurons in the SN after 6-OHDA treatment (a). The dopaminergic neurons left in SNpc from the rats transfected with CYP2J3 expression vector were increased, compared with the 6-OHDA group (b). Compared with 6-OHDA-treated rats, the number of rotations in rats with high CYP2J3 levels was decreased at day 12 (c) and day 21 (d) after 6-OHDA treatment. $^{***}p < 0.001$ compared with respective controls.

consistent with a previous report that 14,15-EET treatment significantly increased the accumulation of Nrf2 in lung epithelial cells [28]. The downstream target genes of Nrf2 related to mitochondrial oxidative defense were upregulated following CYP2J transfection, suggesting that Nrf2 can prevent the damage to mitochondria from oxidant injury. The previous study showed that the isolated mitochondria from the myocardium of Nrf2 deficiency mice were more sensitive to mitochondrial membrane permeability transition and swelling compared with the samples from the wild-type mice (Nrf2 protects mitochondrial decay by oxidative stress). The induction of Nrf2 attenuated microglia-induced inflammation in the hippocampus of LPS-treated mice as determined by reduced inducible NO synthase (iNOS) levels and attenuated the production of proinflammatory cytokines IL-6 and TNF-α [29]. Nrf2 overexpression inhibited RAC1-dependent activation of nuclear factor-κB (NF-κB), indicating a cross-talk between Nrf2 and NF-κB pathways [30]. The activation of the Nrf2-ARE pathway following CYP2J overexpression or the treatment of EETs may also inhibit the NF-κB signaling pathway. Recently, Nrf2 was identified as a regulator of the expression of autophagy genes [31, 32]. Our data showed the downregulation of Nrf2 and its downstream genes in both the LPS and 6-OHDA PD models, suggesting that the Nrf2-ARE pathway is associated with both neuroinflammation and oxidative stress. Nrf2 may be a suitable pharmacological target for the treatment of PD [27].

Cardiovascular EETs have been reported to inhibit reactive oxygen species, the inflammatory reaction, vascular smooth muscle migration, and enhancement of the fibrinolytic pathway [33]. Our data suggest that EETs may play a protective role in PD. A previous study showed that sEH deficiency or inhibition attenuated MPTP-induced dopamine neuron loss and behavioral deficits [34]. Our data showed that 14,15-EET decreased miR-340 levels and that the LPS-induced elevation of miR-340 levels was attenuated by CYP2J overexpression. The overexpression of miR-340 decreased Nrf2 mRNA levels in neural cells, which is consistent with a previous study showing that miR-340 directly targets Nrf2 mRNA in hepatocytes [35].

The TLR4-MyD88 signaling pathway is involved in decreasing CYP2J in astrocytes via CREB following LPS treatment. Previous studies have shown that α-synuclein secreted from neurons induced a TLR4-dependent inflammatory response in primary astrocyte cultures [36]. The accumulation of α-synuclein in astrocytes following the overexpression of mutant *SNCA* (encoding α-synuclein) under an astrocyte-specific promoter resulted in the degeneration of DA neurons in the SNpc and the ventral tegmental area (VTA), as well as the onset of a movement disorder [37]. Data from this study indicate that activation of the TLR4 signaling pathway results in the downregulation of antioxidative systems in astrocytes via inhibition of brain CYP2J. Alterations of the CYP2J-dependent metabolism of endogenous substrates may attenuate the LPS- or 6-OHDA-induced loss of DA neurons and accumulation of α-synuclein in the SN.

In conclusion, our data demonstrated that the elevated CYP2J levels strengthen the antioxidative defense system by altering miRNA profiles within the brain. This suggests that the alteration of the metabolism of the endogenous
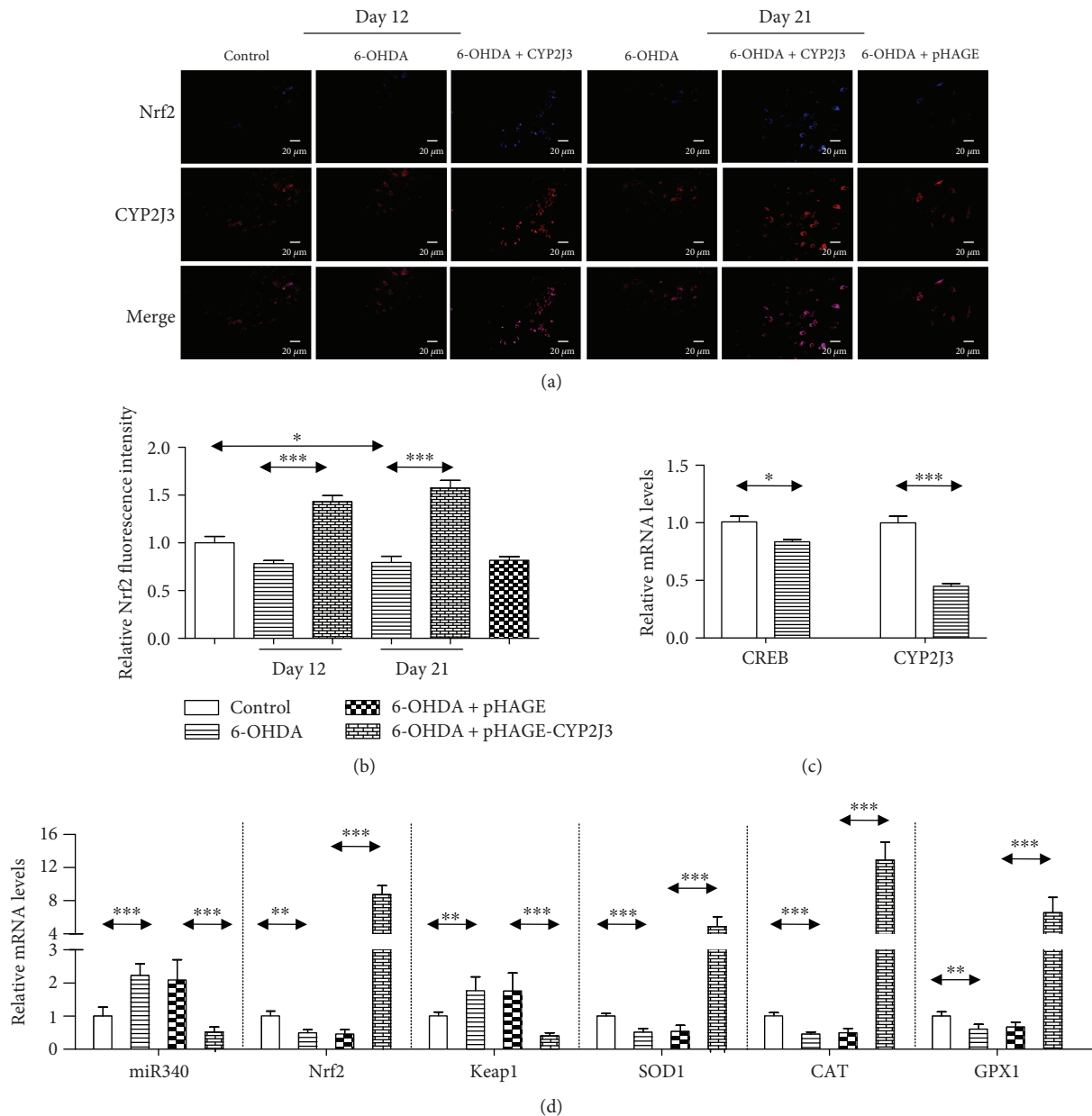
(a)

(b)

(c)

(d)

FIGURE 6: Changes in genes related to mitochondrial oxidative defenses in the 6-OHDA PD animal model. Fluorescent immunocytochemistry data shows reduced levels of Nrf2 (blue) and CYP2J3 (red) protein in rats treated with 6-OHDA for 12 and 21 days (a). Nrf2 protein levels were increased following transfection with the CYP2J3 expression vector (b). Compared with the control, mRNA levels of CREB and CYP2J3 were decreased by 6-OHDA treatment (c). The inhibition of Nrf2, SOD1, CAT, and GPX1 mRNA levels following 6-OHDA treatment was attenuated by transfection with CYP2J3, compared with the 6-OHDA group (d). Data were analyzed by one-way ANOVA. The data are mean ± SEM; $n = 5$, $^*p < 0.05$, $^{**}p < 0.01$, and $^{***}p < 0.001$ compared with respective controls.

substrates (e.g., AA) could affect the risk of neurodegenerative disease induced by neuroinflammation or neurotoxins. The CYP2J-mediated metabolites may activate the Nrf2-ARE pathway and delay PD progression by ameliorating mitochondrial dysfunction.

Abbreviations

AA: Arachidonic acid
ANOVA: Analysis of variance
AUDA: 12-(3-Adamantan-1-yl-ureido)dodecanoic acid
CYP2J2:   Cytochrome P450 2J2
DA: Dopaminergic
EETs: *cis*-Epoxyeicosatrienoic acids
LPS: Lipopolysaccharide
LV: Lentiviral vector
miRNA: MicroRNA
6-OHDA: 6-Hydroxydopamine
PBS: Phosphate-buffed saline
PD: Parkinson's disease
SN: Substantia nigra
SNpc: Substantia nigra pars compacta

TH: Tyrosine hydroxylase
TLR4: Toll-like receptor 4
3'-UTR: 3'-Untranslated region
VTA: Ventral tegmental area.

Data Availability

The data used to support the findings of this study are available from the corresponding author upon request.

Additional Points

Declaration of Transparency and Scientific Rigour. This declaration acknowledges that this paper adheres to the principles for transparent reporting and scientific rigour of preclinical research recommended by funding agencies, publishers, and other organizations engaged with supporting research.

Conflicts of Interest

The authors declare no conflict of interest.

Authors' Contributions

Yueran Li, Jinhua Wu, Shufang Na, and Xuming Yu performed the experiments. Yueran Li, Jinhua Wu, Ke Li, and Jiang Yue analyzed the data. Zheqiong Yang, Xianfei Xie, Jing Yang, and Jiang Yue designed the study. Jiang Yue wrote the article. All the authors gave final approval for the article to be published. Yueran Li and Jinhua Wu contributed equally to this work. Yueran Li and Jinhua Wu are co-first author.

Acknowledgments

Supplementary Materials

Primers used in this study are listed in Table S1. *(Supplementary Materials)*

References

[1] M. T. Herrero, C. Estrada, L. Maatouk, and S. Vyas, "Inflammation in Parkinson's disease: role of glucocorticoids," *Frontiers in Neuroanatomy*, vol. 9, p. 32, 2015.

[2] Q. Wang, Y. Liu, and J. Zhou, "Neuroinflammation in Parkinson's disease and Its potential as therapeutic target," *Translational Neurodegeneration*, vol. 4, no. 1, p. 19, 2015.

[3] K. Saijo, B. Winner, C. T. Carson et al., "A Nurr1/CoREST pathway in microglia and astrocytes protects dopaminergic neurons from inflammation-induced death," *Cell*, vol. 137, no. 1, pp. 47–59, 2009.

[4] T. Tanaka, S. Kai, T. Matsuyama, T. Adachi, K. Fukuda, and K. Hirota, "General anesthetics inhibit LPS-induced IL-1β expression in glial cells," *PLoS One*, vol. 8, no. 12, article e82930, 2013.

[5] X. L. Gu, C. X. Long, L. Sun, C. Xie, X. Lin, and H. Cai, "Astrocytic expression of Parkinson's disease-related A53T α-synuclein causes neurodegeneration in mice," *Molecular Brain*, vol. 3, no. 1, p. 12, 2010.

[6] T. Yamada, T. Kawamata, D. G. Walker, and P. L. McGeer, "Vimentin immunoreactivity in normal and pathological human brain tissue," *Acta Neuropathologica*, vol. 84, no. 2, pp. 157–162, 1992.

[7] C. K. Glass, K. Saijo, B. Winner, M. C. Marchetto, and F. H. Gage, "Mechanisms underlying inflammation in neurodegeneration," *Cell*, vol. 140, no. 6, pp. 918–934, 2010.

[8] G. Dutta, P. Zhang, and B. Liu, "The lipopolysaccharide Parkinson's disease animal model: mechanistic studies and drug discovery," *Fundamental & Clinical Pharmacology*, vol. 22, no. 5, pp. 453–464, 2008.

[9] A. J. Herrera, A. Castano, J. L. Venero, J. Cano, and A. Machado, "The single intranigral injection of LPS as a new model for studying the selective effects of inflammatory reactions on dopaminergic system," *Neurobiology of Disease*, vol. 7, no. 4, pp. 429–447, 2000.

[10] C. S. Sankhla, "Oxidative stress and Parkinson's disease," *Neurology India*, vol. 65, no. 2, pp. 269-270, 2017.

[11] S. K. Biswas, "Does the interdependence between oxidative stress and inflammation explain the antioxidant paradox?," *Oxidative Medicine and Cellular Longevity*, vol. 2016, Article ID 5698931, 9 pages, 2016.

[12] M. von Otter, P. Bergström, A. Quattrone et al., "Genetic associations of Nrf2-encoding NFE2L2 variants with Parkinson's disease - a multicenter study," *BMC Medical Genetics*, vol. 15, no. 1, p. 131, 2014.

[13] M. von Otter, S. Landgren, S. Nilsson et al., "Association of Nrf2-encoding NFE2L2 haplotypes with Parkinson's disease," *BMC Medical Genetics*, vol. 11, no. 1, p. 36, 2010.

[14] D. Alvarez-Fischer, C. Henze, C. Strenzke et al., "Characterization of the striatal 6-OHDA model of Parkinson's disease in wild type and α-synuclein-deleted mice," *Experimental Neurology*, vol. 210, no. 1, pp. 182–193, 2008.

[15] D. Blum, S. Torch, N. Lambeng et al., "Molecular pathways involved in the neurotoxicity of 6-OHDA, dopamine and MPTP: contribution to the apoptotic theory in Parkinson's disease," *Progress in Neurobiology*, vol. 65, no. 2, pp. 135–172, 2001.

[16] M. Decressac, B. Mattsson, and A. Bjorklund, "Comparison of the behavioural and histological characteristics of the 6-OHDA and α-synuclein rat models of Parkinson's disease," *Experimental Neurology*, vol. 235, no. 1, pp. 306–315, 2012.

[17] M. Liu, Q. Zhu, J. Wu et al., "Glutamate affects the production of epoxyeicosanoids within the brain: the up-regulation of brain CYP2J through the MAPK-CREB signaling pathway," *Toxicology*, vol. 381, pp. 31–38, 2017.

[18] X. Fang, T. L. Kaduce, N. L. Weintraub et al., "Pathways of epoxyeicosatrienoic acid metabolism in endothelial cells. Implications for the vascular effects of soluble epoxide hydrolase inhibition," *Journal of Biological Chemistry*, vol. 276, no. 18, pp. 14867–14874, 2001.

[19] F. Dutheil, S. Dauchy, M. Diry et al., "Xenobiotic-metabolizing enzymes and transporters in the normal human brain: regional

and cellular mapping as a basis for putative roles in cerebral function," *Drug Metabolism and Disposition*, vol. 37, no. 7, pp. 1528–1538, 2009.

[20] M. Zimmermann, "Ethical guidelines for investigations of experimental pain in conscious animals," *Pain*, vol. 16, no. 2, pp. 109-110, 1983.

[21] P. E. Scarborough, J. Ma, W. Qu, and D. C. Zeldin, "P450 sub-family CYP2J and their role in the bioactivation of arachidonic acid in extrahepatic tissues," *Drug Metabolism Reviews*, vol. 31, no. 1, pp. 205–234, 1999.

[22] J. Li, M. Xie, X. Wang et al., "Sex hormones regulate cerebral drug metabolism via brain miRNAs: down-regulation of brain CYP2D by androgens reduces the analgesic effects of tramadol," *British Journal of Pharmacology*, vol. 172, no. 19, pp. 4639–4654, 2015.

[23] S. P. Fu, J. F. Wang, W. J. Xue et al., "Anti-inflammatory effects of BHBA in both in vivo and in vitro Parkinson's disease models are mediated by GPR109A-dependent mechanisms," *Journal of Neuroinflammation*, vol. 12, no. 1, p. 9, 2015.

[24] W. Tai, X. Ye, X. Bao, B. Zhao, X. Wang, and D. Zhang, "Inhibition of Src tyrosine kinase activity by squamosamide derivative FLZ attenuates neuroinflammation in both in vivo and in vitro Parkinson's disease models," *Neuropharmacology*, vol. 75, pp. 201–212, 2013.

[25] Y. Q. Cui, Y. J. Jia, T. Zhang, Q. B. Zhang, and X. M. Wang, "Fucoidan protects against lipopolysaccharide-induced rat neuronal damage and inhibits the production of proinflammatory mediators in primary microglia," *CNS Neuroscience & Therapeutics*, vol. 18, no. 10, pp. 827–833, 2012.

[26] R. Ren, C. Shi, J. Cao et al., "Neuroprotective effects of a standardized flavonoid extract of safflower against neurotoxin-induced cellular and animal models of Parkinson's disease," *Scientific Reports*, vol. 6, no. 1, article 22135, 2016.

[27] D. A. Johnson and J. A. Johnson, "Nrf2—a therapeutic target for the treatment of neurodegenerative diseases," *Free Radical Biology & Medicine*, vol. 88, Part B, pp. 253–267, 2015.

[28] Y. Li, G. Yu, S. Yuan et al., "14,15-Epoxyeicosatrienoic acid suppresses cigarette smoke condensate-induced inflammation in lung epithelial cells by inhibiting autophagy," *American Journal of Physiology-Lung Cellular and Molecular Physiology*, vol. 311, no. 5, pp. L970–L980, 2016.

[29] N. G. Innamorato, A. I. Rojo, A. J. Garcia-Yague, M. Yamamoto, M. L. de Ceballos, and A. Cuadrado, "The transcription factor Nrf2 is a therapeutic target against brain inflammation," *Journal of Immunology*, vol. 181, no. 1, pp. 680–689, 2008.

[30] A. Cuadrado, Z. Martin-Moldes, J. Ye, and I. Lastres-Becker, "Transcription factors NRF2 and NF-κB are coordinated effectors of the Rho family, GTP-binding protein RAC1 during inflammation," *Journal of Biological Chemistry*, vol. 289, no. 22, pp. 15244–15258, 2014.

[31] M. Pajares, A. Cuadrado, and A. I. Rojo, "Modulation of proteostasis by transcription factor NRF2 and impact in neurodegenerative diseases," *Redox Biology*, vol. 11, pp. 543–553, 2017.

[32] J. D. Wardyn, A. H. Ponsford, and C. M. Sanderson, "Dissecting molecular cross-talk between Nrf2 and NF-κB response pathways," *Biochemical Society Transactions*, vol. 43, no. 4, pp. 621–626, 2015.

[33] M. Spiecker and J. K. Liao, "Vascular protective effects of cytochrome p450 epoxygenase-derived eicosanoids," *Archives of Biochemistry and Biophysics*, vol. 433, no. 2, pp. 413–420, 2005.

[34] M. Wepler, A. Beloiartsev, M. D. Buswell et al., "Soluble epoxide hydrolase deficiency or inhibition enhances murine hypoxic pulmonary vasoconstriction after lipopolysaccharide challenge," *American Journal of Physiology-Lung Cellular and Molecular Physiology*, vol. 311, no. 6, pp. L1213–L1221, 2016.

[35] L. Shi, Z. G. Chen, L. L. Wu et al., "miR-340 reverses cisplatin resistance of hepatocellular carcinoma cell lines by targeting Nrf2-dependent antioxidant pathway," *Asian Pacific Journal of Cancer Prevention*, vol. 15, no. 23, pp. 10439–10444, 2014.

[36] H. D. E. Booth, W. D. Hirst, and R. Wade-Martins, "The role of astrocyte dysfunction in Parkinson's disease pathogenesis," *Trends in Neurosciences*, vol. 40, no. 6, pp. 358–370, 2017.

[37] X. L. Gu, C. X. Long, L. Sun, C. Xie, X. Lin, and H. Cai, "Astrocytic expression of Parkinson's disease-related A53T alpha-synuclein causes neurodegeneration in mice," *Molecular Brain*, vol. 3, no. 1, p. 12, 2010.